

AD-A106 752

TEXAS A AND M UNIV COLLEGE STATION DEPT OF METEOROLOGY F/G 4/2
PRECIPITATION FIELD AND INTRASTORM FLOW OF SUPERCELL CONVECTIVE--ETC(U)
AUG 81 D J MCMORROW AFOSR-80-0063

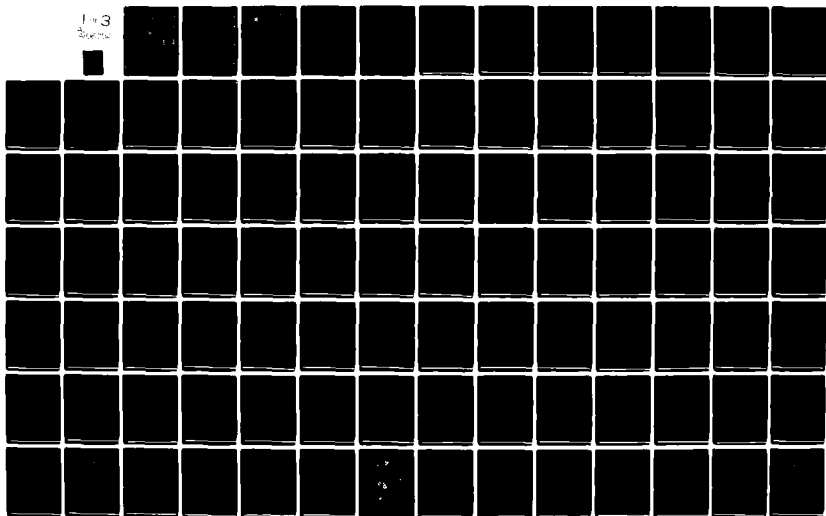
UNCLASSIFIED

AFOSR-TR-81-0699

NL

103

103



19 DOCUMENTATION PAGE		READ INSTRUCTIONS BEFORE COMPLETING FORM	
18 AFOSR TR-81-0699	2. GOVT ACCESSION NO. AD-A106752	3. RECIPIENT'S CATALOG NUMBER	
4. TITLE (and Subtitle) Precipitation Field and Intrastorm Flow of Supercell Convective Storms		5. TYPE OF REPORT & PERIOD COVERED Final report	
6. AUTHOR(s) Daniel James McMorrow		6. PERFORMING ORG. REPORT NUMBER	
7. PERFORMING ORGANIZATION NAME AND ADDRESS Texas A & M University Department of Meteorology College Station, Texas 77843		8. CONTRACT OR GRANT NUMBER(s) AFOSR-80-0063	
9. CONTROLLING OFFICE NAME AND ADDRESS Air Force Office of Scientific Research/NC Bldg. 410, Bolling AFB, DC 20332		10. PROGRAM ELEMENT, PROJECT, TASK AREA & WORK UNIT NUMBERS 61102F 2310/A1	
11. MONITORING AGENCY NAME & ADDRESS (if different from Controlling Office)		12. REPORT DATE August 1981	
13. SECURITY CLASS. (of this report) Unclassified		14. NUMBER OF PAGES 284	
15. DECLASSIFICATION DOWNGRADING SCHEDULE		16. DISTRIBUTION STATEMENT (of this Report) Approved for public release; distribution unlimited.	
17. DISTRIBUTION STATEMENT (of the abstract entered in Block 20, if different from Report)			
18. SUPPLEMENTARY NOTES			
19. KEY WORDS (Continue on reverse side if necessary and identify by block number) Doppler Radar Supercell Convection Precipitation Rate Thunderstorm Rainfall Rate Squall Line			
20. ABSTRACT (Continue on reverse side if necessary and identify by block number) Single-Doppler radar data, when supplemented by surface and upper-air information, provides good estimates of the intrastorm kinematic structure of supercell storms. Spatially derived fields of radial velocity, defined as radial stretching and cross-beam shear, can be used to identify and track major intrastorm kinematic features. These fields can be computed quickly and required neither storm motion information nor a favorable beam-flow alignment. Comparisons between multi-Doppler analyses (and numerical simulation) and the single-Doppler fields show good correlations of the updraft and downdraft zones as			

AD A106752

LEVEL II

DTIC
ELECTE
S NOV 6 1981
H

WTC FILE COPY

DD FORM 1 JAN 73 1473

UNCLASSIFIED

SECURITY CLASSIFICATION OF THIS PAGE (When Data Entered)

400161

81 TR 06 088

Well as storm inflow and outflow areas. Changes in surface precipitation rates, from isolated and squall line supercells, are reflected in changes in the intra-storm flow inferred from single-Doppler data. This offers a new technique for single-Doppler radar analyses. In addition, a detailed study of the changes in supercell surface rainfall rates, over a high-resolution raingage network, suggests that a simple linear relationship exists between the maximum point rainfall rate and the areal coverage of threshold rates of 25 mm hr-1 and 55 mm hr-1. Point-area statistical models are presented for individual rain cores, the storm rainfall, and for rainfall over a 4000 km2 watershed. This investigation is the first known detailed study of single-Doppler data and surface rainfall observed over a short time interval. Temporal changes in supercell kinematic structure are related to changes in surface rainfall rates. Supercell rainfall in several different environments are presented. The results suggest that changes in surface rainfall rates are related to changes in intra-storm kinematic flow.

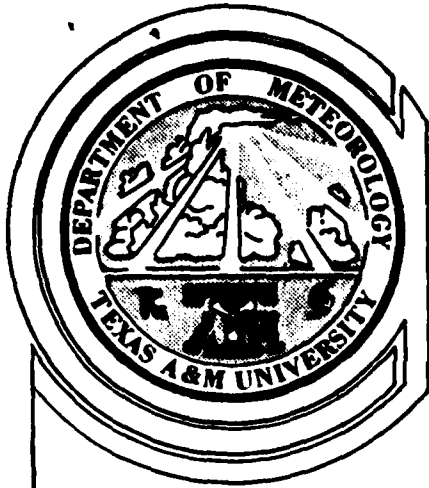
47

Accession For	
NTIS Grant	<input checked="checked" type="checkbox"/>
NTIS TAB	<input type="checkbox"/>
NTIS Document	<input type="checkbox"/>
NTIS Report	<input type="checkbox"/>
By	
Distribution	
Available Dates	
Time Interval	
A	

UNCLASSIFIED

SECURITY CLASSIFICATION OF THIS PAGE(When Data Entered)

Final
12 AUG 1981



TEXAS A&M UNIVERSITY

DEPARTMENT OF METEOROLOGY

PRECIPITATION FIELD AND INTRASTORM FLOW OF SUPERCELL CONVECTIVE STORMS

DANIEL JAMES MCMORROW

August 1981



Approved for public release.
distribution unlimited.

AIR FORCE OFFICE OF SCIENTIFIC RESEARCH (AFSC)

NOTICE OF INFORMATION TO DTIC

This technical report has been reviewed and is
approved for publication in accordance with IAW AFM 190-12.

Distribution is unlimited.

MATTHEW J. KERPER

Chief, Technical Information Division

ABSTRACT

PRECIPITATION FIELD AND INTRASTORM FLOW
OF SUPERCELL CONVECTIVE STORMS. (August 1981)

Daniel James McMorro, B.S., New York University;

M.S., New York University;

M.A., Webster College

Chairman of Advisory Committee: Dr. George L. Huebner, Jr.

Single-Doppler radar data, when supplemented by surface and upper-air information, provides good estimates of the intrastorm kinematic structure of supercell storms. Spatially derived fields of radial velocity, defined as radial stretching and cross-beam shear, can be used to identify and track major intrastorm kinematic features. These fields can be computed quickly and require neither storm motion information nor a favorable beam-flow alignment.

Comparisons between multi-Doppler analyses (and numerical simulation) and the single-Doppler fields show good correlations of the up-draft and downdraft zones as well as storm inflow and outflow areas. Changes in surface precipitation rates, from isolated and squall line supercells, are reflected in changes in the intrastorm flow inferred from single-Doppler data. This offers a new technique for single-Doppler radar analyses.

In addition, a detailed study of the changes in supercell surface rainfall rates, over a high-resolution raingage network, suggests that a simple linear relationship exists between the maximum point rainfall rate and the areal coverage of threshold rates of 25 mm hr^{-1} and

55 mm hr⁻¹. Point-area statistical models are presented for individual rain cores, the storm rainfall, and for rainfall over a 4000 km² watershed.

This investigation is the first known detailed study of single-Doppler data and surface rainfall observed over a short time interval. Temporal changes in supercell kinematic structure are related to changes in surface rainfall rates. Supercell rainfall in several different environments are presented. The results suggest that changes in surface rainfall rates are related to changes in intra-storm kinematic flow.

TABLE OF CONTENTS

	Page
ABSTRACT.	iii
ACKNOWLEDGEMENTS.	v
DEDICATION.	viii
TABLE OF CONTENTS	ix
LIST OF TABLES.	xi
LIST OF FIGURES	xiii
CHAPTER I	1
INTRODUCTION	1
Overview.	1
Previous Work	1
General.	1
Supercell Storms	2
Mesocyclones and Supercell Precipitation	4
Splitting Storms	5
Intrastorm Flow from Single-Doppler Data	7
Statement of Problem.	8
CHAPTER II.	12
DATA	12
Introduction.	12
Raingage Data	12
Radar Data.	14
Surface and Upper Air Data.	14
Error Analysis.	15
CHAPTER III	16
RAINFALL AREA-INTENSITY RELATIONSHIPS.	16
General	16
Watershed Rainfall Area and Maximum Point Rainfall Intensity	17
Storm Rainfall Area and Maximum Point Rainfall Intensity.	24
Cell Rainfall Area and Maximum Point Rainfall Intensity	27

	Page
CHAPTER IV.	30
KINEMATIC PATTERNS AND SUPERCCELL STORM MODEL	30
Introduction.	30
Single-Doppler Pattern Models	30
Supercell Model	45
CHAPTER V	50
SINGLE-DOPPLER KINEMATIC PATTERNS AND STORM MODEL, INFERENCES .	50
Merging Storms.	50
Introduction	50
Methods of Analysis.	50
Mesoscale Environment.	51
Time Sequence of Single-Doppler Fields	54
Single-Doppler Fields Plus Storm Model Interpretations .	65
Summary of Findings.	75
Mesocyclone Patterns and Rainfall	76
Introduction	76
General.	77
Time Sequence of Single-Doppler Fields	77
Single-Doppler Fields Plus Storm Model Intrepretations .	87
Summary of Findings.	104
Squall Line Supercell	105
Introduction	105
Mesoscale Environment.	105
Time Sequence of Single-Doppler Fields	107
Single-Doppler Fields Plus Storm Model Interpretations .	112
Summary of Findings.	131
Splitting Echo Case	131
Introduction	131
Mesoscale Environment.	132
Time Sequence of Single-Doppler Fields	132
Single-Doppler Fields Plus Storm Model Interpretations .	141
Summary of Findings.	150
CHAPTER VI.	152
CONCLUSIONS AND RECOMMENDATIONS.	152

	Page
Conclusions	152
Recommendations	155
REFERENCES.	156
APPENDIX A.	167
APPENDIX B.	174
APPENDIX C.	183
APPENDIX D.	196
APPENDIX E.	204
APPENDIX F.	221
APPENDIX G.	243
APPENDIX H.	245
APPENDIX I.	252
APPENDIX J.	255
APPENDIX K.	258
APPENDIX L.	262
VITA.	266

LIST OF TABLES

Table	Page
1 Comparison of linear models relating areas and rainfall rates by spatial stratification (all data)	20
2 Comparison of linear models relating areas and rainfall rates by spatial stratification (conditional on non-zero 55 mm hr ⁻¹ rate contours associated with 25 mm hr ⁻¹ rate contours)	22
3 Predictive models of surface rainfall areas for the Washita Watershed	25
B.1 Comparison of outflow error as a function of wind speed . .	180
D.1 Radial stretching calculations ($\times 10^{-3} \text{ s}^{-1}$) as a function of velocity model, maximum velocity, core size, and distance from the radar	197
E.1 Norman Doppler radar characteristics (1977)	204
F.1 Errors in potential wet-bulb temperature with altitude. . .	242
H.1 Precipitation data for Oklahoma City, Oklahoma, 1968-1977 .	247
H.2 Clock hour precipitation rate distributions (number of hours).	248
H.3 Clock hour precipitation rate distributions - annual (number of hours)	248
H.4 Estimated 1-min rainfall distribution (in hours) for Oklahoma City, OK (May)	250
H.5 Maximum grid point 15-min rainfall rates (mm hr ⁻¹) and ending times of occurrence (CST).	251
I.1 Summary of peak rainfall rates and areas of Del City-Hailstorm complex	253
J.1 Summary of peak rainfall rates and areas for the Ft. Cobb storm	256
K.1 Summary of squall-line precipitation.	259
L.1 Summary of peak rainfall rates and areas of splitting storm (Cell A) and companion storm (Cell B)	263

LIST OF FIGURES

Figure		Page
1	Example of the comparative sizes of the radar, surface mesonet, and raingage areas	13
2	Horizontal view of single-Doppler radial velocity for cyclonic vortex	32
3	Horizontal view of single-Doppler radial velocity of pure circular divergence	33
4	Idealized single-Doppler radial velocity patterns for rotational and divergent flows.	35
5	Example of horizontal superimposed single-Doppler flow patterns for pure rotation and circular divergence.	36
6	Schematic single-Doppler radial velocity patterns of a divergent circular source and a symmetric deformation field sampled over time	38
7	Sample geometry for computing cross-beam shear.	41
8	Single-Doppler flows; cyclonic and anticyclonic rotation.	43
9	Single-Doppler flows; circular divergence and convergence	44
10	Schematic precipitation model	45
11	Composite wind hodograph from the 1500 CST Ft. Sill and 1620 CST Elmore City soundings.	53
12	Total surface rainfall (in) for 20 May 1977 (adapted from Park and Sikdar, 1979).	53
13a	Del City storm and the Hailstorm (20 May 1977) 1 km time sequence of reflectivity (dBZ), contoured in 10-dBZ intervals starting at 15 dBZ	55
13b	Del City storm and the Hailstorm (20 May 1977) 1 km time sequence of radial velocity (m s^{-1}), contoured at 5 m s^{-1} intervals	56
13c	Del City storm and the Hailstorm (20 May 1977) 1 km time sequence of radial stretching ($\times 10^{-3} \text{ s}^{-1}$), contoured in $2 \times 10^{-3} \text{ s}^{-1}$ intervals greater than $2 \times 10^{-3} \text{ s}^{-1}$ (solid lines) and less than $-2 \times 10^{-3} \text{ s}^{-1}$ (dashed lines)	57

Figure	Page
13d Del City storm and the Hailstorm (20 May 1977) 1 km time sequence of cross-beam shear ($\times 10^{-3} \text{ s}^{-1}$), contoured in 2×10^{-3} intervals greater than $2 \times 10^{-3} \text{ s}^{-1}$ (solid lines) and less than $-2 \times 10^{-3} \text{ s}^{-1}$ (dashed lines).	58
14a Same as Fig. 13a, except at 5 km.	60
14b Same as Fig. 13b, except at 5 km.	61
14c Same as Fig. 13c, except at 5 km.	62
14d Same as Fig. 13d, except at 5 km.	63
15 North-south cross section 58 km west of NSSL at 1645. . . .	68
16 East-west cross section 55 km south of NSSL at 1645	69
17 Rainfall rate time sequence (mm hr^{-1}) contoured in 10 mm hr^{-1} intervals starting at 15 mm hr^{-1}	74
18a Ft. Cobb storm (20 May 1977) 1 km time sequence of reflectivity (dBZ), contoured in 10 dBZ intervals starting at 15 dBZ	78
18b Ft. Cobb storm (20 May 1977) 1 km time sequence of radial velocity (m s^{-1}), contoured at 5 m s^{-1} intervals.	79
18c Ft. Cobb storm (20 May 1977) 1 km time sequence of radial stretching ($\times 10^{-3} \text{ s}^{-1}$), contoured in 2×10^{-3} intervals greater than $2 \times 10^{-3} \text{ s}^{-1}$ (solid lines) and less than $-2 \times 10^{-3} \text{ s}^{-1}$ (dashed lines)	80
18d Ft. Cobb storm (20 May 1977) 1 km time sequence of cross-beam shear ($\times 10^{-3} \text{ s}^{-1}$), contoured in 2×10^{-3} intervals greater than $2 \times 10^{-3} \text{ s}^{-1}$ (solid lines) and less than $-2 \times 10^{-3} \text{ s}^{-1}$ (dashed lines)	81
19a Same as Fig. 18a, except at 5 km.	83
19b Same as Fig. 18b, except at 5 km.	84
19c Same as Fig. 18c, except at 5 km.	85
19d Same as Fig. 18d, except at 5 km.	86
20 Ft. Cobb storm rainfall rate time sequence (mm hr^{-1}) contoured in 10 mm hr^{-1}	88
21 North-south cross section 93 km west of NSSL at 1645. . . .	91

Figure	Page
22 North-south cross section 75 km west of NSSL at 1645. . . .	92
23 North-south cross section 75 km west of NSSL at 1715. . . .	93
24 East-west cross section 16 km north of NSSL at 1715	99
25 19 May 1977 afternoon combined hodograph.	106
26a Squall Line (19 May 1977) 1 km time sequence of reflectivity (dBZ), contoured in 10 dBZ intervals starting at 15 dBZ.	108
26b Squall Line (19 May 1977) 1 km time sequence of radial velocity (m s^{-1}), contoured at 5 m s^{-1} intervals.	109
26c Squall Line (19 May 1977) 1 km time sequence of radial stretching ($\times 10^{-3} \text{ s}^{-1}$), contoured in $2 \times 10^{-3} \text{ s}^{-1}$ intervals greater than $2 \times 10^{-3} \text{ s}^{-1}$ (solid lines) and less than $-2 \times 10^{-3} \text{ s}^{-1}$ (solid lines) and less than $-2 \times 10^{-3} \text{ s}^{-1}$ (dashed lines).	110
26d Squall Line (19 May 1977) 1 km time sequence of cross-beam shear ($\times 10^{-3} \text{ s}^{-1}$), contoured in $2 \times 10^{-3} \text{ s}^{-1}$ intervals greater than $2 \times 10^{-3} \text{ s}^{-1}$ (solid lines) and less than $-2 \times 10^{-3} \text{ s}^{-1}$ (dashed lines).	111
27a Same as Fig. 26a, except at 5 km.	113
27b Same as Fig. 26b, except at 5 km.	114
27c Same as Fig. 26c, except at 5 km.	115
27d Same as Fig. 26d, except at 5 km.	116
28 Squall Line rainfall rate time sequence (mm hr^{-1}) contoured in 10 mm hr^{-1} intervals starting at 15 mm hr^{-1}	117
29 North-south cross section 88 km west of NSSL at 1345. . . .	127
30 North-south cross section 65 km west of NSSL at 1415. . . .	129
31 Oklahoma City hodograph, 1 May 1977, 0000 GMT	133
32a Splitting storm (1 May 1977) 1 km time sequence of reflectivity (dBZ), contoured in 10 dBZ intervals starting at 15 dBZ.	134

Figure	Page
32b Splitting storm (1 May 1977) 1 km time sequence of radial velocity (m s^{-1}) contoured at 5 m s^{-1} intervals	135
33a Splitting storm (1 May 1977) 5 km time sequence of reflectivity (dBZ), contoured in dBZ intervals starting at 15 dBZ.	136
33b Splitting storm (1 May 1977) 5 km time sequence of radial velocity (m s^{-1}).	137
33c Splitting storm (1 May 1977) 5 km time sequence of radial stretching ($\times 10^{-3} \text{ s}^{-1}$) contoured in 2×10^{-3} intervals greater than $2 \times 10^{-3} \text{ s}^{-1}$ (solid lines) and less than $-2 \times 10^{-3} \text{ s}^{-1}$ (dashed lines)	138
33d Splitting storm (1 May 1977) 5 km time sequence of cross-beam shear ($\times 10^{-3} \text{ s}^{-1}$) contoured in 2×10^{-3} intervals greater than $2 \times 10^{-3} \text{ s}^{-1}$ (solid lines) and less than $-2 \times 10^{-3} \text{ s}^{-1}$ (dashed lines)	139
34 North-south Cross section 60 km west of NSSL at 1815.	144
35 North-south cross section 79 km west of NSSL at 1815.	146
36 Rainfall rate time sequence (mm hr^{-1}) contoured in 10 mm hr^{-1} intervals starting at 15 mm hr^{-1}	148
A.1 Example of comparative sizes of the Washita and Oklahoma raingage networks	168
B.1 Rainfall maps 1600-1700	176
B.2 Rainfall maps 1700-1800	177
C.1 Radial velocity isopleths for a single-Doppler radar viewing a west-to-east flow	189
C.2 Typical horizontal plane view of a mesocyclone.	191
C.3 Rotation and deformation flow fields as viewed by a single-Doppler radar	195
D.1 Change in maximum-minimum radial stretching ($\times 10^{-3} \text{ s}^{-1}$) (Linear-linear model at 50-km range).	201
D.2 Change in maximum-minimum stretching ($\times 10^{-3} \text{ s}^{-1}$) (Square-square model at 50-km range).	202
E.1 Computer processing flow.	208

Figure	Page
E.2 Computation geometry.	211
F.1 Typical unfolding	229
F.2 Spatial density spectrum.	238

CHAPTER I

INTRODUCTION

Overview

This investigation is divided into two parts. Part one attempts to determine if maximum point rainfall rates of supercell storms are related to the areal coverage of rates greater than selected threshold values. Part two contrasts the inferred kinematic fields derived from single-Doppler observations for supercell storms with fields derived from multi-Doppler observations and storm models. In addition, part two will also examine the relationship between surface rainfall and the inferred kinematic fields along with integrated liquid water. Parts one and two are related only in the sense that both deal with supercell rainfall. Results from part one are discussed in Chapter III. Results from part two are discussed in Chapter V.

Previous Work

General

Ludlam (1963) and Barnes (1976) have provided excellent reviews of the early theories of severe local storms. The severe thunderstorm model of Humphreys (1964), first published in 1914, has been largely verified by many authors (see Browning and Ludlam, 1962; Newton, 1963; and Kropfli and Miller, 1976).

This paper follows the style of the Journal of the Atmospheric Sciences.

Today, we classify thunderstorms into two basic categories—multicell and supercell storms. Multicell storms develop in an ambient wind pattern with light to moderate speed shear with little directional shear. Several cells coexist in different phases of growth. Updrafts show little tilt with height, thus forcing precipitation to fall into the updraft, which causes a rapid decay of the convection. The outflow from the precipitation-induced downdraft increases low-level convergence, and another cell develops in a preferred location (see Chisholm, 1973; Ulanski and Garstang, 1978; and Leary and Houze, 1979). This investigation concerns the supercell or steady-state thunderstorms which are discussed below.

Supercell Storms

Supercell or steady-state storms frequently persist for hours. While they comprise a relatively small portion of thunderstorms; they do provide most of the severe weather. Supercell storms can exist as isolated cells, develop from a multicell storm, or maintain their identity in a squall line configuration (Crawford and Brown, 1972). The first well documented supercell occurred in Workingham, England (Browning and Ludlam, 1962). Since then they have been reported throughout the United States, east of the Rocky Mountains, in Canada (Chisholm, 1973), and the Soviet Union (Marwitz, 1971).

Supercell storms exist in a strongly sheared environment with the wind usually veering with height. Such storms normally track to the right of the mid-level environmental wind. Hammond (1967) and Charba and Sasaki (1971) have observed storms that track to the left (severe

left-moving storms), but these are relatively rare.

In severe right-moving storms, the environmental wind causes the updraft to turn clockwise with height (Klemp and Wilhelmson, 1978) as it slopes over the colder downdraft air. The downdraft air usually originates in the mid level (Barnes, 1978a, b, c) at about 5 km and is fed by precipitation falling into it from the updraft overhead. The surface outflow of the downdraft interacts with the moist inflow of the updraft which then established a balanced or steady-state updraft-downdraft configuration. A gust front is usually observed along the line where the outflow-inflow interaction is strongest. Fankhauser (1971) and Lemon and Doswell (1979) have suggested models with two downdrafts. In Fankhauser's model they are aligned on the sides of the sloping updraft. In the Lemon and Doswell model the downdrafts are upshear (dry) and downshear (wet) with the dry downdraft originating at the 9-10 km level, which is considerably higher than the wet downdraft source at 5 km. Multi-Doppler radar analysis (Nelson, 1977 and Heymsfield, 1978), surface mesonet measurements (Charba and Sasaki, 1971; Lemon, 1976; and Barnes, 1978a), and numerical simulation (Schlesinger, 1978) support the dual downdraft model. Another feature of the supercell storm is a long anvil cloud extending from the summit. This is caused by strong winds carrying the updraft moisture that does not feed the downdraft immediately downwind. This helps to prevent the precipitation from damping the updraft. The updrafts of supercell storms are commonly observed as weak echo regions or regions of bounded weak echoes in radar observations. Not all supercell storms will have a bounded weak echo region, but severe

storms without a weak echo region are rare. On the other hand, many multicell storms do have weak echo regions that persist for a relatively short period.

Observations show that supercell storms normally acquire their low-level flow from the front of the storm and their mid-level flow from the rear or right flank. Multi-Doppler data show that the 20 May 1977 storms studied in this investigation have low-level flow entering from the right rear flank and mid-level flow entering from the left rear flank. These storms observed on 1 and 19 May 1977 provide an interesting contrast between the storms reported in the literature which have a more typical flow configuration.

Mesocyclones and Supercell Precipitation

Precipitation patterns of supercell storms have been handled in a very qualitative manner. Browning's (1964) model of severe right-moving storms shows a clockwise twisting downdraft originating in the mid level and a clockwise turning updraft. Browning's model puts the heaviest precipitation on the left storm flank. Snider (1971), in an empirical study using hourly precipitation data, reported a rainfall maximum ahead and to the left of tornado tracks. However, these maxima were frequently weak (25 mm hr^{-1} or less), and some tornadoes developed with no rainfall. Lemon et al. (1975) have suggested increased rainfalls with mesocyclones due to theory whereby precipitation is temporarily reduced due to rotation. Davies-Jones et al. (1975) reported very light rainfall with a tornadic storm observed near Norman in 1973. Brandes (1977) observed a peak storm rainfall

rate of 24 mm hr^{-1} associated with the southern flank of a severe storm in central Oklahoma that tracked toward 065° at 20 m s^{-1} . Burgess et al. (1978) investigated the relationship between mesocyclone tracks and 24-hr precipitation. They noted that some mesocyclones are associated with high rainfalls and some are not. Ulanski and Garstang (1978) studied precipitation from a variety of convective storms in southern Florida with data resolution of the same order that was used in this investigation. They found that surface convergence fields existed well before the initiation of convection. These fields could also be used to estimate storm rainfall. Their work was limited to multicell thunderstorms and rainshowers. Little effort has been spent investigating the relationship of single-Doppler kinematic patterns and rainfall.

Splitting Storms

Storms in which the original echo splits comprise a rare subset of severe storms. Brown et al. (1973) and Lemon et al. (1978) have detailed the life cycle of such storms in central Oklahoma.

Many investigators have suggested reasons for splitting radar echoes. Since these reasons are fundamental to the resulting surface precipitation, several are summarized here. Fujita and Grandoso (1968) have suggested that echoes split after anticyclonic and cyclonic wake vortices form in the lee of the reflectivity core. The cyclonic vortex propagates to the right of the environmental wind while the anticyclonic vortex moves to the left. Intensification is produced by low-level convergence along the gust front. Observational

evidence of storm cores acting as solid bodies has been reported by Heymsfield (1978) and Lemon (1976). Klemp and Wilhelmson (1978) have produced similar effects by numerical simulation with a moist fully-compressible three-dimensional model. This model showed that echo splitting was initiated by a precipitation induced downdraft that splits the low-level updraft. Rotating vortices were not required for initiating the splitting process. Later simulations of multiple splitting storms (see Wilhelmson and Klemp, 1978) have shown that a split can result from a new updraft on the right flank that arises from convergence associated with an extension of the gust front to the right of old updrafts. If this outflow is too strong, it will choke off the moisture source and initiate dissipation. If the outflow is too weak (low rainfall rates), the storm must be maintained by an intense low-level inflow. In either case splitting is unlikely.

Another important parameter in initiating splitting is the vertical wind profile (e.g., Schlesinger, 1978; Cotton and Tripoli, 1978; and Wilhelmson and Klemp, 1978). Apparently, strong shear at or just above the cloud base is required for splitting. In addition, low-level inflow must balance the gust front outflow to maintain a strong low-level convergence source. Klemp and Wilhelmson (1978) have shown that winds which veer with height will enhance a right-moving storm, while backing winds strengthen a left-moving storm after splitting.

The splitting storm that was examined in this study (1 May 1977) existed in a weakly veered environment. Many of the observations will be compared with those of Bluestein and Sohl (1979) who have studied the same storm.

Intrastorm Flow from Single-Doppler Data

Ideally, one would like to estimate two basic kinematic quantities from single-Doppler data, viz., horizontal velocity divergence and the vertical component of relative vorticity. With these quantities one can estimate vertical fluxes through the continuity equation after making some assumptions (Brown et al., 1980). To calculate velocity divergence (or vorticity), however, one needs to know the true wind velocity. With single-Doppler data, the Doppler velocity contains information only on the radial component of the true velocity. This has led investigators to different approaches in an effort to approximate the horizontal storm flow.

Lhermitte (1969) suggested that flow lines could be constructed if one assumed that the zero relative radial velocity represents horizontal motion perpendicular to the radar beam. The other interpretation of zero velocity, i.e., calm wind, was considered unlikely. The second assumption is that changes in the radial velocity along a radar radial were due to a change in direction of the maximum isopleth line, i.e., a turning of the flow. No speed changes were allowed so that the spacing of the flow lines did not represent the speed of the flow. Kraus (1973) and Lemon et al. (1978) have used this technique successfully.

A different approach was proposed by Peace et al. (1969). Their theory assumes that the intrastorm flow field is in a steady state with reference to a coordinate frame that is moving with the storm echo. This implies that time variations at a fixed point in space are caused only by the displacement of a steady-state field. A

single-Doppler radar viewing a given volume in the echo from two different aspects (at two different times) of steady-state flow is equivalent to having two radars (at two different locations) viewing the volume at the same time. Bonesteele and Lin (1978) have used a variation of this approach to model the storm flow with synthetic dual-Doppler data. In many cases, especially supercell storms, the steady-state assumption appears to work well.

The approach used in this study involves an examination of the spatial derivative fields of the radial velocity defined as radial stretching and cross-beam shear. Battan and Theiss (1971) and Donaldson et al. (1972) have used these deformations in an effort to explain the variance of Doppler spectrum-width fields but with little success. The shears accounted for approximately 15% of the variance. Apparently changes in the spectrum width are due to eddies smaller than the radar sampling volume. A comment in the paper by Donaldson et al. (1972) however, provided the germ for this investigation. "Differences in radial shear (radial stretching in the report) do appear to be significantly related to convective intensity and to scale."

Statement of Problem

This investigation is divided into two parts, both involving supercell thunderstorms. The first part is to determine whether or not a relationship exists between the maximum surface point rainfall rate and the areal coverage of rainfall rate above selected threshold values. The second part is to determine whether or not the kinematic

fields inferred from single-Doppler radar data, supplemented with mesoscale surface and upper air data, can be used to sense changes in the intrastorm structure. An additional part of the investigation will be to determine whether or not the changes in the inferred kinematic fields of radial stretching and cross-beam shear of supercell storms are related to changes in surface rainfall rates. Radial stretching and cross-beam shear fields are spatial derivative fields of the radial velocity and are discussed in detail in Appendix C.

Part one will be examined by statistically testing the following null hypotheses.

(1) There is no relationship between the maximum watershed grid point surface rainfall rate for supercell storms and the total watershed area encompassing a 25 mm hr^{-1} rate or a 55 mm hr^{-1} rate.

(2) There is no relationship between maximum storm grid point surface rainfall rate from supercell storms and the total storm area encompassing a 25 mm hr^{-1} rate or the 55 mm hr^{-1} rate.

(3) There is no relationship between maximum cell grid point surface rainfall rate from supercell storms and the total cell area encompassing a 25 mm hr^{-1} rate or the 55 mm hr^{-1} rate.

The first hypothesis for part two is that supercell kinematic features, inferred from single-Doppler, mesoscale surface and upper air data, are related to the true kinematic structure of the storm. To test this hypothesis the "true kinematic structure" is defined as that observed by multi-Doppler observations. When these data are not available the test is made against published storm models, preferably derived from multi-Doppler data. Several specific sub-hypotheses will

be tested to build support for the main hypothesis. They are:

(1) Supercell updraft regions can be located by single-Doppler radar and supplemental data in the middle and lower levels of the storm.

(2) Supercell downdraft regions can be inferred by the same data.

(3) The alignment of the intrastorm flow and the radar beam is not crucial in gaining significant information about storm flow.

(4) Complex kinematic processes, such as echo splitting, can be sensed with single-Doppler data.

(5) Inferred kinematic patterns of isolated, splitting, merging, and squall line supercells are similar.

The second major hypothesis for part two is that changes in inferred kinematic structure of supercell storms are directly related to changes in surface rainfall rates. The sub-hypotheses to be tested are:

(1) Changes in mid- and low-level radial contraction and cross-beam shear are related to changes in surface rainfall rates.

(2) Inferred kinematic fields give better estimates of short-term changes in surface precipitation than conventional reflectivity observations.

This research is unique in several respects. It documents small-scale supercell rainfall rate fluctuations for short time intervals over a high resolution raingage network. It also details the surface rainfall patterns resulting from a splitting echo, merging cells, and supercells with mesocyclones. Thus far, Doppler radar research has

not been exploited in hydrologic research. The interaction of intra-storm kinematic flow with surface precipitation has been largely ignored. This research addresses the more difficult problem of using single-Doppler radar data to sense changes in surface rainfall rates. Single-Doppler two-dimensional kinematic patterns are developed for rotational and divergent flows. The spatial derivative fields of the radial velocity are offered as a new method for sensing significant changes in intrastorm flow. Temporal histories of the radial stretching and cross-beam shear fields provide a new technique for gleaned additional information from single-Doppler radar data. This research also shows that the inherent ambiguity of single-Doppler radar data and unfavorable beam-flow alignment are not a serious problem in supercell storms, especially in an environment with strongly veering wind.

CHAPTER II

DATA

Introduction

Four separate data sources were used in this investigation: surface raingage data, single-Doppler radar data, standard meteorological surface observations from a mesoscale network, and mesoscale rawinsonde data. As a part of this study computer techniques were designed to grid and analyze objectively the first two data types; these are described in detail in Appendices A and B. The surface mesonet data were gridded and objectively analyzed by the NSSL. Most of the rawinsonde data were also processed by the NSSL. A computer program was written to compute mesoscale divergence and potential wet-bulb temperature.

Raingage Data

A comprehensive discussion of the processing of the rainfall data is described in Appendix A. In brief, the data were recorded in analog form. After being digitized they were placed on a rectangular grid by a technique described by Barnes (1973). The gridded field was then objectively contoured by an objective analysis routine.

The grid box and outline of the raingage network is illustrated in Fig. 1. The radar grid and the rainfall grid are identical.

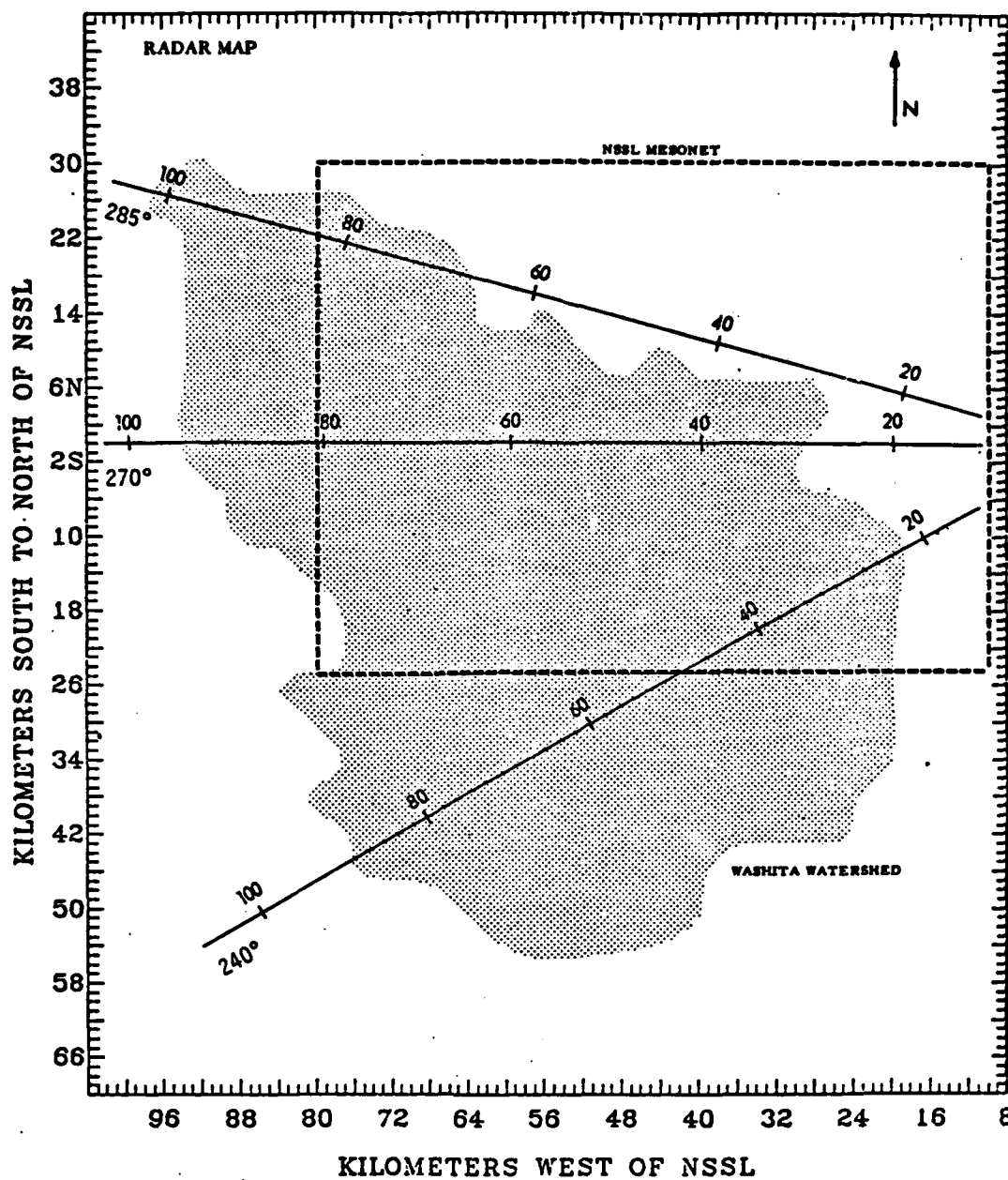


Fig. 1. Example of the comparative sizes of the radar, surface mesonet, and raingage areas.

Radar Data

The data from the NSSL Norman Doppler radar were used in this investigation. Three observed radar fields, namely, reflectivity, radial velocity, and spectrum width were investigated; the fields of vertically integrated liquid water (above and below 4 km), radial stretching, and cross-beam shear were computed and analyzed.

Appendix E describes the details of the data processing. Raw uncalibrated data were used as input. After the velocity data were adjusted for folding, the three basic Doppler measurements were placed on a three-dimensional grid using an exponential weighting function with a circular radius of influence. All derived fields were calculated from the gridded data. Horizontal or vertical cross sections were then produced to estimate changes in intrastorm flow.

Surface and Upper Air Data

The NSSL mesometeorological network was used to estimate the surface fields. Objectively analyzed maps of streamflow, wind components, temperature, dew point, pressure, divergence, vorticity, mixing ratio, and isotachs were examined.

Most of the upper air data were acquired from the NSSL upper-air network, as described by Ray et al. (1977). This network consists of four stations approximately 100 km apart and the data were taken at approximately 90 min intervals. Synoptic rawinsonde data were also used.

Error Analysis

Every effort was made to estimate and minimize the effects of possible errors in the original data. These procedures are detailed in Appendix B for the radar data and Appendix F for the radar and mesoscale data.

CHAPTER III

RAINFALL AREA-INTENSITY RELATIONSHIPS

General

In convective rainfalls, the relationship between rainfall area and point intensity is not always clear. Gringorten (1976) has examined this problem by employing a Monte Carlo approach with multi-station inputs. Winner (1968) and McMorow (1978) have examined similar relations for point intensities and line distributions by a variety of curve-fitting techniques. These approaches are each restricted by the complexity of the problem.

One can easily visualize several scenarios, all of which are reflected in the sample data used in this study. As precipitation rate increases, the area of a preselected threshold rate may grow. However, the precipitation may fall in a small intense core with a high rate gradient as is common in tropical convective rainfall. This would imply a sharp increase in the point rainfall with only a small increase (or perhaps a decrease) in the threshold area. In cases prior to thunderstorm or supercell development, a common feature is several small isolated showers with small threshold areas and point rates. During the mature stages of convective cells, extremely high rainfall intensities die out, but relatively large areas of light to moderate showers remain. In a combined data set, these competing effects tend to mask area-intensity relations. Consequently expectations from this portion of the study were modest.

Watershed Rainfall Area and Maximum Point Rainfall Intensity

Three basic items of data were used in these analyses: maximum grid-point rainfall rates and the areas of the 25 mm hr⁻¹ and 55 mm hr⁻¹ rates. Each 15 min map was examined for minimum threshold area of 25 mm hr⁻¹. Maps that did not have a 25 mm hr⁻¹ contour were not used. The areas were computed with a polar planimeter. Each area was read at least three times. Many maps contained several 25 mm hr⁻¹ threshold areas. The "map area" was computed by totaling all the threshold areas. Consequently, many maps included areas not directly associated with the point maximum intensity. This technique was selected in an effort to estimate a total watershed area-point relationship. A later section examines the direct relationship between maximum point rainfall and cell area associated with the maximum intensity. Conclusions were tested at the 90% level of significance. An F test was used to determine the linearity of the models. The amount of variance accounted for by the model was tested by the coefficient of determination (R^2). The coefficient of determination estimates the amount of association between the regression parameters. High positive values (near + 1.0) indicate a strong direct relationship. One must view the implications drawn from R^2 values (and the F ratio test) with caution, especially when the sample size changes. An increase in R^2 with an increase in sample size may not mean additional significance. Also, large R^2 values show only a mathematical link and do not necessarily imply a cause-effect relationship. The reader is reminded that the data in this investigation are not strictly independent random samples, thus implying that a high R^2 may occur for

other than physical reasons.

The residual plots were also used to test the assumption for using linear regression. All models showed the residual errors to be normally distributed with a mean of zero and a constant variance. It was assumed that these errors were uncorrelated random variables. A second requirement for using linear regression is a linear relationship between the dependent and independent variables. This condition was assumed to be valid from heuristic reasoning that rainfall rate and rainfall area are probably related in a simple manner. The third assumption, and the most difficult to accept, is that the observed values were measured without error. Huff (1970) has reported errors of 5% in the rainfall catch. In some cases errors climb as high as 40% (Woodly et al., 1975). Systematic sampling errors, such as clock time errors, have been corrected. It is assumed that no systematic error is introduced in the data reduction and objective analysis process.

The data consisted of 58 samples of which 36 contained areas with rates equal to or greater than 55 mm hr^{-1} . Areas of 25 mm hr^{-1} rates, not associated with areas of 55 mm hr^{-1} , ranged from 1 km^2 to 365 km^2 . This wide variation does not appear to be related to rainfall rate. A linear model of these data, with the 25 mm hr^{-1} area as the independent variable, accounted for only 28% of the variance. Other models also performed poorly. In comparison, the unconditional linear model (all data) with 25 mm hr^{-1} and 55 mm hr^{-1} areas as the independent variables accounts for 76% of the variance. A linear model accounting

for interaction of the 55 mm hr⁻¹ and 25 mm hr⁻¹ areas had an R² value of 0.800. With these models stratified to evaluate the independent effects of the 25 mm hr⁻¹ areas and the 55 mm hr⁻¹ areas, the R² values are 0.73 and 0.71, respectively (see Table 1). These data appear to show that a 55 mm hr⁻¹ area threshold is required to achieve a significant area-intensity relationship. Given a 55 mm hr⁻¹ area, with the 25 mm hr⁻¹ areas (which are poorly correlated with intensity for weak rainshowers) filtered out, does not improve the area-intensity relationship. Only a slight increase in the R² is noted in the two parameter models.

Table 1 also contains a linear model relating the 55 mm hr⁻¹ area to the 25 mm hr⁻¹ area. The high R² of this model (0.841) is especially interesting because of the 58 samples, 22 are composed of a 25 mm hr⁻¹ area with a zero 55 mm hr⁻¹ area. In spite of this poorly correlated subset, the model suggests a strong direct relation between the two threshold areas. This is also reflected in the area-intensity models. The model that accounts for inter-correlations (three parameter model) accounts for significantly more variance than the principal effect (two parameter) model.

Table 2 shows similar models conditional on having a 55 mm hr⁻¹ area. Again, the interaction model performs best, but a significance test of the interaction effect failed at the 90% level by a considerable margin (15%). This suggests that once the data are filtered in this manner, area interactions become less important. A comparison of Tables 1 and 2 also reveals lower R² values when the poorly correlated 25 mm hr⁻¹ area-rate data are removed. This is probably a relative

TABLE 1. Comparison of linear models relating areas and rainfall rates by spatial stratification (all data).

MODEL CLASS	WATERSHED	STORM	CELL
Linear Model: Rate = β_3 (area 55) + β_2 area 55 + β_1 area 25 + β_0			
# Samples	58	92	92
R^2	0.800	0.777	0.803
Linearity Sig at 90% Level	Yes/Yes/Yes	Yes/Yes/Yes	Yes/Yes/Yes
β_3 /SE β_3	(-0.0003)/(0.00008)	(-0.00004)/(0.00006)	(-0.0006)/(0.00008)
β_2 /SE β_2	0.39/0.01	0.46/3.06	0.62/0.07
β_1 /SE β_1	0.06/0.02	0.07/0.02	0.09/0.02
β_0 /SE β_0	45.45/4.31	43.57/3.06	41.99/2.78
Linear Model: Rate = β_2 area 55 + β_1 area 25 + β_0			
# Samples	58	92	92
R^2	0.756	0.683	0.672
Linearity Sig at 90% Level	Yes/Yes	Yes/Yes	Yes/Yes
β_2 /SE β_2	0.12/0.05	0.22/0.05	0.25/0.06
β_1 /SE β_1	0.06/0.02	0.13/0.06	0.05/0.02
β_0 /SE β_0	49.64/4.46	50.25/3.34	50.33/3.29

SE = Standard error. The linearity test is made on each coefficient in the model from β_3 thru β_1 .

TABLE 1. (Continued).

MODEL CLASS	WATERSHED	STORM	CELL
Linear Model: Rate = β_1 area 55 + β_0			
# Samples	58	92	92
R^2	0.714	0.674	0.650
Linearity			
Sig at 90% Level	Yes	Yes	Yes
β_1 /SE β_1	0.26/0.02	0.30/0.02	0.27/0.03
β_0 /SE β_0	57.30/3.97	53.61/2.92	54.01/3.06
Linear Model: Rate = β_1 area 25 + β_0			
# Samples	58	92	92
R^2	0.734	0.627	0.600
Linearity			
Sig at 90% Level	Yes	Yes	Yes
β_1 /SE β_1	0.10/0.01	0.11/0.01	0.12/0.01
β_0 /SE β_0	46.43/4.37	46.10/3.45	47.63/3.55
Linear Model: area 55 = β_1 area 25 + β_0			
# Samples	58	92	92
R^2	0.841	0.840	0.758
Linearity			
Sig at 90% Level	Yes	Yes	Yes
β_1 /SE β_1	0.34/0.02	0.34/0.02	0.30/0.02
β_0 /SE β_0	-27.74/10.70	-17.42/6.12	-10.90/6.05

TABLE 2. Comparison of linear models relating areas and rainfall rates by spatial stratification (conditional on non-zero 55 mm hr⁻¹ rate contours associated with 25 mm hr⁻¹ rate contours).

MODEL CLASS	WATERSHED	STORM	CELL
Linear Model: Rate = β_3 (area 55) * (area 25) + β_2 area 55 + β_1 area 25 + β_0			
# Samples	36	47	47
R ²	0.700	0.651	0.687
Linearity			
Sig at 90% Level	No/Yes/Yes	Yes/Yes/Yes	Yes/Yes/Yes
β_3 /SE β_3	(-0.0001)/(0.00009)	(-0.0002)/(0.00007)	(-0.00004)/(0.0001)
β_2 /SE β_2	0.22/0.11	0.33/0.08	0.45/0.08
β_1 /SE β_1	0.04/0.02	0.04/0.02	0.07/0.02
β_0 /SE β_0	68.76/7.48	66.37/6.33	61.64/5.90
Linear Model: Rate = β_2 area 55 + β_1 area 25 + β_0			
# Samples	36	47	47
R ²	0.677	0.590	0.566
Linearity			
Sig at 90% Level	Yes/Yes	Yes/No (by 54%)	Yes/No (by 14%)
β_2 /SE β_2	0.11/0.05	0.19/0.06	0.19/0.06
β_1 /SE β_1	0.02/0.02	0.01/0.02	0.02/0.02
β_0 /SE β_0	73.18/6.51	76.53/5.49	75.79/5.55

TABLE 2. (Continued).

MODEL CLASS	WATERSHED	STORM	CELL
Linear Model: Rate = β_1 area 55 + β_0			
# Samples	36	47	47
R^2	0.648	0.588	0.552
Linearity			
Sig at 90% Level	Yes	Yes	Yes
β_1 /SE β_1	0.19/0.02	0.21/0.03	0.26/0.03
β_0 /SE β_0	79.51/5.47	77.64/4.90	78.53/5.06
Linear Model: Rate = β_1 area 25 + β_0			
# Samples	36	47	47
R^2	0.633	0.510	0.475
Linearity			
Sig at 90% Level	Yes	Yes	Yes
β_1 /SE β_1	0.07/0.01	0.07/0.01	0.08/0.01
β_0 /SE β_0	69.77/6.61	74.43/5191	75.39/6.03
Linear Model: Area 55 = β_1 area 25 + β_0			
# Samples	36	47	47
R^2	0.802	0.815	0.712
Linearity			
Sig at 90% Level	Yes	Yes	Yes
β_1 /SE β_1	0.35/0.03	0.34/0.02	0.29/0.03
β_0 /SE β_0	-30.71/20.49	-11.26/13.06	-2.11/13.03

effect. The 25 mm hr^{-1} areas are bounded by 25 to 54 mm hr^{-1} rates. If this subset is examined in isolation, a large area variation ($0-365 \text{ km}^2$) exists and poor correlations result. The area variations for the entire data set however, are considerably larger. This is due to the high variation in the area data ($23-1215 \text{ km}^2$ for 25 mm hr^{-1} areas) conditional on a 55 mm hr^{-1} contour. While the area-intensity relationships for data conditional on no 55 mm hr^{-1} show poor correlations, they tend to anchor the regression curves in the larger data sample to a relatively small dynamic range in the area variations.

A possible application of these results would be a method of estimating total watershed area rainfall based on monitoring the maximum precipitation rate over a raingage network. It should be stressed that this experiment was not designed for the purpose of deriving a prediction relation. The maximum point values are grid-point values, not actual station values, both of which probably underestimate the true rainfall. Nonetheless, the data have been reworked for area prediction to show that no significant difference exists in the model results (see Table 3). In practice, confidence intervals would be required for the regression line to formalize the probabilistic prediction process.

Storm Rainfall Area and Maximum Point Rainfall Intensity

This section describes the simple linear regression models relating grid-point maximum rainfall and the 25 mm hr^{-1} and 55 mm hr^{-1} threshold storm areas. Instead of relating one maximum point rainfall to total watershed area, now the maximum point rainfalls and areas for

TABLE 3. Predictive models of surface rainfall areas for the Washita Watershed.

MODEL TYPE: WATERSHED		
	ALL DATA	CONDITIONAL ON A 55 mm hr ⁻¹ AREA
Linear Model: Area 55 = β_1 rate + β_0		
# Samples	58	36
R ²	0.714	0.649
Linearity		
Sig at	Yes	Yes
90% Level		
β_1 /SE β_1	2.72/0.23	3.40/0.43
β_0 /SE β_0	-126.66/22.04	-212.25/50.13
Linear Model: Area 25 = β_1 rate + β_0		
# Samples	58	36
R ²	0.734	0.634
Linearity		
Sig at	Yes	Yes
90% Level		
β_1 /SE β_1	7.46/0.60	8.66/1.13
β_0 /SE β_0	-244.07/57.45	-397.57/132.01

each storm are examined to determine if higher correlations exist on a smaller scale. Effectively, this scale reduction reduces the averaging area and refine possible conclusions about area-intensity relationships.

The input data were examined in the same manner discussed in the previous section. Again, the 25 mm hr⁻¹ and 55 mm hr⁻¹ areas may contain some areas not directly associated with the maximum core. Each storm was stratified into a maximum of four cells. Each 15-min map contained from one to three active storms. This process increased the data sample from 58 to 92. Two basic data sets were analyzed (all data, and conditional on a 55 mm hr⁻¹ area) in various stratifications. Of the 92 samples, 45 contained no 55 mm hr⁻¹ areas, about 12% more than the watershed sample.

The interarea correlations (all data) still maintained a 0.84 R² value, but the variance in this relation was now reduced by 40% in comparison to the watershed model. This may account for the increase in R² from the two parameter to the three parameter model. In the watershed model, this difference was a mere 0.04. In the storm model, the difference is 0.09. A similar, but less dramatic improvement, was noted in the models in Table 2 for the conditional data set. Table 2 also shows that, in the two parameter storm model, the 25 mm hr⁻¹ area failed the 90% significance test. When interaction was considered, the same parameter became significant. Apparently, area interaction is more important in small-scale area-intensity relationships. The reduction in R² values for the storm model prompted additional checks of the data and the models used. The hypothesis for this section was

that decreasing the scale size would improve the area-intensity relationships. The poorer R^2 values for the storm models may illustrate a degree of statistical confounding discussed previously. Increasing threshold area with increasing point rate may be the dominant effect, but it may not be the only effect resident in the sample. In an experiment with minimum controls, such as this investigation, one can only speculate about masking or secondary effects.

Cell Rainfall Area and Maximum Point Rainfall Intensity

In this section the relationships between maximum grid-point rainfall for each storm are correlated with the areas of the 55 mm hr^{-1} and 25 mm hr^{-1} contours. Some areas not directly associated with the maximum cells are included in the area tabulations. A direct comparison between each cell's maximum rate and its threshold areas is not possible with these data because of overlapping effects. The results of the previous sections suggest an hypothesis that the linear models of maximum cell intensity and threshold areas will have poorer correlations than the storm intensity-area models. (Note that the rate variables are the same in the cell-area and storm-area models; the threshold areas, however, are different.)

The results of the cell intensity-area models are summarized in Tables 1 and 2. The interaction effect, as revealed in the 25 mm hr^{-1} area and 55 mm hr^{-1} area models, shows poorer R^2 values than the previous models. Scatter plots of these data showed a slight tendency toward a quadratic model. Higher-order models did not account for additional variance. The interaction models performed significantly

better than the two parameter models for "all data" and "data conditional on a 55 mm hr⁻¹ contour." While the cell intensity-area three parameter models explained more of the variance than the storm intensity-area models, the reverse was true for the two parameter (and stratified) models. This may imply that interaction is a more important factor in the cell intensity-area models, but the improvement in the R^2 values is small enough to view such a conclusion with caution. The cell intensity-area model group contained the lowest overall R^2 values. Scatter and residual plots were critically examined to estimate if the models or the data were responsible for the increase in unexplained variance. These results suggest that simple adjustment of the model will not improve the R^2 values over those derived from simple linear regression. However, cell intensity-area data do have less variance than the previous data groupings. While the dominant effect of increasing area with increasing rainfall rate is still clearly evident, the overall strength of other effects or noise have become more important. This trend of lowering correlations leads to speculation about the direct link between cell rainfall rates and cell areas. If all cells were examined within each storm instead of only the maximum intensity cell, one might expect poorer correlations between preselected threshold areas and rainfall. These ideas cannot be tested with the data resolution used in this study.

In summary, maximum grid-point rainfall rates and rainfall areas appear to be related by simple linear regression models. Considering the uncontrolled nature of this experiment the correlations are surprisingly good. These correlations would probably decrease if the

data were truly random samples. Nonetheless, the best relations are observed when large spatial averaging is employed, as in the watershed models. The correlations weaken as the scale of investigation is reduced to the intrastorm scale. This effect appears to be due to a slightly poorer model performance in accounting for the variance.

Chapter I contained three null hypotheses that were tested in this chapter. Briefly, they all stated no relationship would exist between rainfall rates and threshold rate areas in supercell storms. Based upon the good correlations the author concludes high rainfall rates are directly related to large areas of selected threshold rates in supercell storms.

CHAPTER IV

KINEMATIC PATTERNS AND SUPERCELL STORM MODEL

Introduction

A discussion of some of the details of radar theory and the basic ideas of Doppler radar are summarized in Appendix C. Readers unfamiliar with Doppler radar may find that Appendix helpful in providing a background for the theory developed in this chapter.

This chapter briefly documents the standard kinematic patterns of radial velocity for a cyclonic vortex. It then develops new kinematic patterns of radial stretching and cross-beam shear for anti-cyclonic vortices, and circular divergence and convergence features as seen by a single-Doppler radar. A basic supercell storm model is also outlined with emphasis on single-Doppler patterns of the kinematics of the storm.

Single-Doppler Pattern Models

Most of the recent signature recognition work involving single-Doppler radar has dealt with vortex identification (see Lemon et al., (1978). Donaldson's (1970) suggestions of semi-objective criteria for vortex recognition have been used by Burgess (1976) to sense mesocyclones and Brown and Lemon (1976) to sense small-scale tornadic rotations. The basic model of a Rankine combined vortex describes the flow across and outside the rotating area and shows the vortex to act as a solid rotating cylinder. These ideas have been confirmed by numerous investigators using multi-Doppler systems (see Brandes, 1977

and Heymsfield, 1978).

Fig. 2 illustrates the Rankine vortex model. When sampled across a series of radar radials, radar radial velocity has the characteristic profile shown in Fig. 2. Since two separate zones of rotation exist, the radial velocity profile can be written:

$$v_t = \begin{cases} a_1 r_v, & r_v \leq r_1 \\ a_2 / r_v, & r_v > r_1 \end{cases}$$

where v_t = tangential velocity of the vortex,

v_{\max} = maximum tangential velocity in the vortex,

r_v = a distance from the center of the vortex,

$a_1 = v_{\max} / r_1$, radius of maximum tangential speed,

r_1 = the distance to the boundary of solid rotation,

and $a_2 = v_{\max} r_1$.

An analogous development can be shown for purely divergent flow (source or sink). Fig. 3 illustrates the geometry of the flow patterns for an extended circular source. In this model a parcel will experience increasing velocity as it moves from the center to the core boundary and decreasing velocity thereafter. Analytically this formulation can be described as:

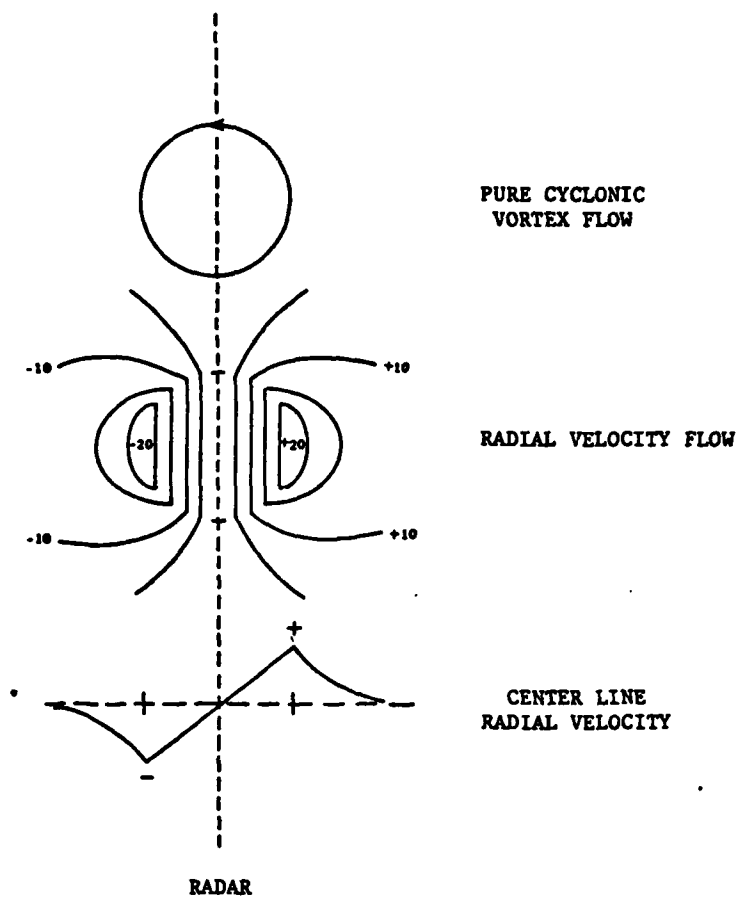


Fig. 2. Horizontal view of single-Doppler radial velocity for cyclonic vortex.

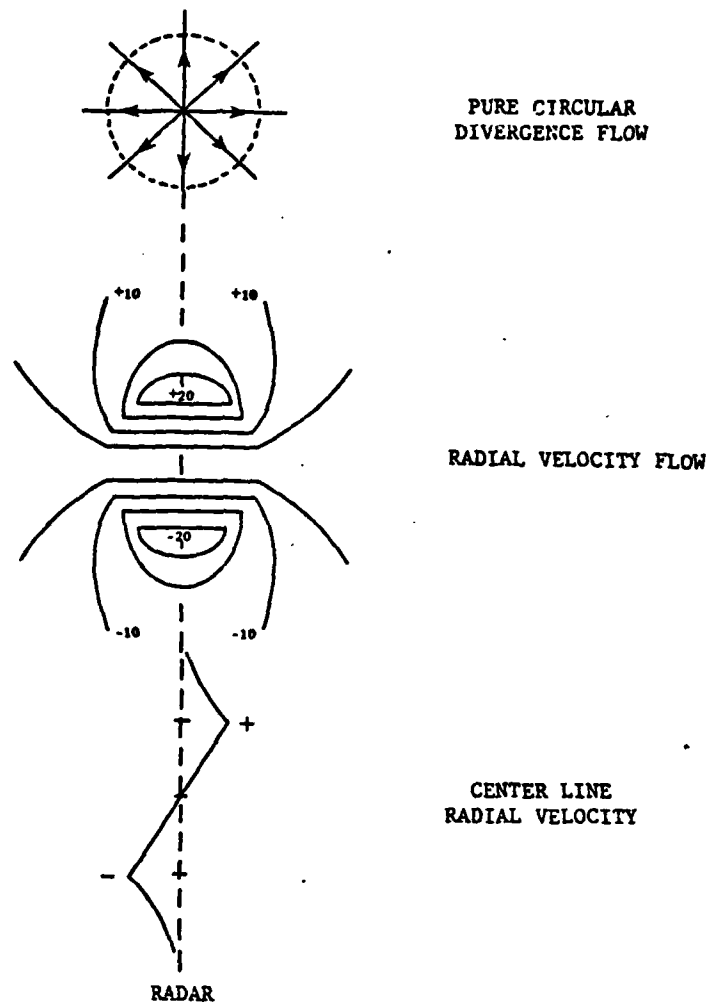


Fig. 3. Horizontal view of single-Doppler radial velocity of pure circular divergence.

$$v_r = \begin{cases} a_1 r_D, & r_D \leq r_1 \\ a_2 / r_D, & r_D > r_1 \end{cases},$$

$$a_1 = \frac{v_{\max}}{r_1}, \quad a_2 = v_{\max} r_1.$$

where v_r = radial flow

r_D = distance from source center

r_1 = distance to velocity maximum (v_{\max}).

Implicit in this formulation is a change in the sign of the flow. The source (or sink) flow is purely radial with respect to the center of the system of sources (or sinks). This will result in a new radar radial velocity signature as illustrated in Fig. 4 with maximum radar-relative radial velocity contours aligned along the radar beam.

Such idealized patterns are not likely to reveal themselves in the single-Doppler velocity maps except under extremely fortuitous circumstances. Many times the beam is not aligned exactly along the flow center line or problems with beam filling make signature recognition difficult. Frequently, two or more fields will superimpose their flow as shown in Fig. 5. Here the effects of divergence and convergence on a cyclonic vortex are evident. When the rotation angle, measured from a line perpendicular to the radar beam, (ϕ), approaches 45° , it becomes unclear if the pattern is due mostly to rotation or a source (sink). Knowledge of the intrastorm location of the patterns and observations over several radar tilt sequences are often helpful in distinguishing the flow patterns. As with the Rankine vortex

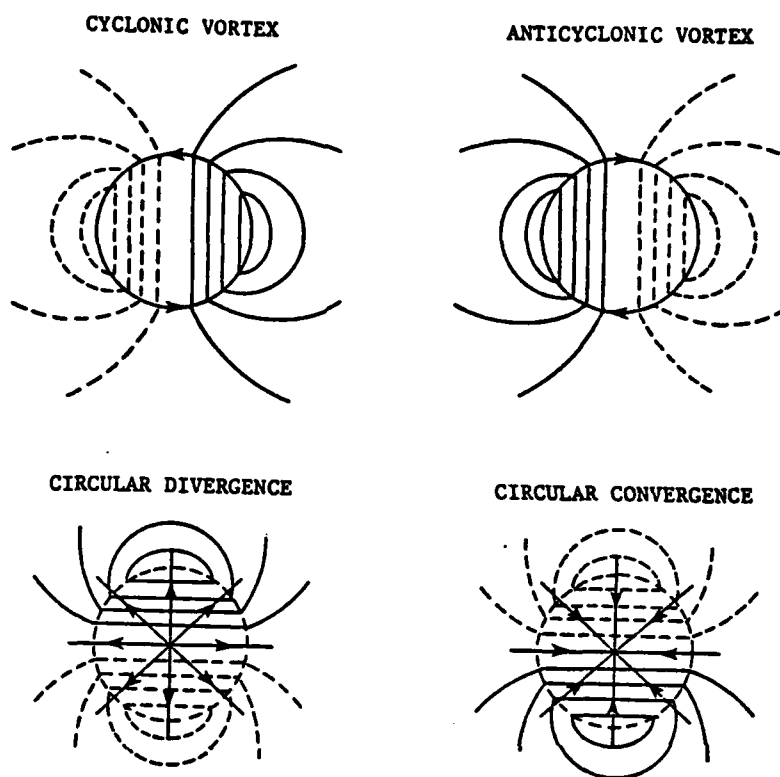
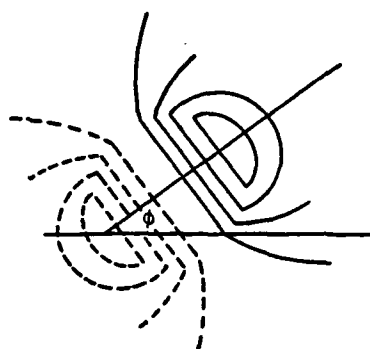
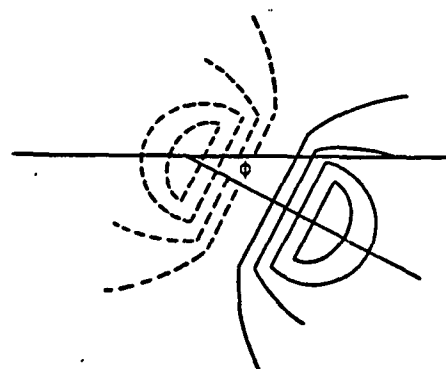


Fig. 4. Idealized single-Doppler radial velocity patterns for rotational and divergent flows. (Solid lines represent flow away from and dashed lines represent flow toward the radar). Radar at bottom of page.



VORTEX WITH POSITIVE VORTICITY
AND DIVERGENCE



VORTEX WITH POSITIVE VORTICITY
AND CONVERGENCE

Fig. 5. Example of horizontal superimposed single-Doppler flow patterns for pure rotation and circular divergence. Radar at bottom of page, solid lines indicate flow away, dashed lines are flow toward the radar.

model, there is always some uncertainty in deciding whether or not an apparent source (sink) pattern represents divergence (convergence) or merely a deformation field. As Fig. 6 illustrates, viewing a signature pattern over time gives some clue to solving this problem. A deformation field pattern which will look the same as an invariant isotropic divergence field at a particular instant, will look different as the pattern tracks across the viewing angle. At 45° from the original location, the deformation field will show zero center-beam radial velocities, while a purely divergent field will maintain its positive-zero-negative (PZN) pattern along the radial. Beyond 45° , the deformation field will reverse its pattern while the divergence field will remain unchanged.

There are other situations with mixed patterns. A deformation field could be superposed upon a rotational flow so as to present the same face toward the radar throughout its life cycle. A divergence (convergence) field could weaken or strengthen, thus misleading one to conclude that a deformation field exists. Considering all possible options involving flow superpositioning, one sees that unambiguous conclusions are impossible. While this is true, meshing single-Doppler flow patterns with background knowledge of storm models can aid in improving our understanding of storm kinematic processes.

An underlying goal of pattern recognition is to estimate significant kinematic quantities. The two most sought after quantities are velocity divergence (δ) and vorticity (ζ). In polar form they are defined as:

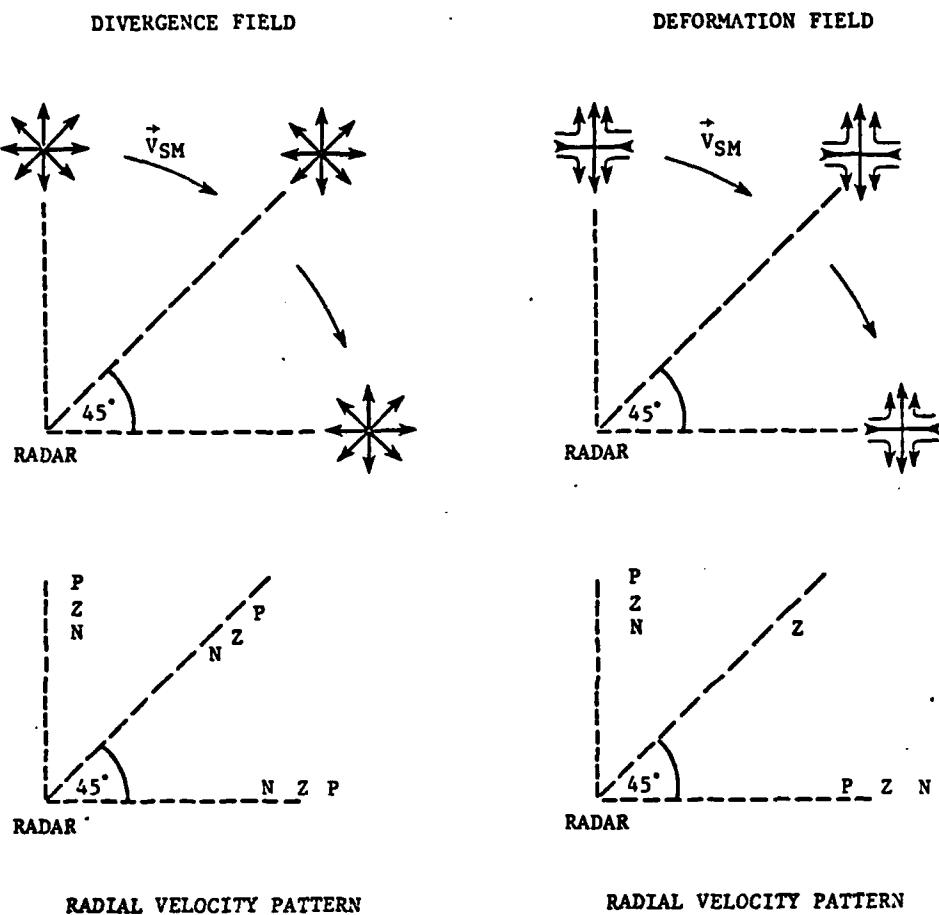


Fig. 6. Schematic single-Doppler radial velocity patterns of a divergent circular source and a symmetric deformation field sampled over time. Source moves counterclockwise across the field of view.

$$\delta = \frac{v_r}{r} + \frac{\partial v_r}{\partial r} + \frac{1}{r} \frac{\partial v_\theta}{\partial \theta} , \quad (1)$$

$$\zeta = \frac{v_\theta}{r} + \frac{\partial v_\theta}{\partial r} - \frac{1}{r} \frac{\partial v_r}{\partial \theta} . \quad (2)$$

These quantities cannot be measured with a single-Doppler radar, but radial stretching and cross-beam shear can be determined. These quantities, along with their orthogonal compliments, are defined as:

radial stretching of
the radial velocity
vector ($\vec{v}_r \equiv v_r \hat{r}$)

$$\equiv \frac{v_r}{r} + \frac{\partial v_r}{\partial r} ,$$

tangential stretching of
the tangential velocity
vector ($\vec{v}_\theta \equiv v_\theta \hat{\theta}$)

$$\equiv \frac{1}{r} \frac{\partial v_\theta}{\partial \theta} ,$$

cross-beam shear of
the tangential velocity
vector

$$\equiv \frac{v_\theta}{r} + \frac{\partial v_\theta}{\partial r} ,$$

cross-beam shear of
the radial velocity
vector

$$\equiv - \frac{1}{r} \frac{\partial v_r}{\partial \theta} .$$

In this investigation the quantity cross-beam shear (CBS) is used to estimate tangential shear across the radar beam. This quantity is a generalization of Donaldson's (1970) rotational vortex model discussed in Appendix C. If the calculations are restricted to low

elevation angles and small azimuths are used the CBS is defined as:

$$CBS \equiv \frac{\Delta v_r}{\Delta s} = \frac{v_{r2} - v_{r1}}{r\theta}, \quad (3)$$

and illustrated in Fig. 7. Following Donaldson's logic, these components can be used to define a Cartesian computational approximation of the radial velocity vorticity as:

$$\zeta_r \equiv \sin \alpha \frac{\partial v_r}{\partial x} - \cos \alpha \frac{\partial v_r}{\partial y} \quad (4)$$

where α is defined by the grid point in reference to the radar. Fig. 7 shows that the radial velocity shear computed across the beam (assuming rotation) is not exactly the same as that computed by the finite difference Cartesian approximation. The shears are computed for slightly different spatial locations. The contribution due to their spatial difference is less than 1% (about 0.2% for Fig. 7 in the worst case used in this study). Values of positive radial velocity vorticity will be defined as contributing to positive cross-beam shear while negative vorticity contributes to negative cross-beam shear. It must be emphasized that vorticity of radial velocity is necessary for rotation, but it is not sufficient. Vertical continuity and viewing the pattern as it tracks across the viewing field need to be used to confirm the presence of rotation.

In this study, radial stretching of the radial velocity vector is called radial stretching or simply stretching, since no information about the radial stretching of the tangential velocity is available.

Similarly the cross-beam shear of the radial velocity vector is called cross-beam shear. These quantities, as expected, will also have distinctive signature patterns depending upon the true flow. Some of these are shown schematically in Figs. 8 and 9. The ambiguities of the single-Doppler sensor and the objective analysis will modify the shape of these patterns, but relative areas of maxima and minima are normally distinguishable from the background flow. Appendix D shows how different circular formulations affect the radial stretching. Signatures involving four maxima-minima (dual couplets) will frequently show one couplet considerably stronger than the other with the front couplet (toward the radar) usually the stronger one.

One advantage of using the radial stretching and cross-beam shear signature patterns to recognize distinct flows lies in their essential invariance to storm motion. This assumes a small change in the radial component of storm motion across the computation grid distance (2 km). The slope of the patterns, with storm motion filtered from the Doppler velocity field, are slightly different from uncorrected data but tests made during this investigation have shown the differences to be small. Uncorrected data will show a slight bias toward one side of the signature pattern, but the basic pattern is still obvious. This is convenient for it obviates the necessity of correcting the entire Doppler velocity field to find areas of interest within the storm.

The radial stretching and cross-beam shear signatures may also be good representations of velocity divergence. In areas where the alignment of inflow and outflow sources are parallel to the radar beam good estimates of velocity divergence can be made. In areas around a

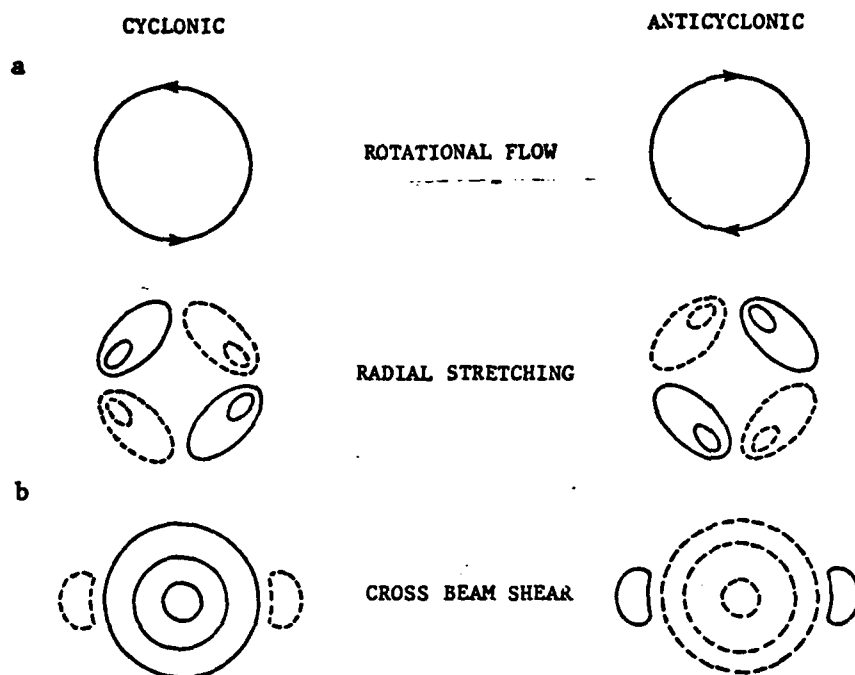


Fig. 8. Single-Doppler flows; cyclonic and anticyclonic rotation. (a) Schematic single-Doppler flow patterns of radial stretching for rotation. Solid lines are stretching, dashed lines are contraction. (b) Single-Doppler flow pattern of cross-beam shear for rotation. Solid lines are positive (cyclonic) shear, dashed lines are negative (anticyclonic) shear. Radar at bottom of page.

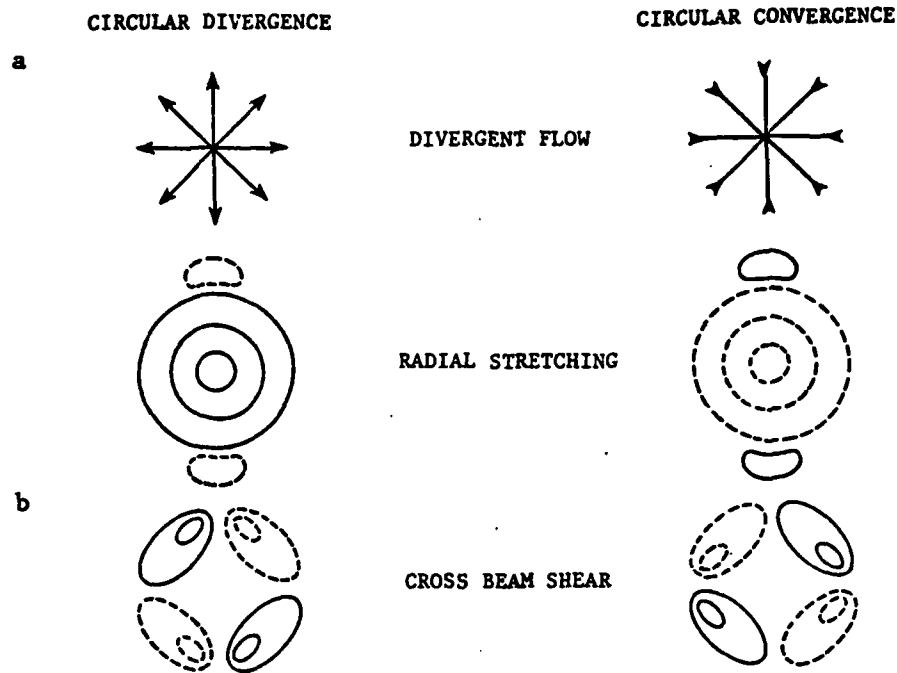


Fig. 9. Single-Doppler flows; circular divergence and convergence. (a) Schematic single-Doppler flow patterns of radial stretching for a circular divergent source. Solid lines are stretching, dashed lines are contraction. (b) Single-Doppler flow patterns of cross-beam shear for a circular convergent source. Solid lines are positive (cyclonic) shear, dashed lines are negative (anticyclonic) shear. Radar at bottom of page.

point where the alignment is perpendicular to the beam, the stretching or cross-beam shear should be rather small and thus render this analysis uncertain. In practice, however, an unfavorable alignment of this sort is only local so patterns are often evident. Knowing that one is viewing a pattern in a situation of unfavorable beam-flow alignment may allow the observer to subjectively adjust his estimate of divergence.

Supercell Model

The basic steady state supercell model used in this study is shown in Fig. 10. This is a composite model derived from the literature cited in Chapter I. It is assumed that changes in this static model can be sensed by single-Doppler radar and that these changes affect rainfall. In the basic model low-level warm moist air is fed into an updraft by surface convergence. The updraft rapidly transports this inflow air into the higher levels of the cloud where the vapor condenses and forms precipitation. The precipitation falls from the updraft, which is tilted in strong supercells, into dry, cooler, mid-level air entering the cloud. The mid-level air, which cools additionally by evaporation, produces a downdraft downwind. Of course, the storm system is three-dimensional and the updraft-downdraft "tubes," which may contain rotations, twist with height when there is directional shear of the environmental wind. In a veering environment the dominant updraft rotation will be cyclonic and the storm will move to the right of the mean mid-level environmental wind. On the other hand a backing wind will produce a model storm with an

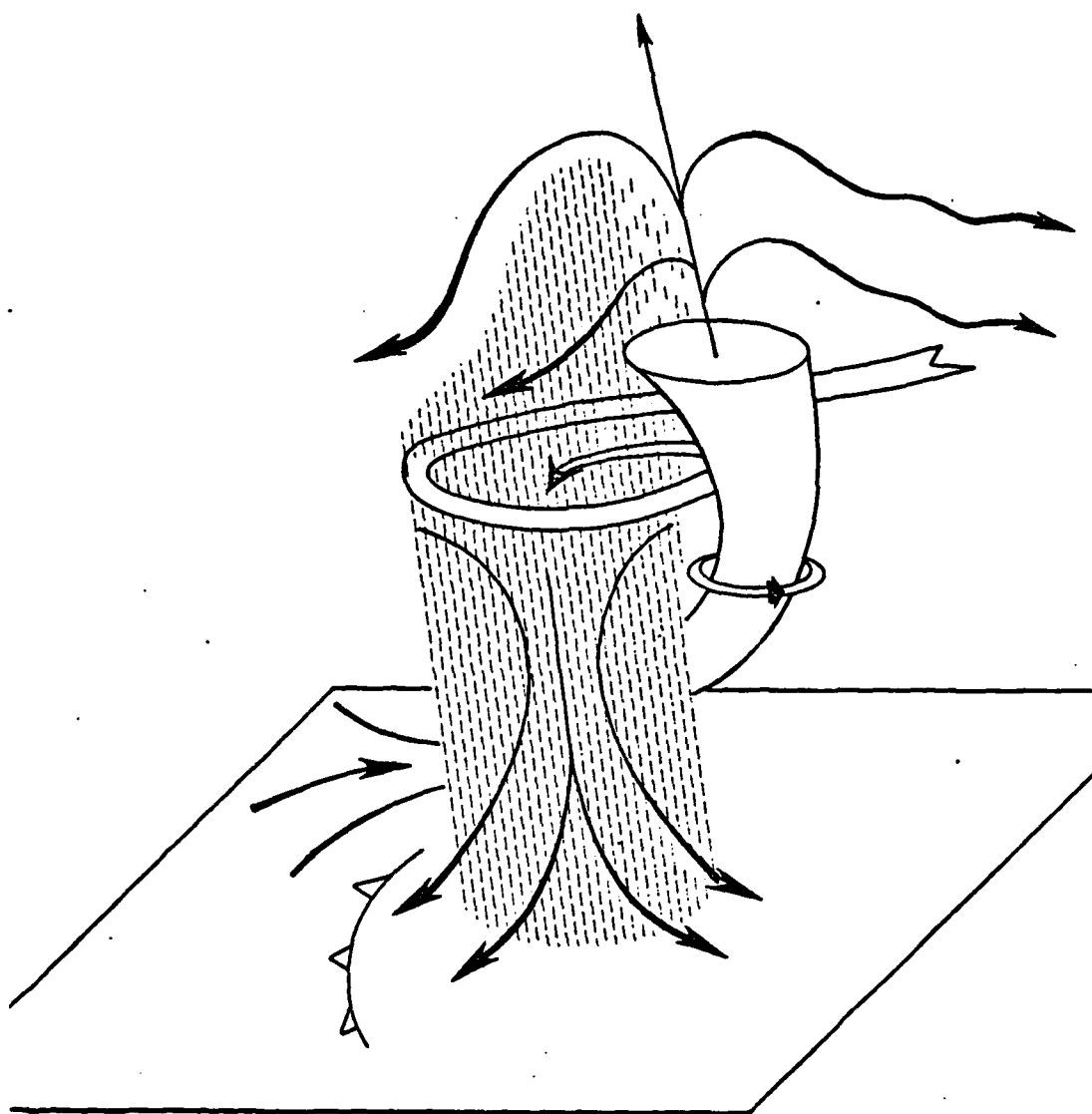


Fig. 10. Schematic precipitation model. Shaded area represents precipitation; arrows indicate air flow.

anticyclonic updraft rotation and a translation to the left of the wind. Another important point of the model is that the updraft may contain a combined cyclonic-anticyclonic rotational pattern or a rotation couplet. The idealized kinematic pattern of the rotational couplet is, for practical purposes, a combination of two solid rotational vortices with an opposite rotational sense.

This model is also an oversimplified view of many complex interactions on the microphysical scale which result in precipitation. A prior assumption in this study is that changes in the microphysical conditions will be reflected in changes in the kinematic flow and, eventually, changes in the surface rainfall.

The idea that a downdraft originates in the mid levels has been confirmed by many investigators using multi-Doppler data (in this study, mid-level is defined as 5 km AGL, which is also the melting level). While mid-level contraction may in fact signal a downdraft, other interpretations are also possible.

An attractive link between surface precipitation and downdraft strength involved the low-level downdraft outflow. The horizontal divergence in the outflow can be estimated if the vertical velocity of the air (V_a) in the draft zone is known. This can be calculated by subtracting the terminal drop velocities (V_T) from the net draft velocity (V_{NET}). Wilson and Fujita (1979), using a vertically pointing Doppler radar, have measured net downdraft velocity on the order of 20 m s^{-1} below the melting level. Using the Gunn and Kinser (1949) estimate of fall speeds for large drops (8 m s^{-1}) enables one to calculate the air draft velocity. In this example $V_a = 12 \text{ m s}^{-1}$

downward. If one employs the incompressible continuity equation to estimate divergence at 1 km, such an average divergence would be about $6 \times 10^{-3} \text{ s}^{-1}$. If the flow is purely isotropic, the radial stretching portion of the velocity divergence would be $3 \times 10^{-3} \text{ s}^{-1}$. Browning et al. (1976) have measured divergence outflow only as high as $4 \times 10^{-3} \text{ s}^{-1}$ in intense Colorado hailstorms. This value is slightly above the acceptable threshold isopleth of radial stretching of $2 \times 10^{-3} \text{ s}^{-1}$ (see Appendix E for a discussion of the acceptable threshold) and it assumes an optimum beam-flow orientation.

Numerical simulations of downdrafts by Eskridge and Das (1976) appear to show that significant downdraft spread will not occur above 500 m. The amount of raw radar data available and unbiased by ground clutter below 500 m is extremely small. Consequently, detection of downdraft outflow by radial stretching will require extremely strong outflow and a fortuitous radar and outflow alignment. Such conditions are rare.

A more promising area of investigation for estimating changes in the downdraft intensity appears to be in the detection of the downdraft source at 5 km. The 5-km level was selected because it represents the melting level during the period of this investigation, and many investigators have previously ascribed mid-level storm features to 5 km. The available radar data should make pattern recognition considerably more reliable at this altitude.

The role of updraft-downdraft rotation in the supercell precipitation process is also complex. Since incoherent weather radars do not sense intrastorm rotation, the importance of this role has been

largely ignored in previous radar investigations.

The supercell model presented in this section must be kept in mind when viewing the single-Doppler patterns. Most patterns discussed in the next chapter could be interpreted in several ways. For clarity the most probable interpretation is emphasized.

CHAPTER V

SINGLE-DOPPLER KINEMATIC PATTERNS AND STORM MODEL INFERENCES

Merging Storms

Introduction

This section presents an analysis of two supercell storms which merged into one larger storm. It is shown that the intrastorm kinematics inferred from the single-Doppler velocity fields and their derivatives can be quite close to reality when full use is made of the vertical structure of radar reflectivities, observed environmental soundings, and certain models of supercell storms. It also is shown that the inferred kinematic fields represent changes in surface rainfall better than the volume or intensity of the radar echoes or vertically-integrated liquid water deduced from the radar-reflectivity observations.

Methods of Analysis

The first method of analysis employed in this phase of the investigation consists of determining the vertical continuity of the echoes from the reflectivity maps. The 1-, 3-, 5-, and 7-km levels are normally employed. The supercell storm model (Chapter IV) is used to infer a downdraft through the reflectivity core if it contains good continuity below the mid-levels and weak reflectivity above. Any tilt of the inferred downdraft is noted, since it may have a relationship to the updraft which, while frequently observed upwind of the

downdraft in terms of the lower level of flow, cannot be inferred with confidence. The direction as well as the strength of the low- and mid-level (5-km) flow are obtained from surface mesoanalyses and sounding data. In order to determine the intrastorm kinematics we assume that a significant portion of the environmental air flowing toward the storm enters it. This assumption is then validated against the single-Doppler kinematic model for convergence.

The kinematics of a storm inferred from the procedure outlined above are still quite uncertain; their reliability, therefore, needs to be ascertained—which, for this investigation, is done by comparison with multiple-Doppler observations, if they are available. It will be seen later that the kinematic structure inferred by our methodology is supported by multi-Doppler analysis.

Once the kinematic structure is inferred we refer back to the storm model in order to delineate areas under the storm where the rainfall intensity should be high and/or be increasing, or vice versa. The areal distribution of actual rain intensities obtained from the analysis of the raingauge data is used as the "ground truth" for the analytical inference. This inference is also compared with the inferences obtainable from radar-determined vertically-integrated liquid water contents.

Mesoscale Environment

The Oklahoma City morning sounding on 20 May 1977 indicated unstable air with strong vertical wind shear. The winds veered from 140° at the surface to 270° at 4.5 km and backed to about 240° for the

higher levels.

A combined hodograph based upon the 1500* Fort Sill and 1620 Elmore City soundings (Fig. 11) shows veering wind to 10 km with strong speed shear. The 5 km flow, which is used to define mid-level flow in this study, is approximately from 190° at 25 m s^{-1} . The explicit low-level flow cannot be determined directly from the NSSL mesonet data because the storms are well south of the network. A good estimate of the low-level flow can be made from continuity with synoptic-scale hourly observations. The radial grid point $240^\circ/55 \text{ km}$ (with reference to the Norman radar) is the approximate southern boundary of the mesonet data. From 1500 to 1630 the low-level flow appeared to be mostly from the east-southeast (120°) at speeds less than 10 m s^{-1} . The mesonet winds were generally stronger in the eastern portion of the analysis grid than in the western region, thus indicating potential convergence to the west.

In the early afternoon of 20 May 1977, impulses from a squall line in western Oklahoma combined with strong southeasterly surface flow to produce severe local storms. Sixteen tornadoes, extremely high rainfalls, and hail were reported throughout central Oklahoma during the evening and early morning hours of 20-21 May.

There were quite a few supercell storms that formed on that day. One of these storms, called the Fort Cobb storm, contained two mesocyclones with damaging tornadoes. This storm will be examined in the next section. In this section the emphasis will be on the so-called Del City storm and a hail-producing storm to be referred to as the

*All times are Central Standard Time.

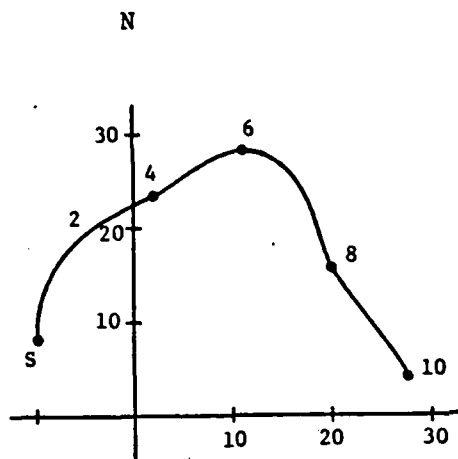
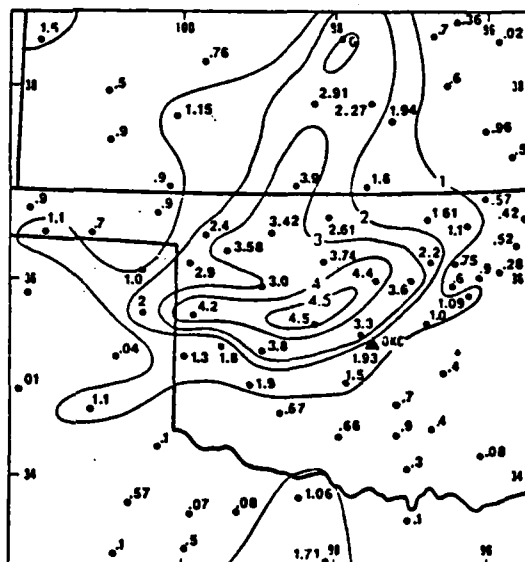


Fig. 11. Composite wind hodograph from the 1500 CST Ft. Sill and 1620 CST Elmore City soundings. Speeds are in m s^{-1} (adapted from Klemp *et al.*, 1979).

Fig. 12. Total surface rainfall (in) for 20 May 1977 (adapted from Park and Sikdar, 1979).



"Hailstorm" in this study.

The Del City storm formed just south of the radar observational box and moved rapidly to the northeast where it merged with the Hailstorm at about 1722. Before 1722, the Hailstorm had been moving toward the north-northeast at approximately 15 m s^{-1} . The two merged and the complex traveled to the northeast (toward 35° at 17 m s^{-1}) as the Hailstorm weakened. The Del City storm went on to produce a mesocyclone and tornado at 1843 after passing Oklahoma City.

The maximum 24-hr precipitation occurred northwest of Oklahoma City, or just north of the raingage network (see Fig. 12). The 15-min rainfall rates within the network were extremely high, as they reached over 150 mm hr^{-1} .

Time Sequence of Single-Doppler Fields

Fig. 13 contains the time sequence of reflectivity (dBZ), radial velocity (m s^{-1}), radial stretching ($\times 10^{-3} \text{ s}^{-1}$), and cross-beam shear ($\times 10^{-3} \text{ s}^{-1}$) for the 1-km level. The 240° radial, with reference marks in km from NSSL, is superimposed upon the panels.

Reflectivity scans prior to 1630 (not shown) revealed that the Del City storm had formed after the Hailstorm at about 1630. The 1630 reflectivity scan showed an intense echo with a large area encompassed by the 45 dBZ contour. The radial velocity map showed the area south of the peak echo (greater than 55 dBZ) to be moving toward the radar faster than the mid-sections of the echo. This area is associated with a zone of contraction (Fig. 13c) and an area of positive and negative shear in the cross-beam shear (Fig. 13d) upwind and over the

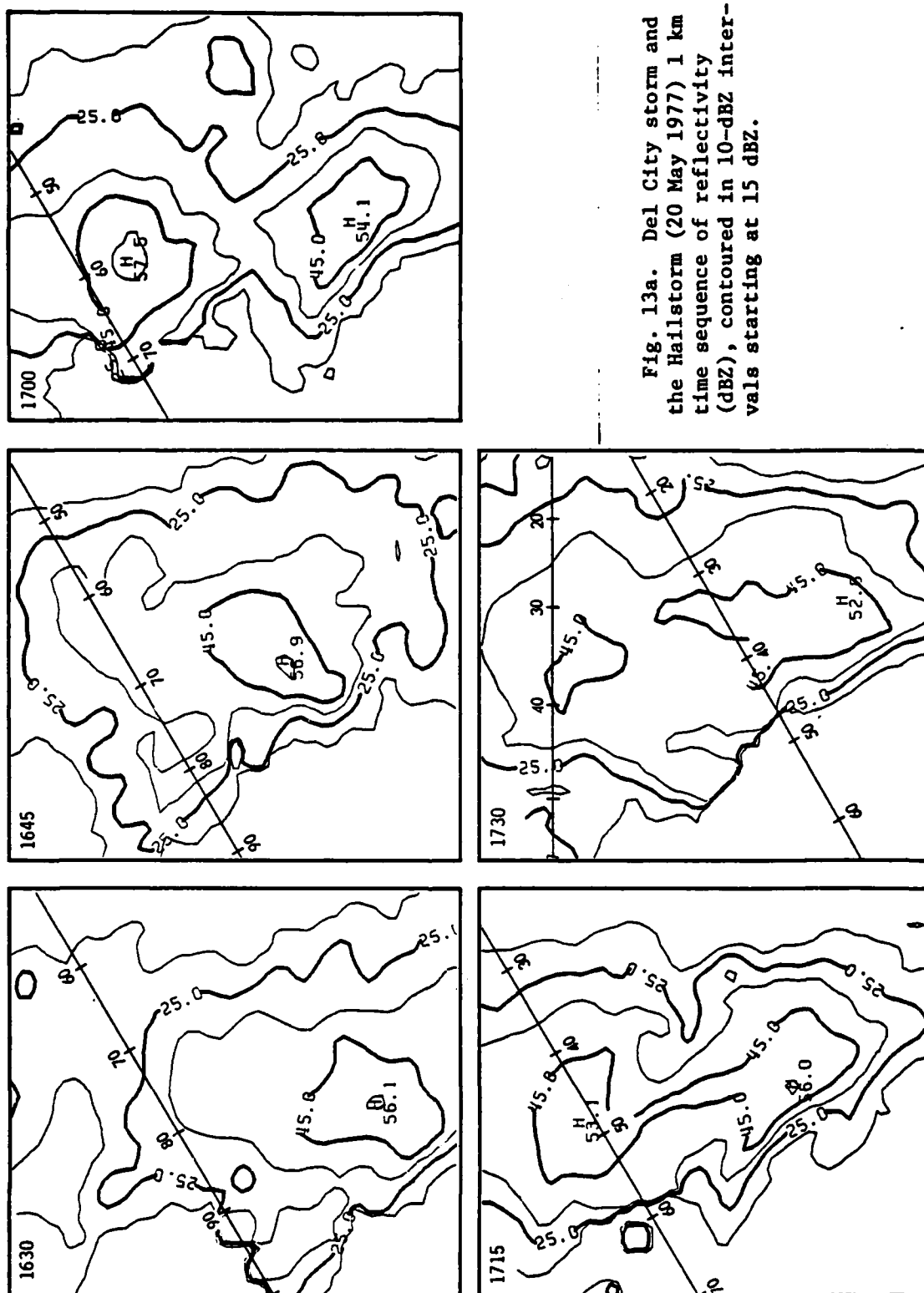
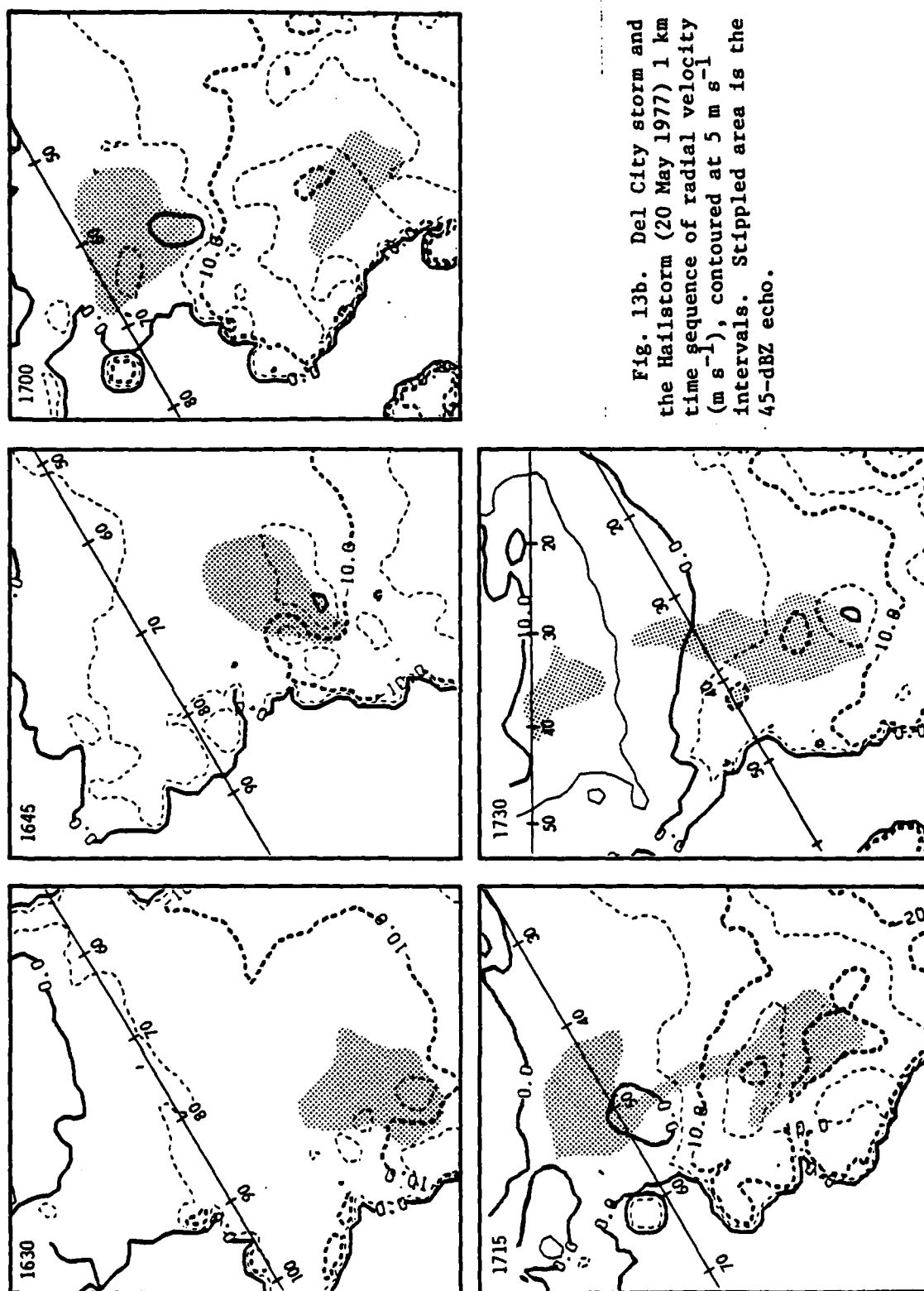


Fig. 13a. Del City storm and the Hailstorm (20 May 1977) 1 km time sequence of reflectivity (dBZ), contoured in 10-dBZ intervals starting at 15 dBZ.



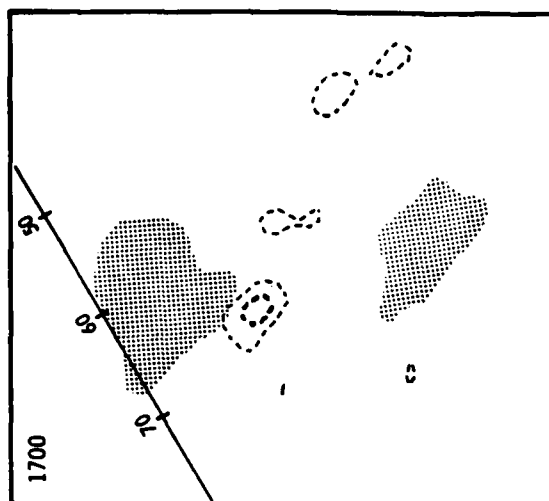
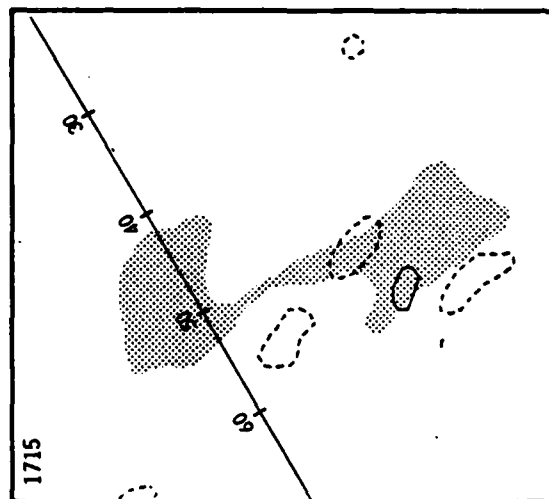
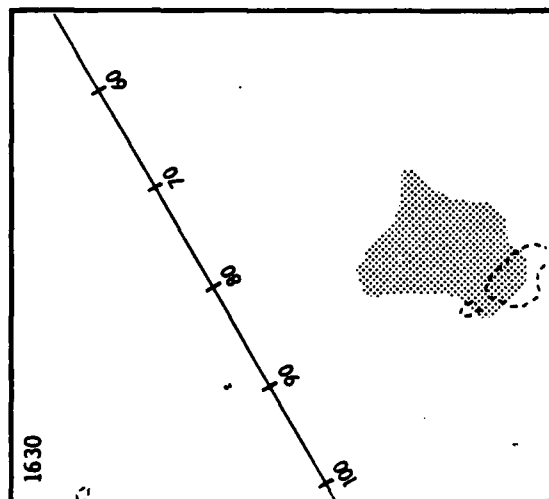
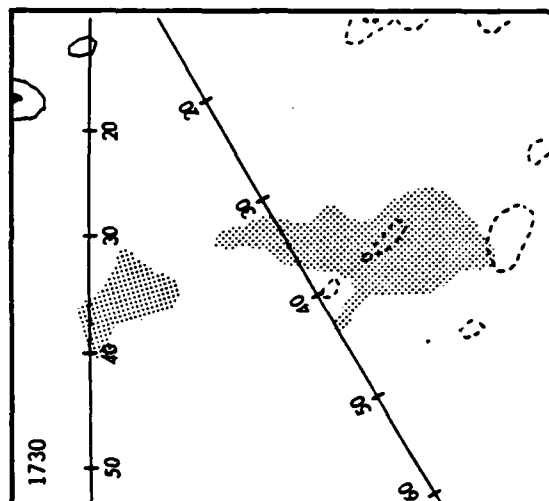
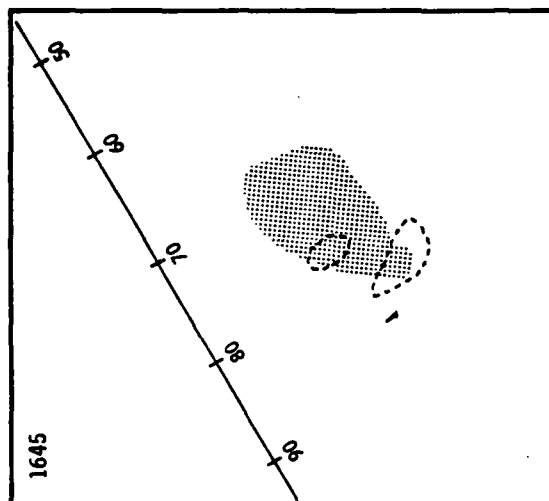


Fig. 13c. Del City storm and the Hailstorm (20 May 1977) 1 km time sequence of radial stretching ($\times 10^{-3} \text{ s}^{-1}$), contoured in $2 \times 10^{-3} \text{ s}^{-1}$ intervals greater than $2 \times 10^{-3} \text{ s}^{-1}$ (solid lines) and less than $-2 \times 10^{-3} \text{ s}^{-1}$ (dashed lines). Stippled area is the 45-dBZ echo.



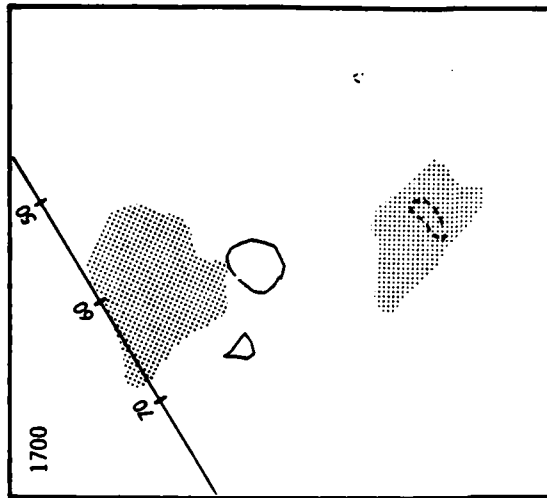
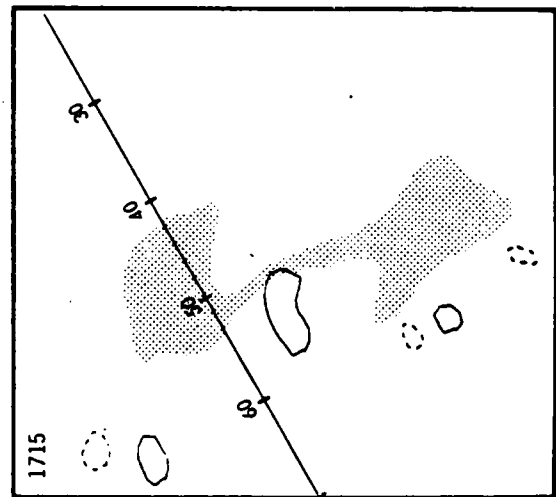
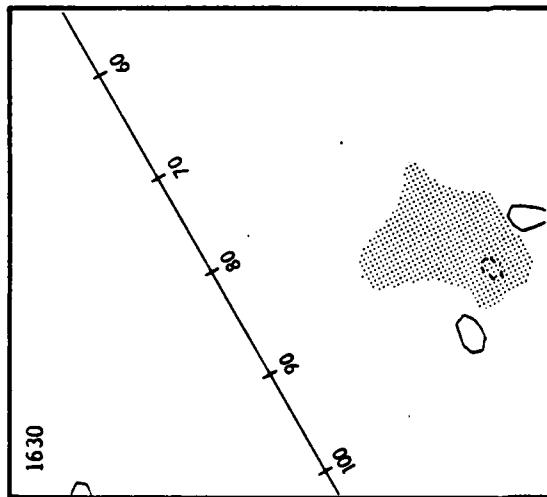
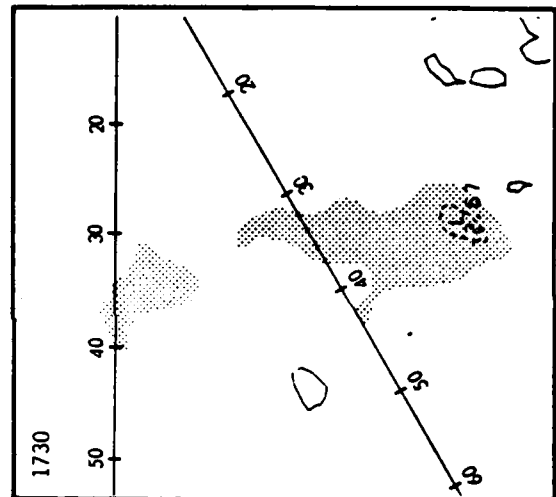
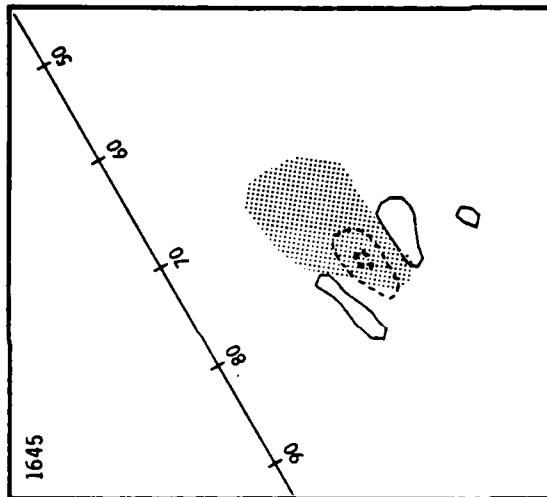


Fig. 13d. Del City storm and the Hailstorm (20 May 1977) 1 km time sequence of cross-beam shear ($\times 10^{-3} \text{ s}^{-1}$), contoured in 2×10^{-3} intervals greater than $2 \times 10^{-3} \text{ s}^{-1}$ (solid lines) and less than $-2 \times 10^{-3} \text{ s}^{-1}$ (dashed lines). Stippled area is the 45-dBZ echo.



rear flank. West of the 45 dBZ contour, a small area of positive cross-beam shear was also observed.

At 1645 the reflectivity panel (Fig. 13a) suggested a hook echo pattern developing on the rear of the storm. This part of the storm was still associated with a large area of contraction (Fig. 13c) and a larger zone of positive and negative cross-beam shear (Fig. 13d).

At 1700 the two storms were clearly evident (Fig. 13a). Contraction still dominated the south side of the Hailstorm but the cross-beam shear panel (Fig. 13d) showed only strong positive shear in the same location.

The merging process is seen in the reflectivity field at 1715 (Fig. 13a). A contraction zone was now located south of the Hailstorm along with a stretching and contraction area west of the Del City storm (Fig. 13c). Strong positive cross-beam shear remained on the rear flank of the Hailstorm (Fig. 13d).

The 1730 panels (Fig. 13) showed the Hailstorm weakening and losing its low-level contraction and cross-beam shear patterns. The Del City storm however, developed a large area of contraction on the rear with a nondescript cross-beam shear pattern.

In order to illustrate the vertical structure as well as to have a better understanding of the storm with the help of vertical continuity of various fields, the fields of reflectivity, radial velocity, radial stretching, and cross-beam shear at the 5 km level are presented in Fig. 14. The 5 km reflectivity fields have the same overall structure as those at the lower levels.

At 1630, the echoes pertaining to the Hailstorm showed a

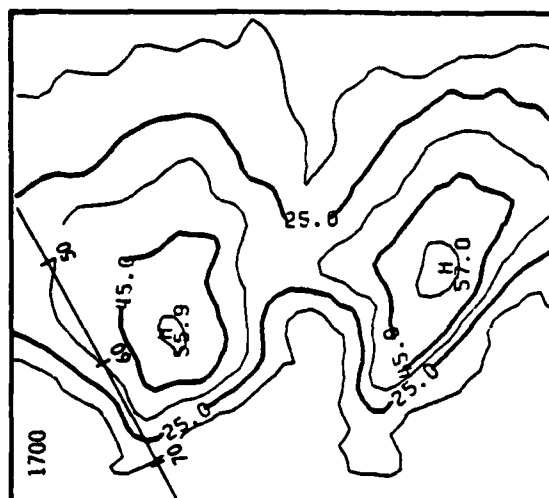
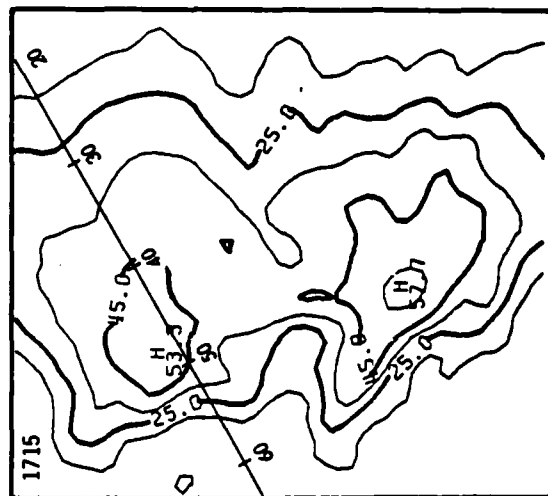
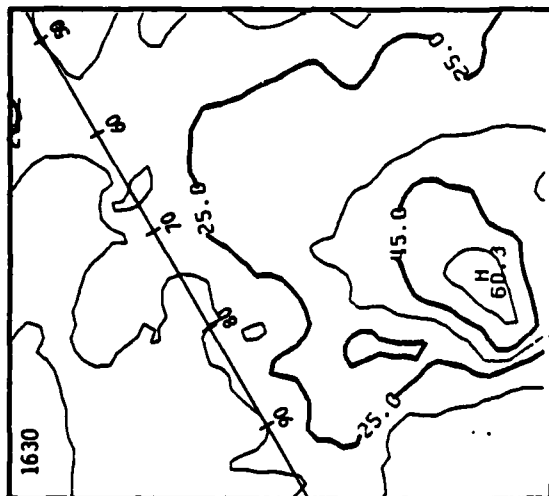
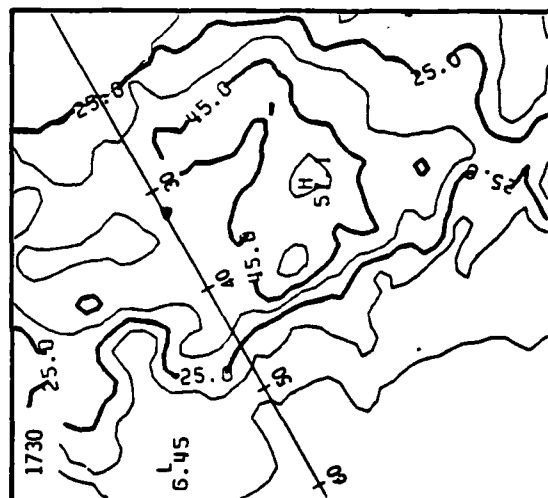
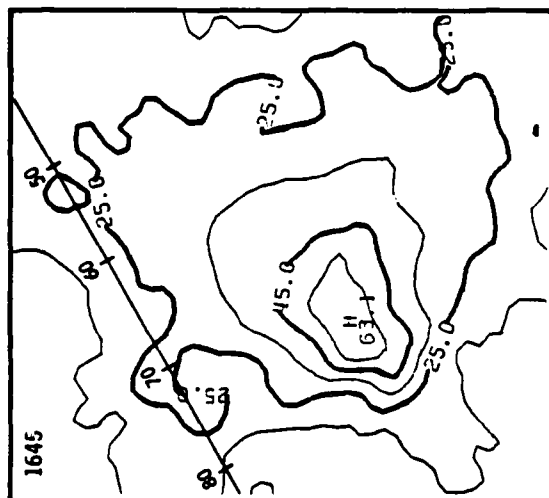


Fig. 14a. Same as Fig. 13a,
except at 5 km.



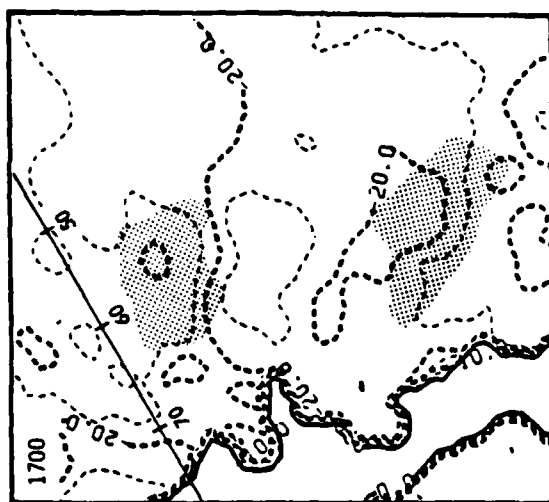
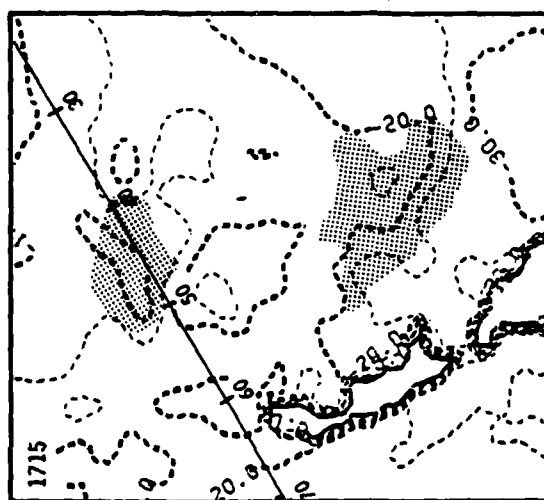
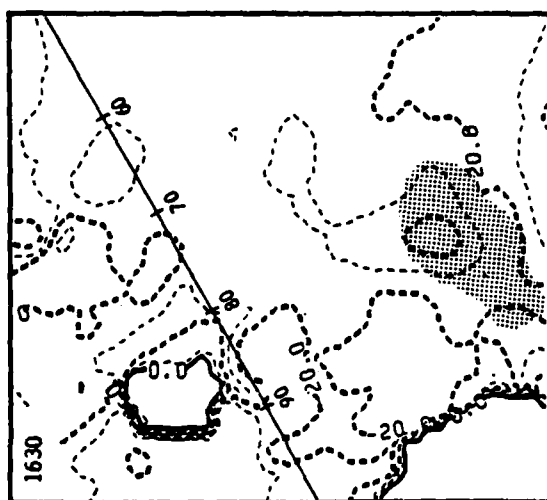
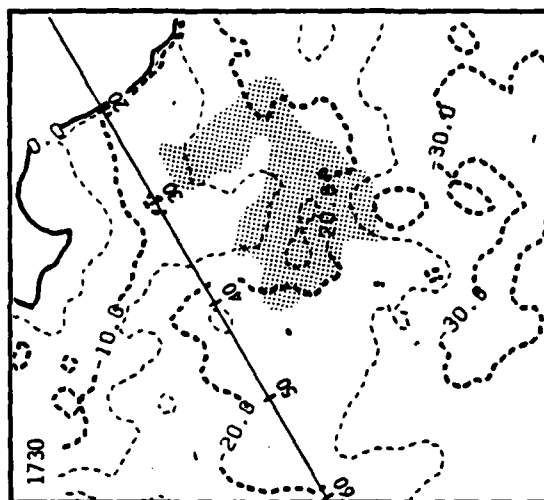
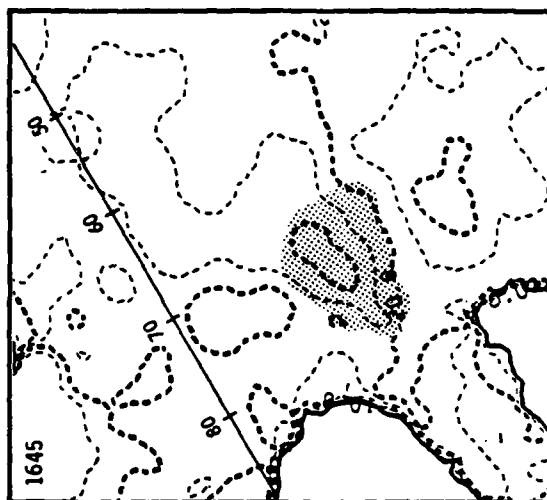


Fig. 14b. Same as Fig. 13b,
except at 5 km.



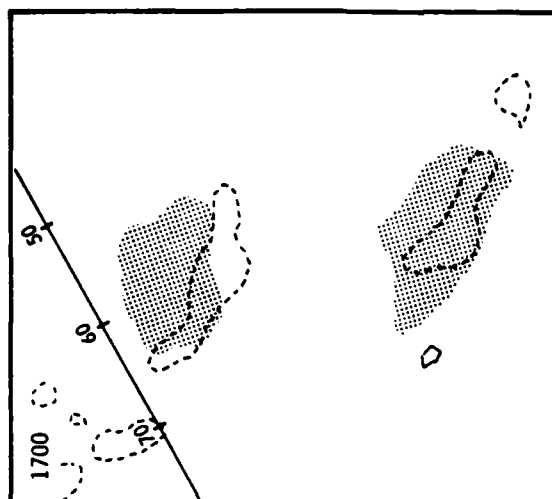
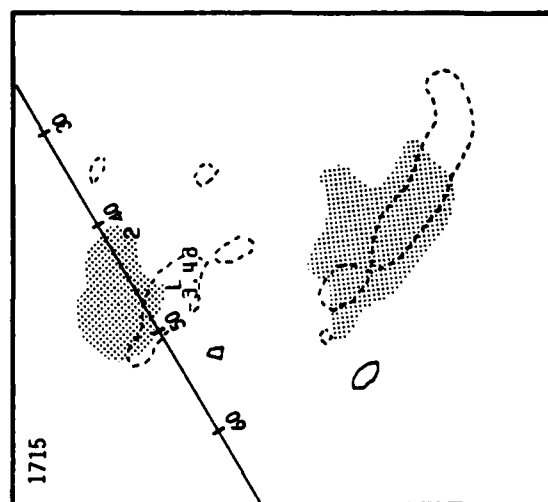
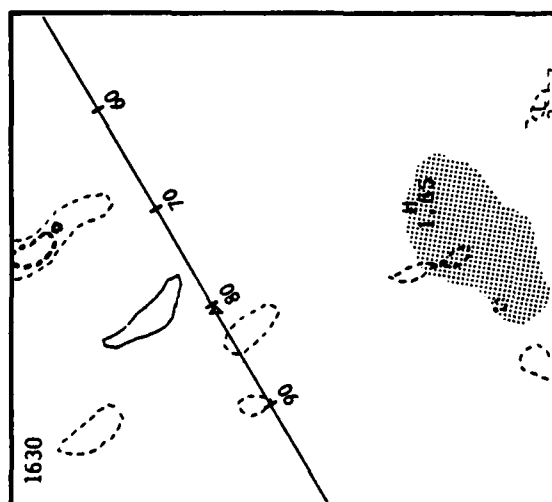
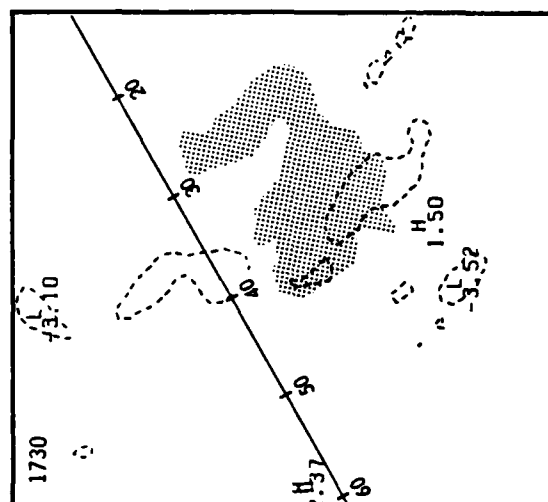
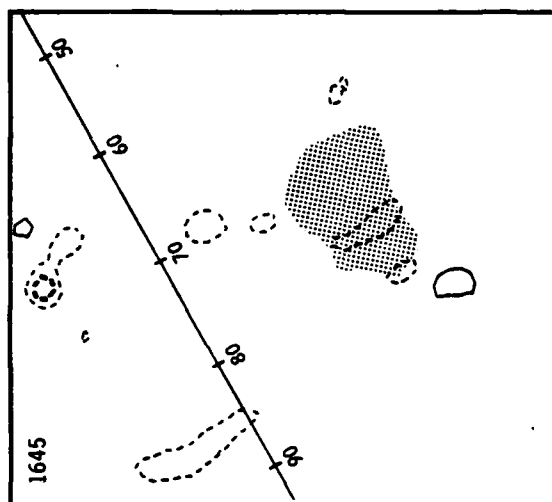


Fig. 14c. Same as Fig. 13c, except at 5 km.



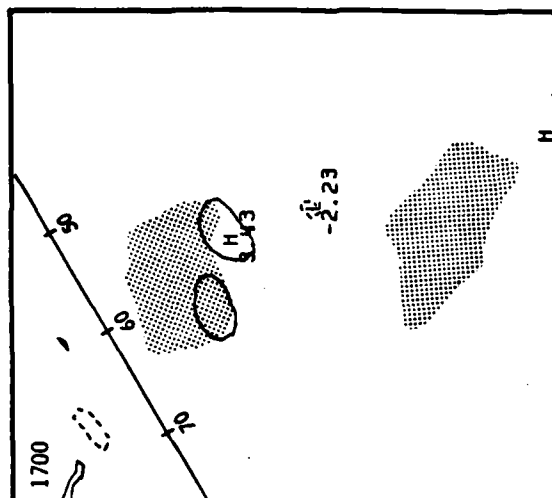
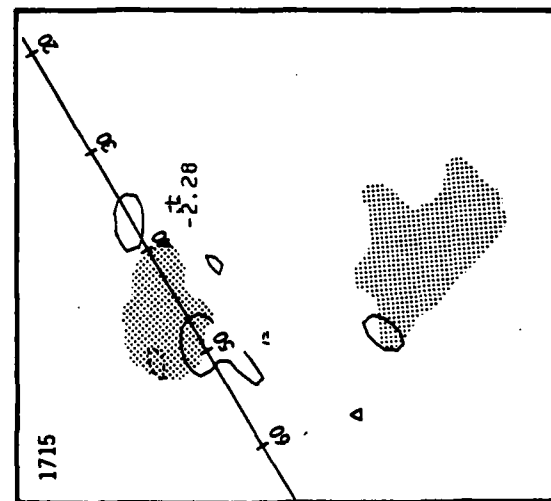
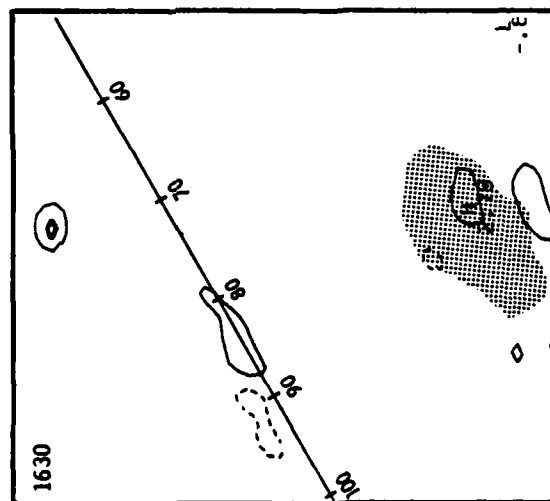
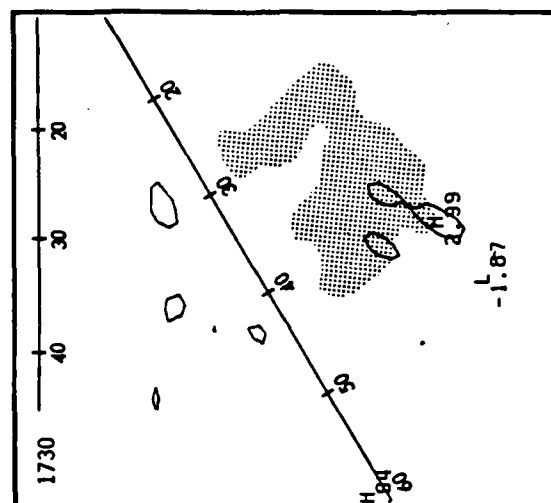
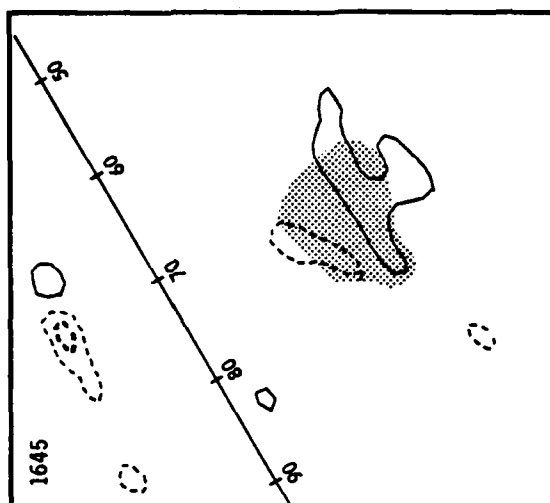


Fig. 14d. Same as Fig. 13d,
except at 5 km.



clockwise twisting with height. The 5-km radial stretching map showed contraction upwind of the echo core, both on the west side as well as over the core. The 3-km, 5-km, and 7-km cross-beam shear panels at 1630 (not shown) showed good vertical continuity of the positive and negative cross-beam shear zone. Like the reflectivity core, these shear-zones also twisted clockwise with height.

The mid-level patterns at 1645 showed little change in reflectivity (Fig. 14a) but now significant contraction was observed with the reflectivity core (Fig. 14c). The positive-negative cross-beam shear pattern again showed good vertical continuity (Fig. 14d). The combination of the radial stretching and cross-beam shear fields may suggest a couplet rotation, as described in Chapter IV. The spread of the cross-beam shear pattern moving toward the radar may be responsible for the lack of stretching near the center of the echo as implied by a couplet rotation.

At 1700 large areas of contraction were observed with the Hailstorm core (Fig. 14c). The contraction zone of the Del City storm was closer to the echo core than that of the Hailstorm. The Hailstorm showed a weakening in the cross-beam shear (Fig. 14d) while no significant cross-beam shear was seen in the Del City storm.

The 1715 reflectivity panel (Fig. 14c) did not show the echo merging as in the lower levels. Contraction dominated both storms with the Del City storm containing a larger area of contraction over the center of the storm (Fig. 14c).

The 1730 mid-level reflectivity showed a breakup of the Hailstorm echo with a strengthening of the Del City echo (Fig. 14a).

Contraction dominated the Del City echo (Fig. 14c) and positive cross-beam shear was now observed on the rear of the storm (Fig. 14d).

Single-Doppler Fields Plus Storm Model Interpretations

In the previous section it was noted that a cyclonic vorticity on the rear of the Hailstorm could be inferred from the single-Doppler reflectivity radial velocity, radial stretching and cross-beam shear data. The supercell model used in this study also suggests some cyclonic rotation since the storm tracks to the right of the mean mid-level wind in a veering environment. No rotation was observed in the Del City storm, which moved with the flow toward the Hailstorm. Multi-Doppler analyses of these storms (Klemp *et al.*, 1980) have shown the dominant intrastorm low-level flow to be easterly (090°) while the upper-level flow was from the south (180°). These flows were nearly parallel to the environmental winds. The reflectivity core at this time showed a clockwise turning with height. Radial stretching maps revealed a zone of contraction on the southern side of the 45-dBZ reflectivity contour at 1 km. Such a zone suggests an area of convergence and a possible updraft source based upon the storm model. While southeasterly flows are nearly perpendicular to the radar beam, the 1-km wind was approximately 150° at 20 m s^{-1} .

This raises an important point. In a storm environment having winds with strong directional shear in the vertical, the radar data will contain information from several heights with different beam-flow alignments. This is why "reasonably good" patterns are frequently observed under what appears to be hopelessly ambiguous beam-flow

alignments.

The 5-km radial stretching map showed contraction upwind of the echo core on the west side and over the core. The 3-km (not shown) and 5-km cross-beam shear panels at 1630 showed good vertical continuity, especially of the positive cross-beam shear zone east of the 45-dBZ core. Like the reflectivity core, this positive zone also twisted clockwise with height. The storm model suggests this zone to be the updraft which probably contains a rotational couplet. The dominant rotational sense, if any, is difficult to verify from the mid-level kinematic pattern. Multi-Doppler observations of this storm (Klemp et al., 1980) showed an updraft with cyclonic rotation on the rear right flank.

The radar reflectivity showed a near vertical alignment of the peak reflectivity. The 45-dBZ contours turned counterclockwise with decreasing height. If the downdraft turns with the 45-dBZ reflectivity, the dominant 5-km feeder flow will be on the right storm flank. The general slope of the updraft, toward the northeast with height, suggests that right flank air will be more influenced by evaporative cooling than left flank air. The left flank contraction at 1630 may be due to the left portion of the couplet having access to more precipitation sized particles, since it is within the 45-dBZ core.

At 1645 little change was evident in the Hailstorm reflectivity patterns. The strongest reflectivity gradient remains on the rear of the storm and the 1-km cross-beam shear continued to show a possible couplet rotation with additional positive shear to the west. This

may be associated with a partial divergence pattern resulting from downdraft outflow. Rainfall in the next 15-min period was particularly intense, which leads the author to believe that the 1-km cross-beam shear pattern developed from a super-positioning of several causes. In cases like this, temporal and vertical spatial continuity should be employed in the interpretation process.

At 1645 maximum mid-level contraction is not aligned over the reflectivity core. The storm model suggests this represents convergence associated with the downdraft. The association between this contraction and intense rainfall will be discussed later in this section.

Figs. 15 and 16 illustrate the vertical continuity of the reflectivity core and the updraft zone. One can clearly see the updraft tilting toward the northwest with height, against the reflectivity tilt which was toward the southeast with height. Notice that these cores cross at 5 km, the level of maximum contraction. Notice the vertical continuity of the large positive-negative shear core in the north-south cross section. This lends support to the couplet rotation suggested by the model. Temporal plots of the vertical cross section fields showed that these features persisted for at least 30 min.

While, at 1700, the Hailstorm maintained the higher reflectivities, it is important to note its demise was apparent from the stretching and shear fields. The 1-km radial stretching actually showed an increase in intensity but its upper-level support had started to move away from the echo core. In contrast, the Del City storm, which showed no low-level support in the stretching field, was

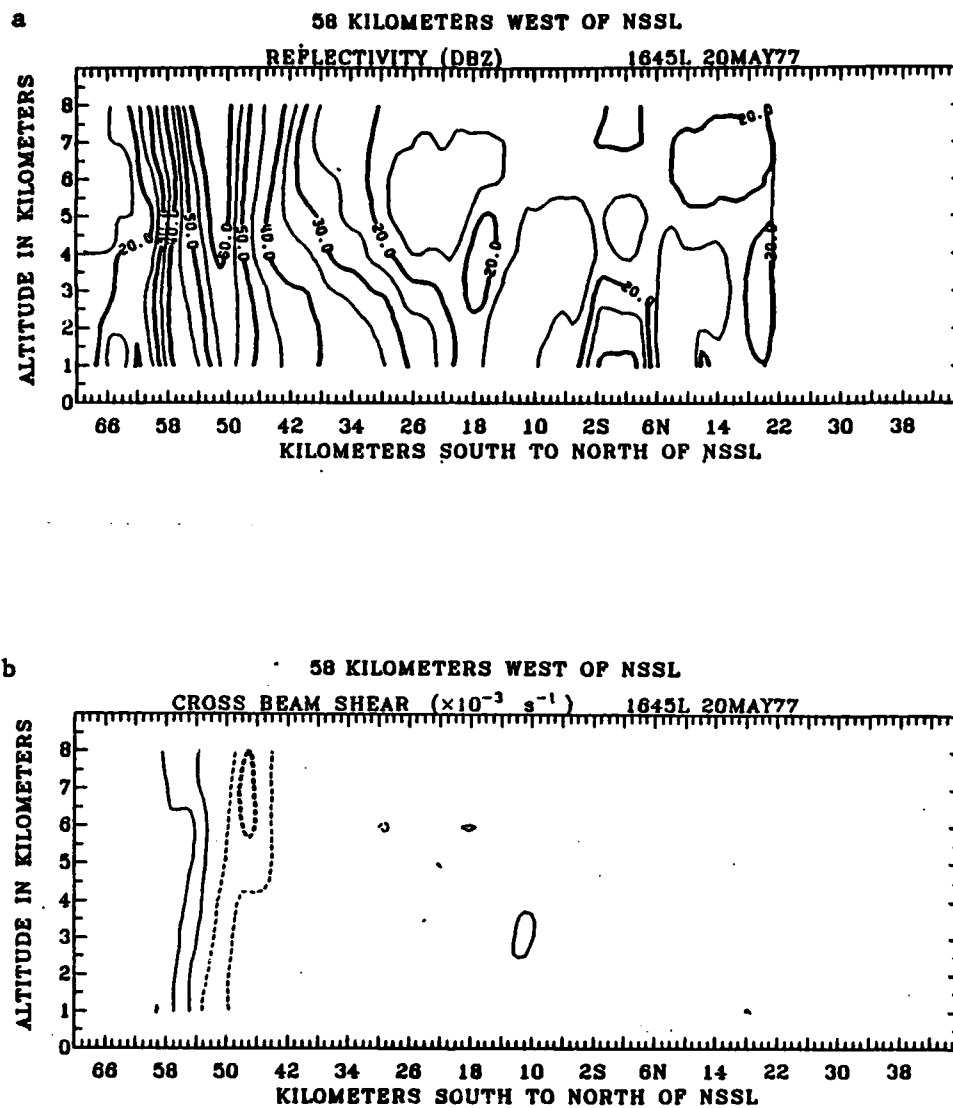


Fig. 15. North-south cross section 58 km west of NSSL at 1645.
 (a) Reflectivity (dBZ). (b) Cross-beam shear ($\times 10^{-3} \text{ s}^{-1}$).

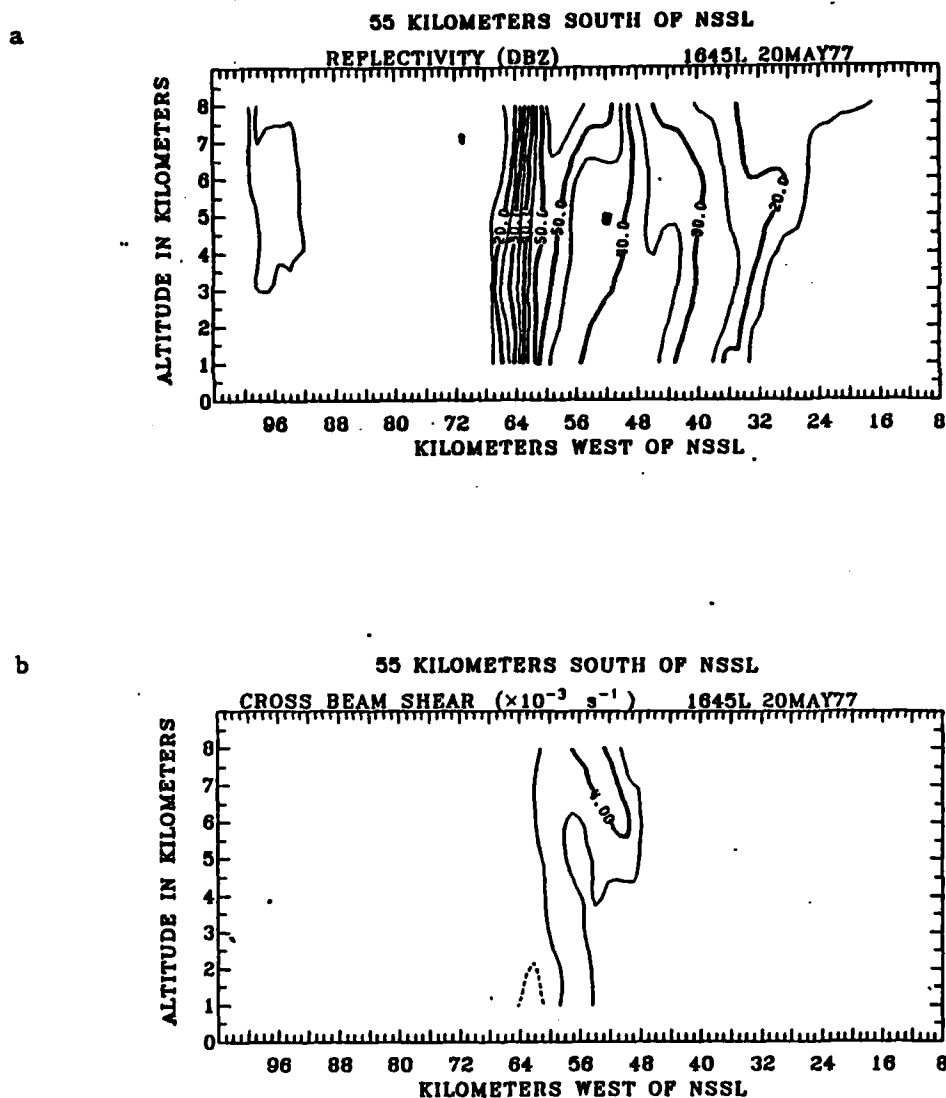


Fig. 16. East-west cross section 55 km south of NSSL at 1645.
 (a) Reflectivity (dBZ). (b) Cross-beam shear ($\times 10^{-3} \text{ s}^{-1}$).

aligning its mid-level contraction over the reflectivity core, which suggests at least a steady state of high rainfall. The suspected couplet rotation on the southeast side of the Hailstorm had weakened at all levels.

The 1715 reflectivity maps showed the storms just before the merging process. The Hailstorm, until now, had been the dominant storm, but the Del City storm now clearly had taken over. The stretching maps at 1715 showed strong contraction of the Del City air over the reflectivity core at 5 km, and a weaker contraction, off the core, for the Hailstorm. The 1-km stretching map showed an unusually complicated pattern. This was probably due to a super-position of two effects, inflow which is usually present and outflow which is seldom observed. The dashed-solid-dashed isopleths (Fig. 13c) along a southwest radial may be the result of outflow associated with the intense rainfall of the Del City storm. Goff (1976) has shown that such outflow is usually confined to the lower 500 m. The contraction zone south of the 240° radial at the 55-km range is the remnant of the updraft contraction zone for the Hailstorm. Such an interpretation, while not unique, does support the idea of a weakening Hailstorm due to interaction with the Del City outflow and is compatible with the supercell model.

A plot of echo cores and the derivative fields showed a significant increase in slope, along with the 5-km contraction and shear maxima outside the echo core. This suggests that considerable updraft moisture will fall out as precipitation before the updraft reaches the center of the storm. Such a condition will decrease the size of the

storm echo, in the mid-level. The 1730 reflectivity map showed the Del City storm absorbing the Hailstorm. No 45-dBZ echoes associated with the Hailstorm could be found at 5 km. The overall size of the complex seemed to be increasing at 5 km while remaining about the same in the lower layers. The inflow region remained south of the data mesonet even at this time, but a high-pressure core is obvious in the area of the Del City downdraft. An anomalous wind, 180° of 15 m s^{-1} was observed at a mesonet station 19S, 37W, which suggests the passage of a gust front. A θ_w minimum (14°C) was also observed just west of the high-pressure core. The 1622 Elmore City sounding showed 14°C θ_w air to be located at 4.0 km, near the melting level. This was probably the source region for the downdraft. It also contained the region of strongest directional shear with the environmental wind veering from 170° to 200° . These observations lend additional credence to the supercell model.

At 1730 the low-level cross-beam shear, showed a strong negative and weak positive pattern in the rear of the storm. This was also associated with a contraction zone. The vertical continuity of these features was good. The mid-level stretching still showed strong contraction across the echo core, thus suggesting continued high precipitation. The lower-level environmental flow was now aligned more from the south-southeast, which makes the lower-level patterns slightly more reliable.

Some additional comments about the verification of the single-Doppler inferences presented above may be worthwhile. This experiment was designed so that the single-Doppler patterns could be

compared with multi-Doppler analyses of the same storms and supplemented with similar analyses of other supercell storms.

The idea that low-level contraction plus cross-beam shear signals an updraft zone appears reasonably good even under an unfavorable beam-flow configuration. Single-Doppler radar may also be able to sense the updraft couplet feature observed in multi-Doppler observations of similar storms (Heymsfield, 1978). In the Del City-Hailstorm complex, the updraft-downdraft configuration is in good agreement with multi-Doppler observations of B. C. Johnson et al. (1980). The tilt of the updraft with height matches that deduced by Klemp et al. (1979) and other investigators. The twisting of updraft-downdraft "tubes" inferred from the single-Doppler data is surprisingly similar to that envisioned by Browning (1964) and shown to exist in three-dimensional compressible simulations (see Klemp and Wilhelmson, 1978). The storm inflow at low- and mid-levels inferred from rawinsonde and surface data match that computed from multi-Doppler observations. Even the apparent importance of the mesoscale environment in forcing the supercell storm features that is suggested by the single-Doppler data was also noted by Klemp et al. (1980).

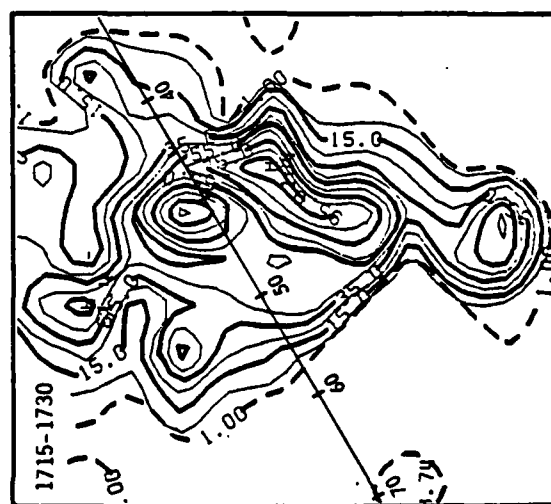
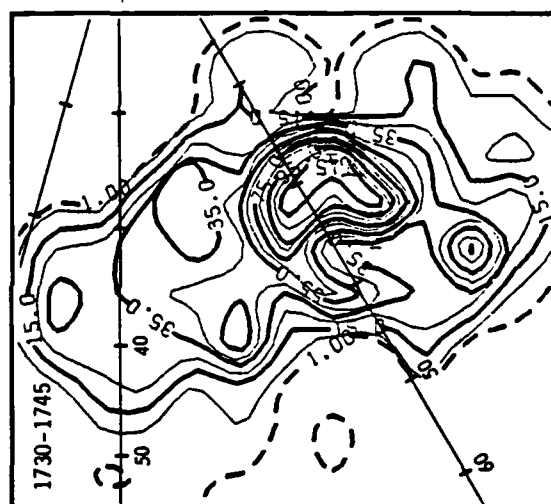
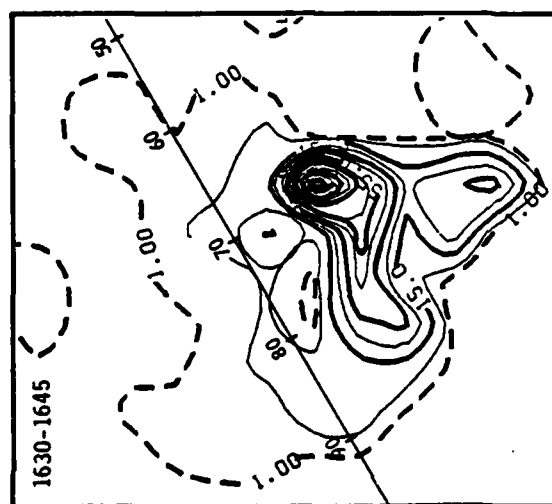
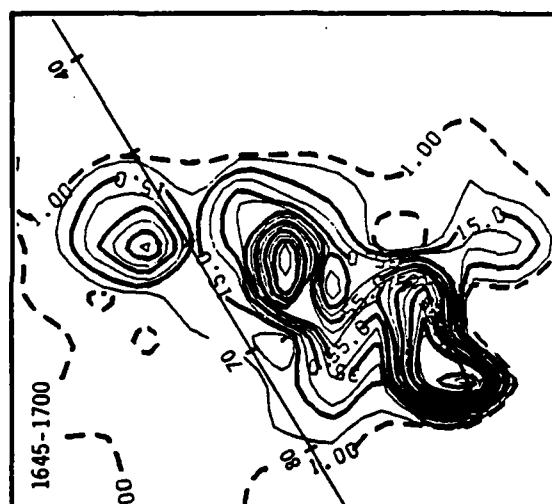
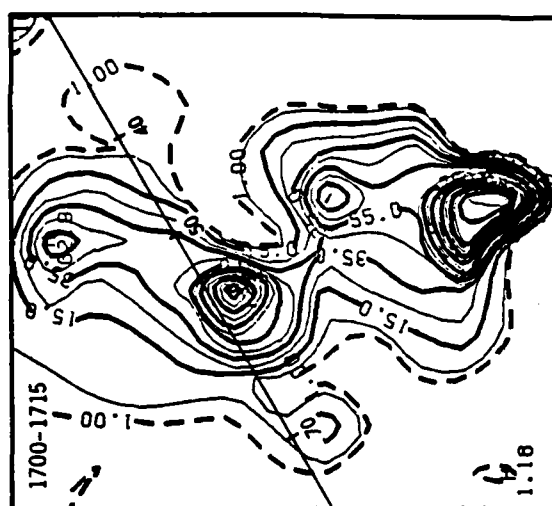
Overall, the agreement between storm flow inferred from single-Doppler data and that computed from multi-Doppler data is very good. These observations also contrast favorably in the larger context of observations of other supercell storms. When one recalls the inherent problems of using single-Doppler for this purpose, the agreement is remarkable.

As noted previously, a goal of this paper is to demonstrate the

value of single-Doppler kinematic fields in sensing changes in surface precipitation. The Del City-Hailstorm complex provides an excellent illustration of this capability. Fig. 17 shows the rainfall rate (mm hr^{-1}) analyses for the storms. A summary of the precipitation data is shown in Appendix I.

At 1630, integrated liquid water maps (not shown) of the Hailstorm showed concentrations as high as 22 kg m^{-2} in the lower layers and 30 kg m^{-2} above and below the melting level respectively. It is assumed that a considerable portion of the reflectivity was due to hail (see Appendix D). The size of the areas (130 km^2 below the melting level and greater than 140 km^2 above) within the 5 kg m^{-2} isopleth of liquid water suggests high rainfall at the surface. The rainfall period ending at 1645 showed that one cell dominated the rainfall. This cell contained a maximum rainfall rate of 131 mm hr^{-1} with a 25-mm hr^{-1} isopleth of 109 km^2 and a 55-mm hr^{-1} isopleth of 33 km^2 . The 1645 rainfall map showed that the peak rainfall rates occurred on the left front flank and were located ahead of the peak reflectivity by approximately 7 km. This lends credence to the idea of hail contamination of the liquid water maps.

At 1645 the 1-km radial stretching map contained a larger area of contraction on the southern and western flanks of the Hailstorm. The 5-km radial stretching panel showed a significant increase in the contraction over the echo core, which suggests an intensification of the downdraft and possible higher surface rainfall rates. The increase in the strength of the suspected couplet rotation also suggests a more intense updraft. Despite these changes in the kinematic features, the



low-level integrated liquid water map showed little change in the area with the peak values decreasing slightly. At mid-levels the 5-kg m^{-2} area blossomed to 172 km^2 (from 140 kg m^{-2}). The 1645-1700 rainfall panel showed a larger and more intense rainfall pattern. Such dramatic changes were not revealed in the reflectivity or integrated liquid water patterns. Similar comparisons for other time periods showed that, in the Hailstorm, changes in rainfall appeared to be sensed better by storm kinematics than reflectivity or integrated liquid water. In fact, tracking the changes in liquid water would lead to incorrect conclusions. This is probably due to significant hail contamination of precipitation estimates. In the Del City storm however, the amount of estimated liquid water remained modest, suggesting little hail contamination. In this storm changes in surface precipitation were sensed equally well with the integrated liquid water and kinematic patterns.

Summary of Findings

The results of this analysis suggest that important details in the life cycle of supercells can be observed with single-Doppler data. In the Hailstorm supercell, persistent low-level contraction existed on the upwind, rear flank of the storm in the lower levels. This zone was associated with an area of positive and negative cross-beam shear. Both features twisted clockwise with height and generally remained upwind of the reflectivity maximum. The vertical and temporal continuity of these features were excellent.

The storm model of Chapter IV suggests that the contraction and

cross-beam shear patterns observed may be an updraft zone, perhaps with a rotational couplet. A breakdown of the Hailstorm updraft pattern preceeded the merging process.

The movement of mid-level contraction zones as well as changes in their size inferred tilt of the storm updraft offer considerable insight into the resulting surface precipitation. Reliance on radar reflectivity to estimate changes in surface rainfall may be seriously hampered by hail contamination in supercell storms.

Mesocyclone Patterns and Rainfall

Introduction

The principal goal of this section is to examine mesocyclone rainfall and the associated single-Doppler kinematic fields. The inferred kinematic fields are compared with multi-Doppler observations of the Ft. Cobb storm. Again, the kinematic-rainfall relationships are contrasted with the integrated liquid water rainfall relationships. In this section this comparison is integrated into the kinematic chronology.

In addition, new signature patterns of mesocyclones are discussed involving the radial stretching and cross-beam shear fields. These fields often enable one to identify mesocyclones more readily than with conventional radial velocity patterns.

Conclusions based upon the Ft. Cobb analysis are compared with the mesocyclones observed on 1 May 1977.

General

The general environmental background conditions are identical to those of the Del City storm and the Hailstorm of the same day. In facet, the double storm complex existed during the same time period, 1630 to 1745 CST, in relatively close proximity (within 30 km) to the Ft. Cobb storm. The Ft. Cobb storm produced mesocyclones with tornadoes at 1643 and 1709. The mean mid-level environmental wind was from the south-southwest (190°) at 25 m s^{-1} . Low-level flow toward the storm was from 120° at 10 m s^{-1} . Storm motion was toward 030° at 17 m s^{-1} . The dominant low-level inflow from the east-southeast was over the NSSL mesonet.

In a northwest radar scan quadrant, the Ft. Cobb low-level flow toward the storm was nearly parallel to the radar beam. The storm motion was nearly perpendicular to the beam, implying that the Doppler radial velocities were quasi-radial relative velocities with respect to the storm. The mid-level flow was nearly perpendicular to the beam, thereby reducing confidence in possible inferences.

Time Sequence of Single-Doppler Fields

Fig. 18 contains the time sequence of reflectivity (dBZ), radial velocity (m s^{-1}), radial stretching ($\times 10^{-3} \text{ s}^{-1}$), and cross-beam shear ($\times 10^{-3} \text{ s}^{-1}$) for the 1-km level. The 285° and 270° radials, with reference marks in km from NSSL, are superimposed upon the panels.

Reflectivity patterns at 1630 (Fig. 18a) showed a large area of 45 dBZ entering the map. This core was associated with strong

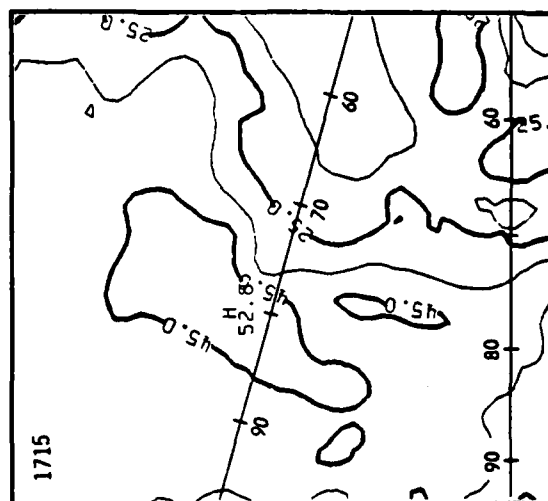
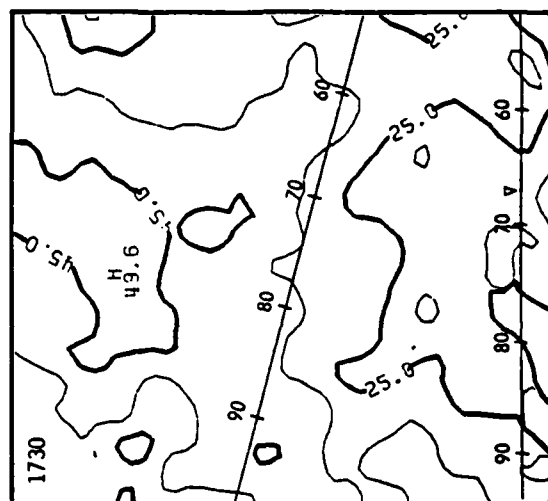
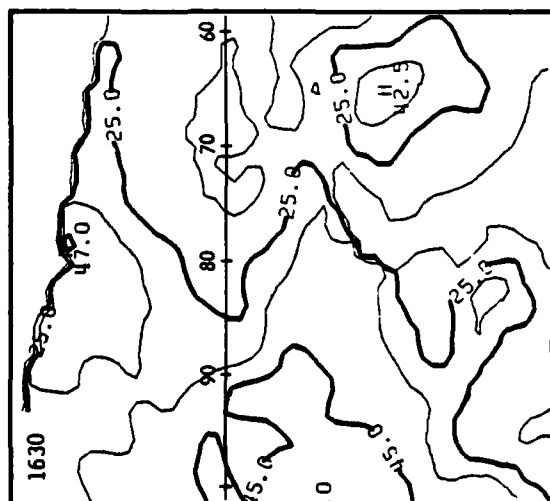
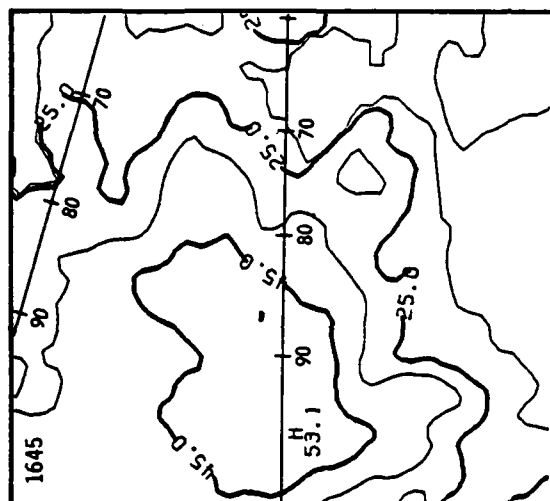
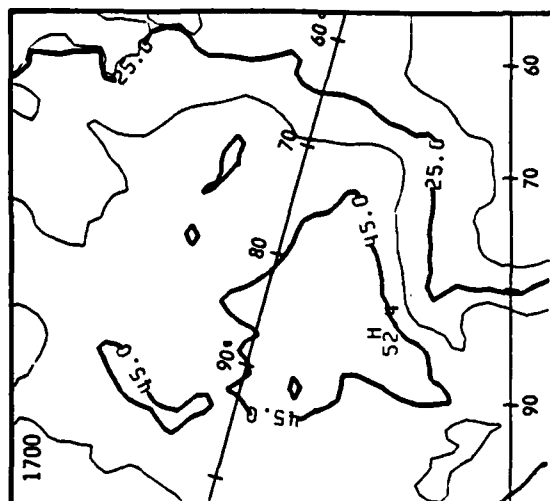


Fig. 18a. Ft. Cobb storm
(20 May 1977) 1 km time sequence
of reflectivity (dBZ), contoured
in 10 dBZ intervals starting at
15 dBZ.

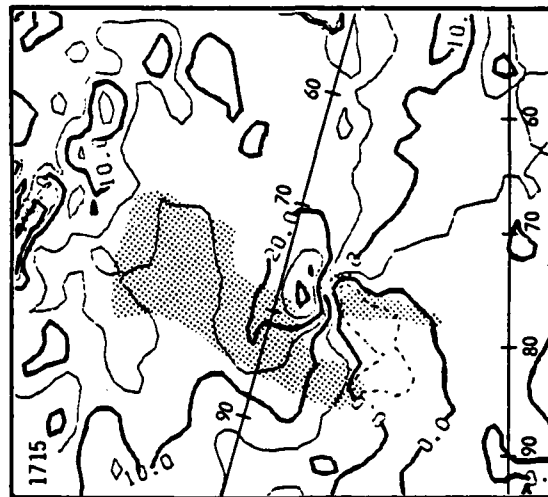
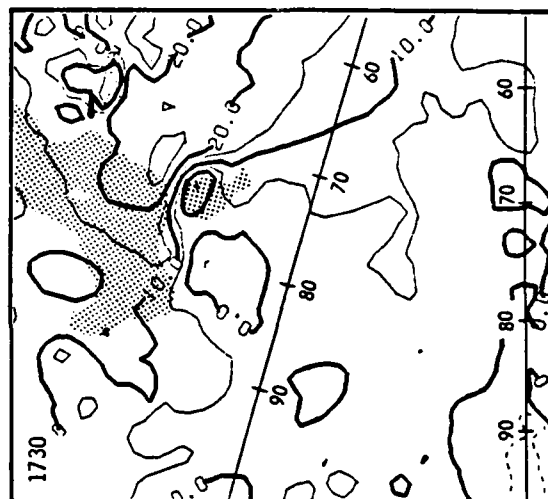
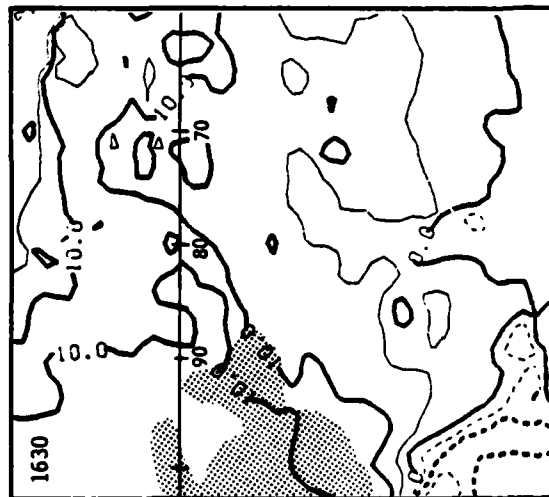
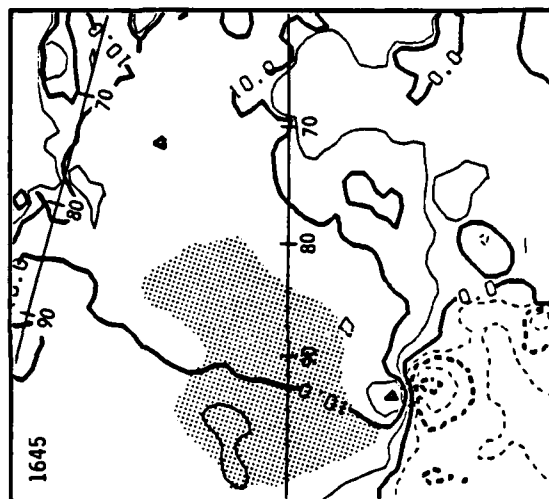
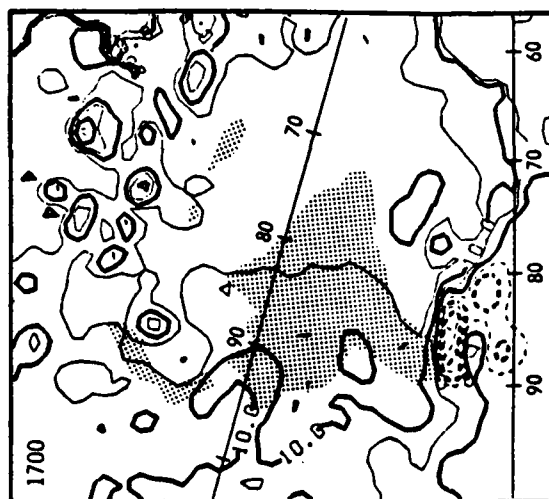


Fig. 18b. Ft. Cobb storm (20 May 1977) 1 km time sequence of radial velocity (m s^{-1}), contoured at 5 m s^{-1} intervals. Stippled area is the 45-dBZ echo.

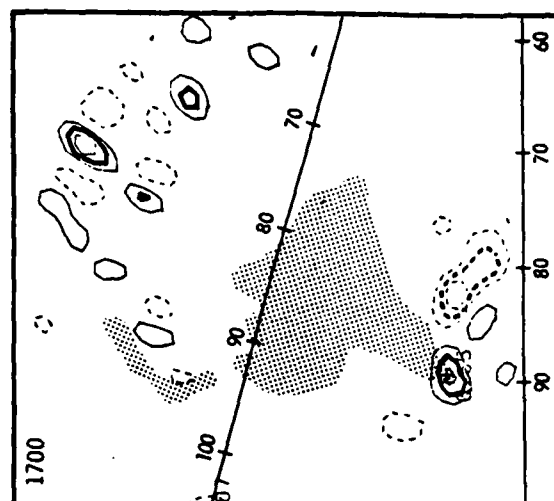
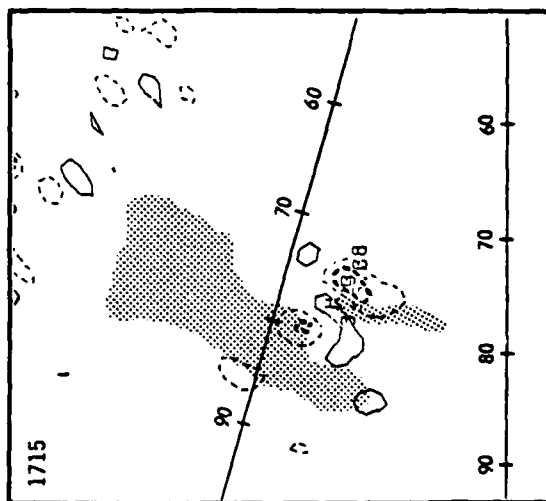
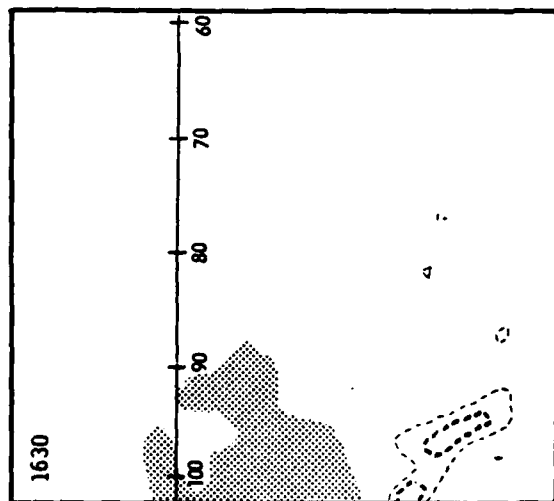
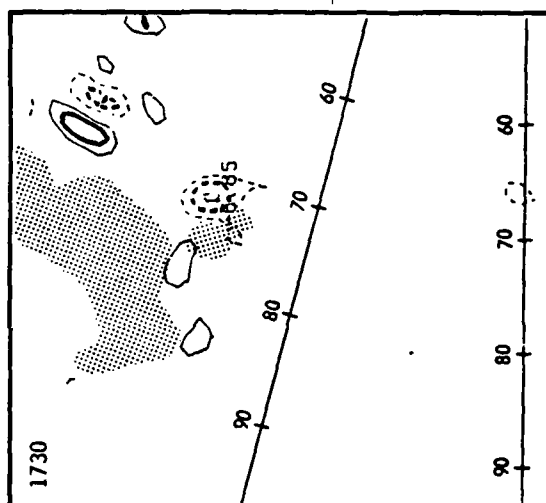
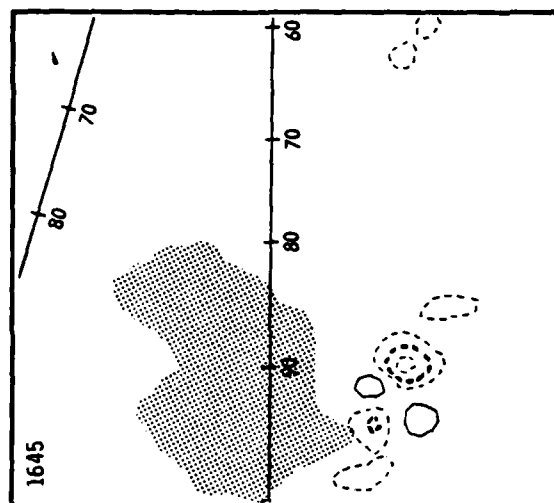


Fig. 18c. Ft. Cobb storm (20 May 1977) 1 km time sequence of radial stretching ($\times 10^{-3} \text{ s}^{-1}$), contoured in 2×10^{-3} intervals greater than $2 \times 10^{-3} \text{ s}^{-1}$ (solid lines) and less than $-2 \times 10^{-3} \text{ s}^{-1}$ (dashed lines). Stippled area is the 45-dBZ echo.



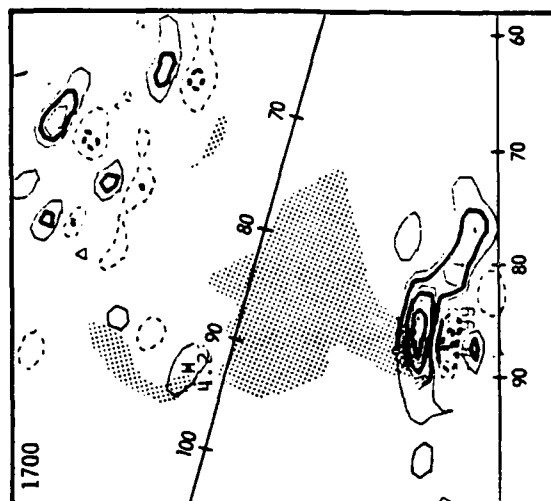
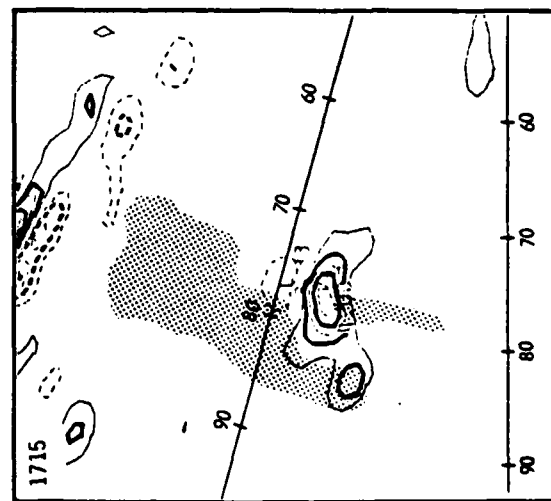
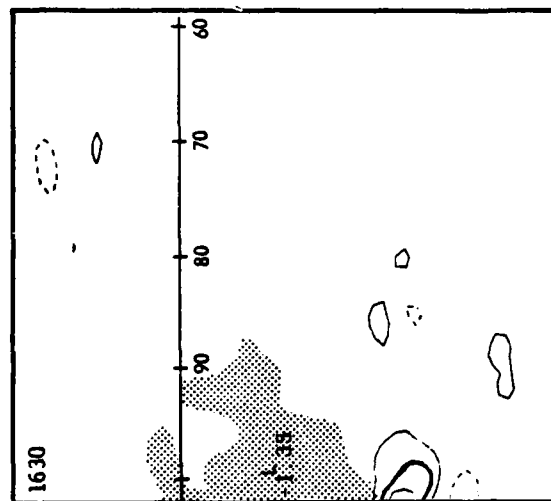
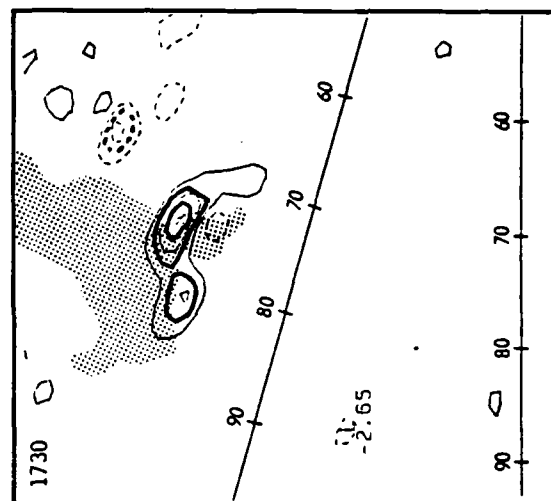
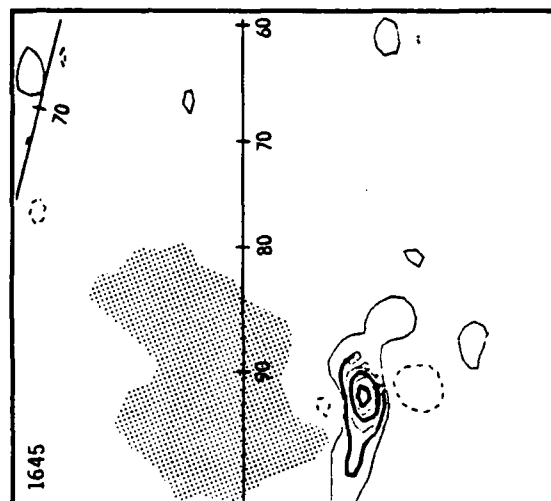


Fig. 18d. Ft. Cobb storm (20 May 1977) 1 km time sequence of cross-beam shear ($\times 10^{-3} \text{ s}^{-1}$), contoured in 2×10^{-3} intervals greater than $2 \times 10^{-3} \text{ s}^{-1}$ (solid lines) and less than $-2 \times 10^{-3} \text{ s}^{-1}$ (dashed lines). Stippled area is the 45-dBZ echo.



AD-A106 752

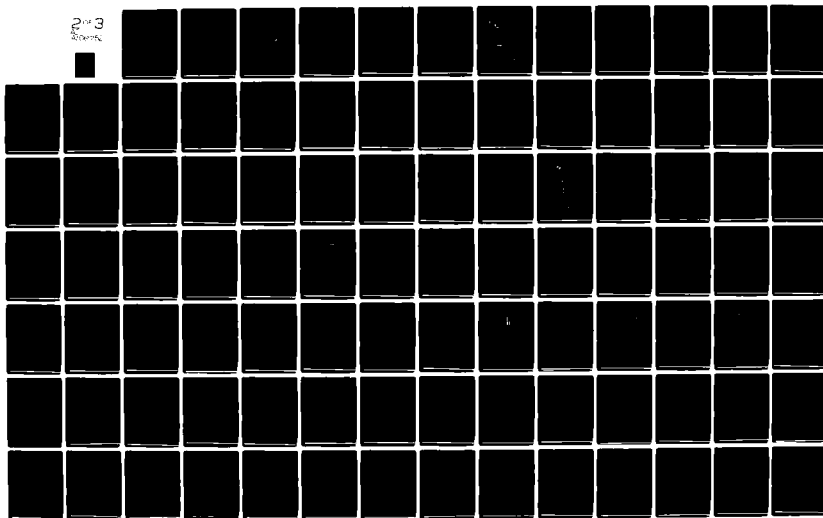
TEXAS A AND M UNIV COLLEGE STATION DEPT OF METEOROLOGY F/6 4/2
PRECIPITATION FIELD AND INTRASTORM FLOW OF SUPERCELL CONVECTIVE--ETC(U)
AUG 81 D J MCMORROW AFOSR-80-0063

UNCLASSIFIED

AFOSR-TR-81-0699

NL

2 of 3
AD-000000



low-level contraction on the upwind rear flank (Fig. 18c) and large positive cross-beam shear (Fig. 18d). The axis of the cross-beam shear was aligned parallel to the low-level wind. The radial velocity field suggested a potential rotation on the rear flank.

At 1645 the reflectivity core contained a cyclonic vortex pattern on the right rear flank (Fig. 18b). Low-level inflow was superpositioned on this pattern. A large area of positive cross-beam shear was also associated with this feature (Fig. 18d). A portion of this pattern contained a cyclonic vortex signature.

The 1700 time panel showed the 45-dBZ reflectivity contour as a triangular shape (Fig. 18a). The kinematic patterns showed a complex formulation in the radial stretching, perhaps due to a combination of divergent outflow, convergent inflow, and rotation (Fig. 18c). A large area of positive cross-beam shear was also associated with this feature (Fig. 18d).

At 1715 the reflectivity core elongated with its axis parallel to the mid-level flow. Fig. 18c shows a cyclonic vortex located on the left rear flank of the 45-dBZ echo within a bounded, weak echo region. Strong positive cross-beam shear is still associated with this feature (Fig. 18d).

The 1730 panels show the 45-dBZ reflectivity on the edge of the map (Fig. 18a). The cyclonic vortex pattern was not evident in the radial stretching map (Fig. 18c), but strong positive cross-beam shear remained (Fig. 18d).

Fig. 19 contains the same fields discussed above at 5 km. At 1630, Fig. 19c shows contraction on the rear and right rear flank of

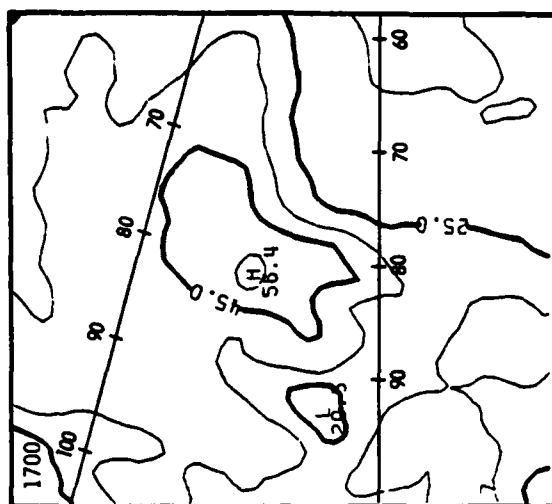
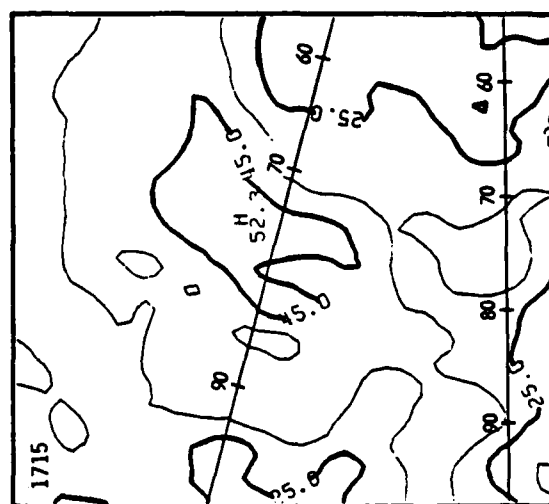
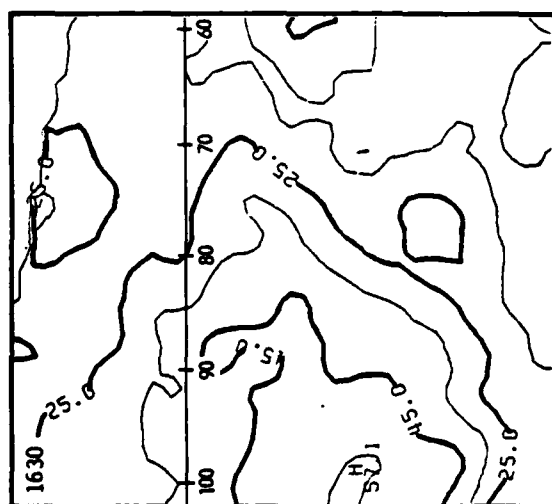
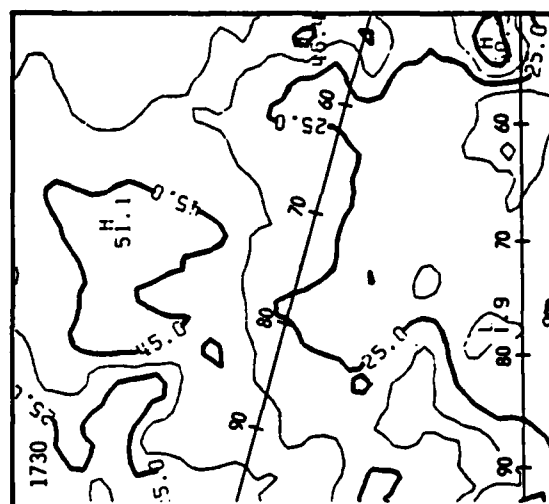
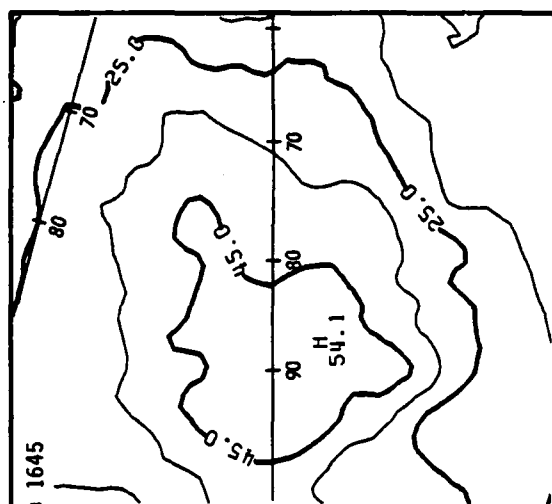


Fig. 19a. Same as Fig. 18a,
except at 5 km.



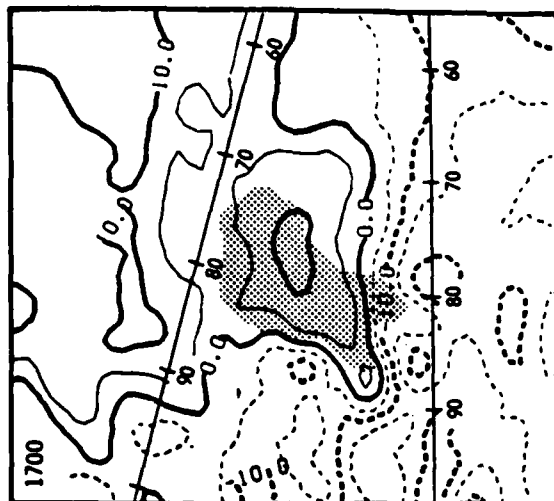
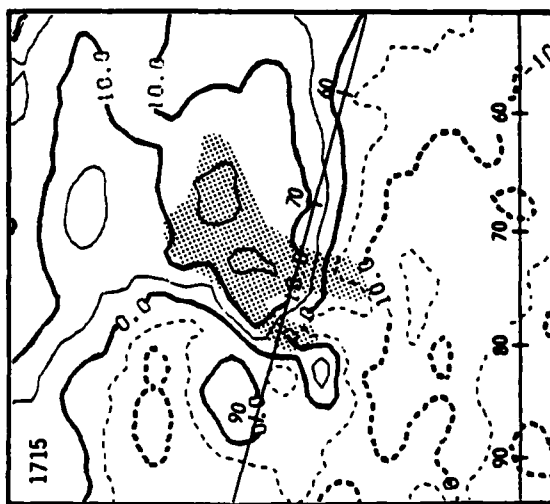
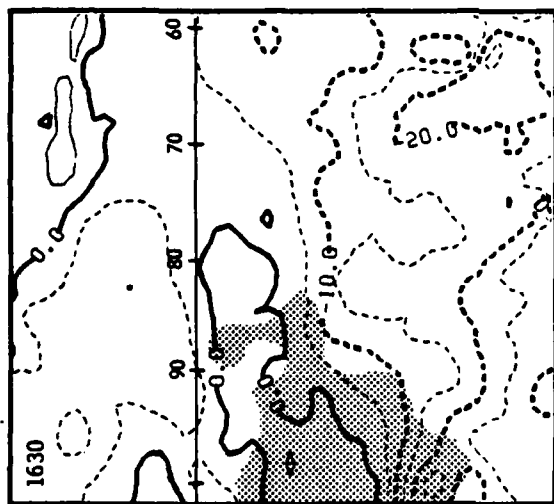
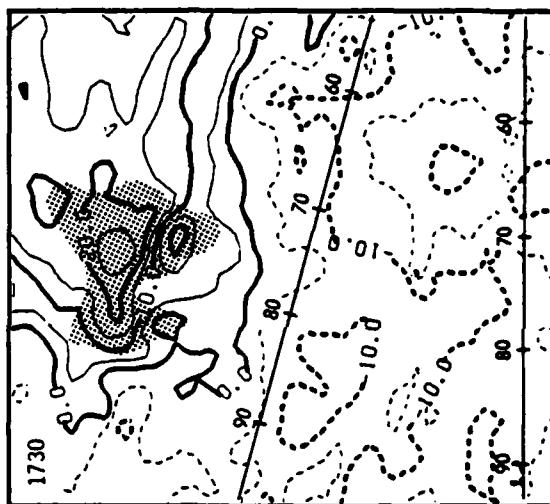
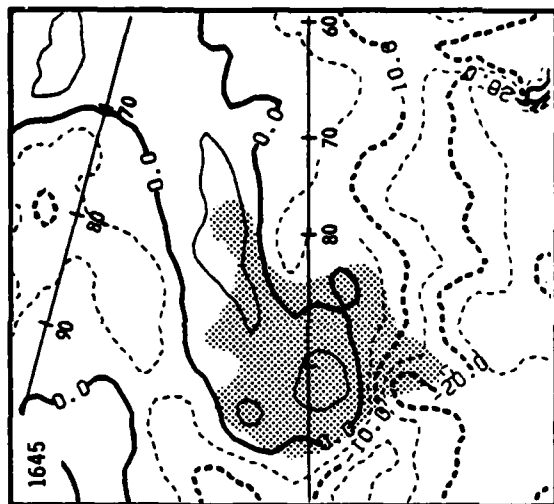


Fig. 19b. Same as Fig. 18b, except at 5 km.



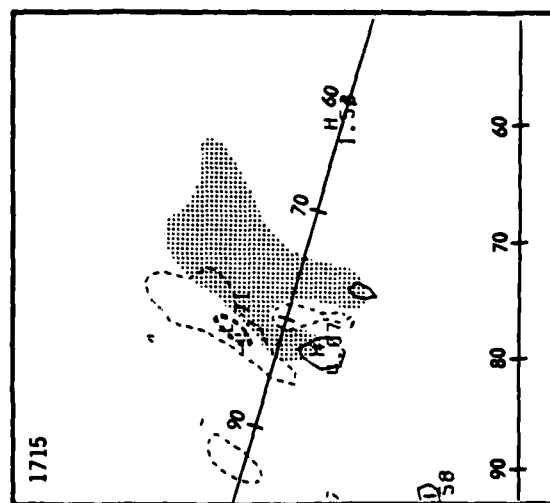
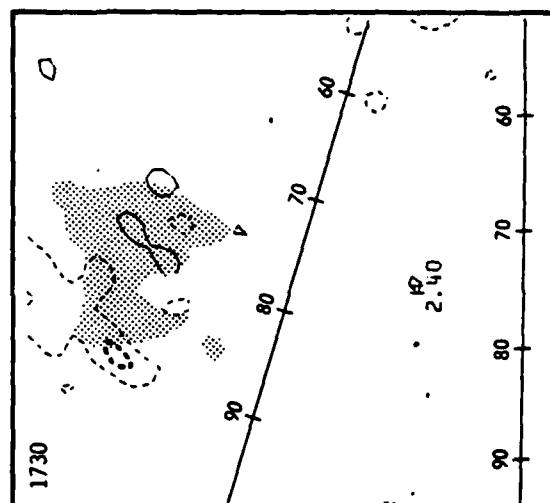
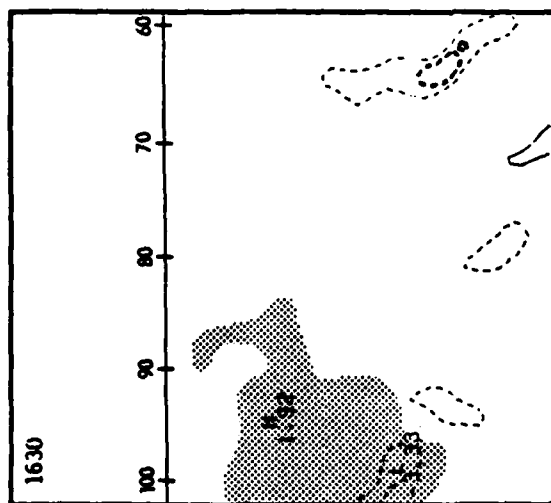
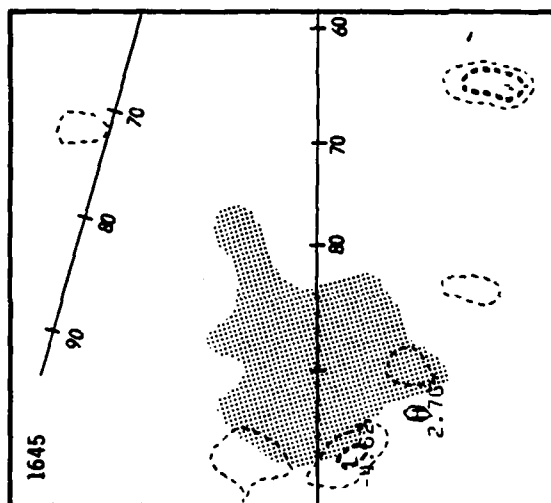
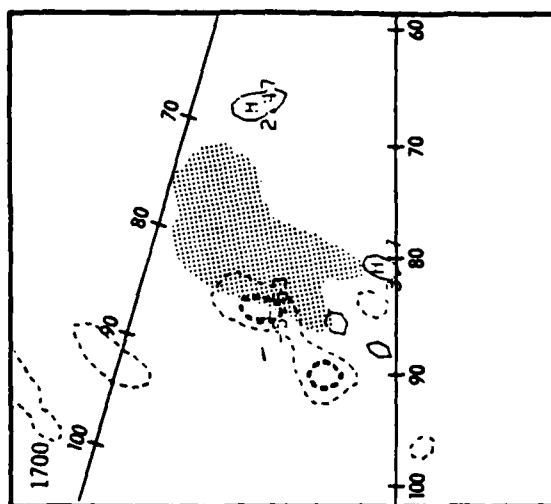


Fig. 19c. Same as Fig. 18c,
except at 5 km.

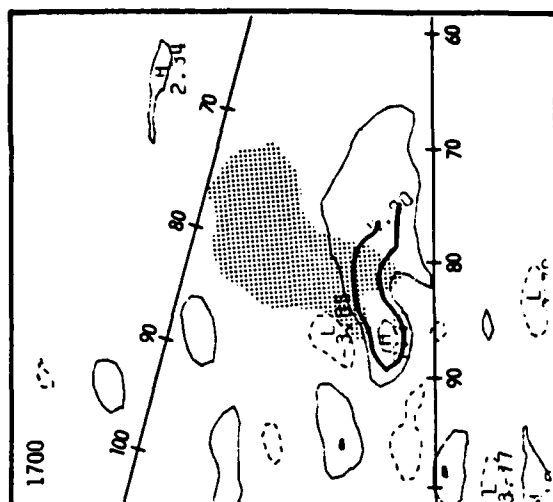
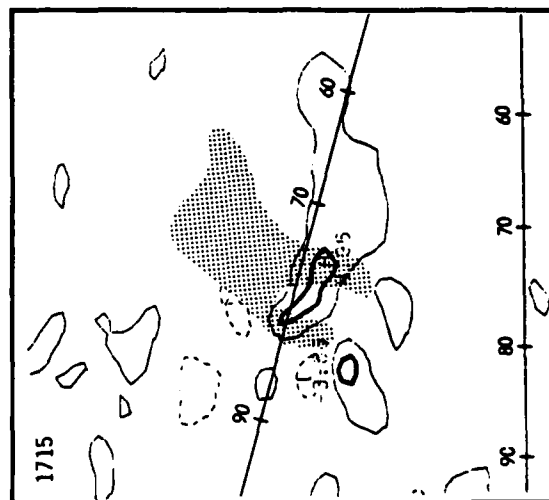
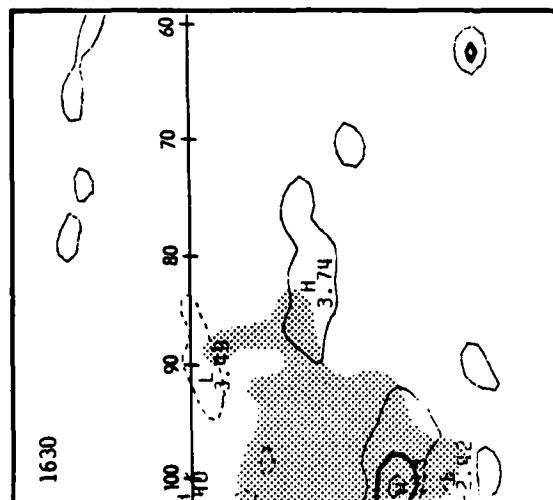
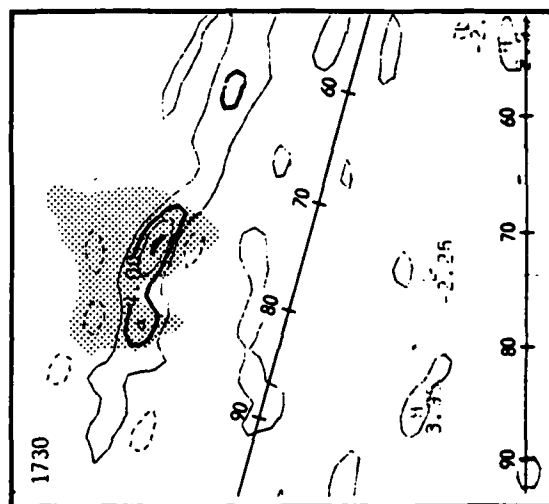
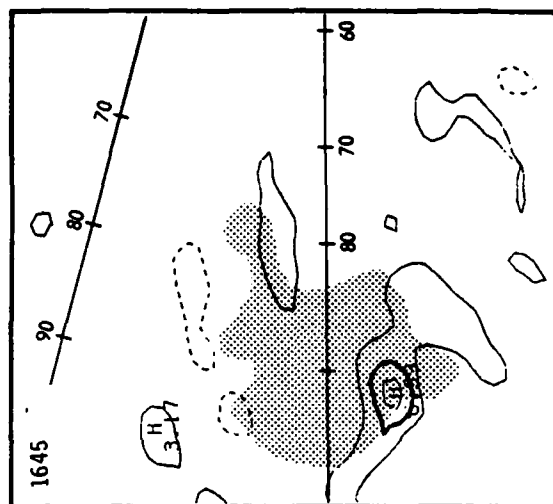


Fig. 19d. Same as Fig. 18d,
except at 5 km.



the storm. Strong positive cross-beam shear was associated with this feature (Fig. 19d). A tilt of the reflectivity to the southeast with height was complemented by a tilt of the positive cross-beam shear zone to the northeast.

The 1645 stretching (Fig. 19c) showed dominant contraction of the left flank, again associated with a large area of positive cross-beam shear (Fig. 19d).

The 1700 stretching patterns (Fig. 19c) reflected a similar pattern with a superimposed cyclonic vortex rotation. The cyclonic vortex can also be seen in the cross-beam shear panel (Fig. 19d).

At 1715 the strong contraction zone was still evident on the left flank (Fig. 19c) while the vortex pattern was not clearly evident. It will be shown later that the mid-level contraction pattern is associated with the location of the highest rainfall rates. Strong positive cross-beam shear still remained on the rear flank of the storm (Fig. 19c).

Single-Doppler Fields Plus Storm Model Interpretations

This section employs the kinematic patterns of Figs. 18-19 along with Fig. 20 the surface rainfall rate analysis (mm hr^{-1}) for the Ft. Cobb storm. A summary of the precipitation data is given in Appendix J.

At 1630 the Ft. Cobb storm was on the northwestern edge of the Washita Watershed network. Surface flow was more easterly than southerly at speeds of about 10 m s^{-1} . Confluence was evident on the south side of the main echo. Surface divergence and vorticity maxima

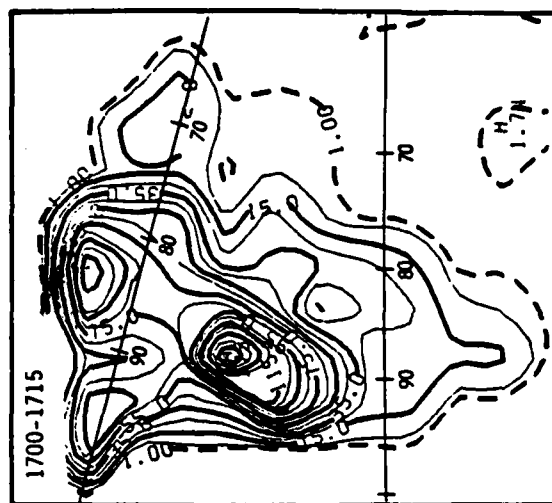
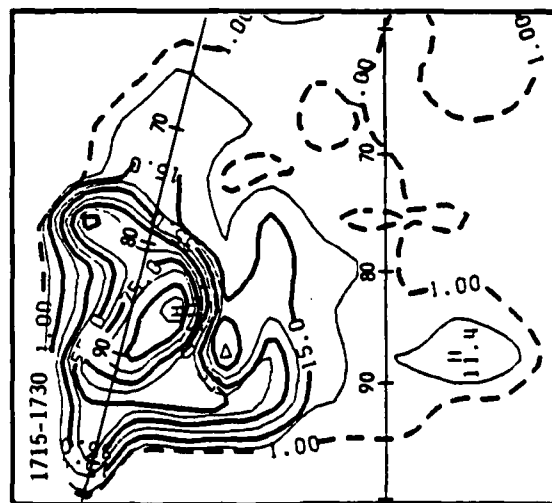
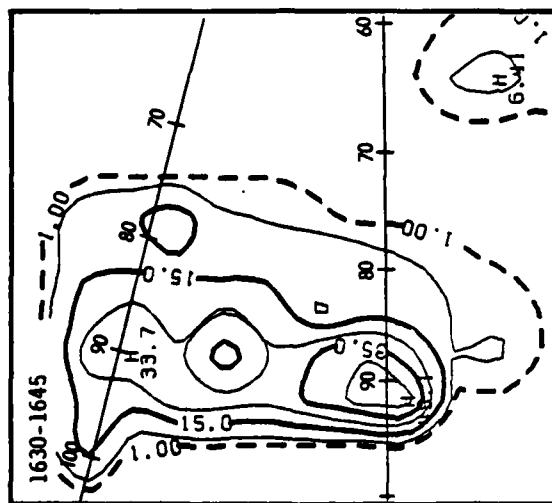
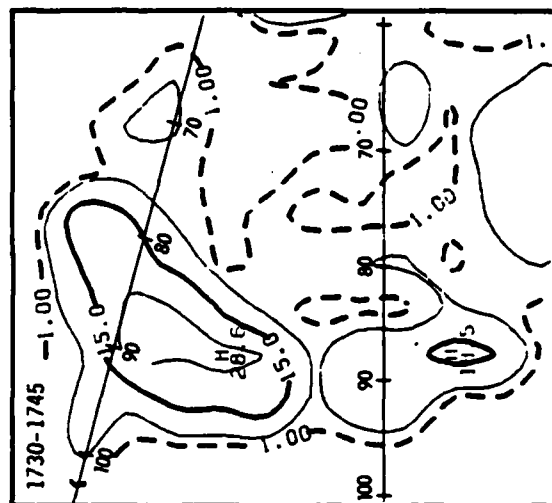
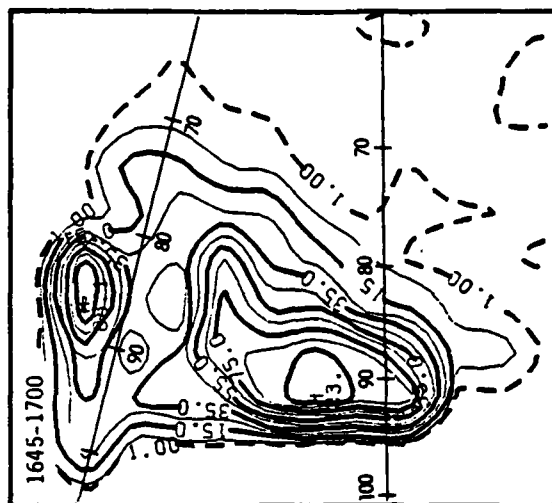


Fig. 20. Ft. Cobb storm rainfall rate time sequence (mm hr^{-1}) contoured in 10 mm hr^{-1} . Dashed contour includes all rainfall greater than 1 mm hr^{-1} .



of $5 \times 10^{-4} \text{ s}^{-1}$ (in both fields) existed ahead of the right front flank of the storm with the vorticity maximum being closer to the storm by about 10 km. The reflectivity core had a dramatic tilt with the 5-km core located roughly the same tilt had been noted in the Del City-Hailstorm. The 1-km and 5-km radial velocity maps showed strong cyclonic rotation on the south side of the storm. The cross-beam shear maps seemed to confirm this rotation by a partial cyclonic vortex signature.

The stretching maps showed strong contraction in the southeastern portion of the storm with mid-level contraction northeast of the 1-km pattern. The mid-level contraction was within the 45-dBZ contour, suggesting heavy precipitation.

The integrated liquid water maps showed relatively high values of 13 kg m^{-2} and 14 kg m^{-2} for the lower 4-km and upper 4-km layers, respectively. A more important feature was the large size of the 5-kg m^{-2} isopleth, which nearly matched the size of the 45-dBZ contour at the 1-km level. The storm contained considerable liquid water at this time both below and above the melting level.

The rainfall pattern for the 1630-1645 time period showed weak cores truncated by the rain gauge boundary. The highest rainfall rates (40 mm hr^{-1}) appeared to be represented in the southern portion of the storm.

The 1645 reflectivity maps suggested a hook echo on the left rear flank of the storm. A tornado was observed on the ground at this time. The cross-beam shear maps continued to show a tilt of the rotational core toward the northeast with heights. An elongated

signature pattern of a cyclonic vortex was clearly evident at 1 km while strong positive shear (probably cyclonic rotation) dominated the 5-km level. Multi-Doppler analyses (B. S. Johnson et al., 1980) have shown a mesocyclone to exist only at 2 km. The stretching map at 1 km also showed another obvious signature for a cyclonic vortex (see Chapter IV), while the 5-km map showed only strong contraction on the southern and western side of the echo.

Figs. 21 and 22 show a comparison of north-south cross sections through the mesocyclone (93W) and through the leading edge of the storm (75W). The 93W slice shows a weak echo region centered around 7S. The same feature is less evident on the 75W slice farther east. This suggests nearly easterly flow into the storm complex as described by the supercell model. The peak reflectivity cores are aligned nearly vertically in both cross sections. The cross-beam shear map at 93W shows a typical mesocyclone signature in the lower layer with a slope toward the north. A portion of the same pattern is also seen on the 75-km slice at approximately 8N and still sloping northward. This may suggest a northeast tilt of the mesocyclone with height as expected from the environmental wind profile. Notice the vertical continuity of the cyclonic rotation zone and its resemblance to the expected kinematic patterns discussed in Chapter IV.

The integrated liquid water maps revealed that the 5-kg m^{-2} isopleth increased in size from the previous period. The lower-level area of the Ft. Cobb storm was roughly double the Hailstorm area and the upper-level area was about 50% greater than that associated with

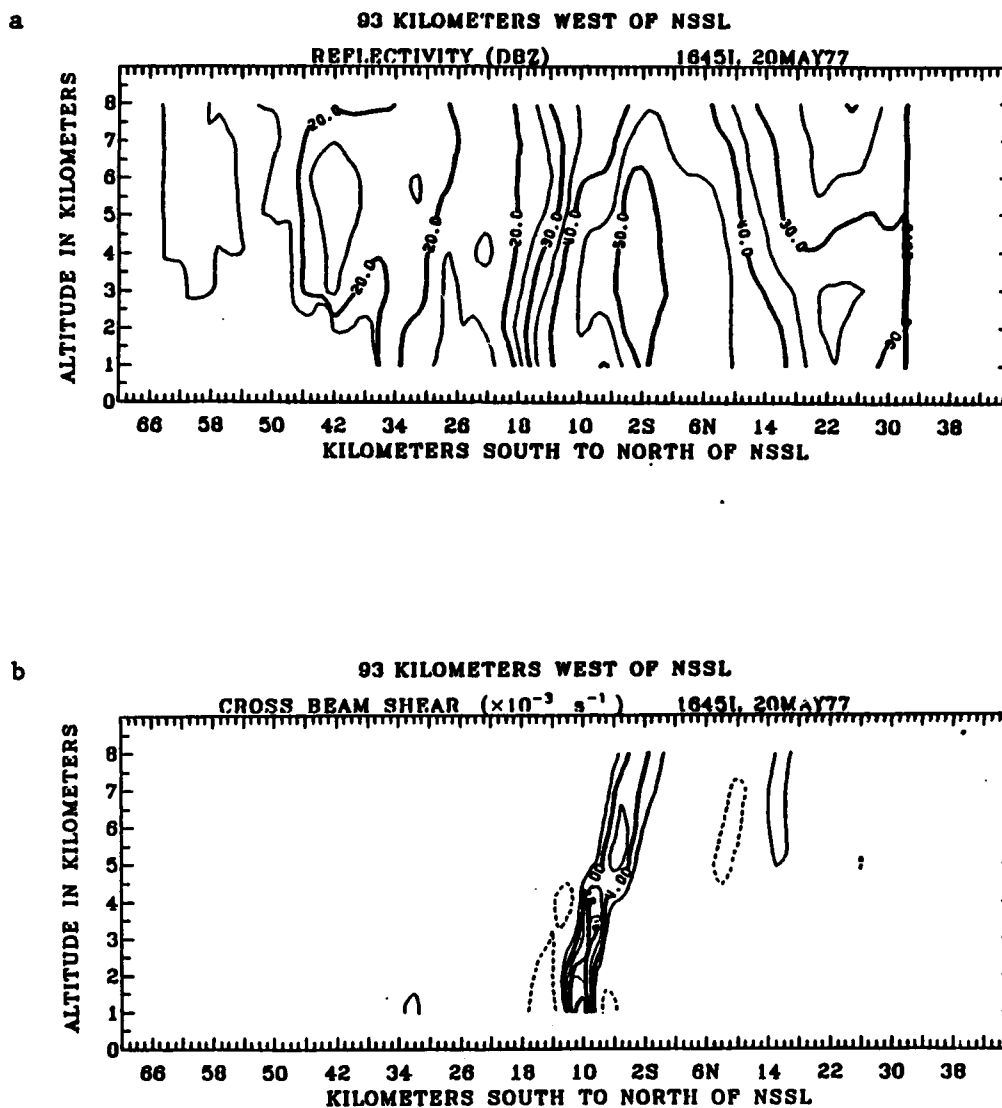


Fig. 21. North-south cross section 93 km west of NSSL at 1645.
 (a) Reflectivity (dBZ). (b) Cross-beam shear ($\times 10^{-3} \text{ s}^{-1}$).

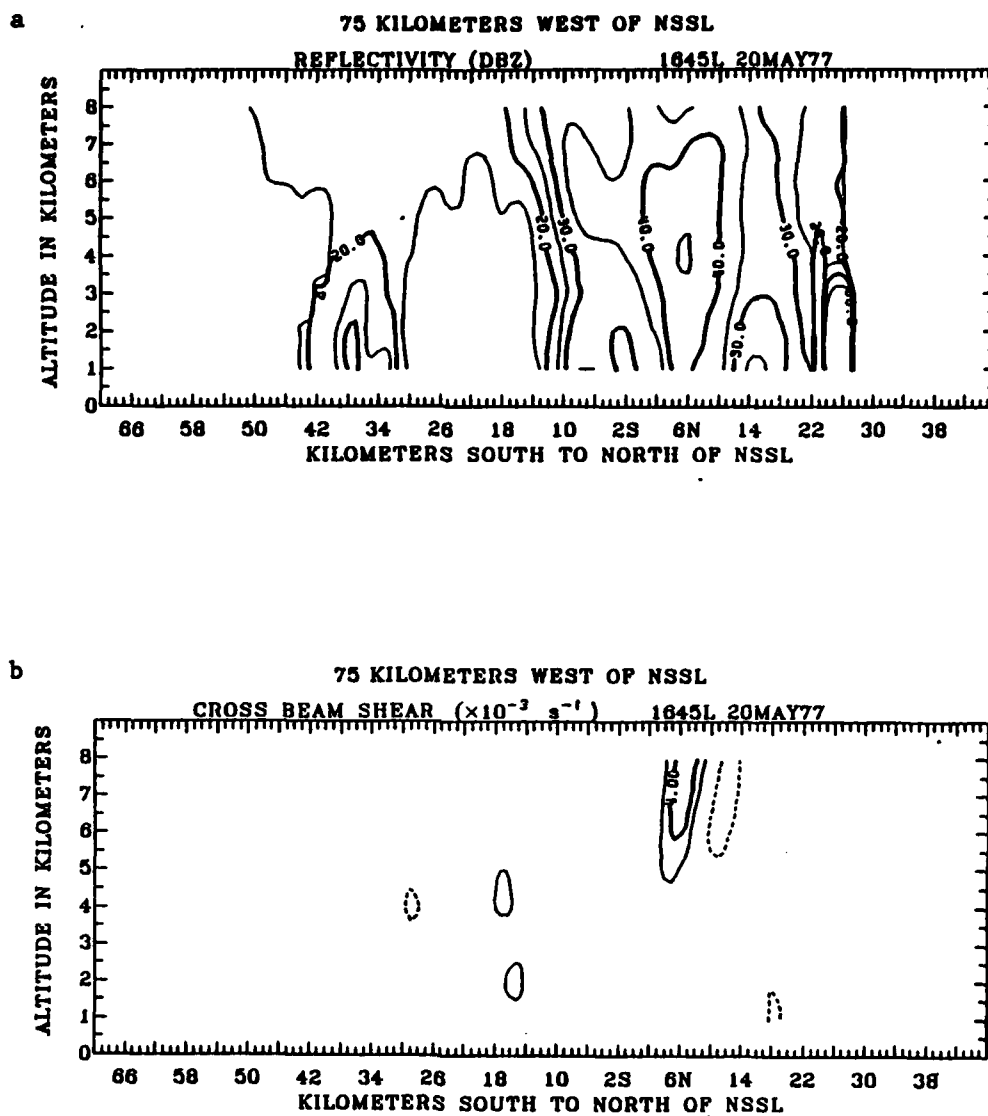


Fig. 22. North-south cross section 75 km west of NSSL at 1645.
 (a) Reflectivity (dBZ). (b) Cross-beam shear ($\times 10^{-3} \text{ s}^{-1}$).

the Hailstorm. Peak values remained strong, about 13 kg m^{-2} , but were not excessive, thus suggesting little hail contamination. High rainfalls over a large area appeared likely.

The rainfall map for the 1645-1700 period still showed some western boundary effects but two strong cores were noted. The peak rainfall area (103 mm hr^{-1}) was just northwest of the mesocyclone on the left flank of the storm and aligned north-south under the mid-level contraction. A secondary core (88 mm hr^{-1}) existed north of the main echo with an east-west alignment. This pattern was similar to the one observed in the Hailstorm during the same period, however the integrated liquid water of the Ft. Cobb storm suggested more intense and larger rainfall areas for this storm. The reverse was observed. The kinematic structure of the storm, however, would lead one to believe that the intense rotation was increasing the water loading and not allowing significant precipitation to reach the surface. Rainfall rates would be considerably lower than the liquid water would predict. Recall in the last section a similar problem was noted with hail contamination of the liquid water estimates. In this case, one is reasonably confident of small hail contamination (due to moderate liquid water values) but the link between surface rainfall and liquid water does not account for the impact of strong rotation.

The surface mesonet analyses at 1700 provided little new information since the western extremity of the storm was 80 km from the radar. Strong confluence into the southern side of the storm was still evident. A pressure drop to 1000 mb (from 1004 mb) was evident due east of the mesocyclone. The divergence maxima had vanished,

while strong cyclonic vorticity remained apparent east of the mesocyclone. Since a downdraft will induce anticyclonic rotation to the right of the storm track, due to surface friction, the presence of cyclonic vorticity tends to confirm the lack of downdraft influence upon the network at this time.

The 1700 reflectivity map showed a more obvious hook echo at 1 km. The tilt of the reflectivity core increased, with the 5-km core now 7 km to the southeast of the 1-km core. No tornado was reported on the ground at 1700. The 1-km cross-beam shear map probably contained a combination of effects. Strong cyclonic rotation was still obvious, but an intense zone of strong anticyclonic rotation had developed. The supercell model suggests this may be part of divergent outflow. Notice the formation of a new rotation center 10 km east-southeast of the old one on the 1 km CBS panel. This is a reflection of a second mesocyclone in the developing phase. The radial stretching fields were also composed of partial signatures with no obvious kinematic feature dominating the flow. Very strong right-rear flank contraction was noted at 1 km, thus suggesting the inflow direction. The mid-level contraction continued to remain strong on the left flank, once again above the heaviest rainfall areas. The southern portion of the maximum is composed of the northwest contraction zone of a cyclonic vortex mesocyclone pattern discussed in Chapter IV. Burgess (1976) has shown that similar patterns exist in the mid-levels of the radial velocity field, often more than 30 min before surface tornadoes are observed. It is very significant to note that these patterns were revealed with a relatively unfavorable beam-flow

alignment.

The lower-level integrated liquid water map showed a slight decrease in the size of the 5-kg m^{-2} isopleth with the peak value increasing to 20 kg m^{-2} . The upper-level area remained unchanged during the period, thereby suggesting continued high rainfall rates affecting a slightly smaller area.

The rainfall pattern for the period 1700 to 1715 showed an intense precipitation core west of the hook echo region. The intensity increased to 175 mm hr^{-1} . The secondary cell also showed a strong increase in intensity to 127 mm hr^{-1} . This may be due to a sudden increase in available energy and moisture to the downdraft after tornado dissipation through the vortex valve mechanism (Lemon *et al.*, 1972). The area of the 55-mm hr^{-1} rate increased from 192 km^2 in the previous 15 min to 292 km^2 . This increase was not apparent in the reflectivity or the integrated liquid water data. However, an increase in mid-level contraction was apparent at 1700.

At 1715 the reflectivity pattern contained an obvious bounded weak echo region on the storm rear flank. The echo tilt remained unchanged. A characteristic mesocyclone signature was evident in the 1-km radial velocity. The 1-km cross-beam shear showed a partial cyclonic vortex pattern within the bounded weak echo region, while the 5-km pattern suggested a weakening in the rotation. A strong northerly tilt with height was still apparent. The low-level radial stretching map contained another cyclonic vortex signature similar to the kinematic model results. Again, the mid-level map was not explicit, but a weak convergence signature was seen over the

mesocyclone with a strong contraction zone over the left flank.

The integrated liquid water showed an increase to 127 km^2 in the 5 kg m^{-2} isopleth in the lower layers with a decrease in the upper layers to 60 km^2 . The rainfall for 1715-1730 showed a weakening in intensity and areal coverage with peak rates dropping to 116 mm hr^{-1} . While the mid-level contraction remained strong over the rain core, the intense rotation of the mesocyclone suggested an increase in suspended liquid water and light rainfall. Again, the kinematic information proved to be more accurate in estimating changes in surface rainfall.

North-south and east-west cross sections through the mesocyclone at 1715 are presented in Figs. 23 and 24. The bounded weak echo region is evident at 16N and 78W. Note that the southeasterly tilt with height of the reflectivity core is opposite to the northwesterly tilt of the mesocyclone rotation. A similar opposite tilt was noted in the Hailstorm. (The mid-level maximum to the west in Fig. 21 is due to the 1645 mesocyclone rotation.) This suggests mid-level air will initiate the downdraft on the right side of the updraft and reach to the front of the storm after it has begun its downward trajectory. This configuration is very similar to the one Browning (1964) suggested with the drafts rotated 90° clockwise from the direction of storm motion.

An interesting contrast can be made between Figs. 23 and 24 (a strong low-level mesocyclone), and Fig. 35 (a weak upper-level mesocyclone). The peaked radial velocity pattern is distinctive in both storms, as is the vertical continuity of the cross-beam shear. In

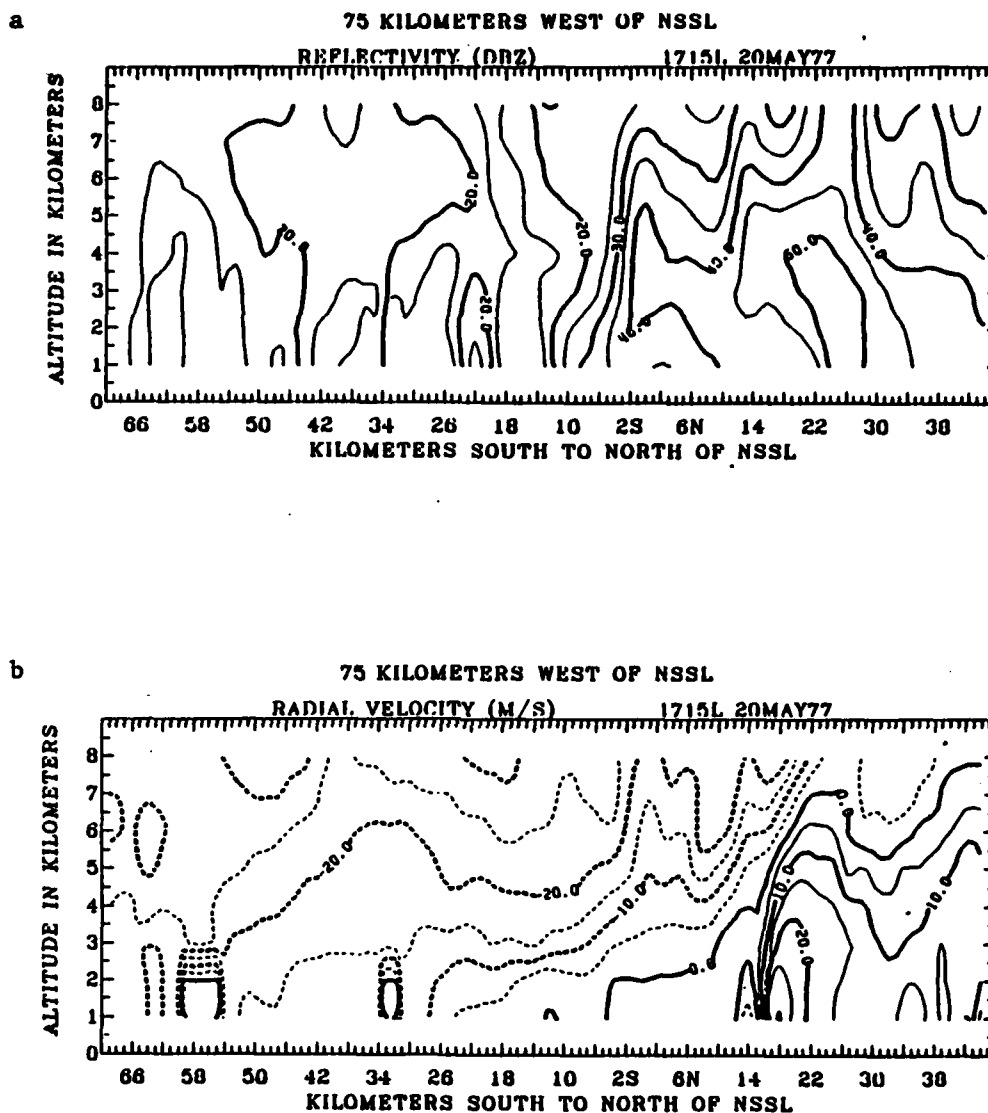


Fig. 23. North-south cross section 75 km west of NSSL at 1715.
 (a) Reflectivity (dBZ). (b) Radial velocity (m s^{-1}).

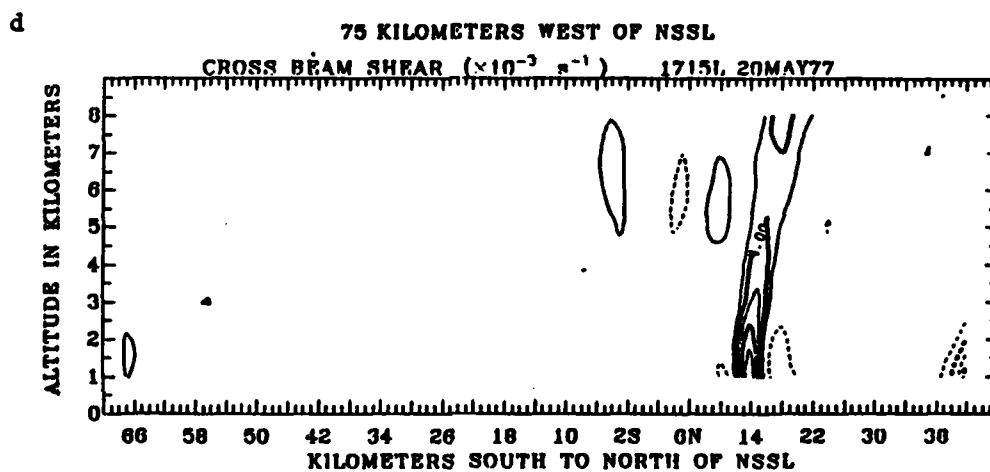
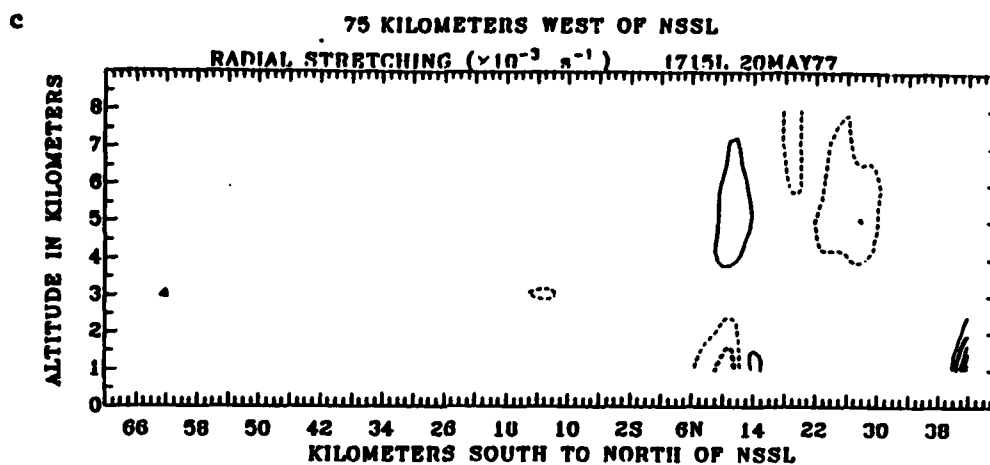
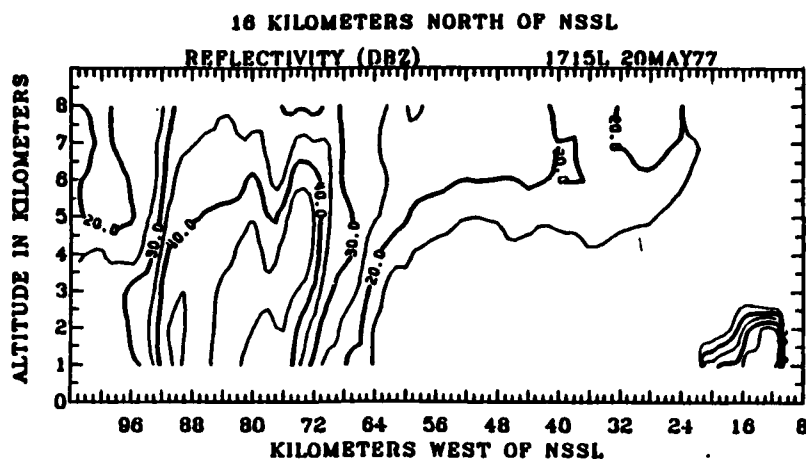


Fig. 23. (Continued) (c) Radial stretching ($\times 10^{-3} \text{ s}^{-1}$).
 (d) Cross-beam shear ($\times 10^{-3} \text{ s}^{-1}$).

a



b

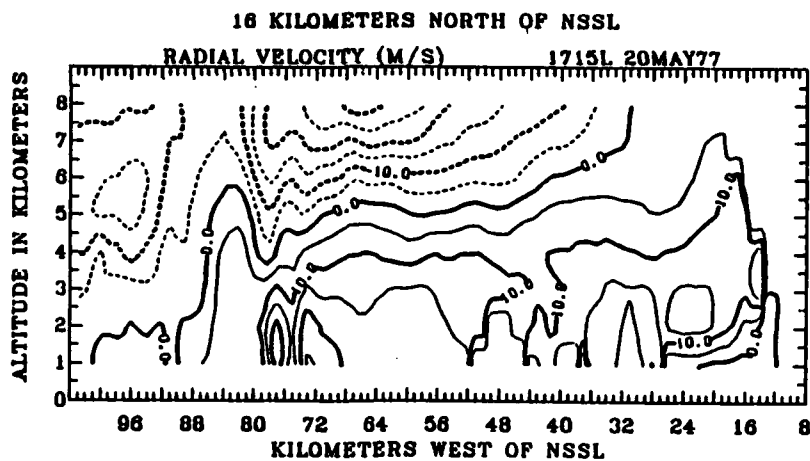


Fig. 24. East-west cross section 16 km north of NSSL at 1715.
 (a) Reflectivity (dBZ). (b) Radial velocity (m s^{-1}).

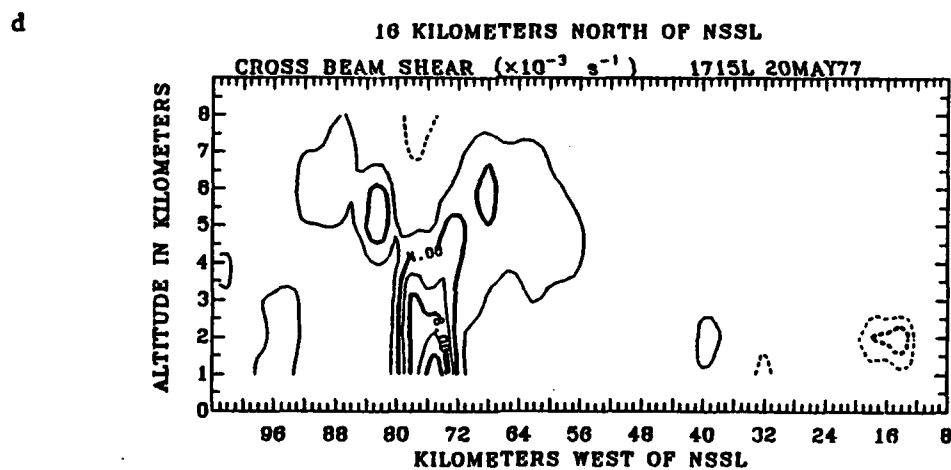
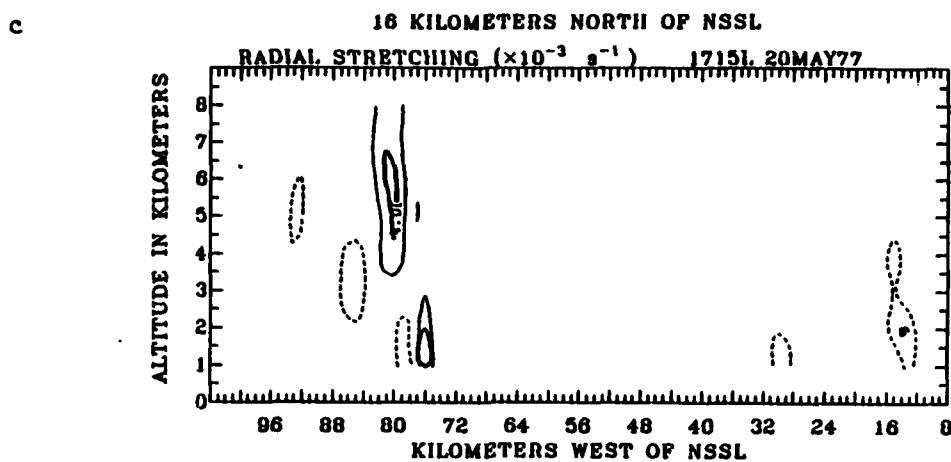


Fig. 24. (Continued) (c) Radial stretching ($\times 10^{-3} \text{ s}^{-1}$).
 (d) Cross-beam shear ($\times 10^{-3} \text{ s}^{-1}$).

low-level mesocyclones, the radial stretching pattern will show a reversal of the stretching-contraction pattern in the mid-levels. This is suggested in Fig. 24 and shown more clearly in Fig. 23. Like all signature patterns, this feature is sensitive to the slice angle.

The surface analyses at 1730 showed extremely strong confluence toward the Ft. Cobb storm. The vorticity east of the storm now reached $10 \times 10^{-4} \text{ s}^{-1}$, while a convergence zone greater than $5 \times 10^{-4} \text{ s}^{-1}$ developed. The θ_w values dropped below 14°C in the extreme northwestern corner of the network, thereby suggesting a downdraft zone. Strong pressure perturbations, however, were not observed.

The reflectivity maps at 1730 showed some development to the west of the 45-dBZ contour. The storm's southern half remained within the radar box, and it continued to show strong cyclonic rotation on the southern flank in both the lower and upper levels. No patterns existed on the 1-km stretching map that had a large positive cross-beam shear at the right rear flank. The 5-km radial stretching showed contraction along the western flank with stretching dominating the center and right flank. This increase in mid-level stretching should signal a weakening of the downdraft and reduced surface rainfall. The cross-beam shear maps, however, continued to show two cores of cyclonic rotation at 1 km with considerable rotation along a northwest-southeast axis across the southern flank of the storm. Such strong rotation will also work to reduce the surface rainfall.

The liquid water maps showed the area of the 5-kg m^{-2} isopleths unchanged for the lower level, but dropping to a mere 17 km^2 (from 60 km^2) in the upper level. It is important to note that in this time

frame the low-level integrated liquid water (and reflectivity) showed little change while the two kinematic signatures, mid-level stretching and strong rotation, signaled reduced surface rainfall.

The rainfall map ending at 1745 was biased by northern boundary truncation; however, the low rates and weak gradients lead one to suspect lighter rates throughout the storm.

The idea that mid-level contraction zones should lie over the center of the reflectivity core to produce high rainfall requires some modification in the presence of mesocyclones. In the Ft. Cobb storm, high rates were maintained with the strongest and largest mid-level contraction displaced toward the left flank of the storm. Peak rainfalls were still observed under the peak mid-level contraction zones.

A comparison of the single-Doppler inferences of the Ft. Cobb storm were also compared with multi-Doppler observations. B. C. Johnson et al. (1980) have shown horizontal and vertical cross sections of vertical vorticity for the Ft. Cobb storm. They noted a dual circulation at 1712 on their 0-km horizontal projection. A close look at the 1-km cross-beam shear map at 1715 also shows two zones of cyclonic rotation, about 8 km apart. While the eastern half of the rotation is evident on the 1-km stretching map, the western rotation zone is not. B. C. Johnson et al. (1980) also showed horizontal maps of the vertical velocity. They noted an updraft-downdraft-updraft configuration lying along the radar radial in the area of the mesocyclone. The 1645, 1700, and 1715 stretching maps do suggest two possible contraction zones in a similar alignment, but such an inference is weak. It is extremely difficult to decipher contraction

centers in the presence of other effects such as rotation. If a storm inflow region or updraft is close to a strong mesocyclone, a superpositioned pattern may dominate the flow and make signature recognition difficult, even under favorable beam-flow configurations.

The vertical velocity maps of the Ft. Cobb storm show the strongest downdrafts east of the tornadoes. In this study the highest rainfall rates appear west and north of the mesocyclone, and are more aligned with the maximum reflectivities than the maximum downdraft velocities. The maximum downdraft velocities appear to be more associated with a dry downdraft (see Lemon and Doswell, 1979), and are revealed more as a surface gust front than a precipitation maximum. The mesocyclone-precipitation alignment found in this investigation is in good agreement with the conceptual Lemon and Doswell (1979) model.

K. W. Johnson et al. (1980) investigated the vorticity development within the Ft. Cobb storm, again with multi-Doppler observations. They noted "at low levels the area of maximum vorticity was coincident with and extended to the southeast of the main updraft." A comparison of the cross-beam shear maps of this investigation and the vorticity maps presented by K. W. Johnson et al. showed excellent agreement. The shape, size, and location of the centers were similar, with the cross-beam shear accounting for 60 to 80% of the vorticity at 1 km.

K. W. Johnson et al. also noted that the peak vorticity during the time tornadoes were on the ground occurred between the surface and 2 km. This tends to confirm observations of strongest cross-beam shear occurring in the lower levels in this investigation. A

comparison of several vertical cross sections of vorticity and cross-beam shear also showed good agreement.

Again, the overall match of the single-Doppler inferred flows with the analyses derived from multi-Doppler radars was most encouraging.

Summary of Findings

This section appears to accumulate additional evidence to support the idea that major storm features revealed by single-Doppler radar data accurately reflect the more precise picture of storm flow revealed by multi-Doppler observations. Poor beam-flow alignments do not appear to be a serious problem in pattern recognition in supercell storms. The consistency of the inferred kinematic patterns suggests the potential ambiguity problem of interpreting single-Doppler fields is not a dominant concern.

Strong and weak mesocyclones seem to have consistent kinematic signatures as do mesocyclones observed near the surface and in the mid-levels.

Again, changes in the surface rainfall follow the inferred kinematic fields more closely than changes in radar reflectivity or integrated liquid water. In supercells with mesocyclones the prominent mid-level contraction core is displaced toward the left flank. Heaviest rainfalls are observed under this zone. The rapid rotation of mesocyclones tend to maintain more liquid water aloft (and produce less surface rainfall) than the reflectivity data suggest. Heavy rainfalls were observed after a weakening of the mesocyclone.

Squall Line Supercell

Introduction

This section describes the kinematic patterns of squall line supercells and contrasts them with the patterns of isolated supercells. The storm model is employed to set the kinematic patterns within a larger framework. Changes in surface rainfall again seem to be better correlated with the single-Doppler kinematic patterns than radar reflectivity or integrated liquid water.

Mesoscale Environment

A squall line entered the western portion of the radar box at 1330. The line was moving eastward at 12 m s^{-1} with the strongest activity north of the 270° radar radial. A gust front containing moderate speed shear and a sharp temperature discontinuity preceded the line. The pressure change across the line was relatively weak. Light precipitation generally began a few minutes ahead of the gust front. Several cells in the squall line contained extremely high rainfall rates over a large area. Flash flooding was reported at several sites throughout the Washita watershed.

The environmental flow ahead of the front was determined from a combined hodograph of soundings taken at Ft. Sill (1346), Elmore City (1432), and the KTVY Tower (1435) near Oklahoma City (Fig. 25). Strong veering winds were observed from the surface to 10 km.

The mean mid-level flow ahead of the line was from 180° at 18 m s^{-1} . Mean storm motion of the strongest echoes within the line was

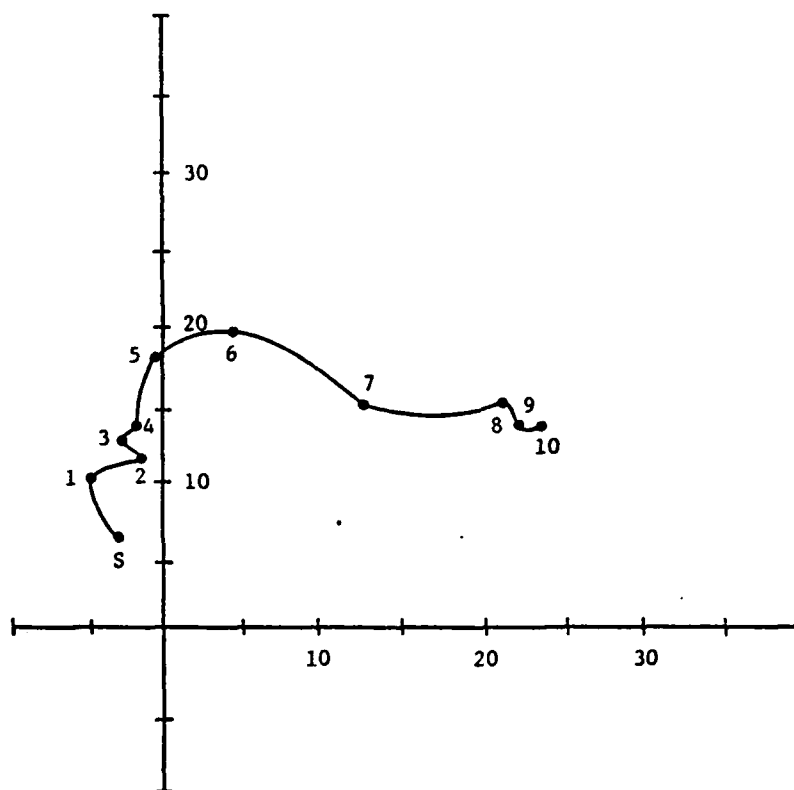


Fig. 25. 19 May 1977 afternoon combined hodograph.

from 230° at 12 m s^{-1} . This implied a beam-flow angle of nearly 90° for the main supercell echo. The low-level flow was from 160° at 10 m s^{-1} and resulted in a beam-flow angle of 70° . Radar sector scans were often truncated south of the 240° radial during the squall line passage.

Time Sequence of Single-Doppler Fields

This section documents the single-Doppler fields for the first hour that the squall line was in the radar box. The line took approximately 3 hr to traverse the radar box.

Fig. 26 contains the reflectivity (dBZ), radial velocity (m s^{-1}), radial stretching ($\times 10^{-3} \text{ s}^{-1}$), and cross-beam shear ($\times 10^{-3} \text{ s}^{-1}$) for the 1-km level. The 270° and 285° radials are superimposed upon the panels.

At 1345 the reflectivity panel showed a large echo (greater than 45 dBZ) south of the 270° radial at the 90-km range (Fig. 26a). Intense contraction was noticeable ahead of this echo (Fig. 26c), along with strong positive cross-beam shear (Fig. 26d). Within the echo, a zone of stretching with negative cross-beam shear was evident.

Two 45-dBZ cores associated with the dominant supercell were evident at 1400 (Fig. 26a). The radial stretching showed the same contraction-stretching pattern inside and outside the echo, as noted at 1345 (Fig. 26c). The cross-beam shear continued to show a strong positive zone along the forward edge of the storm and negative values inside the principle echo (Fig. 26d).

The reflectivity weakened at 1415 (Fig. 26a) but the same radial

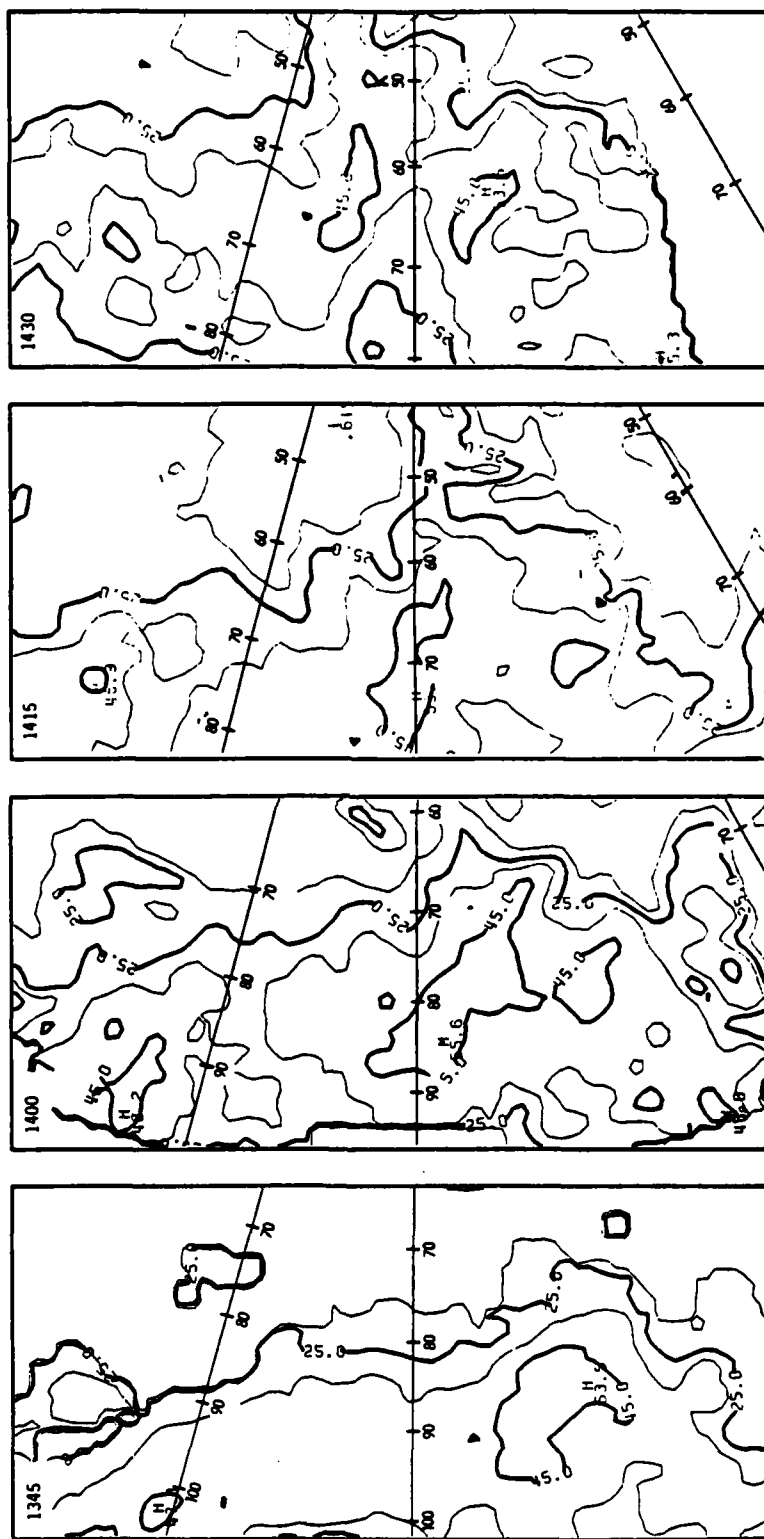


Fig. 26a. Squall Line (19 May 1977) 1 km time sequence of reflectivity (dBZ), contoured in 10 dBZ intervals starting at 15 dBZ.

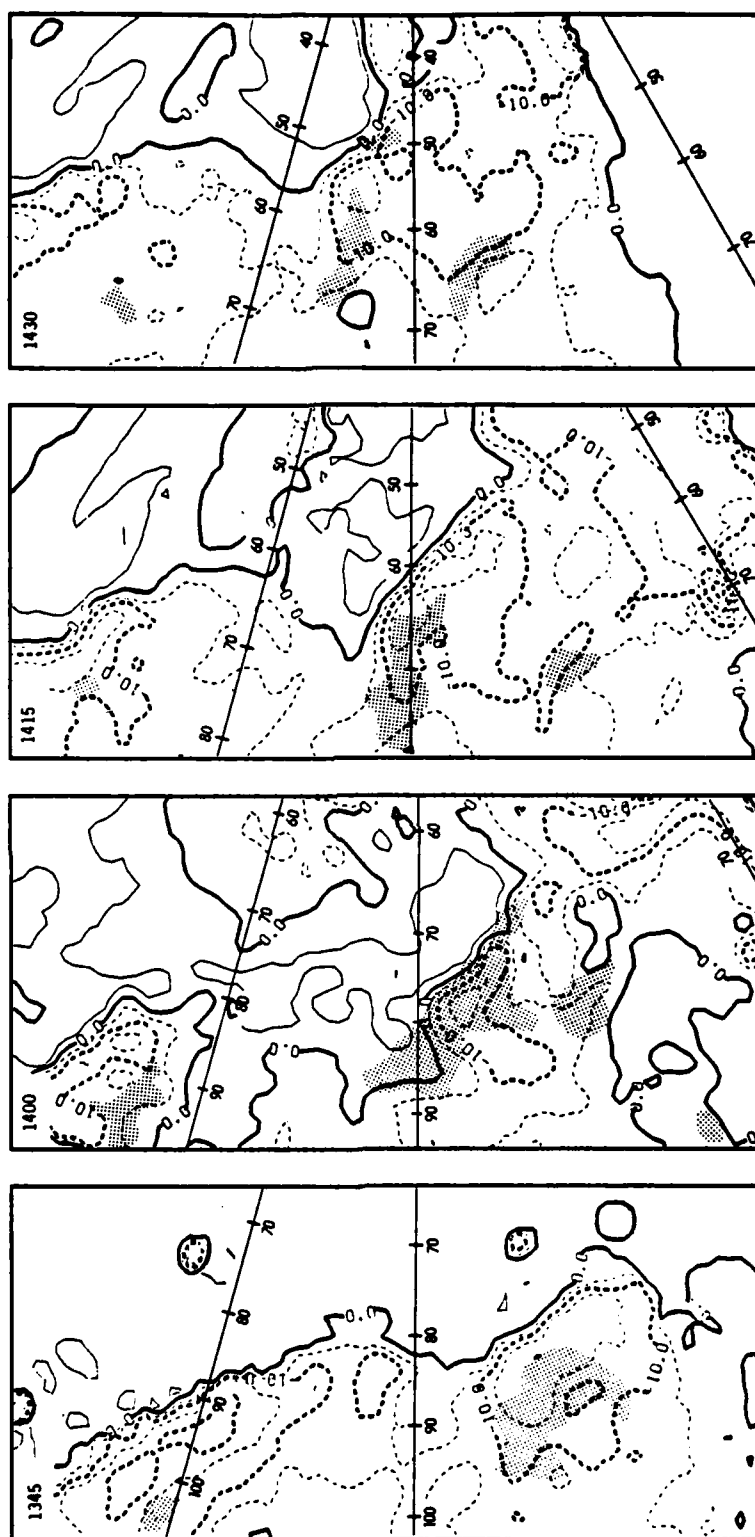


Fig. 26b. Squall Line (19 May 1977) 1 km time sequence of radial velocity (m s^{-1}), contoured at 5 m s^{-1} intervals. Stippled area is the 45-dBZ echo.

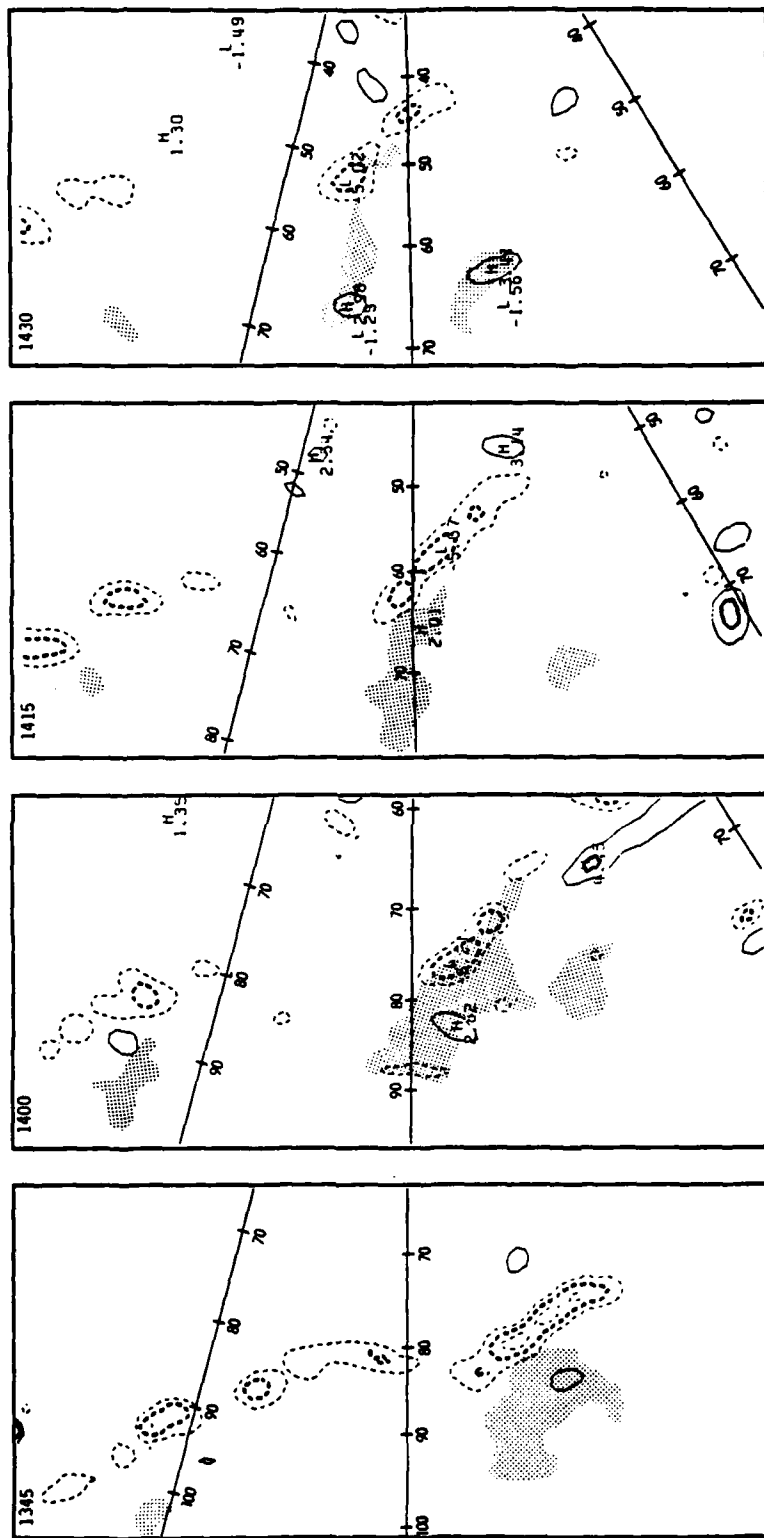


Fig. 26c. Squall Line (19 May 1977) 1 km time sequence of radial stretching ($\times 10^{-3} \text{ s}^{-1}$), contoured in $2 \times 10^{-3} \text{ s}^{-1}$ intervals greater than $2 \times 10^{-3} \text{ s}^{-1}$ (solid lines) and less than $2 \times 10^{-3} \text{ s}^{-1}$ (dashed lines). Stippled area is the 45-dBZ echo.

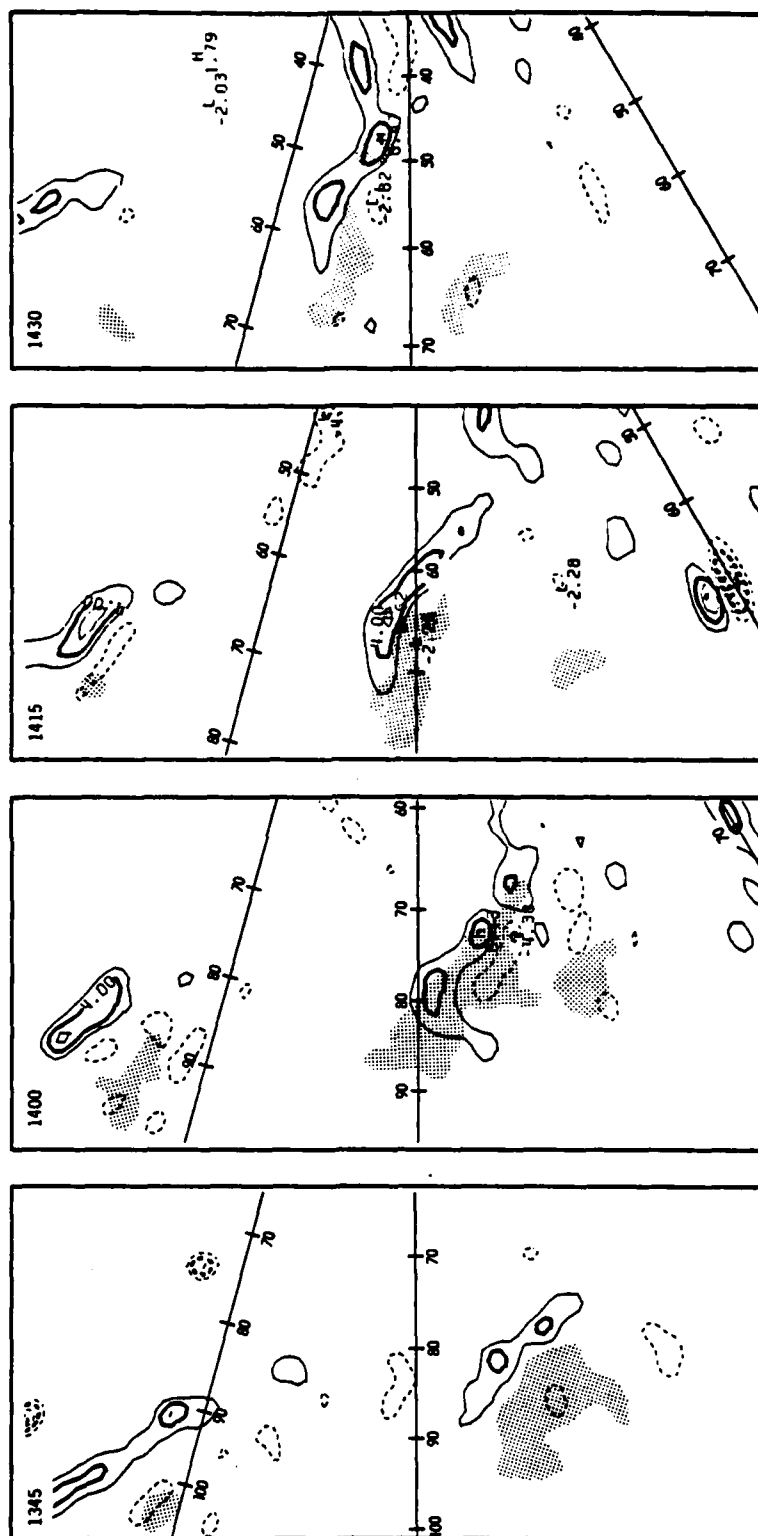


Fig. 26d. Squall Line (19 May 1977) 1 km time sequence of cross-beam shear ($\times 10^{-3} \text{ s}^{-1}$), contoured in $2 \times 10^{-3} \text{ s}^{-1}$ intervals greater than $2 \times 10^{-3} \text{ s}^{-1}$ (solid lines) and less than $2 \times 10^{-3} \text{ s}^{-1}$ (dashed lines). Stippled area is the 45-dBZ echo.

stretching (Fig. 26c) and cross-beam shear (Fig. 26d) zones were evident.

The final reflectivity panel at 1430 showed two 45-dBZ cores of equal size (Fig. 26a). The northern one contained the stretching and negative cross-beam shear inside the echo with the strong contraction and positive cross-beam shear outside of the echo. The southern echo contained the stretching and negative cross-beam shear inside but no noticeable patterns ahead of the storm.

A study of 5-km reflectivity maps showed a northeast tilt of the echoes with height (Fig. 27a). A large area of mid-level contraction was noted on the front flank of the main echo (Fig. 27c). The highest surface rainfall rates were again associated with this zone. There was, coincident with the mid-level contraction, a zone of positive cross-beam shear, flanked by a smaller area of negative cross-beam shear to the south (Fig. 27d). These patterns persisted until 1430, at which time, the principle echo contained weak contraction with weak positive cross-beam shear. A similar, but less dramatic, change developed within the southern echo. This weakened kinematic pattern eventually was reflected in a reduction in surface rainfall.

Single-Doppler Fields Plus Storm Model Interpretations

In this section the kinematic patterns, noted in the last section, are compared with those expected from the storm model and surface rainfall. The rainfall rate (mm hr^{-1}) maps are presented in Fig. 28 and a summary of the rainfall is discussed in Appendix J.

The 1345 radar reflectivity maps showed a strong line of echoes

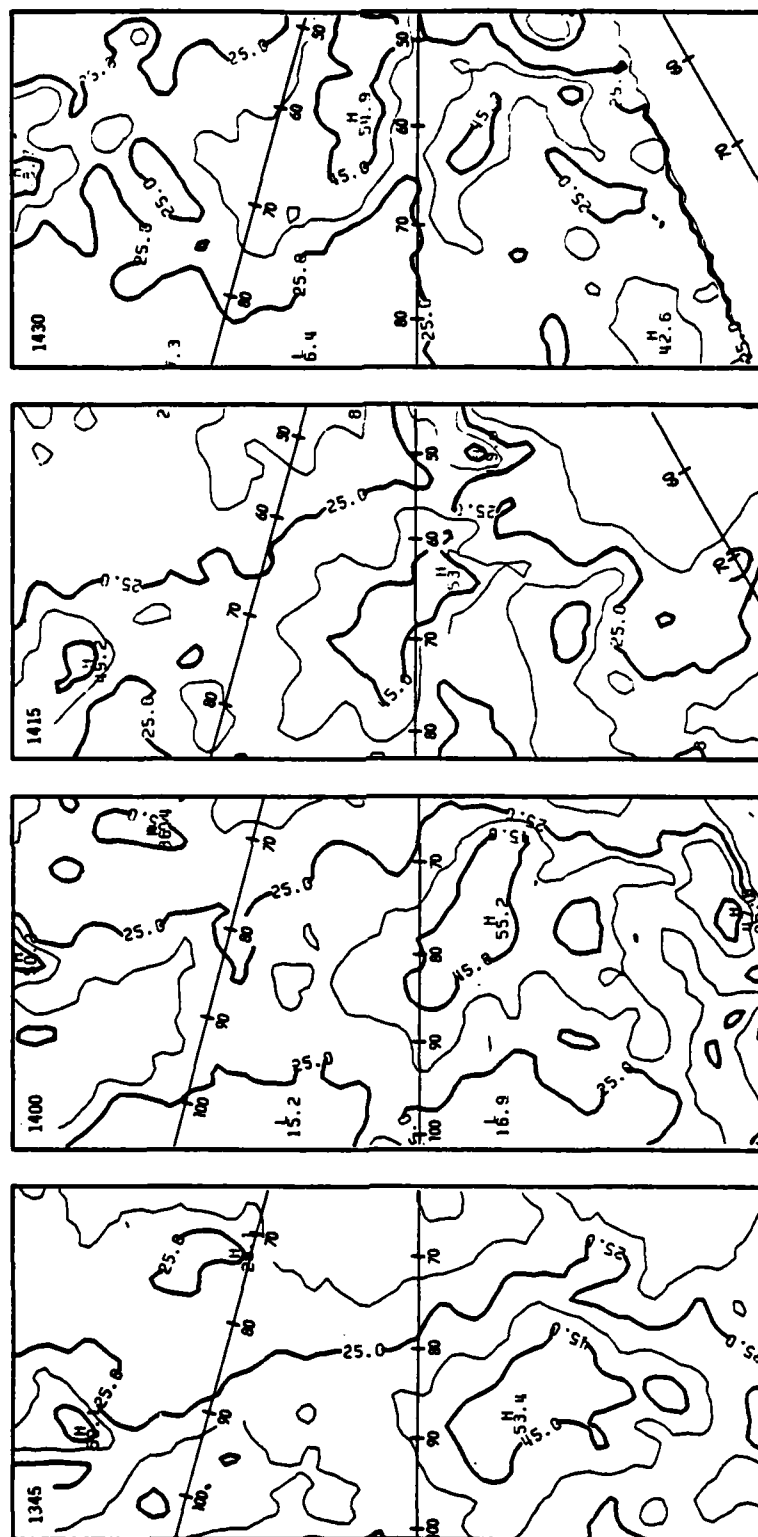


Fig. 27a. Same as Fig. 26a, except at 5 km.

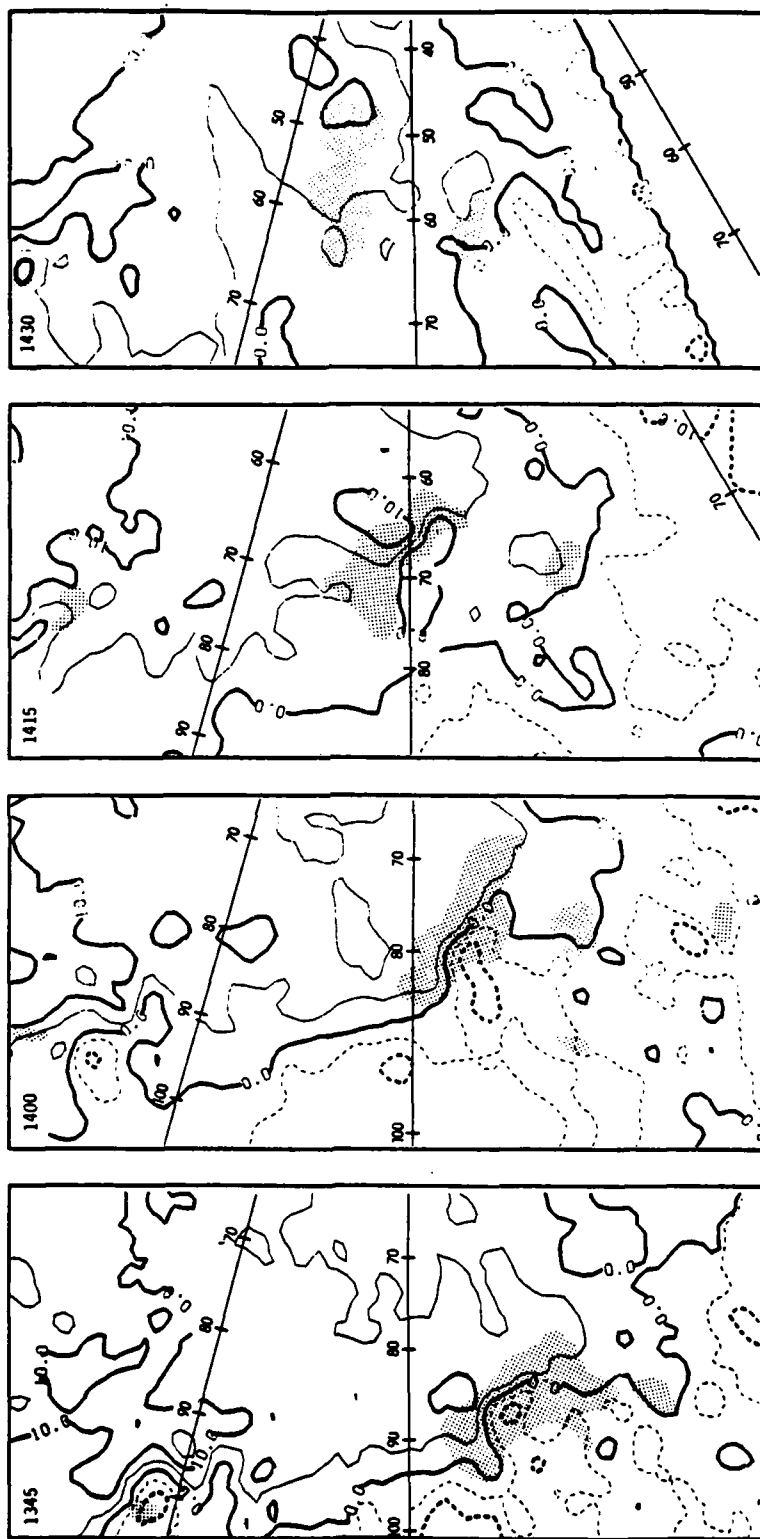


Fig. 27b. Same as Fig. 26b, except at 5 km.

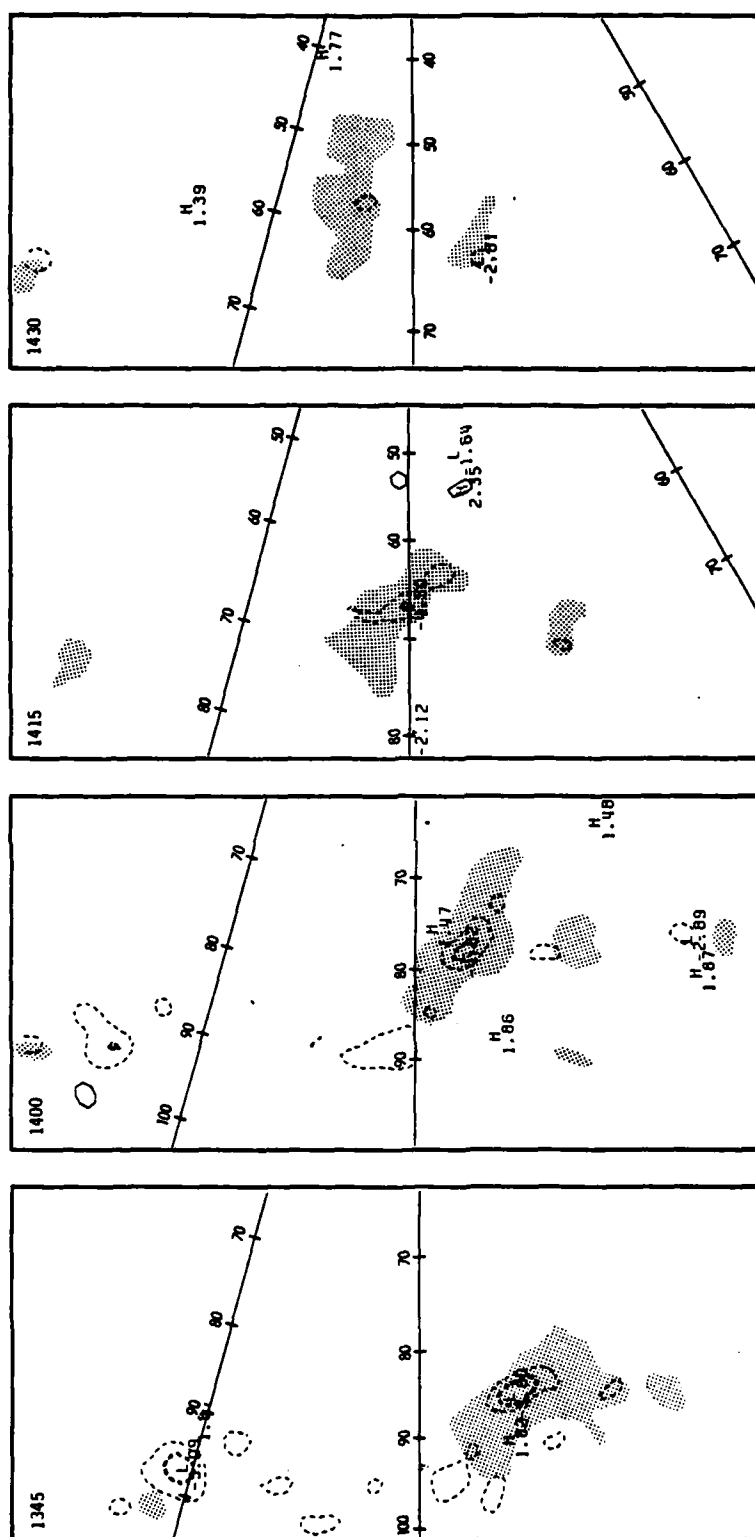


Fig. 27c. Same as Fig. 26c, except at 5 km.

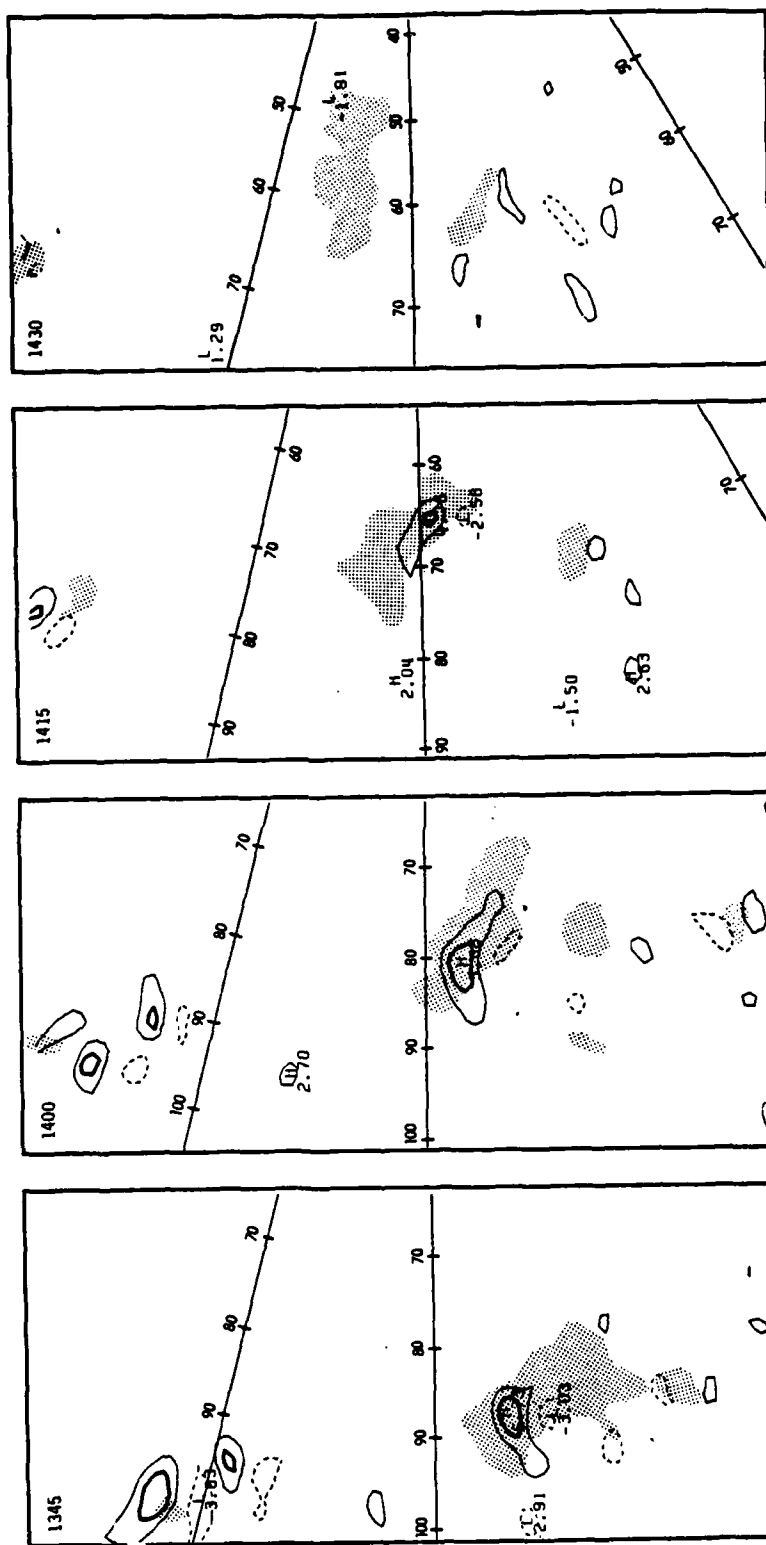


Fig. 27d. Same as Fig. 26d, except at 5 km.

moving into the radar box with the leading edge at a range of 80 km from NSSL. There was little tilt with height of the line, but the strongest echoes showed a strong tilt to the northeast with height. The higher-level reflectivities encompassed a slightly larger area than the lower cores, while the peak reflectivity values (approximately 53 dBZ) were about the same. The radial velocity field at 1 km revealed two zones of strong motion toward the radar, one along the 250° radial (the Ft. Cobb echo) and another along the 285° radial (the northern echo). Relative radial motions toward the radar can be estimated by subtracting -10 m s^{-1} . A dramatic slope of the overall radial velocity field with height was evident with the lower flow preceeding the 5-km flow by approximately 15 km. The strong areas of flow toward the radar evident at 1 km also appeared at the mid levels with the speed gradients noticeably less.

The 1-km layer radial stretching showed a large contraction zone running parallel to the squall line with maximum contraction ahead of the echo protrusions. At 1345 the contraction areas appeared to lie ahead of the squall line (defined by the 35-dBZ contour) in the lower layer but they were behind the leading edge of the line at the mid-levels. As noted previously, strong mid-level contraction over an echo core tends to induce significant precipitation. This configuration may be explained by the eastward tilt of the echoes with height but, in addition, the contraction zones themselves have a noticeable westward tilt with height. This pattern is consistent with the other supercell observations. The cross-beam shear maps illustrate that the strong contraction zones were also associated with strong positive

shear extending toward the direction of the low-level flow. Recall the multi-Doppler analyses of the 20 May supercell storms have shown these conditions to be associated with principle updraft sources. At this point, one can speculate about a couplet rotation. This can be shown by superimposing the low-level stretching and cross-beam fields. The storm model implies that couplet rotations may be updraft zones. The alignment of the derived fields, while not ideal at this time, is better illustrated in the following maps.

The 1345 integrated liquid water maps showed two areas of maximum liquid water coincident with the rotation and stretching maximums within the storm. Peak values ranged for the Ft. Cobb echo from 9 kg m^{-2} below the melting level to 12 kg m^{-2} above the level. The 5-kg m^{-2} areas were roughly 175 km^2 and 100 km^2 for the lower and upper levels, respectively.

The surface rainfall map (see Fig. 28) for the 15-min period ending at 1400 showed considerable rainfall. (A summary of the rainfall for the squall line is in Appendix J.) Two cells contained rates of over 70 mm hr^{-1} and one reached 120 mm hr^{-1} . The cells associated with the Ft. Cobb echo with rates greater than 55 mm hr^{-1} encompassed an area of over 100 km^2 .

The first series of surface mesonet maps was available at 1400. The surface data showed strong outflow at the Gracemonts site (73W, 7S) and strong inflow north of Dutton Corner (58W, 4S). This configuration reinforces a key feature of the model storm with strong outflow feeding a surface convergence area which feeds a strong moisture flux into the storm. The θ_w map showed the surface air to be

less than 13°C in the area of the outflow, while the pocket of inflow air was over 16°C . A slight pressure maximum was revealed in the pressure patterns east of the downdraft. The surface divergence values associated with the line were greater than $5 \times 10^{-4} \text{ s}^{-1}$, while the convergence zone contained values above $-15 \times 10^{-4} \text{ s}^{-1}$. Strong cyclonic vorticity was also associated with the convergence zone with values greater than $10 \times 10^{-4} \text{ s}^{-1}$. Classic alignment patterns (see Fujita, 1963) of positive vorticity generation left of the rain area and negative vorticity generation to the right were very evident. A partial pattern of convergence to the right of the precipitation divergence zone was also seen. The remaining portion of the pattern (convergence to the left of the rainfall) was not within the range of the mesonet.

The reflectivity fields at 1400 showed a slight increase in peak values of the Ft. Cobb echo with little change in the size of cores. Some northwest-southeast elongation of the 45-dBZ contour was evident and the strong tilt with height of the previous period was reduced. A general increase in size of the 35-dBZ isopleth was also apparent. The northern echo had reduced in size, and a break in the line was evident between the two principal echoes.

On the radial velocity maps the size of the toward-the-radar cores decreased in both areas as the maximum gradient moved within the 35-dBZ echo line. The area along the 260° radial (also the area of peak reflectivity) appeared to be moving faster than the northern area. The tilt with height of the zero velocity line was also less dramatic than previously observed. The break in the line was also

reflected in a strong away-from-the-radar jet at both levels (see Crawford and Brown, 1972).

Radial stretching at 1 km showed two strong contraction zones within the 35-dBZ isopleth and just east of the 45-dBZ core. The northern zone was associated with a stretching maximum to the west. In the mid-levels the maximum contraction zone was over the center of the 45-dBZ contour, which suggests that heavy rainfall would continue. The mid-level cross-beam shear maps showed an increase in the area of the Ft. Cobb cyclonic rotation, but with decreasing peak values. In the lower levels the apparent cyclonic rotational area of the Ft. Cobb echo increased significantly. By superpositioning the stretching and cross-beam shear fields we can again see the suggestion of a couplet rotation centered between the maximum and minimum stretching with cyclonic rotation to the north and anti-cyclonic rotation to the south. Such a deduction can be made solely by reference to the kinematic patterns.

The integrated liquid water maps showed a general decrease in the estimated water available for precipitation in the lower level while the area of the 1-km reflectivity increased. The upper level of the Ft. Cobb echo showed increased water loading both in area size (to 131 km^2) and magnitude of the peak value, which now increased to beyond 14 kg m^{-2} . These changes gave conflicting signals of the rainfall during the next period.

The rainfall pattern for 1400-1415 showed a larger area of high rainfall rates than in the previous period. Four cores could be identified with rates over 65 mm hr^{-1} . The peak rate remained over

120 mm hr⁻¹, while the total area of the 55-mm hr⁻¹ rates increased from 103 km² to 293 km². This rainfall was totally due to the Ft. Cobb echo. The kinematic interpretation of a more intense updraft couplet suggests more intense rainfall.

At 1415 the closest approach of the 35-dBZ contour at the lower levels had moved to 56 km along the 270° radial. Its reflectivity core showed a decrease in size in the lower level (indicating less rainfall) but little change in the upper-level size was noted. Peak values remained constant at 53 dBZ in both levels. A slight increase in the tilt with height was noted with the 5-km core being aligned northeast of the lower core. The mid-level reflectivity map showed a splitting of the 35-dBZ contour. This may help explain the slight decrease in size of the original core. The core due south of the parent echo appeared to have the same translation velocity as the parent cell.

The low-level radial velocity map showed the zero contour still running ahead of the upper-level zero line. The size of the toward-the-radar cores had increased again in the lower levels, while the upper-level support became very diffuse. A zone of environmental air protruding into the line was evident north of the Ft. Cobb echo. Flow away from the radar (uncorrected for storm motion) completely dominated the squall line at 5 km.

The stretching maps showed a slight increase in the peak values, and a noticeable increase in the area of contraction extended toward the inflow source, especially for the Ft. Cobb echo. The southern cell was still sustained by the parent cell inflow in the lower levels. The mid-level contraction over the echo cores remained

strong. Cross-beam shear values also showed little change in peak values, while a slight decrease in area of positive shear for all cores was evident. Strong tilt of the principle positive shear zones was still apparent between 1 and 5 km. The vertical continuity of the suspected couplet rotation was again apparent in the cross-beam shear. The stretching field supports the pattern in the lower but not the upper levels.

The liquid water maps showed a general increase in the available water with peak values remaining relatively constant. The satellite cell increased to 10 kg m^{-2} in the lower levels, but its area remained small (15 km^2). Notice that only modest liquid water values have been observed in these cells, suggesting little hail contamination.

The surface rainfall for the 1415-1430 period showed the parent Ft. Cobb cell dominating the precipitation. The peak rates increased slightly, while the area of the 55-mm hr^{-1} rate decreased to 210 km^2 . The area of the 25-mm hr^{-1} rate had now grown to a respectable 864 km^2 . Highest rates still fell from the front flank of the storm and were associated with strong mid-level contraction and the suspected updraft couplet. Both the kinematic and integrated liquid water provided relatively accurate estimates of the surface rainfall pattern for this period.

The surface mesonet series for 1430 showed a line of convergence aligned parallel to the mid-level contraction zone. A strong area of surface diffluence was also reflected in the lower-level stretching maps. A definite high-pressure nose emanated from the squall line coincident with the lowest θ_w values (less than 11°C) and the lowest

mixing ratio values (less than 15 gm kg^{-1}). The Ft. Cobb rainfall pattern contained surface convergence and positive vorticity on its left. Anticyclonic vorticity was associated with the rainfall divergence zone which had increased to $10 \times 10^{-4} \text{ s}^{-1}$.

The reflectivity maps at 1430 continued to show a tilt toward the east with height with a slight increase in peak intensity of the Ft. Cobb cells. The satellite cell had now grown to rival the parent cell for the moisture supply. A new cell was also developing southwest of the Ft. Cobb storm with a peak 5-km reflectivity of 43 dBZ. This echo, the Gracemont echo, had the same echo tilt as the Ft. Cobb storm, again showing a strong relation between cell structure and the environment. The radial velocity maps showed extremely large zones of strong toward-the-radar flow at 1 km. The zero radial velocity line maintained its position ahead of the squall line in the lower layers, but, in the upper layers, the zero line was well behind the main echoes. This suggests that the lower-level patterns may be out-running their upper-level support and a breakup of the line configuration seemed likely. A marked change was also evident in the stretching maps. The low-level map still showed strong contractions ahead of the protruding echo. The mid-level contraction decreased in peak intensity from over -6×10^{-3} to about -2.5×10^{-6} . More importantly, the size of the contraction zone was dramatically reduced. This seems to imply a weakening of this echo as a precipitation producer. The cross-beam shear maps tell a similar story. Strong cyclonic rotation remained in the lower levels of the Ft. Cobb cells but support weakened in the upper levels. A forecast of an immediate

decrease in rainfall rates from the Ft. Cobb storm would be premature due to the strong low-level patterns, but the weakening of this echo in the near future seems evident.

The reasons for the rapid change in the kinematic patterns along the line is a puzzle. The mid-level flow, from the south, was exerting a shearing effect upon the storm, but without detailed wind sampling in the near-storm environment, it is impossible to establish any cause-effect link. One can imagine the growth of the satellite cell closer to the moisture source weakening the parent cell through downdraft-updraft interaction, as was the case in the Del City-Hailstorm complex. In any event the condition is short lived. Rainfall patterns and radar maps show this lull in kinematic activity to last between 15 and 30 min.

In spite of unfavorable kinematic patterns, liquid water maps at 1430 showed, in general, an increase in size and intensity over 1415. Lower-level peak values of the parent echo remained at 13 kg m^{-2} while the satellite cell jumped from 10 to 14 kg m^{-2} . The area of the 5-kg m^{-2} contour was 158 km^2 below the melting level and 81 km^2 above it for the echo complex. This amounted to a drop of about 30 km^2 for the upper level and no change in the lower level.

The rainfall patterns for 1430-1445 showed a peak rate of 149 mm hr^{-1} associated with the parent Ft. Cobb echo. This is not unexpected. However, the percentage of the total rainfall area associated with the Ft. Cobb echoes decreased from 63% to 53% for the 25-mm hr^{-1} area over the previous 15-min period. The 55-mm hr^{-1} area decreased from 36% and 32% over the same period.

While total rainfall areas were increasing during this period, the Ft. Cobb areas were showing a decrease. This suggests that moisture was now going more to other cells instead of the Ft. Cobb cells. While less dramatic than the Del City-Hailstorm complex, this tends to reinforce the idea that the same process that resulted in the demise of the Hailstorm was in progress. Once again the kinematic patterns seem to provide a better representation of surface rainfall than the integrated liquid water content.

Figs. 29 and 30 illustrate north-south vertical cross sections through the peak reflectivity areas at 1345 and 1415. Several interesting features can be noted. The radial velocity at 1345 (88 km W) shows strong flow into the squall line north of 6S. The inflow gradient is also associated with the northern reflectivity gradient. Note also the strong vertical consistency of the cross-beam shear along the same boundary. This is very similar to updraft patterns observed in isolated supercells. The temporal persistence of these patterns is also significant. At 1415 (now 65 km W), a stretching influx jet was located in the vicinity of 6N. This continued to be associated with the reflectivity gradient, and now also a weak echo region.

The influx jet extended from the surface to at least 8 km. Brown and Crawford (1972) have also observed squall line kinematic flows which show the maximum influx and outflux aligned vertically. Note that the low-level outflow corrected for storm motion will, on occasion, be above 1 km. This tends to support earlier discussions that superpositioned flows may exist in close proximity. The maximum

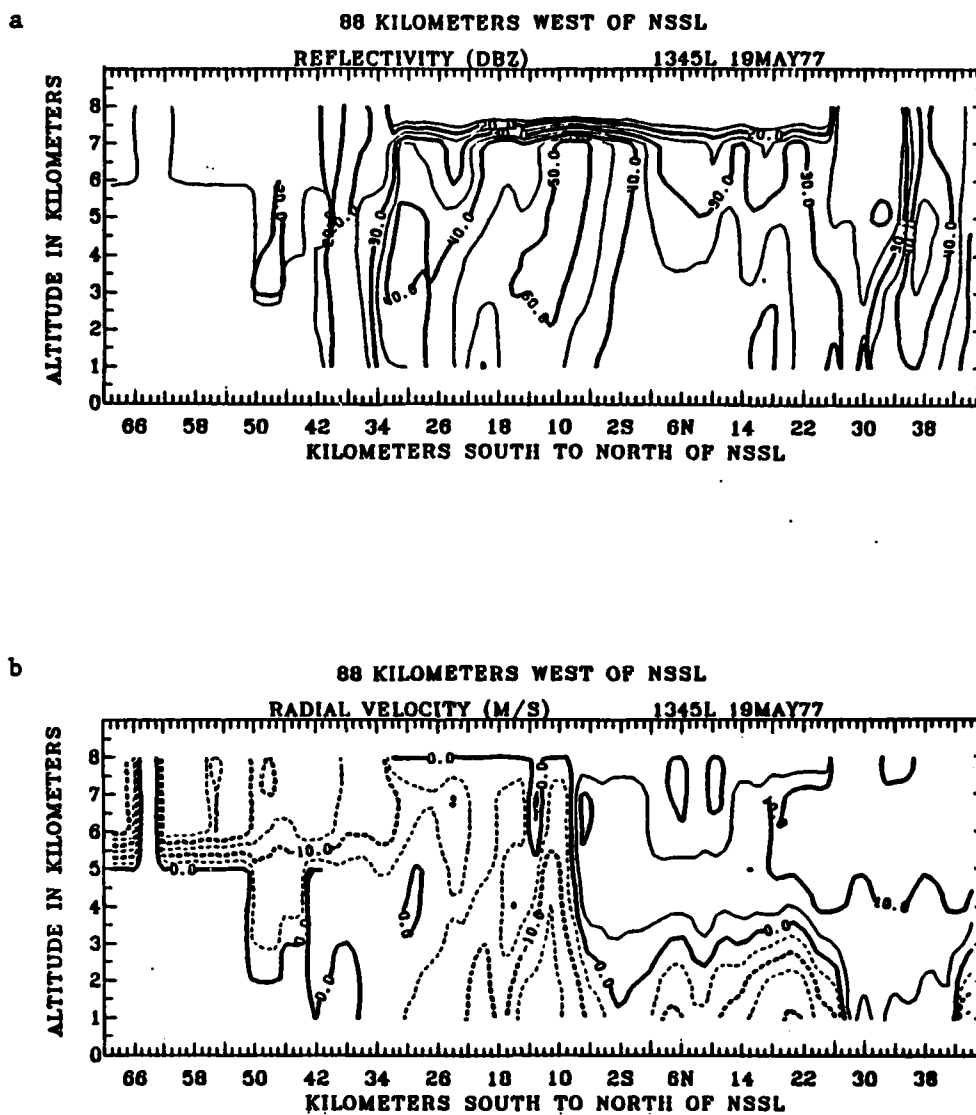


Fig. 29. North-south cross section 88 km west of NSSL at 1345.
 (a) Reflectivity (dBZ). (b) Radial velocity (m s^{-1}).

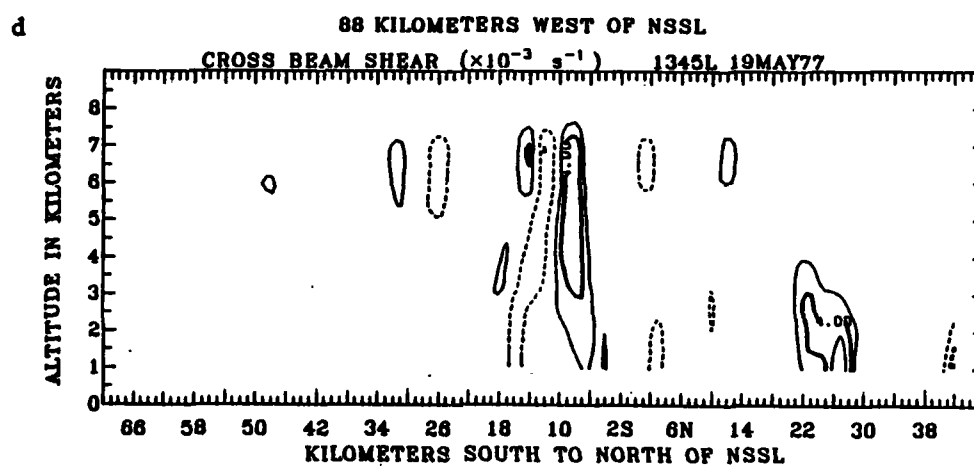
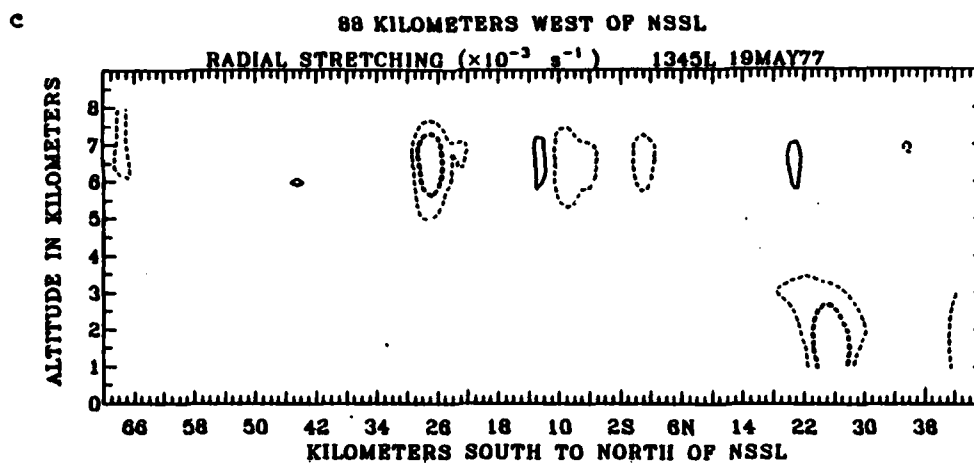


Fig. 29. (Continued) (c) Radial stretching ($\times 10^{-3} \text{ s}^{-1}$).
 (d) Cross-beam shear ($\times 10^{-3} \text{ s}^{-1}$).

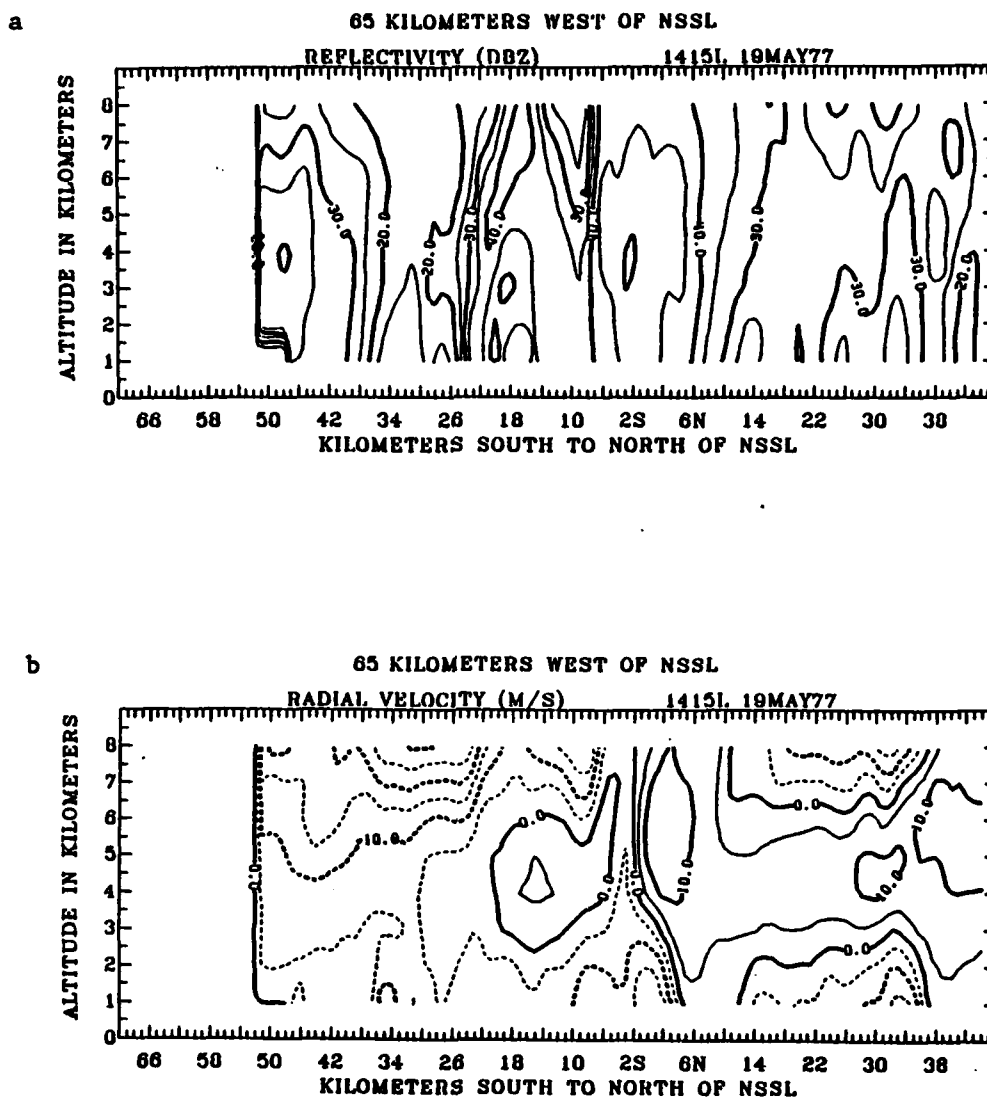


Fig. 30. North-south cross section 65 km west of NSSL at 1415.
 (a) Reflectivity (dBZ). (b) Radial velocity (m s^{-1}).

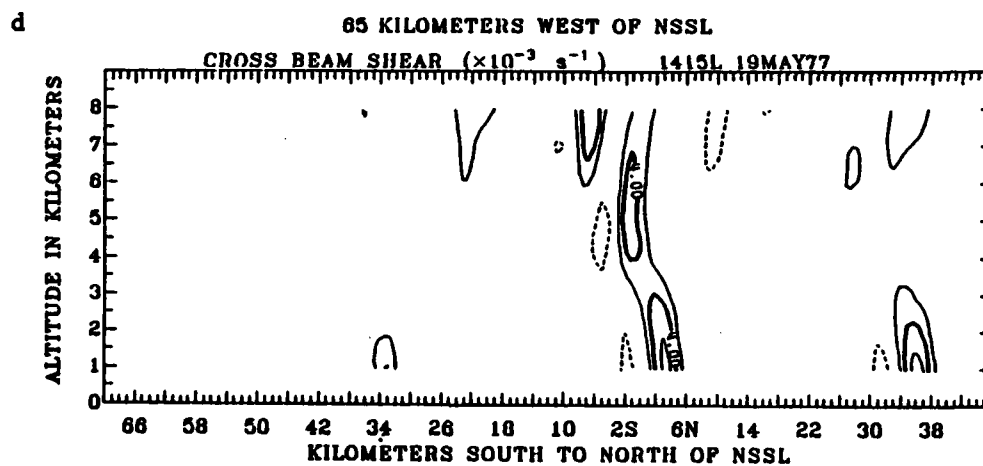
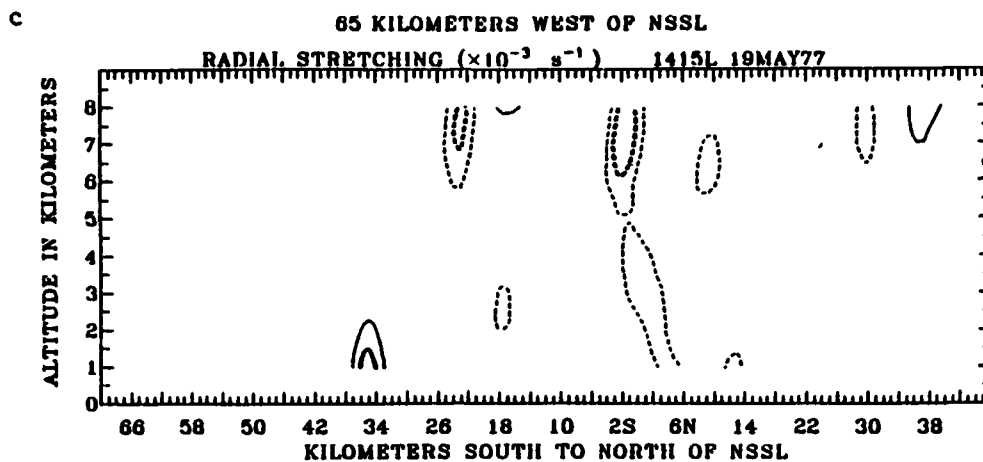


Fig. 30. (Continued) (c) Radial stretching ($\times 10^{-3} \text{ s}^{-1}$).
 (d) Cross-beam shear ($\times 10^{-3} \text{ s}^{-1}$).

shears found in these analyses are on the order of $10 \times 10^{-3} \text{ s}^{-1}$, which are comparable to those found by Brown and Crawford ($30 \times 10^{-3} \text{ s}^{-1}$) for a different storm.

A final observation should be made about the cross-beam shear pattern. In Fig. 29d the suspected updraft couplet rotation is evident which, in turn, lends support to the supercell model. This suggests that couplet patterns may be a generalized feature of supercell storms.

Summary of Findings

Many of the patterns observed in the isolated supercells of 20 May 1977 were similar to those found in the 19 May 1977 squall line. Mid-level contraction was associated with the highest rainfall rates. Low-level contraction was evident and coincident with positive and negative cross-beam shear cores. The squall line may have contained an updraft couplet rotation as noted in the Hailstorm. Again, the relationship between kinematic patterns and surface rainfall appeared to be superior to the integrated liquid water content-rainfall relations.

Splitting Echo Case

Introduction

This section describes some features of intrastorm flow inferred from radar reflectivity and the single-Doppler fields of radial stretching and cross-beam shear. This section also illustrates the

utility of inferred kinematic fields to sense storm splitting. Finally, changes in inferred flow patterns are compared with changes in liquid water loading above and below the freezing level and surface rainfall rates.

Mesoscale Environment

Late in the afternoon of 1 May 1977 convective storms developed over the NSSL mesonet. One storm, which contained a mesocyclone, split into two cores with centers moving to the left and right of the environmental wind. High precipitation intensities occurred just before the splitting became evident in the radar reflectivity.

The surface mesoanalysis revealed strong, warm, moist southeasterly flow into the storm. The environmental wind veered from 130° at 5 m s^{-1} at the surface to 305° at 10 m s^{-1} at 5 km (Fig. 31). The storm motion was a slow drift toward the southeast at 4 m s^{-1} . The 285° , 270° , and 240° radials are superimposed on the panels.

Time Sequence of Single-Doppler Fields

Figs. 32a, 32b, 33a, and 33b show the radar reflectivity (dBZ) and radial velocity (m s^{-1}) for 1 km and 5 km respectively. The 5-km fields of radial stretching ($\times 10^{-3} \text{ s}^{-1}$) and cross-beam shear ($\times 10^{-3} \text{ s}^{-1}$) are presented in Figs. 33c and 33d. The 1-km stretching and cross-beam shear maps contain no significant information and are not presented.

The reflectivity maps (Figs. 32a and 33a) at 1700 showed a small echo tilting toward the northwest with height. The 5-km radial

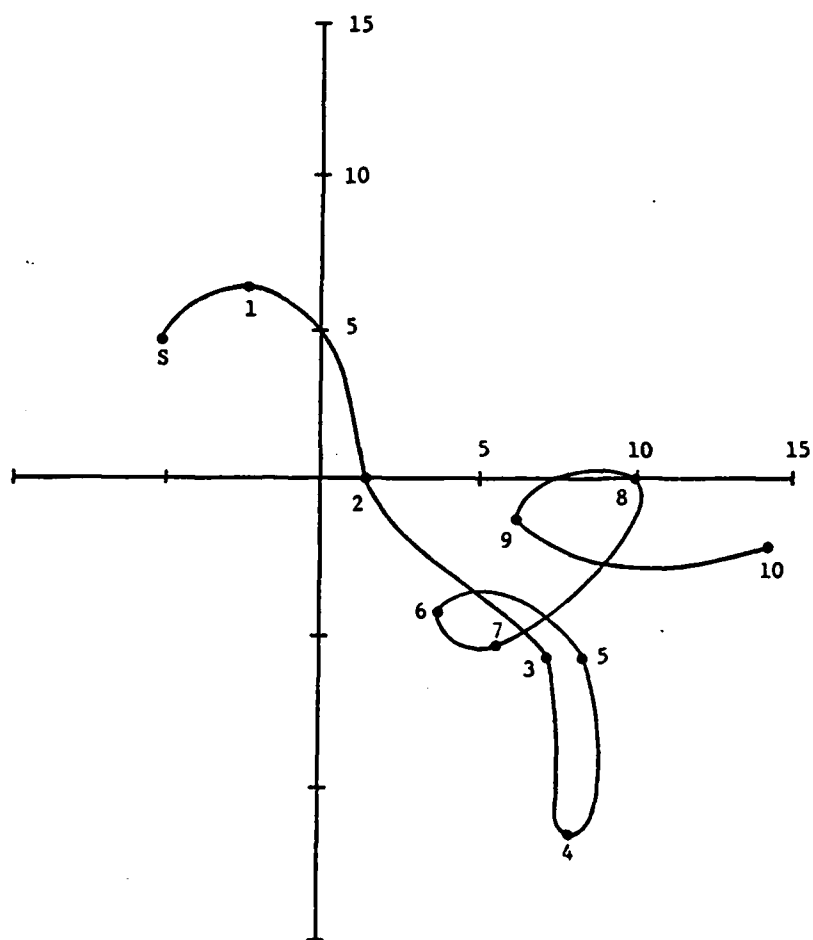


Fig. 31. Oklahoma City hodograph, 1 May 1977,
0000 GMT.

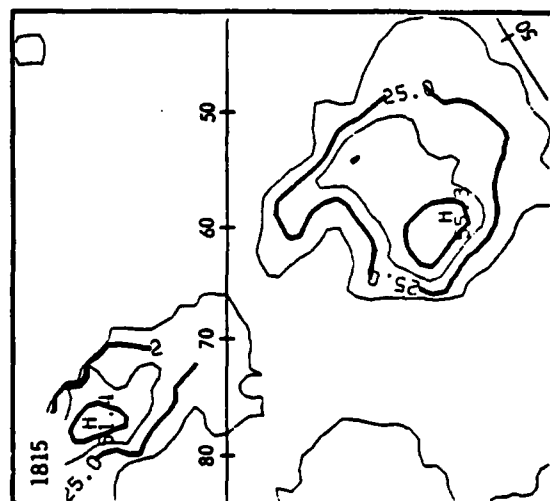
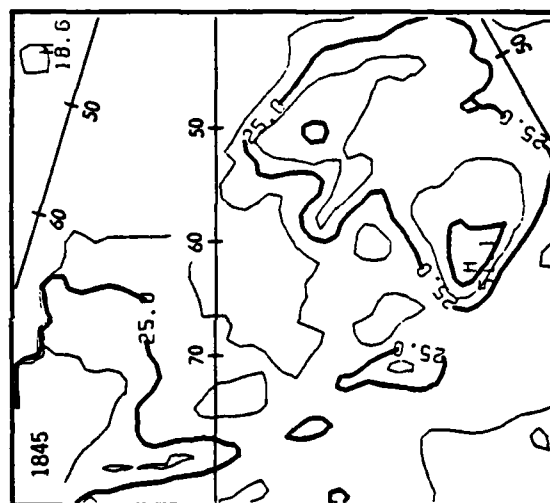
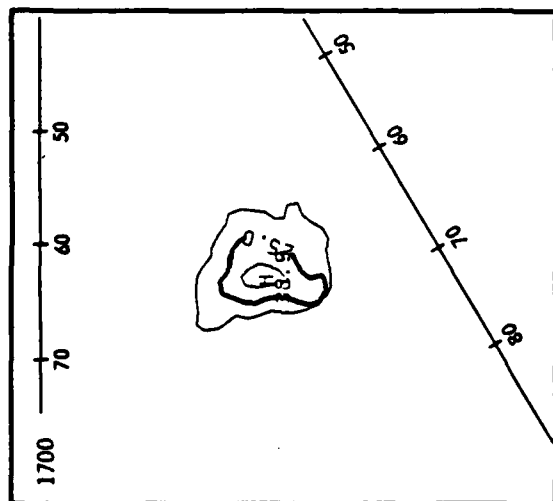
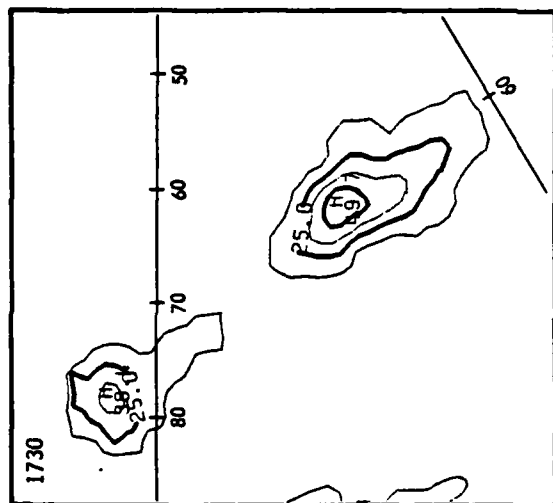
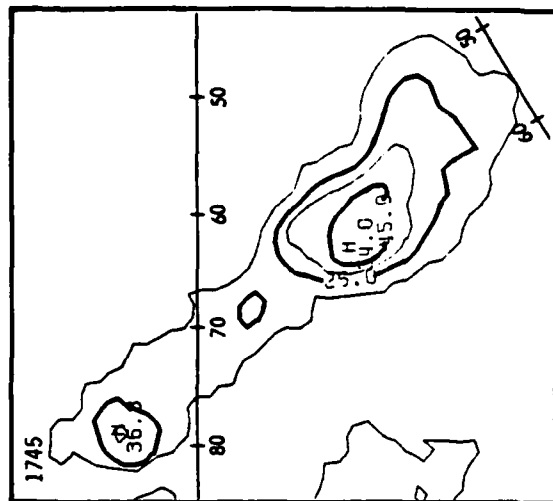


Fig. 32a. Splitting storm
(1 May 1977) 1 km time sequence
of reflectivity (dBZ), contoured
in 10 dBZ intervals starting at
15 dBZ.

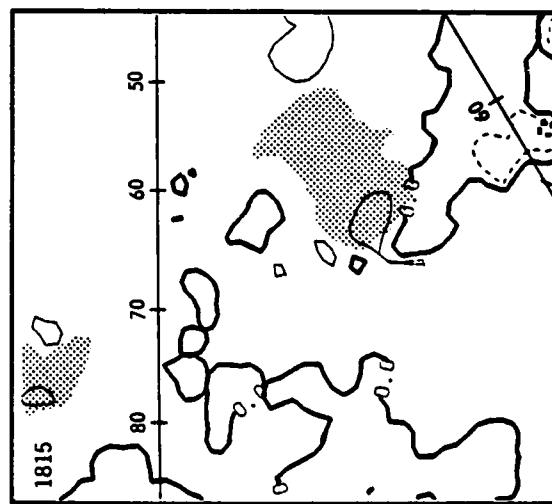
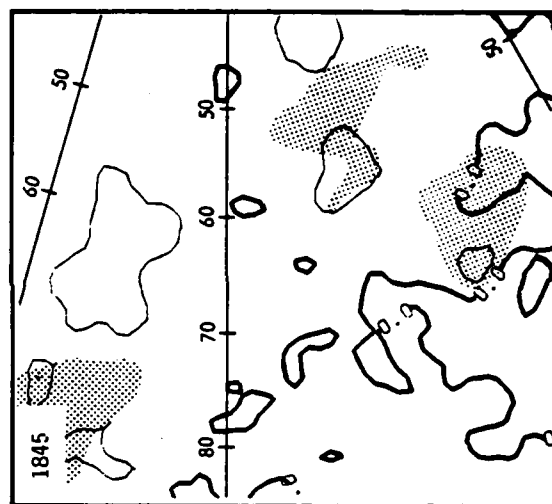
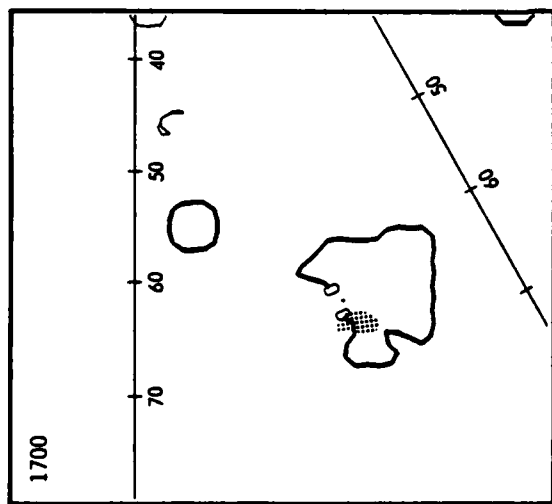
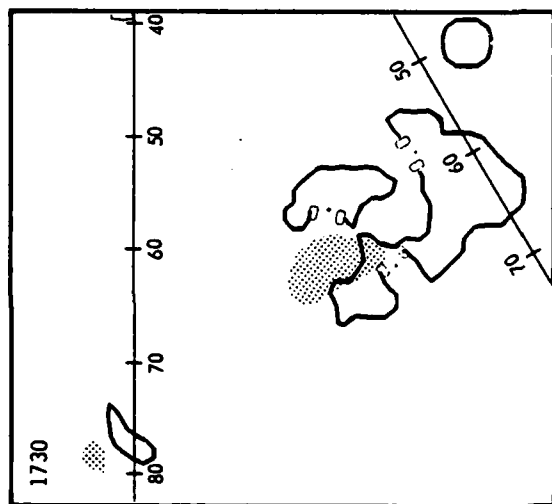
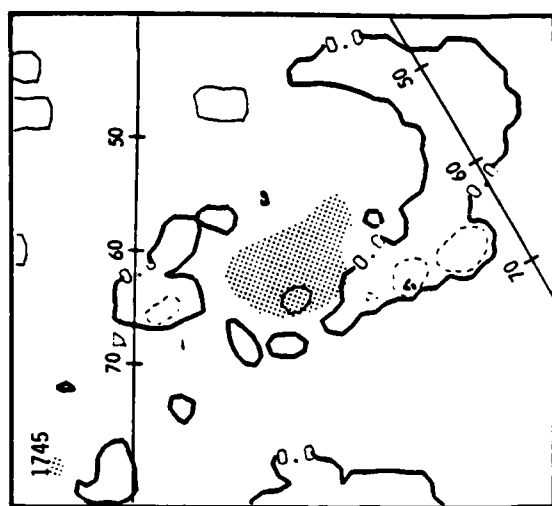


Fig. 32b. Splitting storm (1 May 1977) 1 km time sequence of radial velocity (m s^{-1}) contoured at 5 m s^{-1} intervals. Stippled area is the 35-dBZ echo.

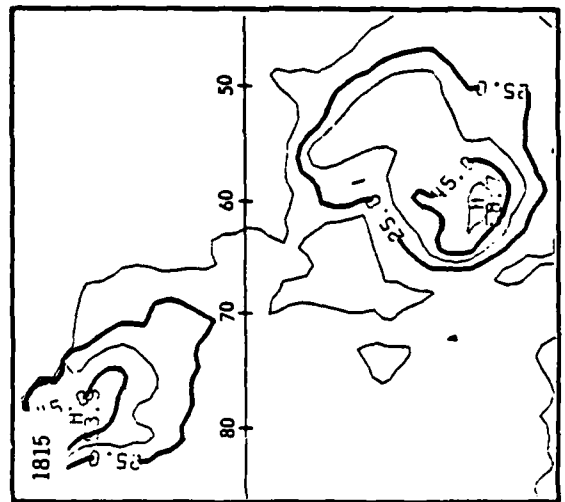
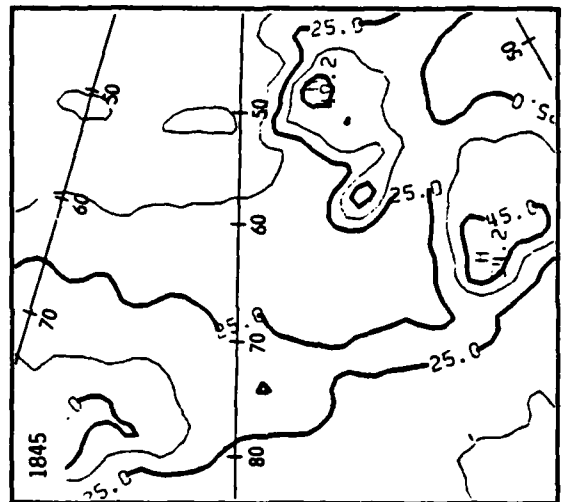
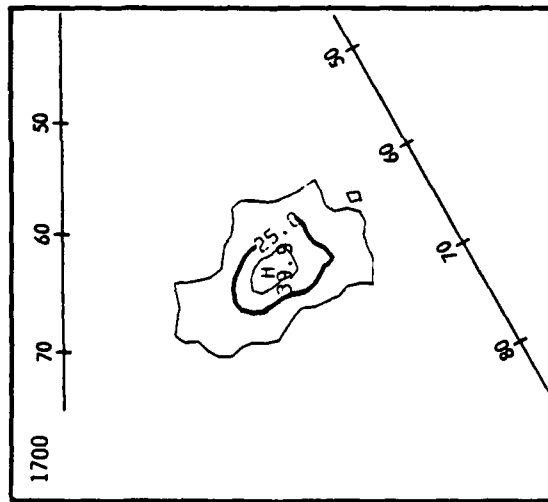
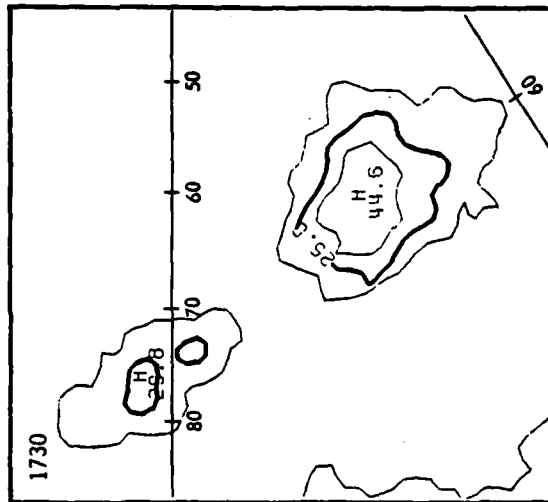
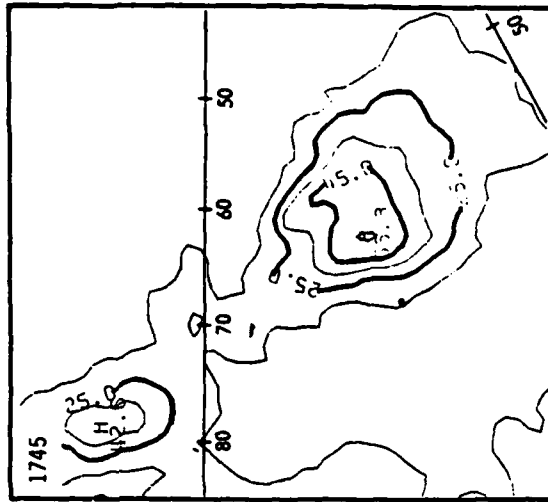


Fig. 33a. Splitting storm
(1 May 1977) 5 km time sequence
of reflectivity (dBZ), contoured
in dBZ intervals starting at
15 dBZ.

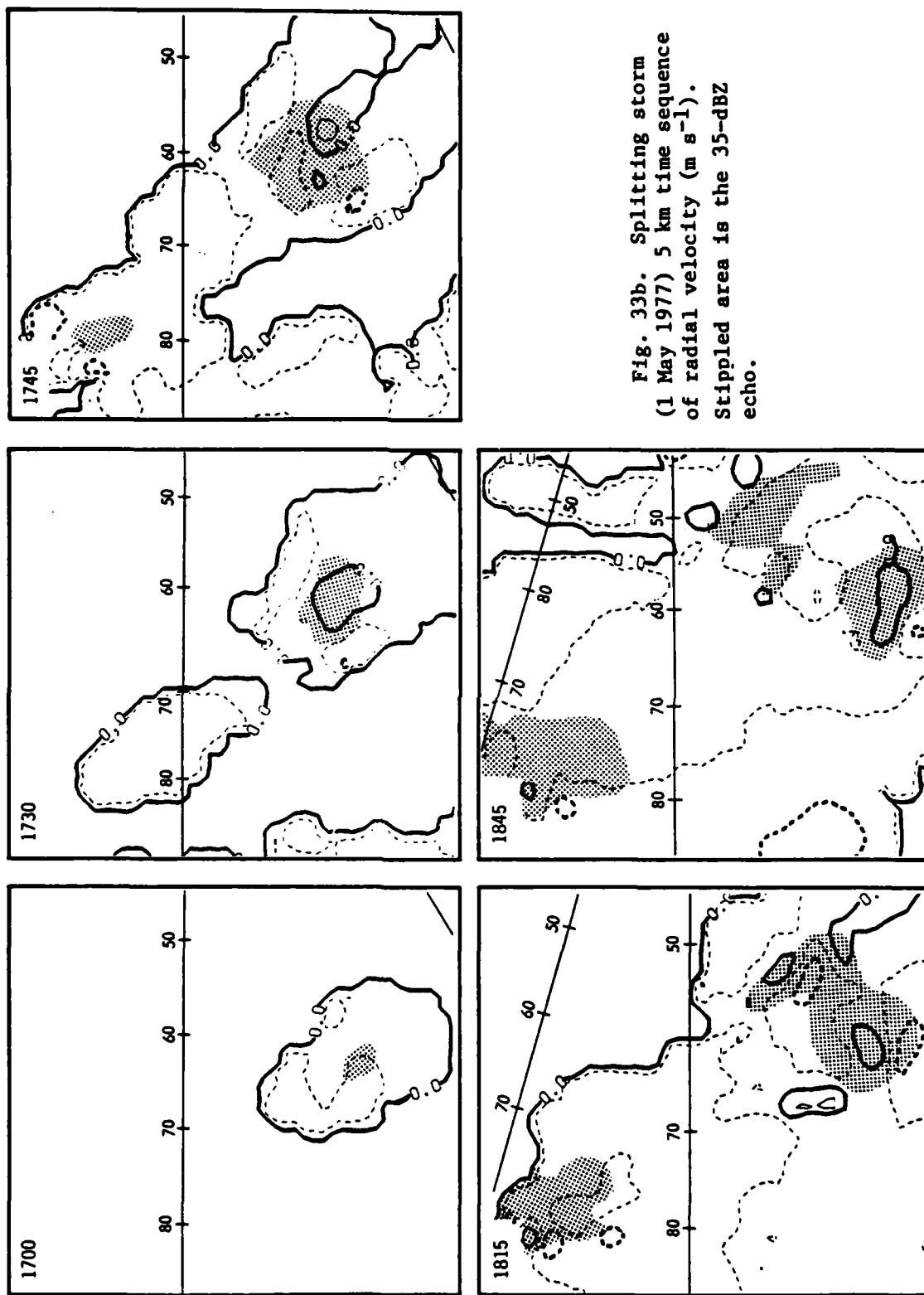


Fig. 33b. Splitting storm
(1 May 1977) 5 km time sequence
of radial velocity (m s^{-1}).
Stippled area is the 35-dBZ
echo.

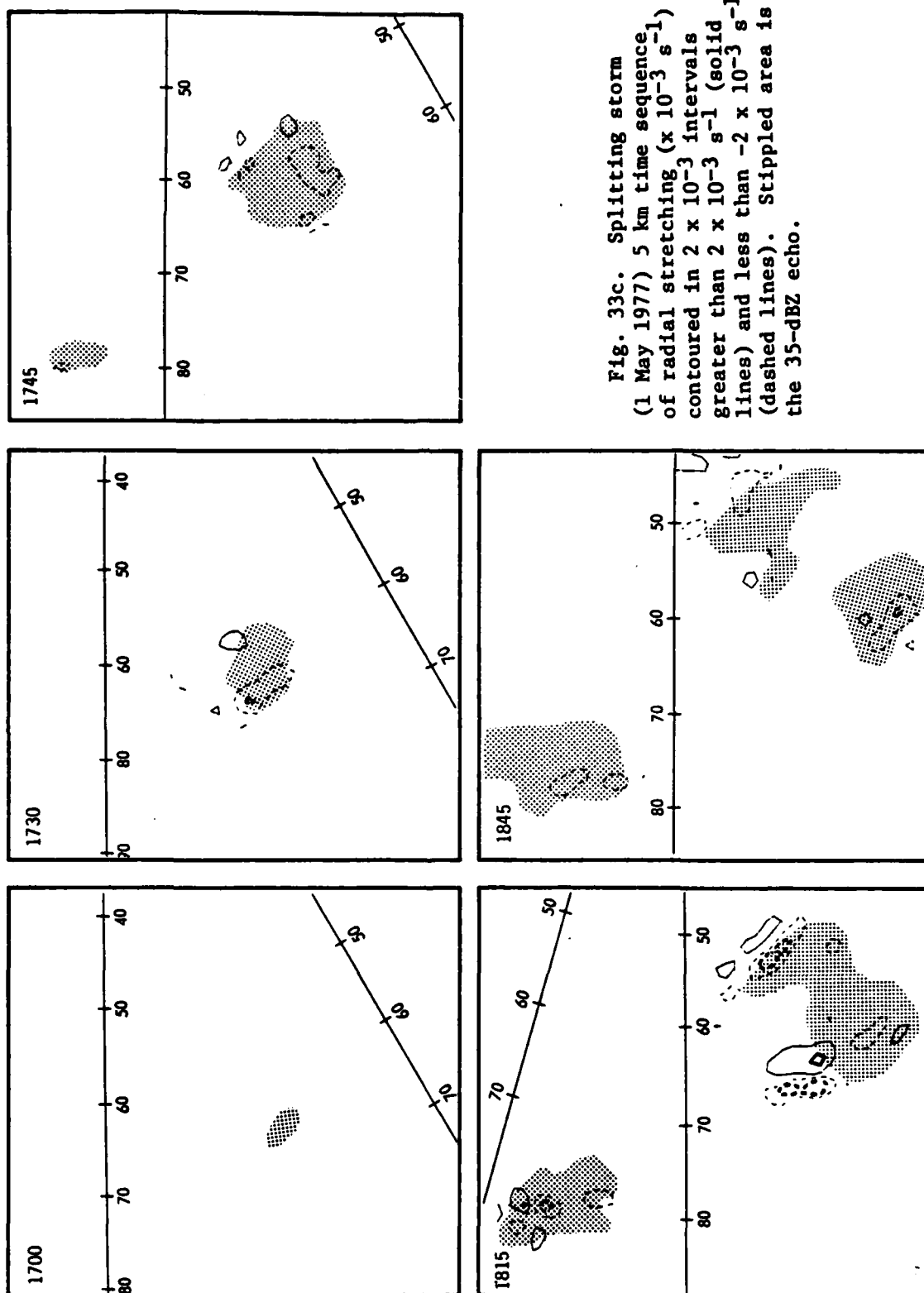


Fig. 33c. Splitting storm
(1 May 1977) 5 km time sequence
of radial stretching ($\times 10^{-3} \text{ s}^{-1}$)
contoured in 2×10^{-3} intervals
greater than $2 \times 10^{-3} \text{ s}^{-1}$ (solid
lines) and less than $-2 \times 10^{-3} \text{ s}^{-1}$
(dashed lines). Stippled area is
the 35-dBZ echo.

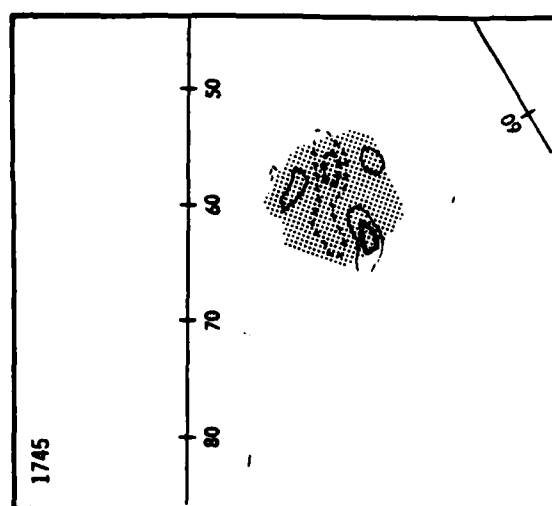
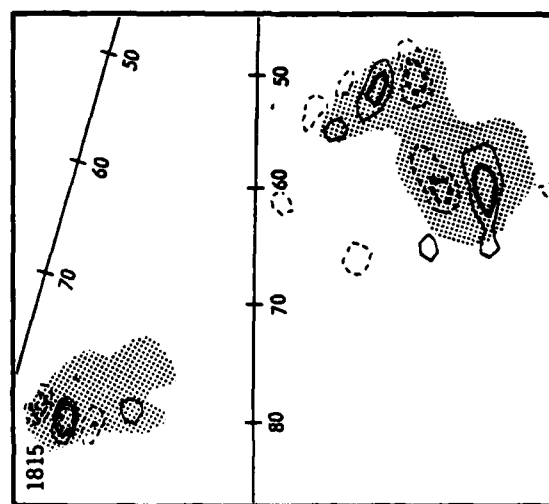
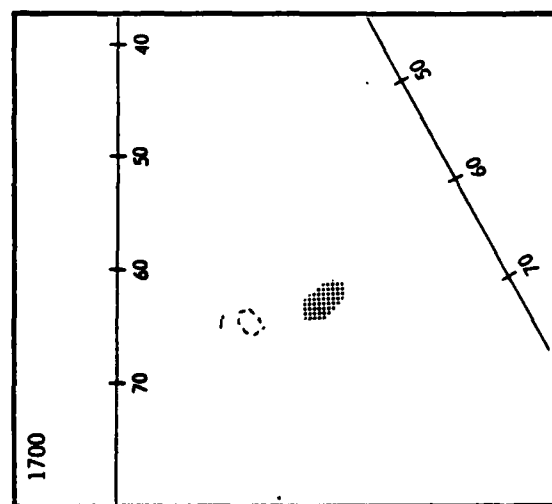
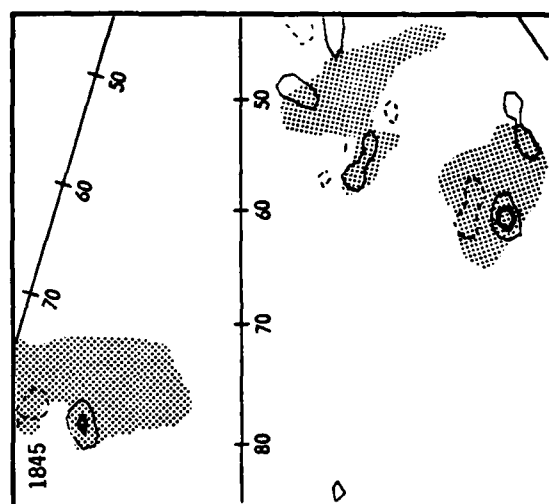
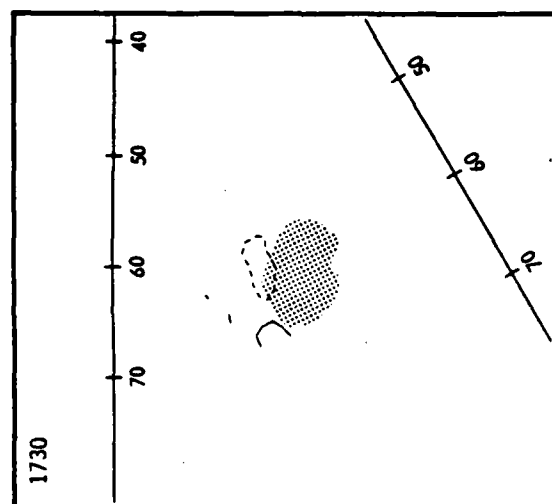


Fig. 33d. Splitting storm (1 May 1977) 5 km time sequence of cross-beam shear ($\times 10^{-3} \text{ s}^{-1}$) contoured in 2×10^{-3} intervals greater than $2 \times 10^{-3} \text{ s}^{-1}$ (solid lines) and less than $-2 \times 10^{-3} \text{ s}^{-1}$ (dashed lines). Stippled area is the 35-dBZ echo.



velocity map showed a diffuse area of negative flow north and west of the echo core.

At 1730, the echo tilt had shifted toward the northeast with height. The 5-km core was bounded by two areas of flow less than -5 m s^{-1} to the west and northeast. This feature produced a distinctive pattern in the radial stretching (Fig. 33c) of strong contraction on the right flank and stretching on the left flank. The cross-beam shear indicated a positive shear west of the echo and a negative shear on the rear flank (Fig. 33d).

The 1745 reflectivity panels (Figs. 32a and 33a) of the splitting echo had grown considerably. Superpositioning of the stretching (Fig. 33c) and cross-beam shear fields (Fig. 33d) shows contraction on the front of the echo core with strong positive cross-beam shear on the right flank and strong negative cross-beam shear on the left flank.

The cross-beam shear panel (Fig. 33d) at 1815 shows the same pattern better than at 1745. The stretching pattern (Fig. 33c), however, had become a very complex but ordered pattern, suggesting a superpositioning of significant information. The radial velocity field at 5 km (Fig. 33b) suggested a weak vortex on the right flank of the splitting storm. Notice the distinctive stretching and cross-beam shear rotational patterns in the echo northwest of the splitting cell at this time.

The final time panel, at 1845, showed two distinct reflectivity cores (Fig. 33a) originating from the original echo. The stretching panels (Fig. 33d) showed that the right moving storm contained the same negative-positive cross-beam shear patterns observed over the

past hour. The stretching map (Fig. 33c) shows contraction over the right flank of both the right and left moving storms.

Single-Doppler Fields Plus Storm Model Interpretations

The first significant features in the splitting cell were becoming evident at 1730. At this time the mid-level cross-beam shear panel shows negative and positive areas with an east-west alignment. By overlaying the stretching pattern one sees the strongest contraction south of a line separating the two cross-beam shear zones. The storm model suggests that such a cross-beam shear pattern may signify couplet rotation, however, the stretching map does not support this interpretation.

At 1745 one can visualize a potential dual couplet rotation in the cross-beam shear fields with a dominant cyclonic sense on the right flank and the reverse on the left flank of the storm. The kinematic model would require a complex stretching pattern which was not observed. This may be the result of the unbalanced nature of the couplet, as seen in the mid-level radial velocity. While the updraft couplet rotation is an attractive interpretation of the cross-beam shear pattern, the second field verification is not as clear as in the squall line case. The heaviest rainfall between 1745 and 1800 occurred across the middle of the storm and again was associated with strong mid-level contraction. The storm model and these fields suggest a counter clockwise turning of the reflectivity core with decreasing height. The suspected right flank couplet, in order to

maintain a favorable alignment, should turn in a similar manner. The continuity of the right flank couplet with height supports these ideas. Vertical continuity of the left flank couplet was poor, indicating it played a supportive role in the storm. It is important to note that the dual couplet existed before the splitting was observed in the reflectivity field. Klemp and Wilhelmson (1978) and Schlesinger (1978, 1980) have shown that rotational couplets are produced by rotating updrafts in idealized storms. The couplets observed in this storm were probably a reflection of storm updrafts.

Echo splitting was clearly evident on the 1815 Doppler reflectivity maps while the WSR-57 reflectivity field suggested the actual split occurred shortly after 1750. The splitting storm, by 1815, had become enmeshed within a large area of convection, but it apparently maintained its favorable position as the cell closest to the moisture source. The reflectivity split did occur relatively soon after the first echo appeared.

The mid-level radial velocity and cross-beam shear maps at 1815 suggested a cyclonic vortex signature (partial mesocyclone pattern) on the right flank of the storm as noted by Ray *et al.* (1977).

The mid-level, dual couplet, pattern noted in the 1745 map was still evident with the inferred updrafts drifting apart. The updraft tilt showed good vertical consistency, while the front flank contraction zone had weakened. Below 3 km the mesocyclone signature was not apparent. Low-level inflow into the right front portion of the storm (below the mesocyclone) was still evident in the radial velocity field.

Some general features of supercells, discussed above, are revealed in a north-south vertical cross section, 60 km west of NSSL. The reflectivity (Fig. 34a) of the splitting cell shows a nearly vertical alignment with the peak values confined to southern portions of the echo in the levels above 2 km. The radial velocity (Fig. 34b), radial stretching (Fig. 34c), and cross-beam shear (Fig. 34d) also show the nearly vertical alignment of the parent cell. Note the distinctive mesocyclone pattern in the cross-beam shear at 18 km south of NSSL. The northwest companion cell (Fig. 35) is a narrow vertical storm with an apparent mesocyclone pattern. Neither cross-beam pattern extended to the surface.

An important hypothesis of this investigation is that changes in radar reflectivity results largely from changes in the intra-storm flow field and these changes are reflected in the single-Doppler data. Consequently changes in surface rainfall rates are related to changes in the single-Doppler fields of radial stretching and cross-beam shear. Fig. 36 shows the rainfall patterns for this storm while Appendix M provides a summary of the rainfall.

The radial stretching and cross-beam shear panels of 1730 showed mid-level contraction on the right flank and cyclonic rotation, respectively. This was associated with high rainfall. During the period 1730 to 1745, the peak rainfall rate was 63 mm hr^{-1} with the 25-mm hr^{-1} isopleth encompassing 23 km^2 . The area of the 55-mm hr^{-1} contour was 1 km^2 . Between 1745 and 1800, the peak precipitation rate increased to 104 mm hr^{-1} (on the right flank) with the 25-mm hr^{-1} and 55-mm hr^{-1} isopleths encompassing 91 km^2 and 36 km^2 , respectively.

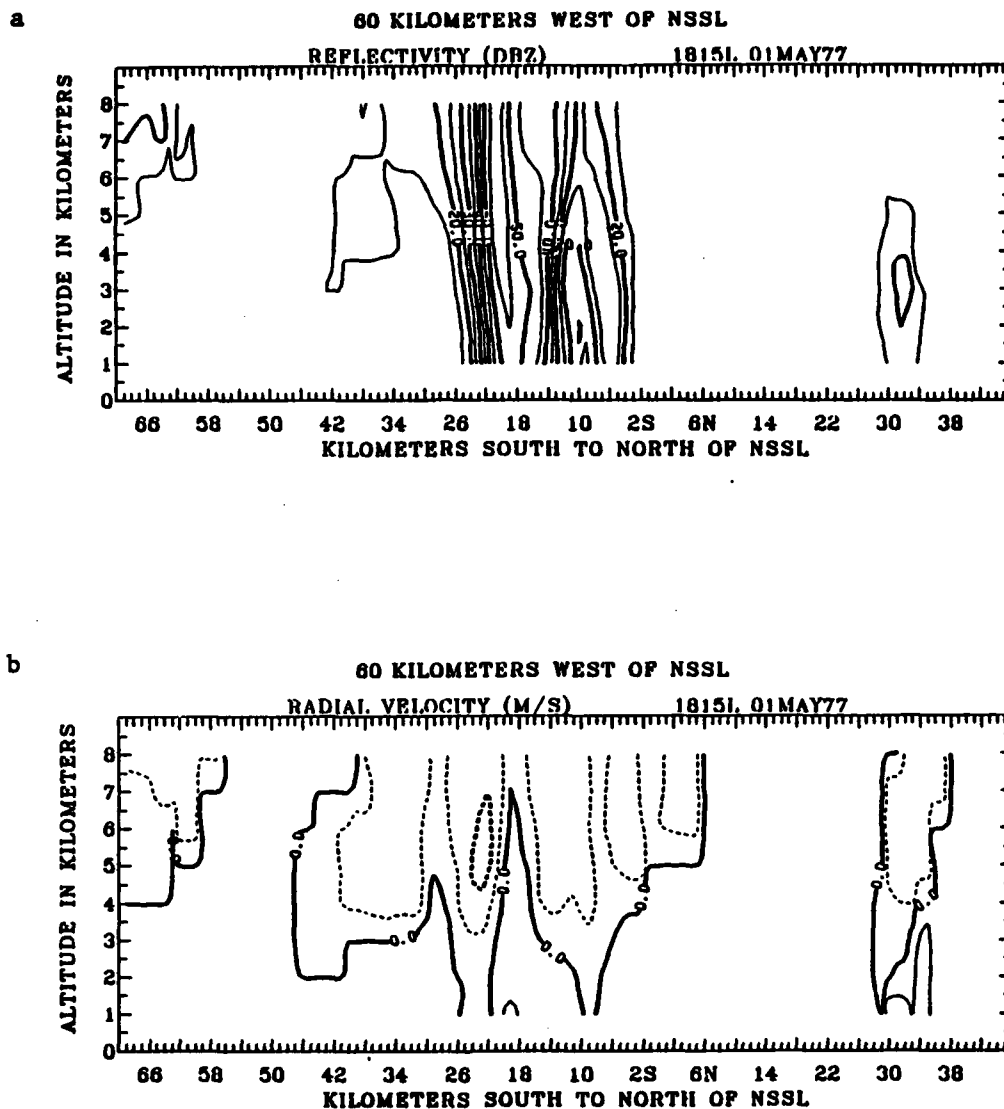


Fig. 34. North-south Cross section 60 km west of NSSL at 1815.
 (a) Reflectivity (dBZ). (b) Radial velocity (m s^{-1}).

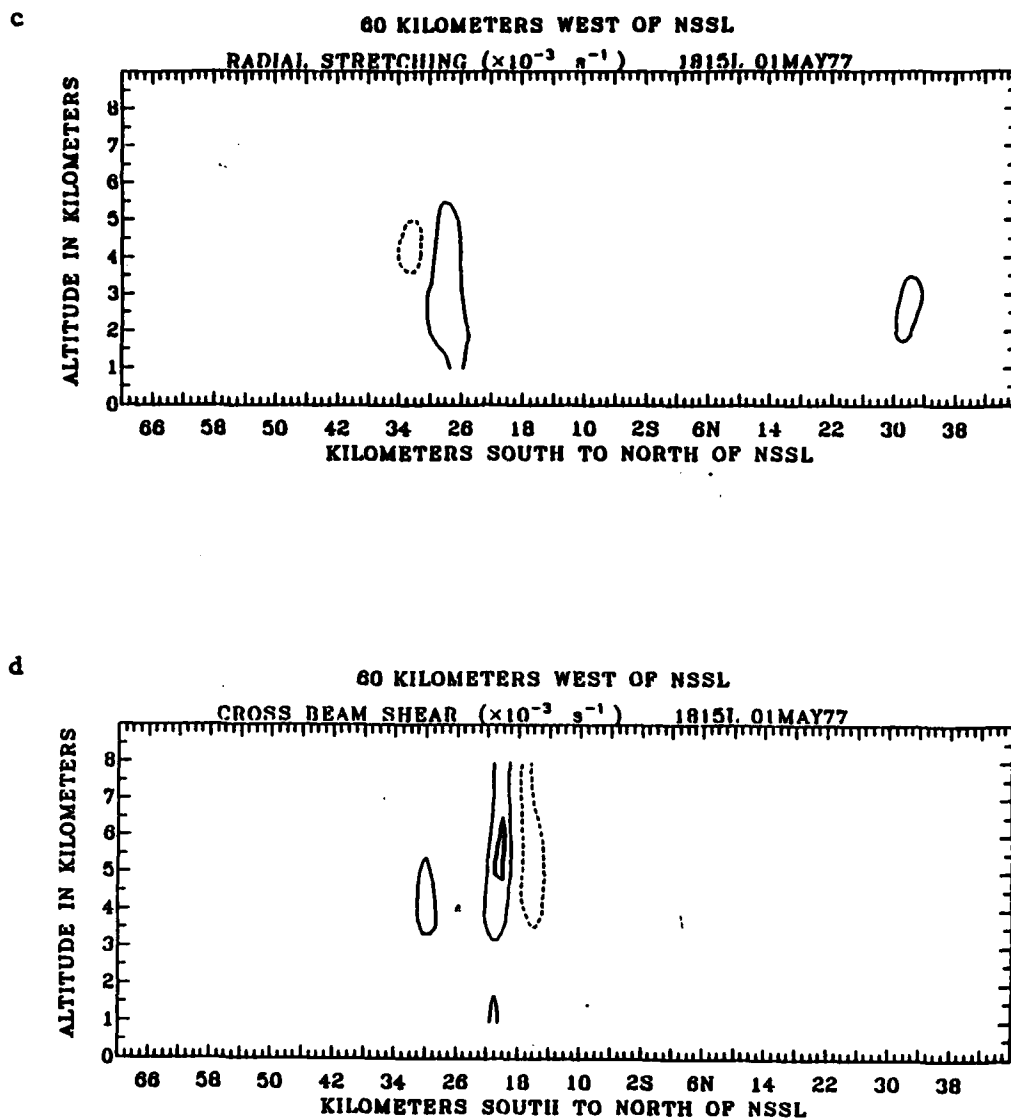


Fig. 34. (Continued) (c) Radial stretching ($\times 10^{-3} \text{ s}^{-1}$).
(d) Cross-beam shear ($\times 10^{-3} \text{ s}^{-1}$).

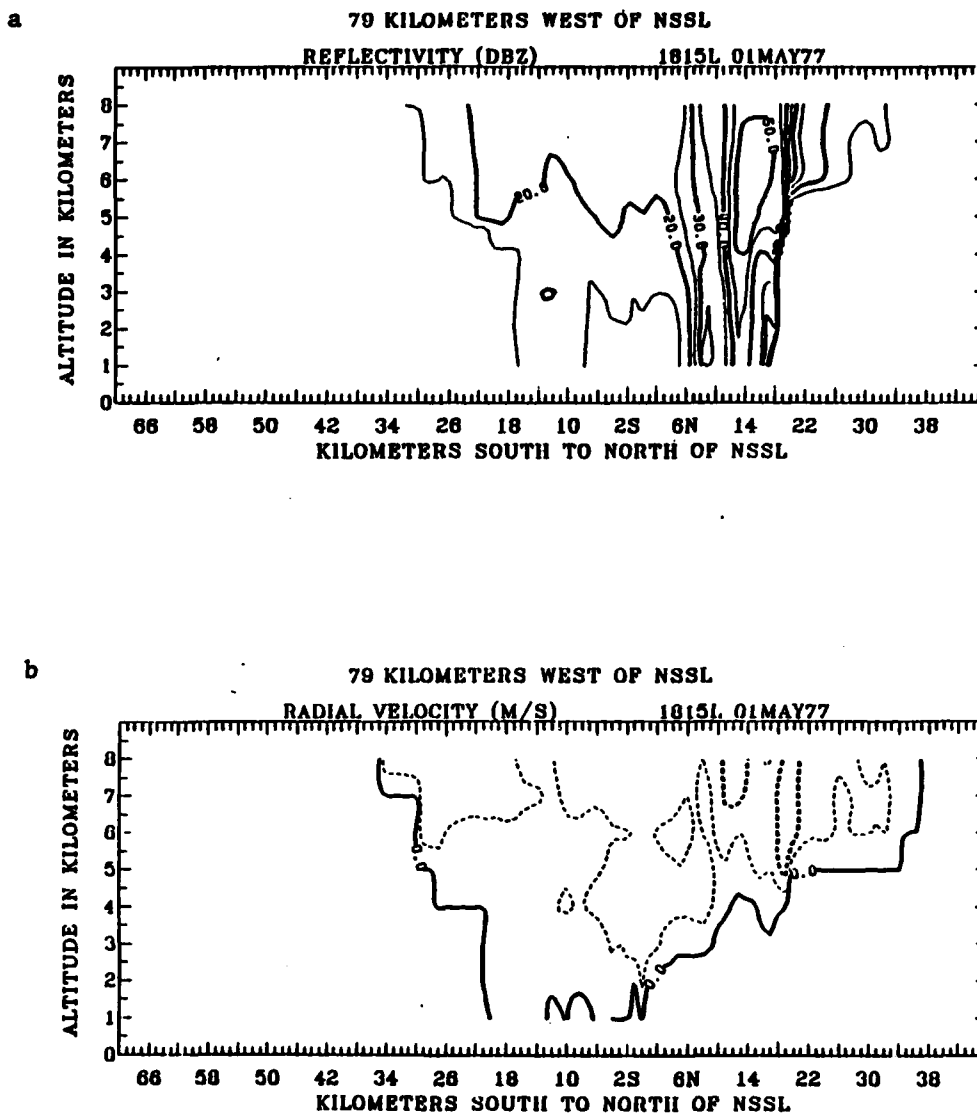


Fig. 35. North-south cross section 79 km west of NSSL at 1815.
(a) Reflectivity (dBZ). (b) Radial velocity (m s^{-1}).

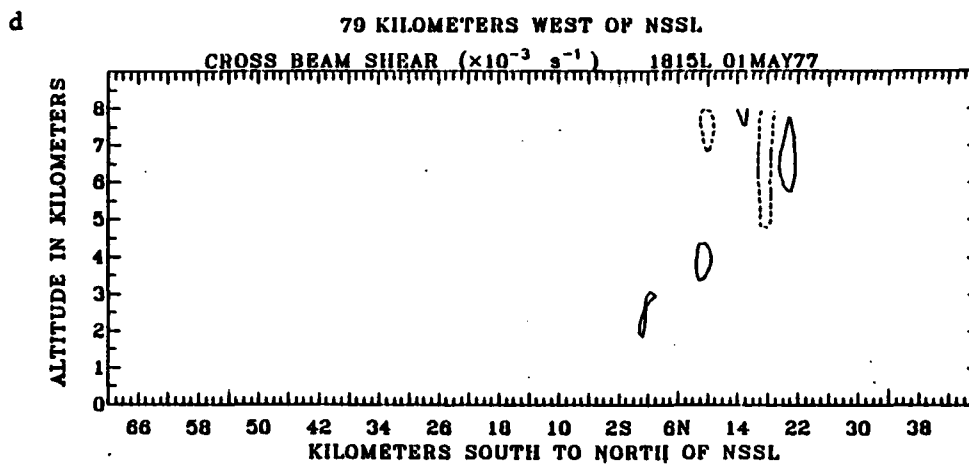
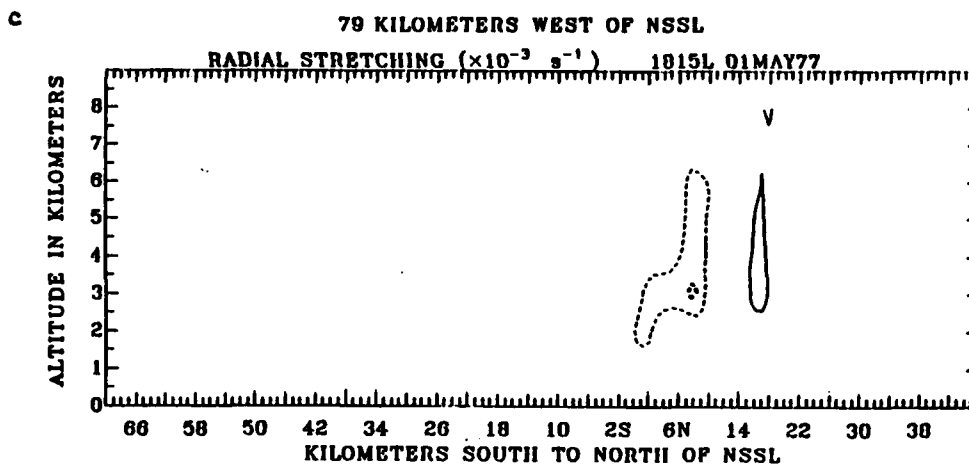


Fig. 35. (Continued) (c) Radial stretching ($\times 10^{-3} \text{ s}^{-1}$).
 (d) Cross-beam shear ($\times 10^{-3} \text{ s}^{-1}$).

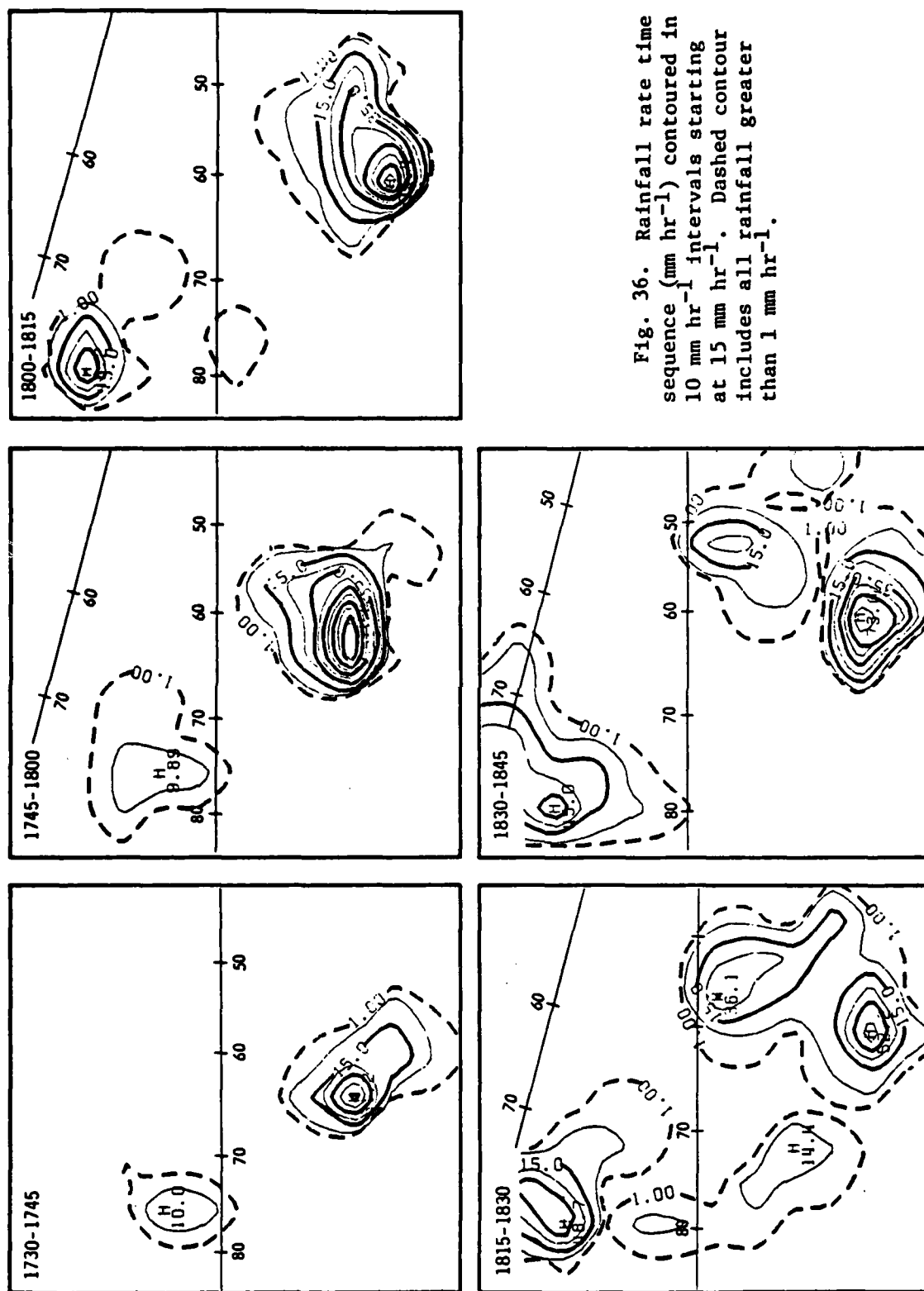


Fig. 36. Rainfall rate time sequence (mm hr⁻¹) contoured in 10 mm hr⁻¹ intervals starting at 15 mm hr⁻¹. Dashed contour includes all rainfall greater than 1 mm hr⁻¹.

Recall that the flow fields at 1745 showed dual couplets with a strong mid-level contraction.

The low- and upper-level integrated liquid water maps of the parent storm showed extremely high values at 1815. Below the freezing level, a peak value of 24 kg m^{-2} was observed, while the upper map showed over 26 kg m^{-2} . These values in themselves would suggest high rainfall rates in the next rain period. Ray *et al.* (1977), however, reported baseball-size hail near Verden, Oklahoma (57W and 18S of NSSL) at 1824. This suggests considerable contamination of the liquid water calculations by hail at this time. Actual rainfall rates for the 1815-1830 period showed a marked decrease in intensity and area.

The total 25-mm hr^{-1} isopleth area had decreased to 56 km^2 (from 97 km^2) and no 55-mm hr^{-1} area could be drawn. This was evident in spite of an increase in the size and intensity of the echo. The kinematic fields, however, anticipated this development by showing that two strong updraft couplets were competing for the available liquid water. This lends support to the vortex valve theory of Lemon *et al.* (1975).

At 1845 the low-level reflectivity pattern showed that two distinct cores had emerged from the parent cell. The parent cell continued to drift to the right of the mid-level environmental wind, while the new core (northeast core) now moved to the left. The parent cell still remained the dominant core. The suspected dual coupler pattern observed at 1815 in the cross-beam shear had now weakened. A mid-level convergence pattern was now evident in the stretching map, thereby suggesting an increase in rainfall. The new core also

contained contraction over the reflectivity core, again suggesting an increase in rainfall.

The surface rainfall of the parent cell showed an increase in peak intensity to 73 mm hr^{-1} (from 52 mm hr^{-1}) with the 25-mm hr^{-1} and 55-mm hr^{-1} areas remaining nearly constant. At 1845 the right flank updraft was dominating the storm complex, implying heavier rainfall for the right moving storm. Very little rain fell from the left-moving core until the parent cell died out between 1900 and 1915.

Summary of Findings

The single-Doppler derived fields of radial stretching and cross-beam shear accurately reflect important kinematic features of the storm of 1 May 1977. Browning's (1964) trajectory model closely approximates the kinematic features found in the single-Doppler data. While downdraft areas are not as obvious as updraft zones, they can be inferred with some reliability. The single-Doppler data suggest storm features which are comparable with multi-Doppler models of Lemon and Doswell (1979) and Heynsfield (1978). This comparison can be made even with an unfavorable beam-flow alignment.

Changes in surface rainfall rates can be sensed by examining changes in the radial stretching and cross-beam shear fields at mid levels. In a veering environment the right moving member of a splitting echo produced the heavier rainfall. In this storm, the single-Doppler kinematic fields sensed changes in surface precipitation better than radar reflectivity (or integrated liquid water).

Hail contamination and the inability to handle the vortex valve effect appears to seriously affect the ability of the relationship between radar reflectivity and surface rainfall to sense changes in rainfall.

CHAPTER VI

CONCLUSIONS AND RECOMMENDATIONS

Conclusions

One of the objectives of this research was to examine possible statistical relationships between point rainfall amounts of supercell storms and the areal coverage of rates greater than a specified threshold. Analysis of the data suggests that a direct relation exists between point and areal rainfall.

Regressing the maximum grid-point rainfall-rate values with the rainfall-rate areas provided the best correlations. Simple linear models consistently outperformed more complex formulations in statistical significance. The data stratification with the best correlations related the maximum intensity to the threshold rate area for the entire watershed. Correlations decreased for intensity-cell area models and decreased further for intensity-storm area models. The best models (least variance) contained two independent variables (area of 25 mm hr^{-1} and the area of 55 mm hr^{-1}) and accounted for parameter interaction. Filtering out data that contained zero areas of 55 mm hr^{-1} lowered the correlations and weakened the statistical tests.

A second objective was to determine if intrastorm kinematic flow could be estimated by single-Doppler radar data with supplemental information about the environmental flow. This investigation suggests this is a reasonable approach when multi-Doppler radars are unavailable. Several sub-hypotheses were outlined in Chapter I to test this

objective. The first two suggested that updrafts and downdrafts could be sensed or inferred from the Doppler fields of radial stretching and cross-beam shear. The weight of evidence supports this idea. Radial contraction in the lower layers of the storm is associated with convergence and an updraft. Strong radial contraction in the mid levels, in conjunction with high reflectivity, is often associated with heavy rainfalls. Positive cross-beam shear or a vortex couplet is frequently observed with regions of low-level contraction. Low-level negative cross-beam shear is sometimes associated with high rainfall rates. Similarly, low-level divergence patterns are revealed as stretching zones, but only rarely. This is probably due to radar sampling problems and the superpositioning of stronger signatures. Cross-beam shears associated with updrafts showed excellent vertical continuity. Vertical cross sections of cross-beam shear patterns for mesocyclones and strong updrafts are very similar. Vertical cross sections of radial stretching through mesocyclones appear to have a pattern of signature reversal with height.

The third sub-hypothesis was that beam-flow alignment is not crucial. Beam-flow alignment may not be a serious problem if one is interested in temporal changes in the radial stretching and cross-beam shear fields. Since these fields are one-dimensional kinematic signature quantities, knowing the precise values is not crucial. Storm motion corrections are also not essential for monitoring changes in the patterns of radial stretching and cross-beam shear if they are computed over a small finite difference. The implied assumption that storm motion is relatively constant over several scans is relatively

good.

The fourth hypothesis suggested that echo splitting could be sensed with single-Doppler data. This has been demonstrated.

The combined results of the four supercell cases investigated have shown remarkable similarity. More importantly, all the significant storm features inferred from single-Doppler data agreed with multi-Doppler analyses (Klemp et al., 1979); B. C. Johnson et al., 1980; K. W. Johnson et al., 1980), numerical simulations (Schlesinger, 1978, 1980; Klemp and Wilhelmson, 1978; Wilhelmson and Klemp, 1979), and numerous conceptual storm models (Browning, 1964; Lemon and Doswell, 1979).

The final objective of this research was an attempt to relate changes in storm kinematics to changes in surface rainfall rates. Some of the results of this effort are highlighted below.

The size of the mid-level contraction zone, its location in the storm, tilt of the inferred updraft, and size of the mid-level reflectivity core are all significant features in estimating changes in surface rainfall.

Heavy rainfalls do appear to be associated with mesocyclones, but the areal coverage of the peak rates is relatively small and requires a high gage resolution for detection. This seems to support the vortex valve theory (Lemon et al., 1975).

The lower-level integrated liquid water (below the melting level) appears to correlate with surface rainfall rates; however, it is often unreliable if there is hail contamination or significant cross-beam shear within the storm. Inferred kinematic fields frequently

correlate better with changes in surface rainfall than integrated liquid water.

Supercells in squall lines act in much the same way as isolated supercells. Similar rainfall patterns are observed with similar kinematic conditions.

Recommendations

A similar effort could be made in the area of single-Doppler kinematic signatures. The techniques developed here should be tested against the other single-Doppler analysis techniques (Chapter I) in an effort to extract optimum information from the data. A more quantitative approach to the analyses is certainly desirable. Attempts along this line were thwarted by the small sample size in this effort.

Additional techniques should also be developed to perform vertical cross-section analyses along an arbitrary azimuth. An in-house dual-Doppler processing program is the obvious next step to aid in the verification of single-Doppler patterns and enable the computation of three-dimensional fluxes. Automation of the superpositioning of cross-beam shear and radial stretching fields would also be of value.

In summary, single-Doppler radar may have a larger role to play in severe storm research than simply monitoring storms for tornadic formations. It will never replace multi-Doppler systems as the current day standard for computing intrastorm flow, but when used with additional environmental data, it can provide the imaginative researcher with valuable kinematic data at relatively small cost.

REFERENCES

- Atlas, P., 1963: Radar analysis of severe storms. Meteor. Monogr., No. 27, 177-220.
- Barnes, S. L., 1964: A technique for maximizing details in numerical weather map analysis. J. Appl. Meteor., 3, 396-409.
- _____, 1973: Mesoscale objective map analysis using weighted time series observations. NOAA Tech. Memo. ERL NSSL-62, Norman, OK, 60 pp.
- _____, 1976: Severe local storms: Concepts and understanding. Bull. Amer. Meteor. Soc., 57, 412-419.
- _____, 1978a: Oklahoma thunderstorm on 29-30 April 1970. Part I: Morphology of a tornadic storm. Mon. Wea. Rev., 106, 673-684.
- _____, 1978b: Oklahoma thunderstorm on 29-30 April 1970. Part II: Radar observed merger of twin look echoes. Mon. Wea. Rev., 106, 685-696.
- _____, 1978c: Oklahoma thunderstorm on 29-30 April 1970. Part III: Tornado characteristics inferred from damage tracks. Mon. Wea. Rev., 106, 697-703.
- _____, J. H. Henderson, and R. J. Ketchum, 1971: Rawinsonde observations and processing techniques at the National Severe Storms Laboratory. NOAA Tech. Memo., ERL NSSL-53, Norman, OK, 246 pp.
- _____, and S. Nelson, 1978: Oklahoma thunderstorm on 29-30 April 1970. Part IV: Study of dissipating severe storms. Mon. Wea. Rev., 106, 704-712.
- Battan, L. J., 1973: Radar Observation of the Atmosphere. Univ. of Chicago Press, Chicago, IL, 324 pp.
- _____, and J. B. Theiss, 1971: Wind gradients and variance of Doppler spectra. Sci. Report No. 26, Institute of Atmospheric Physics, University of Arizona, Tucson, AZ, 12 pp.
- Beaver, T. F., 1980: Digital Doppler radial velocity data compared objectively with digital reflectivity radar data. M.S. Thesis, Texas A&M University, unpublished, May 1980, 110 pp.
- Bendat, J. S., and A. G. Piersol, 1971: Random Data Analysis and Measurement Procedures. Wiley-Interscience, 407 pp.
- Blackman, R. B., and J. W. Tukey, 1958: The Measurement of Power Spectra. Dover, New York, 190 pp.

- Blake, L. V., 1970: Prediction of Radar Range Radar Handbook. Chapter 2, M. I. Skolnik (Ed.), McGraw Hill, New York, 2-51, 2-55.
- Bluestein, H. B., and C. J. Sohl, 1979: Some observations of a splitting severe thunderstorm. Preprints 11th Conf. on Severe Storms, Kansas City, Amer. Meteor. Soc., 453-457.
- Bonesteel, R. G., and Y. J. Lin, 1978: A study of updraft-downdraft interaction based on perturbation pressure and single-Doppler radar data. Mon. Wea. Rev., 106, 62-68.
- Bonewitz, J. D., 1978: Development of Doppler Radar Techniques for Severe Thunderstorm Wind Advisories. M.S. Thesis, Univ. of Oklahoma, unpublished, 64 pp.
- Brandes, E. A., 1975: Optimizing rainfall estimates with aid of radar. J. Appl. Meteor., 14, 1339-1345.
- _____, 1977: Flow in severe thunderstorm observed by dual-Doppler radar. Mon. Wea. Rev., 105, 113-120.
- _____, 1978: Mesocyclone evolution and tornadogenesis: some observations. Mon. Wea. Rev., 106, 995-1011.
- _____, 1979: Tornadic Mesocyclone Finestructure and Implications of Tornadogenesis. Preprints 11th Conf. on Severe Local Storms, Kansas City, Amer. Meteor. Soc., 549-556.
- _____, and D. Sirmans, 1976: Convective rainfall estimation by radar: Experimental results and proposed operational analysis technique. Preprints Conf. on Hydrometeorology, Ft. Worth, Amer. Meteor. Soc., 54-59.
- Brown, R. A., 1976: Single Doppler radar data acquisition and analysis. Appendix E in The Union City, Oklahoma Tornado of 24 May 1973, R. A. Brown (Ed.). NOAA Tech. Memo ERL NSSL-80, Norman National Severe Storms Laboratory (NTIS PB269443/AS), 215-228.
- _____, 1980: Personal communication.
- _____, D. W. Burgess, and K. C. Crawford, 1973: Twin tornado cyclones within a severe thunderstorm: single Doppler radar observations. Weatherwise, 26, 63-71.
- _____, and L. R. Lemon, 1976: Single Doppler Radar Vortex Recognition. Part II: Tornadic Vortex Signatures. Preprints 17th Conf. on Radar Meteor., Seattle, Amer. Meteor. Soc., 104-109.

- _____, C. R. Safford, S. P. Nelson, D. W. Burgess, W. C. Bumgarner, M. L. Weible, and L. C. Fortner, 1980: Multiple Doppler radar analysis of severe thunderstorms: Designing a general analysis system. Bull. Amer. Meteor. Soc., Submitted July, 1980.
- Browning, K. A., 1964: Airflow and precipitation trajectories within severe local storms which travel to the right of the winds. J. Atmos. Sci., 21, 634-639.
- _____, and W. C. Ludlam, 1962: Air flow in convective storms. Quart. J. Roy. Meteor. Soc., 88, 117-135.
- _____, and R. Wexler, 1968: The determination of kinematic properties of a wind field using Doppler radar. J. Appl. Meteor., 7, 105-113.
- _____, J. C. Fankhauser, J. P. Chalon, P. J. Eccles, R. G. Strauch, F. H. Merrem, D. J. Musil, E. L. May, and W. R. Sand, 1976: Structure of an evolving hailstorm. Part V: Synthesis and implications for hail growth and hail suppression. Mon. Wea. Rev., 104, 603-610.
- _____, and G. B. Foote, 1976: Airflow and hail growth in supercell storms and some implications for hail suppression. Quart. J. Roy. Meteor. Soc. 102, 497-534.
- Burgess, D. W., 1976: Single Doppler radar vortex recognition. Part I: Mesocyclone signatures. Preprints 17th Conf. on Radar Meteorology, Seattle, Amer. Meteor. Soc., 97-103.
- _____, J. D. Bonewitz, and D. R. Devore, 1978: Joint Doppler operational project: results year 1. Preprints 18th Conf. on Radar Meteorology, Atlanta, Amer. Meteor. Soc., 442-448.
- Byers, H. R., and R. R. Braham, 1949: The Thunderstorm. U.S. Govt. Printing Office, Washington, D.C., 287 pp.
- Caton, P. G., 1963: The measurement of wind and convergence by Doppler radar. Preprints 10th Weather Radar Conf. Washington, Amer. Meteor. Soc., 290-296.
- Chalon, J. P., J. C. Fankhauser, and P. J. Eccles, 1976: Structure of an evolving hailstorm. Part I: General characteristics and cellular structure. Mon. Wea. Rev., 104, 564-575.
- Charba, J. and Y. Sasaki, 1971: Structure and movement of the severe thunderstorm of 3 April 1964 as revealed from radar and surface mesonetwork data analysis. J. Meteor. Soc. Japan, 49, 191-213.
- Chisholm, A. J., 1973: Alberta hailstorms. Part I: Radar case studies and airflow models. Meteor. Monogr., No. 36, 1-36.

- Cohen, A., and A. Smolski, 1966: The effect of rain on satellite communications earth terminal rigid radomes. Microwave Jour., 4, 1-5.
- Cotton, W. R., and G. J. Tripoli, 1978: Cumulus convection in shear flow-three dimensional numerical experiments. J. Atmos. Sci., 35, 1503-1521.
- Crawford, K. C., and R. A. Brown, 1972: Doppler velocity measurements in an approaching squall line. Preprints 15th Radar Meteorology Conf., Champaign-Urbana, Amer. Meteor. Soc., 27-34.
- Cressman, G. P., 1959: An operational objective analysis system. Mon. Wea. Rev., 87, 367-374.
- Curtis, R. B., and J. Vaccaro, 1961: Survey of ground radomes. Report No. RAOC-TR-61-52. Rome Air Development Center, AFSC USAF, Griffiss AFB, N. Y.
- Davies-Jones, R. P., D. W. Burgess, and L. R. Lemon, 1975: Analysis of the 4 June 1973 Norman Tornadoic Storm. Proceedings 9th Conf. on Severe Local Storms, Norman, Amer. Meteor. Soc., 384-388.
- Davis, A. R., and D. J. McMorro, 1976: Stochastic Models for Deriving Instantaneous Precipitation Rate Distributions. AWS TR 76-263, AWS (MAC), 20 pp.
- Donaldson, R. J., Jr., 1970: Vortex signatures recognition by Doppler radar. J. Appl. Meteor., 9, 661-670.
- _____, G. M. Armstrong, K. J. Banis, and R. Dyer, 1972: Measurement of Wind Gradients in Convective Storms by Doppler Radar. Preprints 15th Conf. on Radar Meteorology, Champaign-Urbana, Amer. Meteor. Soc., 22-26.
- Doviak, R. J., and D. Sirmans, 1973: Reflectivity Equation for NSSL's WDS-71 10 cm Doppler Radar. Unpublished report, NSSL, 8 pp.
- Easterbrook, C. C., 1975: Estimating horizontal wind fields by two dimensional curve fitting of single Doppler radar measurement. Preprints 16th Radar Meteor. Conf., Houston, Amer. Meteor. Soc., 214-219.
- Eskridge, R. E., and P. Das, 1976: Effect of a precipitation-driven downdraft on a rotating wind field: A possible trigger mechanism for tornadoes? J. Atmos. Sci., 70, 70-84.

- Fankhauser, J. C., 1971: Thunderstorm-environment interactions determined from aircraft and radar observations. Mon. Wea. Rev., 97, 171-192.
- Fuelberg, H. E., 1974: Reduction and error analysis of the AVE II pilot experiment data. NASA CR-120496, George C. Marshall Space Flight Center, Huntsville, AL, 131 pp.
- Fujita, T., 1963: Analytical Mesometeorology: A review. Severe Local Storms, Meteor. Monogr., No. 27, 77-125.
- _____, and H. Grandoso, 1968: Split of a thunderstorm into anti-cyclonic and cyclonic storms and their motion as determined from numerical model experiments. J. Atmos. Sci., 25, 416-439.
- Gandin, L. S., 1965: Objective Analysis of Meteorological Fields. Article, Israel Program for Scientific Translations, Jerusalem, 242 pp.
- Goff, R. C., 1976: Vertical structure of thunderstorm outflows. Mon. Wea. Rev., 102, 1429-1440.
- Goodin, W. R., G. J. McRae, and J. H. Seinfeld, 1979: A comparison of interpolation methods for sparse data; application to wind and concentration fields. J. Appl. Meteor., 18, 761-771.
- Greene, D. R., 1973: Numerical Techniques for the Analysis of Digital Radar Data with Applications to Meteorology. R&D Tech. Report ECOM 0073T-4, ECOM U.S. Army Elec, Command, Ft. Monmouth, N. J., 120 pp.
- Gringorten, I. I., 1976: Areal Coverage Estimates by Stochastic Modelling. AFGL TR 76-0148, ERP No. 573, Air Force Geophysics Laboratory, 56 pp.
- Gunn, R., and G. D. Kinzer, 1949: The terminal velocity of fall for water droplets in stagnant air. J. of Meteor., 6, 243-248.
- Haglund, G. T., 1969: A study of a severe local storm of 16 April 1967. ESSA Tech. Memo. ERLTM-NSSL, National Severe Storms Laboratory, Norman, OK, 44 pp.
- Hammond, G. R., 1967: Study of a left moving thunderstorm of 23 April 1964. ESSA Tech. Memo. IERTM-NSSL, National Severe Storms Laboratory, Norman, OK, 31 pp.
- Heymsfield, G. M., 1978: Kinematic and dynamic aspects of the Harrah tornadic storm analyzed from dual Doppler radar data. Mon. Wea. Rev., 106, 233-254.
- Hitschfeld, W., and J. Bordan, 1954: Errors in the radar measurement of rainfall at attenuating wavelengths. J. Meteor., 11, 58-67.

- Howell, D. S., and K. S. Knight, 1980: Tornado detection using computer analysis of Doppler radar data. Unpublished report, Texas A&M University, 68 pp.
- Hudlow, M. D., P. J. Pytlowany, and F. D. Marks, 1976: Objective analysis of GATE collected radar and rain gage data. Preprints 17th Conf. on Radar Meteor., Seattle, Amer. Meteor. Soc., 414-421.
- Huff, F. A., 1970: Sampling errors in measurement of mean precipitation. J. Appl. Meteor., 9, 35-44.
- Humphreys, W. J., 1964: Physics of the Air. Dover publication, New York, 676 pp.
- Jessup, E. A., 1972: Interpretations of chaff trajectories near a severe thunderstorm. Mon. Wea. Rev., 100, 653-661.
- Johnson, B. C., K. W. Johnson, P. S. Ray, J. S. Bradberry, J. J. Stephens, and W. C. Bumgarner, 1980: The Morphology of Some Tornadoic Storms. Preprints 19th Conf. on Radar Meteor., Miami Beach, Amer. Meteor. Soc., 311-316.
- Johnson, K. W., B. C. Johnson, P. S. Ray, J. S. Bradberry, and K. K. Wagner, 1980: Vorticity Development in Two Tornadoic Storms. Preprints, 19th Conf. on Radar Meteor., Miami Beach, Amer. Meteor. Soc., 328-334.
- Jones, D. M., and A. L. Sims, 1978: Climatology of instantaneous rainfall rates. J. Appl. Meteor., 17, 1135-1140.
- Klemp, J. B., P. S. Ray, and R. B. Wilhelmson, 1980: Analysis of Merging Storms on 20 May 1977. Preprints 19th Conf. on Radar Meteor., Miami Beach, Amer. Meteor. Soc., 317-324.
- _____, and R. B. Wilhelmson, 1978: Simulations of right- and left-moving storms produced through storm splitting. J. Atmos. Sci., 35, 1097-1110.
- _____, _____, P. S. Ray, J. Stokes, B. Johnson, and K. Johnson, 1979: Comparison of Modeled and Observed Severe Storms. Preprints 11th Conf. on Severe Local Storms, Kansas City, Amer. Meteor. Soc., 515-522.
- Kraus, M. J., 1973: Doppler radar observations of the Brookline, Massachusetts tornado of 9 August 1972. Bull. Amer. Meteor. Soc., 54, 519-524.
- _____, 1974: Doppler Radar Investigation of Flow Patterns within Thunderstorms. AFCRL TR 74-0290, 86 pp.

- Kropfli, R. A., and L. J. Miller, 1976: Kinematic structure and flux quantities in a convective storm from dual Doppler radar observations. J. Atmos. Sci., 33, 520-529
- Larson, L. W., and E. L. Pack, 1974: Accuracy of precipitation measurements for hydrologic modeling. Water Resour. Res., 10, 857-863.
- Lawson, C. L., 1977: Software for C' surface interpolation. Mathematical Software Journal, Vol. 3, J. R. Rice (Ed.), Academic Press, 161-194.
- Leary, C. A., and R. A. Houze, Jr., 1979: The structure and evolution of convection in a tropical cloud cluster. J. Atmos. Sci., 36, 437-457.
- Lemon, L. R., 1976: Wake vortex structure and aerodynamic origin in severe thunderstorms. J. Atmos. Sci., 33, 678-685.
- _____, 1977: Severe Thunderstorm Evolution: Its use in a Technique for Radar Warnings. Preprints 10th Conf. on Severe Local Storms, Omaha, Amer. Meteor. Soc., 77-80.
- _____, D. W. Burgess, and R. A. Brown, 1975: Tornado production and storm substenance. Proceedings 9th Conf. on Severe Local Storms, Norman, Amer. Meteor. Soc., 100-104.
- _____, _____, _____, 1978: Tornadic storm airflow and morphology derived from single Doppler radar measurements. Mon. Wea. Rev., 106, 48-61.
- _____, and C. A. Doswell, 1979: Severe thunderstorm evolution and mesocyclone structure as related to tornadogenesis. Mon. Wea. Rev., 107, 1184-1197.
- Lhermitte, R. M., 1964: Doppler radars as severe storm sensors. Bull. Amer. Meteor. Soc., 45, 587-596.
- _____, 1969: Doppler radar observations of a convective storm. Preprints 6th Conf. Severe Local Storms, Boston, Amer. Meteor. Soc., 139-145.
- Linsley, R. K. and M. A. Kohler, 1951: Variations in storm rainfall over small areas. Trans. Amer. Geophys. Union, 32, 245-250.
- Ludlum, F. H., 1963: Severe Local Storms: A Review. Severe Local Storms, Meteor. Monogr., No. 27, 1-30 .
- Marwitz, J. D., 1971: The structure and motion of severe hailstorms. Part III: Severely sheared storms. J. Appl. Meteor., 11, 189-201.

- _____, 1971: Supercell storms and the Soviet hailstorm model. Preprints, International Wea. Mod. Conf., Geneva.
- _____, 1972: The structure and motion of severe hailstorms. Part I: Supercell storms. J. Appl. Meteor., 11, 166-179.
- McGuinness, J. L., 1963: Accuracy of estimating watershed mean rainfall. J. Geophys. Res., 68, 4763-4767.
- McMorrow, D. J., 1978: A Technique for Estimating Clock Two-Hourly Precipitation Rate Distributions. Preprints Conf. on Climate and Energy: Climatological Aspects and Industrial Applications, Asheville, Amer. Meteor. Soc., 187-194.
- Miller, R. C., 1972: Notes on analysis and severe-storm forecasting procedures of the Air Force Global Weather Central. AWS Tech. Rep. 200 (REV) May 1972, AWS (MAC), 177 pp.
- Nelson, S. P., 1976: Characteristics of multicell and supercell hailstorms in Oklahoma. Preprints International Conf. on Cloud Physics, Boulder, 335-340.
- _____, 1977: Rear flank downdraft. A hailstorm intensification mechanism. Preprints 10th Conf. on Severe Local Storms, Omaha, Amer. Meteor. Soc., 521-525.
- Newton, C. W., 1963: Dynamics of Severe Convective Storms. Severe Local Storms, Meteor. Monogr., No. 27, 33-35.
- _____, and J. C. Fankhauser, 1975: Movement and propagation of multicellular convective storms. Pure Appl. Geophys. 113, 747-764.
- _____, and S. Katz, 1958: Movement of large convective rainstorms to winds aloft. Bull. Amer. Meteor. Soc., 39, 129-136.
- Nicks, A. D., 1966: Field evaluation of rain gage network design principles. Symposium design of hydrological networks. Inter. Assoc. Sci. Hydrol. Pub. 67, 88-93.
- O'Brien, J. J., 1970: Alternative solutions to the classical vertical velocity problem. J. Appl. Meteor., 9, 197-203.
- Panofsky, H. A., 1949: Objective weather-map analysis. J. Meteor., 6, 386-392.
- Park, S. V., and D. N. Sikdar, 1979: An application of a simple diagnostic cloud model to the May 20 1977 storms over the Oklahoma meso-network. Preprints 11th Conf. on Severe Local Storms, Kansas City, Amer. Meteor. Soc., 474-480.

- Peace, R. L., Jr., R. A. Brown, and H. G. Camnitz, 1969: Horizontal motion field observations with a single pulse Doppler radar. J. Atmos. Sci., 26, 1096-1103.
- Probert-Jones, J. R., 1962: The radar equation in meteorology. Quart. J. Roy. Meteor. Soc., 88, 485-495.
- Prosser, N. E., and D. S. Foster, 1966: Upper air sounding analysis by use of an electronic computer. J. Appl. Meteor., 5, 296-300.
- Ray, P. S., 1976. Vorticity and divergence fields within tornadic storms from dual-Doppler observations. J. Appl. Meteor., 15, 879-890.
- _____, J. Weaver, and NSSL Staff, 1977: 1977 Spring program summary, National Severe Storms Laboratory, Norman, OK, NOAA Tech. Memo. ERL NSSL-84, 173 pp.
- Schalatter, T. W., 1975: Some experiments with multivariate statistical objective analysis scheme. Mon. Wea. Rev., 103, 246-257.
- Schlesinger, R. E., 1978: A three-dimensional numerical model of an isolated thunderstorm. Part I: Comparative experiments for variable ambient wind shear. J. Atmos. Sci., 35, 690-713.
- _____, 1980: A three-dimensional numerical model of an isolated thunderstorm. Part II: Dynamics of updraft splitting and meso-vortex couplet evolution. J. Atmos. Sci., 47, 395-420.
- Showalter, A. K., 1969: Factors influencing patterns of flash flood rainfall. Preprints 6th Conf. on Severe Local Storms, Chicago, Amer. Meteor. Soc., 114-118.
- Sieland, T. E., 1977: Real-Time Computer Techniques in the Detection and Analysis of Severe Storms from Digital Radar Data. Ph.D. Dissertation, unpublished, Texas A&M University, 141 pp.
- Snider, R. C., 1971: One hour rainfall amounts near tornadoes. Preprints 7th Conf. on Severe Local Storms, Kansas City, Amer. Meteor. Soc., 244-249.
- Staff, NSSL, AFGL, NWS, and AWS, 1979: Final Report on the Joint Doppler Operational Project (JDOP) 1976-1978. NOAA Tech. Memo. ERL NSSL-86, Norman, 84 pp.
- Stephens, J. J. and J. M. Still, 1970: Optimum influence radii for interpolation with successive corrections. Mon. Wea. Rev., 98, 680-687.

- Strauch, R. G., and F. H. Merrin, 1976: Structure of an evolving hailstorm. Part III: Internal structure from Doppler radar. Mon. Wea. Rev., 104, 588-595.
- Sumers, P. W., 1972: Project hailstop: A review of accomplishments to date in Alberta hail studies, 1972. Research Council of Alberta, Hail Studies Report 72-2, 47-53.
- Thorpe, A. J., and M. J. Miller, 1978: Numerical simulations showing the role of the downdraft in cumulonimbus motions and splitting. Quart. J. Roy. Meteor. Soc., 104, 873-893.
- Ulanski, S. L., and M. Garstang, 1978: The role of surface divergence and vorticity in the life cycle of convective rainfall. Part I: Observational and Analysis. J. Atmos. Sci., 35, 1047-1062.
- _____, _____, 1978: The role of surface divergence and vorticity in the life cycle of convective rainfall. Part II: Descriptive Model. J. Atmos. Sci., 35, 1063-1069.
- Waldteufel, P., and H. Corbin, 1979: On the analysis of single-Doppler radar data. J. Appl. Meteor., 18, 532-542.
- Wilhelmson, R. B., and J. B. Klemp, 1978: A numerical study of storm splitting that leads to long-lived storms. J. Atmos. Sci., 35, 1974-1986.
- _____, _____, 1979: The effect of gust fronts on the generation of multiple splitting storms. Preprints 11th Conf. on Severe Local Storms, Kansas City, Amer. Meteor. Soc., 291-298.
- Wilk, K. E., and E. Kessler, 1970: Quantitative radar measurements of precipitation. Meteor. Monogr., No 11, 315-329. Meteor. Soc., 315-329.
- Wilson, J. W., 1976: Radar-rain gage precipitation measurements: A summary. Preprints Conf. on Hydrometeorology, Ft. Worth, Amer. Meteor. Soc., 72-75.
- _____, 1978: Observations of radome transmission losses at 5 cm wavelengths. Preprints 18th Conf. on Radar Meteor., Atlanta, Amer. Meteor. Soc., 288-291.
- _____, and E. A. Brandes, 1979: Radar measurements of rainfall: A summary. Bull. Amer. Meteor. Soc., 60, 1048-1058.
- _____, and T. T. Fujita, 1979: Vertical cross section through a rotating thunderstorm by Doppler radar. Preprints 11th Conf. on Severe Local Storms, Kansas City, Amer. Meteor. Soc., 447-452.

Winner, D. C., 1968: Climatological estimates of clock-hour rainfall rates. Air Weather Service Tech. Report 202, HQ AWS (MAC), U.S. Air Force, 26 pp.

Woodley, W., A. Olsen, A. Herndon, and V. Wiggert, 1975: Comparison of gage and radar methods of convective rain measurement. J. Appl. Meteor., 14, 909-928.

Zrnic, D. S., and R. J. Doviak, 1975: Velocity spectra of vortices scanned with a pulse-Doppler radar. J. Appl. Meteor., 14, 1531-1539.

APPENDIX A

RAINFALL DATA AND PROCESSING METHODOLOGY

Source and Reduction Procedures

The rainfall data used in this investigation were acquired from the Agricultural Research Service (ARS) Office, U.S. Department of Agriculture, at Chickasha, Oklahoma. This office maintains a network of weighing-bucket recording raingages over the Washita River watershed. The network is located between 34°45' to 35°35' latitude and 97°30' to 98°30' longitude in central Oklahoma (see Fig. A.1). This area is roughly 4000 km² and extends from 20 km to 95 km west of Norman, and 30 km north to 55 km south of Norman. The topography is mostly rolling plains cut by eroded valleys. The maximum relief is approximately 450 ft in the northwestern portion of the watershed.

The complete network consists of 228 recording raingages with a spatial resolution of 4.8 km. In this study 191 gages were available for the 1 May 1977 analysis, while 193 gages were available for 19 and 20 May 1977. All the gage data were used in the 1 May analysis. Instrument problems reduced the usable data to 94% of the total for 19 May and 91% for 20 May.

The data are recorded in analog form on weekly strip charts. The data had to be manually digitized. The charts can be easily read to an accuracy of ± 0.02 in. (0.508 mm). The raingage data were digitized for times of significant radar echoes. This resulted in 3 hr of data for 1 May 1977 and 8 hr for 19 and 20 May 1977, thereby generating approximately 14,400 15-min observations. To check for errors,

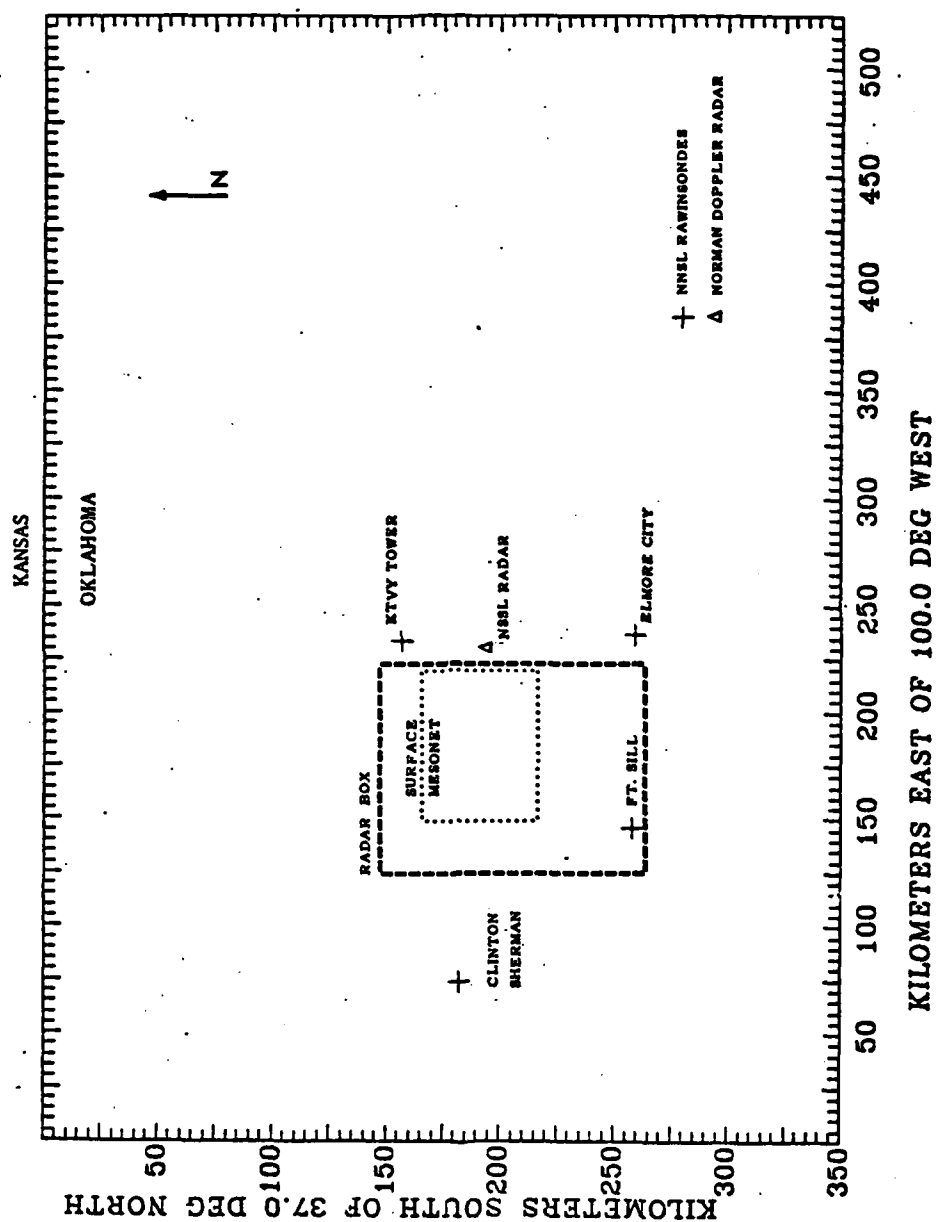


Fig. A.1. Example of comparative sizes of the Washita and Oklahoma raingage networks.

each chart was reread at least three times. About 25% of the charts were read more than three times. In an effort to avoid bias, the second readings were done at random. As an additional check, a Fortran program was written to accumulate the data to daily totals. Daily totals usually are annotated on the charts by the ARS staff. The accumulation process also revealed key punch errors.

Next, the raw data were gridded, plotted and subjectively contoured. The grid map dimensions are identical to those used in the radar analysis. While the map dimensions are 116 km (north/south) and 96 km (east/west), only 37% of the map area (4065 km^2) is covered by gages. These results were compared with objectively analyzed WSR-57 radar reflectivity maps for consistency. The rainfall data were then objectively analyzed and compared with subjectively contoured rainfall maps and the radar maps. In addition, the raw data were also station plotted and subjectively analyzed for selected times and compared with the other analyses. Considerable fine tuning was required to adjust the total objective analysis scheme to match the subjectively analyzed station analyses. The objective analysis techniques are described in the next section.

Processing Methodology

Great care is required in objectively analyzing precipitation data. Objective analysis schemes work best for quasi-smooth continuous data such as temperature, wind, or pressure. Precipitation is not an ideal field to contour objectively because of its discontinuous nature. The observational network required to minimize discontinuity

problems is seldom adequate. A rainfall midway between two rain gages may be an average value of the gages, considerably greater than either gage, or zero. Objective analysis schemes are generally designed to smooth data fields by filtering out noise introduced by small fluctuations in the data. In this study, a prime goal is to analyze spatial and temporal rainfall fluctuations. Filtering out the noise in the data, but maintaining the desired detail, was a considerable problem.

The approach used in this paper was developed by Barnes (1964; 1973) and adapted by Brandes (1975) for precipitation data. The basic idea is simple. Select a radius of influence for each grid point within which stations contribute weighted information to the grid point based upon their distance from the grid point. This approach is often called weighted interpolation, i.e.,

$$A_{ij} = \frac{\sum_{k=1}^n R_k w_k(r)}{\sum_{k=1}^n w_k(r)} ,$$

where R_k is the rainfall at the k^{th} gage, $w_k(r)$ is the weight function for the gage (a function of the distance from the recording point to the grid), and A_{ij} is the grid point value. Without any optimization techniques, all data are tested for their influence at each grid point. A better data fit is possible if the gridded data are bilinearly interpolated back to the original locations, a difference field is computed at the original data sites, and the difference field is then weighted to the grid points. This "correction" field can then be added to original gridded values producing an "adjusted" gridded field. Barnes (1973) has shown that this "two pass" approach is more

efficient than the four or five passes approach described in his 1964 paper. The essence of this method adjusts a parameter in the weighting function on the second pass to speed convergence of station and grid point data.

The weighting function used in this analysis is exponential. Selection of the exponential weighting function was not a straightforward decision. A variety of interpolation schemes have been developed. Several of these are summarized in Goodin *et al.* (1979). Serious consideration was given to Cressman weighting (Cressman, 1959), least-square polynomial interpolation (Panofsky, 1949; Lawson, 1977), optimum interpolation (Gandin, 1963; Schlatter, 1975), and spline curve fitting. Weighted interpolation is probably the method most widely used in meteorology for putting data onto grid points. It is easy to implement and relatively easy to fine tune. Most weighted schemes fall into three categories:

$$\text{Power} \quad w(r) = r^{-n} ,$$

$$\text{Exponential} \quad w(r) = \exp(-Cr^n) ,$$

$$\text{Cressman} \quad W(r) = \left[\frac{R^2 - r^2}{R^2 + r^2} \right]^n .$$

where r is the distance from the grid point, R is the radius of influence, and " C " is a constant. Each of these categories was evaluated before selecting the exponential scheme.

Stephens and Still (1970) have shown that for an average station separation the optimum radius of influence, for a large

signal-to-noise ratio, occurs when $R/d \approx 1.6$. The value of d is defined as $d = \sqrt{A/N}$, where A is the total area and N the total number of stations (see Goodin et al., 1979). To be precise, this result is for random data sampling, but it does give guidance for data sampled by non-random sites. In this study the sampling is non-random with the gages separated by 4.8 km. A 4-km grid was used with a radius of influence of 5 km. A radius of influence suggested by the Stephens and Still method ($R = 7.68$ km) produced excessive smoothing for the precipitation data. The weighting function used is of the form

$$w(r) = \exp - \left[\frac{r^2}{A_k} \right] .$$

The parameter A_k is defined as $R^2/4$, where R is the effective radius of influence. Empirical tests optimized R at 1.25 times the grid spacing (4 km).

Once all the data are scanned for each grid point, the grid point data are bilinearly interpolated back to each observational point, and a difference is computed. The A_k parameter is reduced by 60% and the difference field is then exponentially interpolated onto the grid points. The original gridded field and the difference gridded field are added to produce the adjusted field. Considerable testing was required to achieve the optimum combination of R and the adjusted A_k values on the second pass in order to match the objectively contoured field with the subjective analyses.

The contouring was performed by a software package (adapted

NCAR* CONREC package) and a VERSETEC plotter. Selection of the appropriate contour interval and threshold contour resulted after empirical testing. These parameters are a function of the phenomena under study and the map scale. The 10 mm hr^{-1} contour interval was selected as a compromise between balancing fine scale resolution and presenting the total storm rainfall for each 15-min period. Improvements in resolution are possible by filtering portions of the gridded data, but this sacrifices information on total rainfall.

Since surface rainfall is a two-dimensional field, it was handled before the radar data were analyzed. Many lessons learned in processing the rainfall data were carried over into the radar data processing which is discussed in Appendix E.

*National Center for Atmospheric Research.

APPENDIX B

ERROR ANALYSIS OF RAINFALL DATA

Rainfall Data

An implied premise of this research was that significant convective precipitation features cannot be resolved by synoptic scale precipitation measurements. To test this assumption the precipitation gridding program was modified to accumulate four 15-min rainfall data sets into an hourly rainfall data set. The hourly data (accumulated in a clock hour format) were gridded and objectively analyzed by the techniques described in Chapter III for 20 May 1977. Another modification of the gridding program was developed to grid precipitation from synoptic-scale stations (50-km separation) for the state of Oklahoma. In the state-wide analyses, a grid distance of 25 km was selected for a box origin at 37°N latitude and 100°W longitude. The box was interpolated from a polar stereographic map, true at 35°N latitude. The polar projection gave the minimum distortion of the data sites when linearly computed from the reference latitude. Several schemes were investigated to minimize the site location error introduced by map distortion. For example, site locations were computed from maps true at two and five reference latitudes. These techniques produced better fidelity at the edges of the box, but mesh problems developed at center locations. If the number of grid steps was small (15 east-west, 22 north-south), the error introduced by a central reference latitude was small. Similar problems were encountered in locating sites from the reference longitude due to convergence

of the meridians. In this study it was not critical to know the precise site locations. It was important that all data be projected onto the grid map by the same method. This made the actual position error a negligible factor in the investigation.

The fine-scale mesh used for the Washita watershed data did not involve significant grid distortion due to map projection. This was due to the relatively small extent of the grid.

Fig. A.1 shows a comparison of the Oklahoma and Washita maps. In the synoptic interpolation, data were observed approximately every 50 km, and interpolated onto a 25-km grid. In the Washita interpolation, the data were sampled every 4.8 km and interpolated onto a 4-km grid. In comparison, the radar fields were sampled every 0.5° azimuth at 600-m range gates and interpolated onto a 1-km grid.

All rainfall data for 20 May 1977 were evaluated. Examples of the difference between light and heavy rainfall are shown in Figs. B.1 and B.2. Results of this error analysis show that rainfall rates on the Oklahoma grid are considerably different from those of the Washita grid. The same objective contouring routines were used and the sampling time intervals were the same. These data suggest that a synoptic-scale station spacing does not define adequately convective storm rainfall patterns. If the same grid was used but the sampling times varied, similar difference in the rainfall maps might be observed. Such a study was also made of the variation of the hourly watershed maps and the 15-min watershed maps. Again, significant features in the small-scale analyses were masked by the longer time integration. These findings confirm the idea that studying fine-scale precipitation

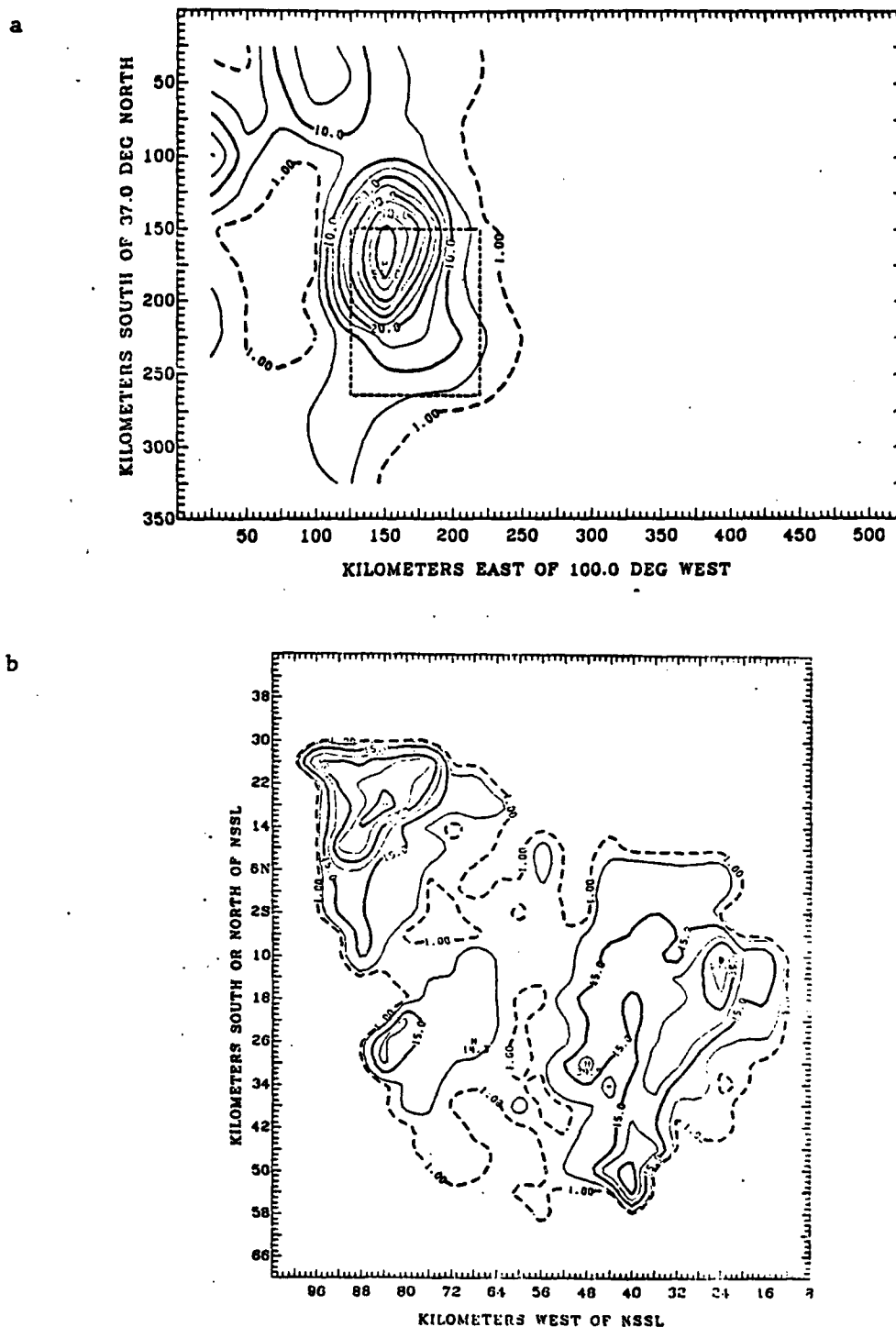


Fig. B.2. Rainfall maps 1700-1800 20 May 1977. (a) Clock hour rainfall rate analysis from synoptic scale data for a portion of Oklahoma. (b) Fine scale rainfall rate analysis for box in Fig. B.2a accumulated from 15-min totals.

F/6 4/2

AFOSR-80-0063

AFOSR-TR-81-0699

NL

3rd 3rd

END
DATE
FILMED
11-81
DTIC

fluctuations requires data sampled on a scale less than the storm scale (25 km) with time intervals less than 1 hour.

Selection of the 15-min time step for this investigation was a compromise. It is possible to read the rainfall weekly strip charts (in analog form) every 5 min. The 5-min resolution was rejected for two reasons. The experiment required a comparison of constant-level radar maps with surface rainfall maps. To produce constant-level radar maps, one must assume a quasi-steady state of the storm for the tilt sequence. If the radar antenna rotates at 1 rpm and we assume a typical scan is 15 tilts, we must assume steady state for 15 min. Some tilt sequences consist of 25 tilts. In practice, the long tile sequences are usually performed in the sector scan mode and even the long sequences last 8-10 min. The second consideration was the number of man-hours required for the hand reduction of the data. A key part of the experiment design was the decision to read the data at least three times. Reading and hand digitizing the data at 5-min intervals would require 130,000 readings rather than the 43,000 actually performed. Since the radar sampling rate required a steady-state assumption for 10 min, it was decided that digitizing the data every 15 min would not significantly affect the accuracy of the qualitative radar-rainfall comparisons. A direct point-by-point comparison of reflectivity and rainfall would require additional precision.

The precision of the digitization process was evaluated in a similar manner. With great patience, the charts can be read to 0.01 in. (0.254 mm), but the time required to achieve this precision was not justified since the objectives of this investigation were to study

variations in high rainfall rates. The charts were read to a precision of 0.508 mm.

Another important concern is the basic accuracy of the measuring instrument, the weighing bucket gage. While the gages can be calibrated in the laboratory to a sensitivity of 0.01 in., they do not operate under ideal conditions in the field. It is assumed field errors are randomized throughout the network.

The effects of turbulence around the gages leads to an underestimate of the total rainfall. Larson and Peck (1974) have reported a deficiency in gage catch of 12% for wind speeds of 5 m s^{-1} and 19% for 10 m s^{-1} . Strong downdraft outflow would probably increase this deficit.

Sampling a highly variable field by point measurements will lead to errors in areal rainfall. Sampling error decreases with increasing area size, increasing time period, increasing gage density, and increasing rainfall amount (Linsley and Kohler, 1951; McGuinness, 1963; Nicks, 1966; Huff, 1971; Woodley *et al.*, 1975). Storm speed may also play a role. Stationary storms may be subject to more bias because they are sampled by fewer gages. Wilson and Brandes (1979) estimate an areal sampling error of less than 5% for regions other than strong downdraft areas.

Quantifying these effects for the data used in this study is difficult. Since we are interested primarily in high rainfall rates, the areal error is minimized. High rainfall, however, is often associated with strong downdraft outflow which maximizes the catch

error at a particular gage. Since the catch error is the worst case error, it is used as the typical worst case. If one extrapolates linearly the catch errors reported above as a function of wind speed, a crude estimate of the underestimation of the rainfall due to downdraft outflow is possible (see Table B.1). These values should

TABLE B.1. Comparison of outflow error as a function of wind speed.

Wind Speed	Gage Error %
5	12
10	20
20	36
30	52

probably be further adjusted with an error band of $\pm 5\%$ due to actual errors. Typical downdraft outflows after gust front passage are 10 m s^{-1} . This leads to a conclusion that the gage data used in this study underestimate the total rainfall.

The effect of gridding and objectively analyzing the data is another source of error. Since these operations are basically smoothing processes, extremely high point rates will be reduced. Since these rates are probably underestimates at the station, minimal smoothing is desired. The approach used in this analysis attempts to preserve the high-rate cores. Once the data were gridded by exponential weighting, the data were bilinearly interpolated back to the gage sites and RMS errors were computed. An iteration process adjusted the weighting function parameters until the difference between the original data and the computed station data was minimized. The selection of

the appropriate weight parameters was a function of total map rainfall. The parameters that minimize the difference field for high rainfall maps were selected.

Error is also introduced in objectively contouring in that the CONREC process bilinearly interpolates a line between four grid points. This error is probably small in comparison to that introduced in selecting the contour interval. All maps are contoured every 10 mm hr^{-1} . This interval is a compromise between high resolution and large area projection. Contours of 5 mm hr^{-1} on page size maps produced unreadable maps. Enlarging the area of interest (which varied from map to map) would require multiple maps. This would introduce distortion errors when comparing the surface rainfall and the radar maps. Contouring every 10 mm hr^{-1} and annotating the peak rainfall amounts for each case provides a good method of preserving the total rainfall pattern while locating the grid point of peak rainfall.

Errors in peak amounts introduced by contouring at 10 mm hr^{-1} intervals can be minimized when the CONREC subroutine fails to identify a peak case. If the data inside a contour are normally distributed, a value 5 mm hr^{-1} above the highest contour line will minimize the peak grid error.

In summary, the area relationships presented by the objectively analyzed precipitation maps are reasonable good estimates of the precipitation fluctuations. The area relations of the high rainfall cases are more reliable than area relations of light rainfall areas. The maximum values presented on the maps are probably underestimates of the total precipitation because of catch errors and areal sampling

errors. These errors are acceptable because the subsequent analysis will involve comparison of changes in the precipitation areas with maximum rates and radar maps. Conclusions about changes in the rainfall areas or the areas themselves will not be significantly affected if the errors described are randomly distributed.

APPENDIX C

THEORETICAL CONSIDERATIONS

Reflectivity Calculations

The Probert-Jones form of the radar equation is used in this investigation. Probert-Jones assumed no significant attenuation of the microwave energy from the radar to the targets and that the scatterers (precipitation-size drops) completely filled the beam volume. He also assumed Rayleigh type scattering, which requires the scatterers to be spherical drops with diameters less than 0.07λ , where λ is the wavelength of the radar energy. Under these conditions one can write the basic form of the radar equation such that the average back-scattered power, \bar{P}_r (watts), is inversely proportional to the distance of the targets from the radar, r (km), and is directly related to the radar constant, C ($\text{w km}^2 \text{ m}^3 \text{ mm}^{-6}$), the dielectric constant, K (dimensionless), of the scatterers, and the effective radar reflectivity Z_e ($\text{mm}^6 \text{ m}^{-3}$). Eq. (C.1) summarizes these ideas:

$$\bar{P}_r = \frac{C|K|^2}{r^2} Z_e \quad . \quad (C.1)$$

The value of C is

$$C = \frac{\pi^3 P_t G^2 h\phi\theta}{512 \lambda^2 (2 \ln 2)} \quad ,$$

where P_t is the transmitted power (watts), G is the antenna gain

(dimensionless), h is the pulse length in space of the transmitted pulse (cm), θ is the horizontal beamwidth (radians), and ϕ is the vertical beam width (radians). The factor $2 \ln 2$ is required to approximate a Gaussian power density across the beam width. In practice Z_e is solved for in (C.1) after some of the restrictions have been relaxed. Eq. (C.2) from Doviak and Sirmans (1973) is the computational form used to calculate the effective reflectivity for the radar used in this study,

$$Z_e = \frac{8.2 \times 10^{18} \lambda^2 r^2 P_r L_c L_a L_r}{G \theta^2 \tau P_t} \quad (C.2)$$

The only new radar quantity is τ (μ s), the pulse width, which is $= h/c$, pulse length divided by the speed of propagation, 2.998×10^{10} cm s⁻¹. The values L_c , L_a , and L_r are loss factors (dimensionless) for the radome, the transmission path, and atmospheric gaseous absorption. Typical values are

$$L_c = 2\text{dB (two way) (Curtis and Vaccaro, 1961).}$$

$$L_r = 4.3 \text{ dB (wave guide and receiver loss for NSSL 10-cm Norman radar).}$$

$$L_a = < 1\text{dB within 100 km (Blake, 1970) for two-way loss.}$$

If one expresses Z_e as dBZ and return power in dBm, where

$$Z_e \text{ (dBZ)} = 10 \log_{10} Z_e \frac{(\text{mm}^6 \text{ m}^{-3})}{1 \text{ mm}^6 \text{ m}^{-3}},$$

$$P_r \text{ (dBm)} = 10 \log_{10} \frac{P_r \text{ (watts)}}{10^{-3} \text{ watts}},$$

one can write

$$\begin{aligned} Z_e \text{ (dBZ)} &= 15.91 + 2 \log \lambda \text{ (cm)} + 2 \log r \text{ (km)} + \frac{P_r \text{ (dBm)}}{10} \\ &\quad - 2 \log G - 2 \log \theta \text{ (rad)} - \log \tau \text{ (}\mu\text{s)} \\ &\quad - \log P_t \text{ (watts)} + .63 + \frac{L_a}{10}. \end{aligned} \quad (\text{C.3})$$

Defining the following parameters leads to an additional simplification:

$$\lambda = 10.52 \text{ cm (measured)}$$

$$G = 4.8 \times 10^4 \text{ (theoretical)}$$

$$\theta = 1.4 \times 10^{-2} \text{ radians (measured)}$$

where

$$\begin{aligned} Z_e \text{ (dBZ)} &= 9.967 + 2 \log r \text{ (Km)} + \frac{P_r \text{ (dBm)}}{10} \\ &\quad - \log P_t \text{ (watts)} + \frac{L_a}{10}. \end{aligned} \quad (\text{C.4})$$

To this point the theory is quite general and could be applied to any meteorological radar, Doppler or non-Doppler, by changing to the appropriate constants.

Doppler Radar

Single-Doppler radar measures the net radial velocity (toward or

away from the radar) of scatterers within the sampled volume. The sampled volume, as with the reflectivity, is defined by the beam characteristics and a discrete gate spacing along the radar beam. It is assumed that the main lobe dimensions are constant so the measurement is valid at the center of the volume. In practice, variations throughout the volume are not considered. Since the pulse repetition frequency (PRF) is the rate of pulse transmission, it can be shown that the maximum Doppler shift frequency detectable is

$$f_{\max} = \frac{\text{PRF}}{2} \quad , \quad (\text{C.5})$$

or in terms of radial velocity (Doppler velocity)

$$f = \frac{2V}{\lambda} \quad . \quad (\text{C.6})$$

The maximum unambiguous Doppler velocity can be written as

$$V_{\max} = \text{PRF} \frac{(\lambda)}{4} \quad . \quad (\text{C.7})$$

A similar constraint applies to maximum unambiguous range (r_{\max}) which is defined as

$$r_{\max} = \frac{c}{2 (\text{PRF})} \quad \text{where } c \text{ is the speed of light.} \quad (\text{C.8})$$

Combining (C.7) and (C.8) gives an equation which highlights the dilemma of a fixed-PRF Doppler radar, i.e.,

$$V_{\max} r_{\max} = \frac{\lambda c}{8} \quad . \quad (\text{C.9})$$

With the NSSL Norman system in 1977 the unambiguous radial velocity was set at 34 m s^{-1} , thereby implying an unambiguous range of 115 km.

Data can be sensed beyond 115 km by operating in the expanded mode and comparing signal to noise ratios (see Ray et al., 1977). If a severe storm beyond 115 km (in the second trip), is aligned with a less severe storm within 115 km, the closer storm would be "blanked out" and the Doppler velocities of the farther one measured. While this is a potentially serious problem, it was not encountered in this investigation. The solution, adjusting the PRF, has been made since the 1977 Spring Program (Brown, 1980).

A discussion of the mechanics of producing the Doppler moments for each gate is beyond the scope of this study. Battan (1973) summarizes many of the techniques that have been used, such as the autocorrelation techniques or using fast Fourier transform algorithms. Electronic spectrum analyses have also been used. The NSSL system uses an autocovariance processor known as a "pulse pair" processor which is a blend of statistical theory, and technological advances involving integrated digital circuits. In this investigation, we are given a pair of power spectral density functions for each gate which are converted into reflectivity and radial velocity. The reflectivity sample (PRF = 325 Hz) is electronically compared with the velocity sample (PRF = 1300 Hz) at each gate to position the velocity data in the correct trip. The variance of velocity spectrum is directly related to the velocity spectrum width.

Storm Motion, Relative Flow, and Doppler Wind Velocity

Accurate measurements of true wind flow within a storm are not possible with single-Doppler radar data. Fairly reliable estimates of

the flow are possible if one assembles pieces of environmental and single-Doppler data in a cautious manner. Since many of the dominant features of thunderstorm flow (anvils, bounded weak echo regions, precipitation downdrafts) are evident from the reflectivity patterns, the single-Doppler radial velocity measurements are needed only to supplement information about the flow patterns. If typical flow patterns are known from multi-Doppler models, or numerical simulations, one can often estimate how they will look when viewed by a single-Doppler radar under a variety of radar beam-intrastorm flow (beam-flow) configurations. Unfortunately, this process does not work in reverse, so the patterns observed with single-Doppler radars do not give unique three-dimensional flow fields. Supplementing single-Doppler information and knowledge of storm models with information on storm motion, radar location, and low- and upper-level environmental flow information enables one to make reasonable estimates of the intrastorm flow fields (see Donaldson, 1970; and Lemon *et al.*, 1978).

There is only one condition where single-Doppler data provides no information about the relative wind and that occurs when all the relative wind is composed of flow perpendicular to the radar beam. Under all other conditions, which are more the rule, some information about true flow is available in the single-Doppler data. Fig. C.1 illustrates these ideas where a single-Doppler radial velocity field is shown for pure west-east flow. Only at radar azimuths 0° and 180° will the single-Doppler detect no wind. This figure also shows another problem with single-Doppler data. Even though the flow (relative wind) does not change, it appears to change with viewing

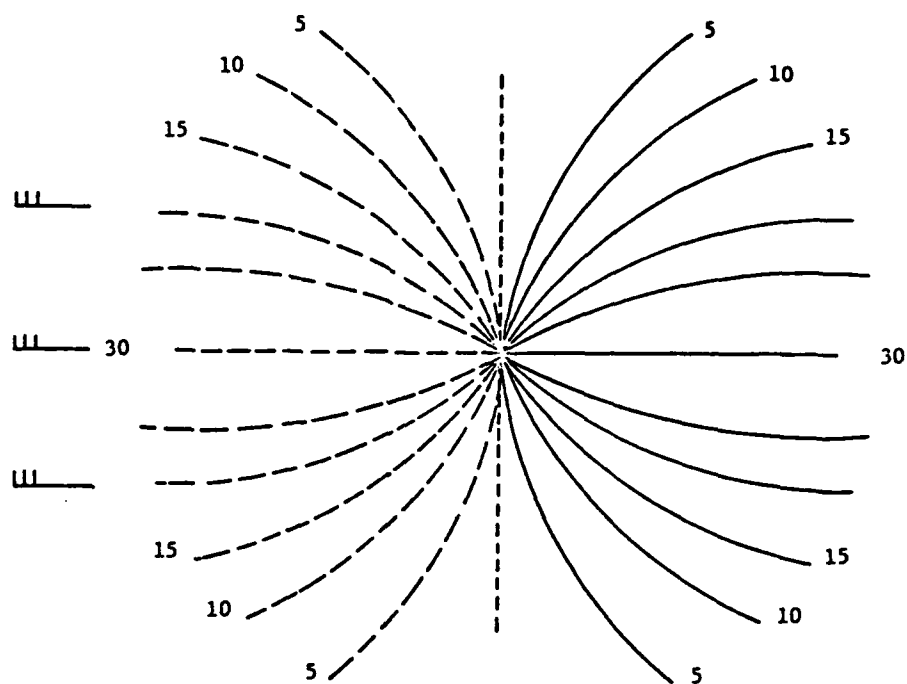


Fig. C.1. Radial velocity isopleths for a single-Doppler radar viewing a west-to-east flow. Dashed lines show flow toward the radar; solid lines are flow away. Radar at center of figure.

angle because only radial relative wind is sensed. This confounds the researcher for he is never certain if changes in the radial velocity are the result of spatial or temporal changes in the kinematic flow field or simply due to different viewing angles.

Vortex Recognition by Single-Doppler Radar

The dilemma mentioned in the preceeding section can be approached in a heuristic manner if the phenomena of interest have relatively small spatial dimensions, such as mesocyclones. While Atlas (1963) and Lhermitte (1964) were among the first to suggest vortex recognition as a possible application of Doppler radar, it was Donaldson (1970) who provided the first objective criteria for such detection. Refinements in his techniques were made by Burgess (1976) and Brown and Lemon (1976) for identifying mesocyclones and tornadoes, respectively.

If one views a vortex as illustrated in Fig. C.2, where +y is north and +x is east, the angle between points 1 and 2 measured from the radar is β , and ϵ is the elevation angle. The radial components of velocity are easily computed as follows. At point 1, the radial component of the v vector is given by

$$v_1 \cos \beta/2 = v_{rv_1}, \quad (C.10)$$

where the minus signs show flow toward the radar and the u component is

$$u_1 \sin \beta/2 = v_{ru_1}. \quad (C.11)$$

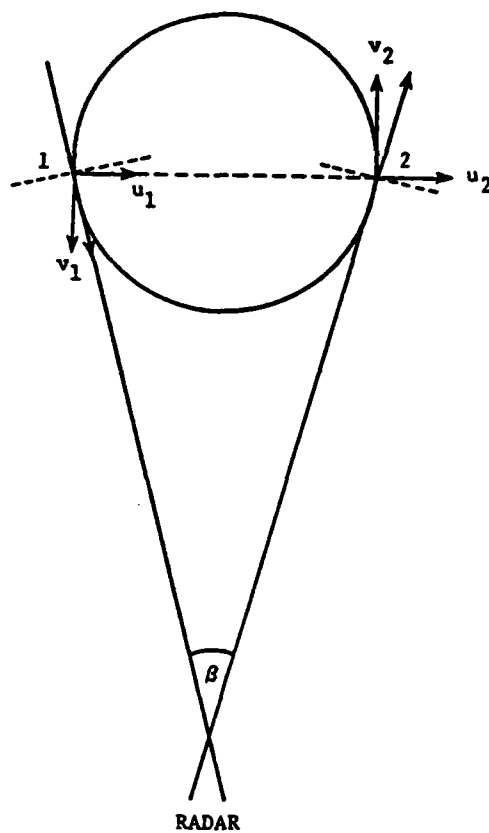


Fig. C.2. Typical horizontal plane view of a mesocyclone.

Similarly at point 2

$$v_2 \cos \beta/2 = v_{rv_2} \quad , \quad (C.12)$$

$$u_2 \sin \beta/2 = v_{ru_2} \quad . \quad (C.13)$$

Combining (C.13) and (C.14) gives the horizontal velocity

$$v_{r1} = v_1 \cos \beta/2 - u_1 \sin \beta/2 \quad \text{at point 1,} \quad (C.14)$$

and

$$v_{r2} = v_2 \cos \beta/2 + u_2 \sin \beta/2 \quad \text{at point 2.} \quad (C.15)$$

A more precise formulation of these component equations that accounts for fall speed of the precipitation tracers is given by (C.16) and (C.17).

$$v_{r1} = v_1 \cos \epsilon \cos \beta/2 - u_1 \cos \epsilon \sin \beta/2 + w_1 \sin \epsilon, \quad (C.16)$$

and

$$v_{r2} = v_2 \cos \epsilon \cos \beta/2 + u_2 \cos \epsilon \sin \beta/2 + w_2 \sin \epsilon, \quad (C.17)$$

where w is the net vertical motion of the particles (difference in vertical flow minus the fall speed of the drops). A common assumption in Doppler research is to assume $\cos \epsilon \approx 1$ for elevation angles (ϵ) below 10° .

The separation between points 1 and 2 is given by

$$2r \cos \epsilon \sin \beta/2.$$

If β is small, 20° or less, $\cos \beta/2 \approx 1$, and $2 \sin \beta/2 \approx \beta$; one can easily compute the shear of the radial components across the vortex.

Donaldson calls this tangential shear and it can be calculated by

$$\text{tangential shear} = \frac{v_2 - v_1}{r\beta} + \frac{u_1 + u_2}{2r} + \frac{w_2 - w_1}{r} \tan \epsilon. \quad (\text{C.18})$$

One can also express the vertical component of vorticity (horizontal plane vorticity) for the vortex in Fig. C.2 as

$$\zeta = \frac{\partial v}{\partial x} - \frac{\partial u}{\partial y}. \quad (\text{C.19})$$

The fact that the first terms on the right of (C.18) and (C.19) are essentially the same (neglecting cord curvature) provides a basis for Donaldson's argument for using single-Doppler radar to identify localized areas of intense vorticity. Since both (C.18) and (C.19) contain additional terms, it is not immediately obvious why the tangential shear should be a good approximation of vertical component of vorticity. If we restrict our investigation to low angles ($\epsilon < 10^\circ$) the third term in (C.18) is small. If the vortex is symmetrical, the radial components of u_1 and u_2 are equal and of opposite signs. This implies at least a dominance of the first term in (C.18) in estimating tangential shear. The only remaining quantity is the second term of (C.19). Since we cannot measure $\frac{\partial u}{\partial y}$ with a single-Doppler radar, we are forced to rely on ideas of symmetric rotation for small vortices and estimate $\frac{\partial u}{\partial y}$ as approximately the same as $\frac{\partial v}{\partial x}$. In other words, the tangential shear should be about half the

horizontal plane vorticity (ζ) or

$$\zeta = 2 \times (\text{tangential shear}) \quad (\text{C.20})$$

These intuitive ideas have been verified by multiple-Doppler observations of mesocyclones.

Before proceeding, it should be noted that even though strong tangential shear is a sign of solid vortex rotation, this pattern can have other interpretations. Consider Fig. C.3, where tangential shear calculations would give the same results. Donaldson (1970) recognized this dilemma and suggested two additional parameters; persistence of the intrastorm pattern with time and vertical continuity. As the vortex moves across the viewing angle, its pattern will be unchanged if the vortex maintains a steady state. The deformation field however will exhibit a different pattern as the view angle is altered. The longer-lasting the pattern, the more certain is the interpretation that tangential shear represents rotation and not deformation.

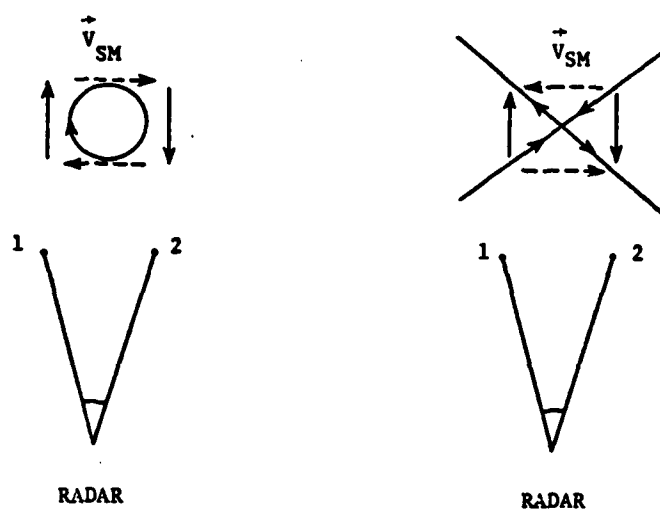


Fig. C.3. Rotation and deformation flow fields as viewed by a single-Doppler radar.

APPENDIX D

SENSITIVITY OF THE STRETCHING-SHEAR MODELS

In Chapter IV it was suggested that radial stretching and cross-beam shear of the radial velocity could be numerically simulated for ideal flow fields of rotation and divergence. Such simulations are a function of the dimensions of the source, its velocity structure, and the range of the modeled flow from the radar. Range effects, which contribute to smoothing the radial stretching calculations, are relatively small effects. This appendix contains sample stretching calculations for one of the idealized sources, pure circular divergence.

One-dimensional stretching calculations are made across the center of the source along the radar radial. The source has a velocity structure that increases as one travels away from the center, reaches a maximum, and then decreases. Several common analytical functions are used to model the velocity profiles. Calculations are made at a range of 50 km from the radar. Table D.1 summarizes these results for a variety of conditions, while Figs. D.1, D.2, and D.3 show the effects of different velocity profiles on the stretching calculations.

Shearing calculations can be computed in a similar manner.

Table D.1. Radial stretching calculations ($\times 10^{-3} \text{ s}^{-1}$) as a function of velocity model, maximum velocity, core size, and distance from the radar.

Linear Model $V=A_1 \cdot R \text{ } R < \text{Core}$ $V=A_2/R \text{ } R > \text{Core}$				
$V_{\text{max}} \text{ } 5 \text{ m s}^{-1}$				
Location Toward/Away From Radar	Core 5 km	10 km	15 km	20 km
R.S. @				
44-39-34-29 km	-0.81	-0.53	-0.43	-0.39
46-41-36-31 km	0.91	0.39	0.20	0.10
50-50-50-50 km	1.00	0.50	0.33	0.25
54-59-64-69 km	1.07	0.58	0.41	0.32
56-61-66-71 km	-0.64	-0.34	-0.22	-0.16
$\Delta \text{ max-min}$ stretching	1.88	1.11	0.84	0.71
Square ₂ Model $V=A_1 \cdot R^2 \text{ } R < \text{Core}$ $V=A_2/R^2 \text{ } R > \text{Core}$				
Location Toward/Away From Radar				
R.S. @				
44-39-34-29 km	-1.30	-0.87	-0.68	-0.59
46-41-36-31 km	1.53	0.80	0.50	0.33
50-50-50-50 km	0.20	0.05	0.02	0.01
54-59-64-69 km	1.66	0.97	0.69	0.54
56-61-66-71 km	-1.16	-0.70	-0.49	-0.37
$\Delta \text{ max-min}$ stretching	2.96	1.84	1.37	1.13
Expon./Square $V=A_1 \cdot \text{EXP}^R \text{ } R < \text{Core}$ $V=A_2/R \text{ } R > \text{Core}$				
Location Toward/Away From Radar				
R.S. @				
44-39-34-29 km	-1.30	-0.87	-0.68	-0.59
46-41-36-31 km	2.12	2.12	2.11	2.10
50-50-50-50 km	0.09	0.00	0.00	0.00
54-59-64-69 km	2.20	2.19	2.19	2.19
56-61-66-71 km	-1.16	-0.70	-0.49	-0.37
$\Delta \text{ max-min}$ stretching	3.50	3.06	2.87	2.78

Table D.1. Continued.

Linear Model				
$V=A_1 \cdot R$ $R < \text{Core}$		$V_{\max} \text{ } 10 \text{ m s}^{-1}$		
$V=A_2/R$ $R > \text{Core}$				
Location Toward/Away From Radar	Core 5 km	10 km	15 km	20 km
R.S. @				
44-39-34-29 km	-1.62	-1.07	-0.86	-0.78
46-41-36-31 km	1.83	0.78	0.41	0.19
50-50-50-50 km	2.00	1.00	0.67	0.50
54-59-64-69 km	2.15	1.15	0.81	0.64
56-61-66-71 km	-1.28	-0.68	-0.45	-0.32
Δ max-min stretching	3.77	2.22	1.68	1.42
Square ₂ Model				
$V=A_1 \cdot R^2$ $R < \text{Core}$				
$V=A_2/R^2$ $R > \text{Core}$				
Location Toward/Away From Radar	Core 5 km	10 km	15 km	20 km
R.S. @				
44-39-34-29 km	-2.61	-1.74	-1.37	-1.18
46-41-36-31 km	3.06	1.60	1.00	0.66
50-50-50-50 km	0.40	0.10	0.04	0.03
54-59-64-69 km	3.32	1.93	1.39	1.08
56-61-66-71 km	-2.33	-1.39	-0.97	-0.74
Δ max-min stretching	5.93	3.68	2.75	2.26
Expon./Square				
$V=A_1 \cdot \text{EXP}^R$ $R < \text{Core}$				
$V=A_2/R$ $R > \text{Core}$				
Location Toward/Away From Radar	Core 5 km	10 km	15 km	20 km
R.S. @				
44-39-34-29 km	-2.61	-1.74	-1.37	-1.18
46-41-36-31 km	4.24	4.23	4.22	4.21
50-50-50-50 km	0.19	0.00	0.00	0.00
54-59-64-69 km	4.39	4.39	4.38	4.38
56-61-66-71 km	-2.33	-1.39	-0.97	-0.74
Δ max-min stretching	7.00	6.13	5.75	5.58

Table D.1. Continued.

Linear Model				
$V=A_1 \cdot R$ R<Core		$V_{\max} \ 20 \text{ m s}^{-1}$		
$V=A_2/R$ R>Core				
Location Toward/Away From Radar	Core 5 km	10 km	15 km	20 km
R.S. @				
44-39-34-29 km	-3.23	-2.13	-1.73	-1.57
46-41-46-31 km	3.65	1.56	0.81	0.39
50-50-50-50 km	4.00	2.00	1.33	1.00
54-59-64-69 km	4.30	2.31	1.63	1.28
56-61-66-71 km	-2.56	-1.37	-0.89	-0.64
$\Delta \text{ max-min}$ stretching	7.53	4.44	3.35	2.84
Square Model				
$V=A_1 \cdot R^2$ R<Core				
$V=A_2/R^2$ R>Core				
Location Toward/Away From Radar	Core 5 km	10 km	15 km	20 km
R.S. @				
44-39-34-29 km	-5.21	-3.48	-2.73	-2.36
46-41-36-31 km	6.12	3.21	2.01	1.32
50-50-50-50 km	0.80	0.20	0.09	0.05
54-59-64-69 km	6.64	3.87	2.76	2.16
56-61-66-71 km	-4.65	-2.78	-1.95	-1.48
$\Delta \text{ max-min}$ stretching	11.85	7.35	5.49	4.52
Expon./Square				
$V=A_1 \cdot \text{EXP}^R$ R<Core				
$V=A_2/R$ R>Core				
Location Toward/Away From Radar	Core 5 km	10 km	15 km	20 km
R.S. @				
44-39-34-29 km	-5.21	-3.48	-2.73	-2.36
46-41-36-31 km	8.49	8.47	8.44	8.41
50-50-50-50 km	0.37	0.00	0.00	0.00
54-59-64-69 km	8.78	8.77	8.76	8.75
56-61-66-71 km	-4.65	-2.78	-1.95	-1.48
$\Delta \text{ max-min}$ stretching	14.00	12.25	11.49	11.11

Table D.1. Continued.

Linear Model				
$V=A_1 \cdot R$ R<Core		$V_{\max} \ 40 \text{ m s}^{-1}$		
$V=A_2/R$ R>Core				
Location Toward/Away From Radar	Core 5 km	10 km	15 km	20 km
R.S. @				
44-39-34-29 km	-6.47	-4.27	-3.46	-3.13
46-41-46-31 km	+7.30	3.13	1.63	0.77
50-50-50-50 km	8.00	4.00	2.67	2.00
54-59-64-69 km	8.59	4.30	3.25	2.55
56-61-66-71 km	-5.12	4.43	-1.78	-1.28
Δ max-min stretching	15.06	8.88	6.71	5.68
Square ₂ Model				
$V=A_1 \cdot R^2$ R<Core				
$V=A_2/R^2$ R>Core				
Location Toward/Away From Radar				
R.S. @				
44-39-34-29 km	-10.43	-6.96	-5.46	-4.72
46-41-36-31 km	12.24	6.41	4.01	2.64
50-50-50-50 km	1.60	0.40	0.18	0.10
54-59-64-69 km	13.27	7.75	5.52	4.32
56-61-66-71 km	-9.30	-5.57	-3.90	-2.96
Δ max-min stretching	23.70	14.71	10.99	9.05
Expon./Square				
$V=A_1 \cdot \text{EXP}^R$ R<Core				
$V=A_2/R$ R>Core				
Location Toward/Away From Radar				
R.S. @				
44-39-34-29 km	-10.43	-6.96	-5.46	-4.72
46-41-34-31 km	16.97	16.97	16.89	16.82
50-50-50-50 km	0.74	0.01	0.00	0.00
54-59-64-69 km	17.57	17.54	17.52	17.51
56-61-66-71 km	-9.30	-5.57	-3.90	-2.96
Δ max-min stretching	27.99	24.50	22.99	22.23

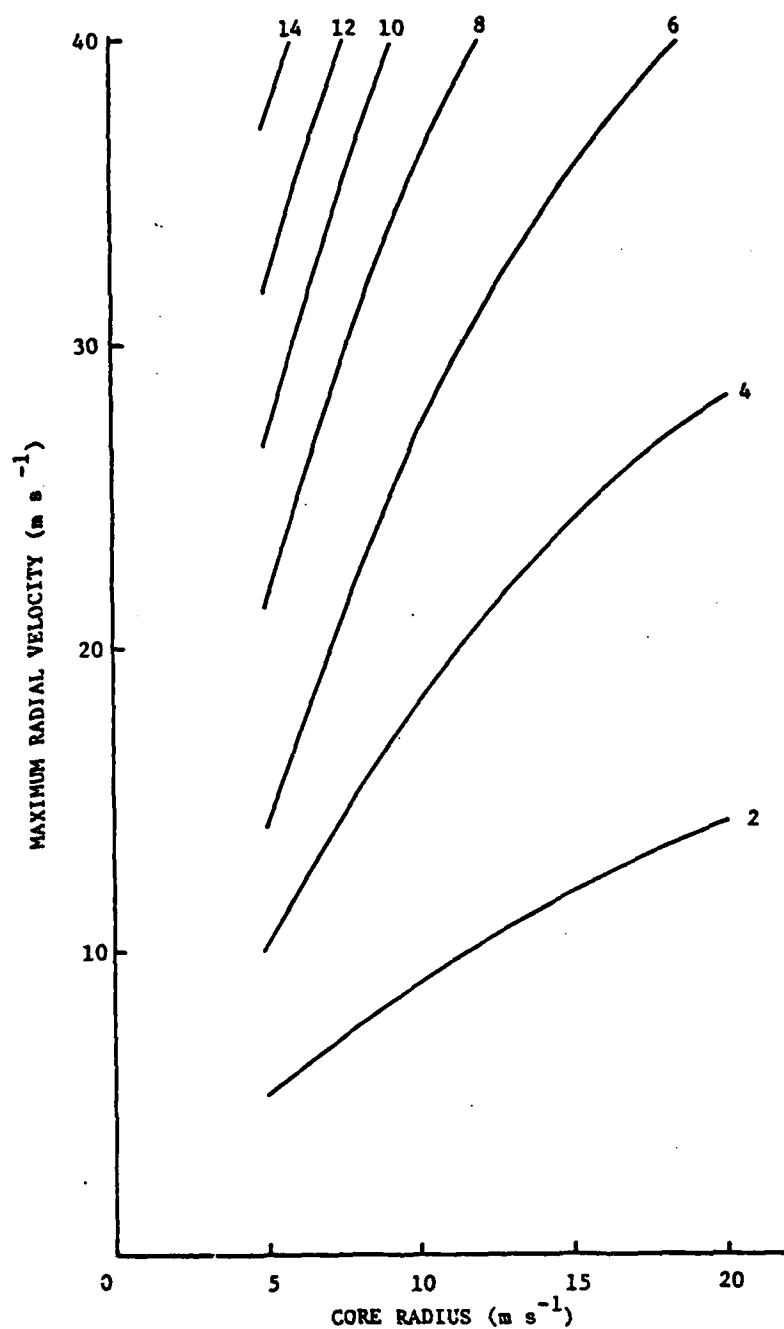


Fig. D.1. Change in maximum-minimum radial stretching ($\times 10^{-3} \text{ s}^{-1}$) (Linear-linear model at 50-km range).

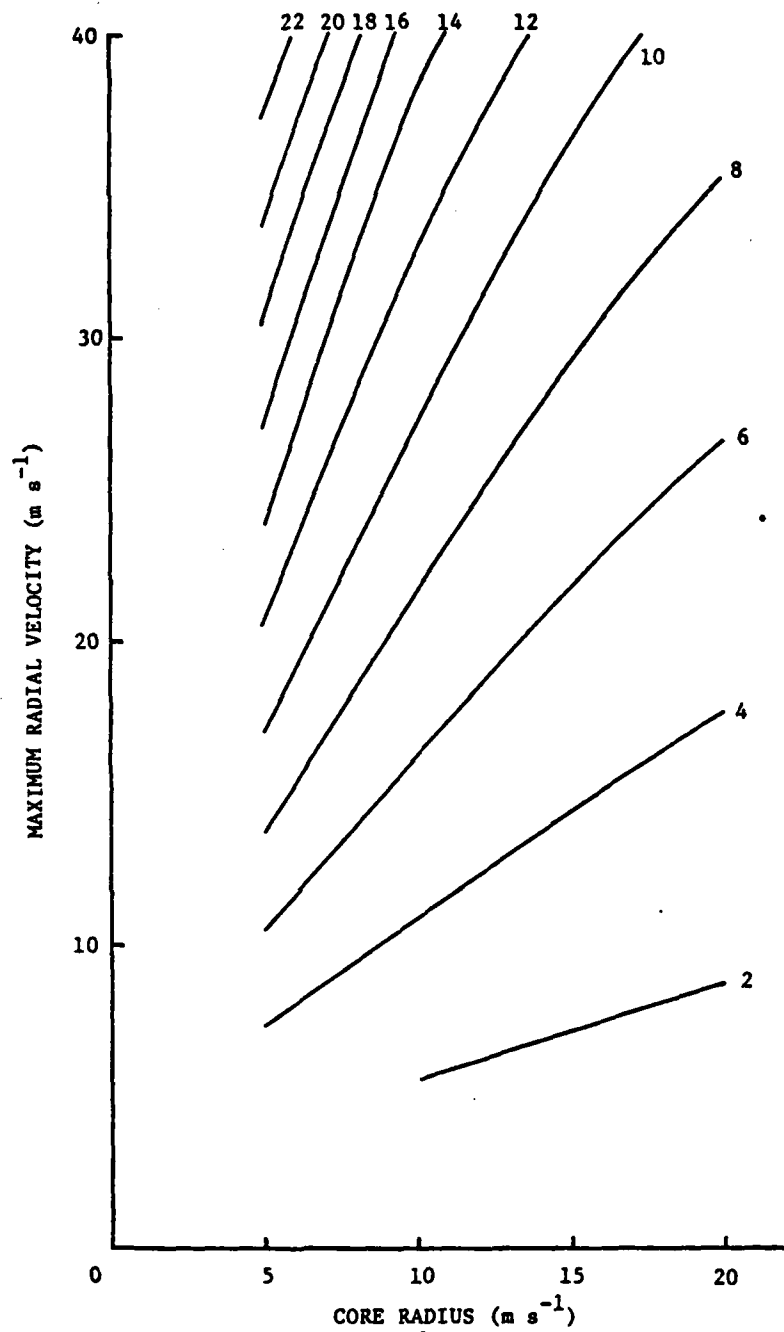


Fig. D.2. Change in maximum-minimum stretching ($\times 10^{-3} \text{ s}^{-1}$) (Square-square model at 50-km range).

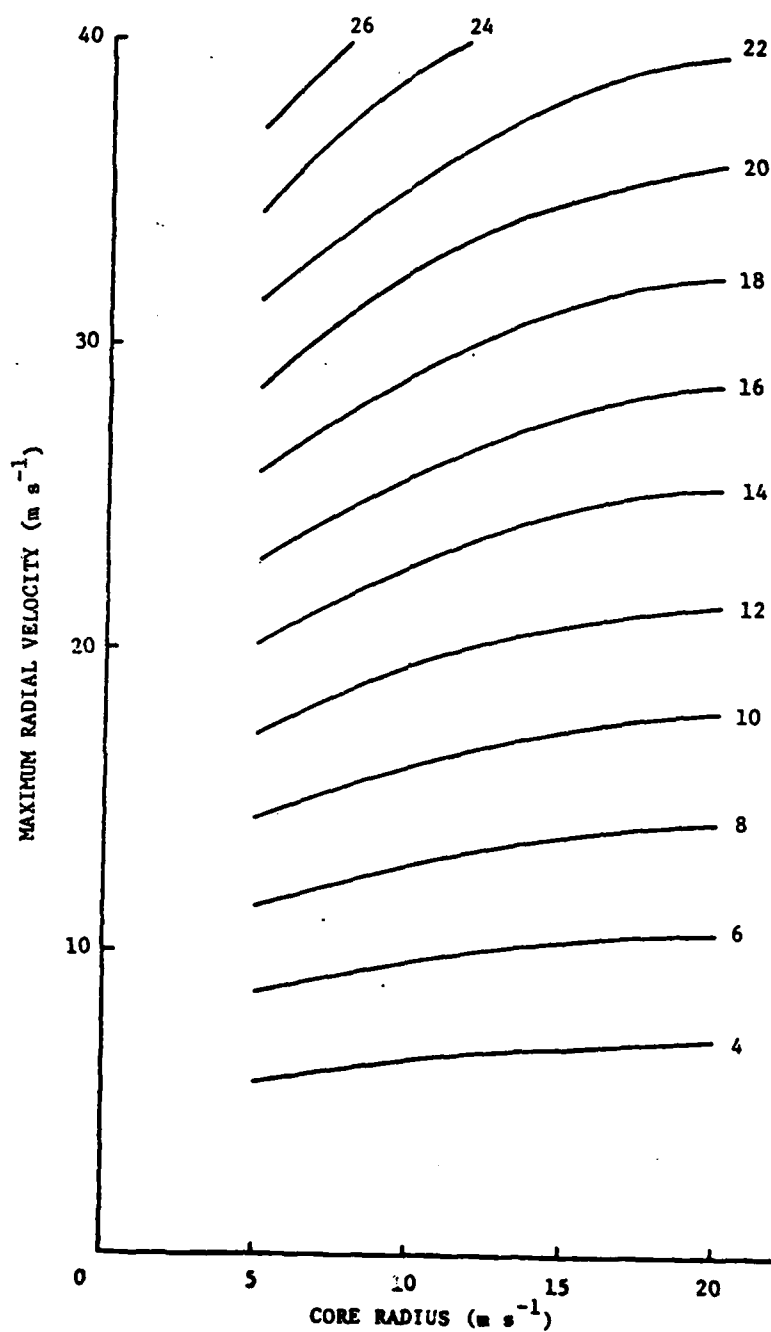


Fig. D.3. Change in maximum-minimum stretching ($\times 10^{-3}$ s⁻¹) (Exponential-square model at 50-km range).

APPENDIX E

RADAR AND MESOSCALE DATA PROCESSING AND METHODOLOGY

Radar Data

Source and Types of Data

The radar data used in this investigation were recorded by the NSSL Norman Doppler radar. The data are part of the data set recorded during the JDOP experiment in 1977. The radar is a modified FPS-18 system that operates at a 10-cm wavelength. The radar characteristics are described in Table E.1. In general, this is a narrow beam radar

TABLE E.1. Norman Doppler radar characteristics (1977). From Bonewitz (1978).

<u>General</u>		
Wavelength (cm)	=	10.52
Peak power (kW)	=	750
Beamwidth (deg)	=	0.81
Pulse length (m)	=	150
Antenna gain (dB)	=	46.8
Antenna rotation rate (deg s ⁻¹)	=	6.0
<u>Reflectivity</u>		
Pulse repetition frequency (Hz)	=	325
Maximum unambiguous range (km)	=	460
Range increment (m)	=	600
Number of data bins per radial	=	762
Intensity resolution	=	1.3
<u>Velocity</u>		
Pulse repetition frequency (Hz)	=	1300
Maximum unambiguous velocity (m s ⁻¹)	=	± 34
Maximum unambiguous range (km)	=	115
Range increment (m)	=	150
Number of data bins per radial	=	762
Velocity resolution (m s ⁻¹)	=	1
Spectral width resolution (m s ⁻¹)	=	0.5

(0.8° beam width) with a dual pulse repetition frequency (PRF). The dual PRF allows intensity data (reflectivity) to be taken during a long pulse repetition period (460-km range) with velocity data interspersed in a short period (115-km range). Velocity estimates are located in space by making comparisons between the reflectivity and velocity samples. This process filters out multiple trip echoes. A complete discussion of this procedure and the system hardware is available in Ray et al. (1977).

Four basic types of Doppler data were sampled in the 1977 program: normal mode (150-m spatial resolution), expanded mode (600-m spatial resolution), high PRF, and high gain. The high-PRF data have a maximum unambiguous range of 43 km and a Nyquist velocity of 91 m s⁻¹. This configuration is designed to detect maximum wind speed. The high-gain data have a dynamic range of only 20 dB and are used to detect clear air turbulence. High-PRF and high-gain data were not used in this investigation.

Each normal and expanded mode datum contains information from three moments of the echo spectrum. The zeroth moment or spectrum power is proportional to the reflectivity factor. The first moment is the mean radial velocity (sometimes called Doppler wind) and the second moment, the spectrum width, is a measure of the variance of the velocity spectrum.

Processing Methodology

Software overview. Processing Doppler radar data is a complex process. The data used in this study were in "raw" form. Raw data

are defined as uncalibrated and unedited data. While NSSL provides calibrated and edited data in "archived" form, the supply of this type of data is limited. Designing computer programs to accept archived data would have accelerated the software development but prevented access to a significant portion of the NSSL data base.

The first step in the reduction process is to unpack the Doppler data, calibrate them, and convert them to nine-track tapes. This is accomplished by the COMBINE program (Knight and Howell, 1980). Since this study is concerned with phenomena over the Washita watershed, only data within 115 km (first trip) are processed. When data from trips beyond the first appear within the 115-km range, these data are flagged and not used in subsequent processing. This procedure accounts for range aliasing of the data. All three moments of the Doppler signal (reflectivity, radial velocity, and spectrum width) are processed by COMBINE. "Bad" data (under the threshold signal-to-noise ratio) are flagged but not filtered at this point. The COMBINE program was not designed to unfold the velocity data or check for errors in azimuth or elevation.

Initial attempts to grid the Doppler fields of reflectivity and radial velocity centered around adapting in-house programs that grid conventional (WSR-57) radar data (see Greene, 1971). These efforts proved to be both rewarding and frustrating. Beaver (1980) highlights the success and problems encountered in this approach. Briefly, smoothing techniques were employed to reduce the data to mean values with 1-km separation along the radials. The data were first interpolated into a cylindrical array, then quadratically interpolated into

a Cartesian array, and finally objectively analyzed and plotted. Considerable effort was spent in writing algorithms to handle variable antenna speeds, clockwise and counterclockwise antenna rotations, and azimuths that contained errors. While this gridding method produced excellent agreement with the reflectivity fields of NSSL WSR-57 data (see Beaver, 1980), the technique was costly and cumbersome.

Conversations with the NSSL staff, especially Rodger Brown, in the spring of 1980 convinced the author of the need to grid Doppler data with a new technique. The basic gridding technique developed for this study consists of weighting the radial Doppler moment values directly onto a three-dimensional Cartesian grid (Brandes, 1976). The details of this process are described in the next section.

Before the Doppler data could be gridded, however, they had to be edited. Incorrect azimuths are, by far, the most common error in the data, occurring about 1% to 2% of the time. These errors are unacceptable because they frequently place data where none exists and the resulting field is erroneously contoured. The editing is done by the FIXIT program (see Fig. E.1). This program makes gross checks for bad azimuth and elevation data and flags the suspect data on a paper printout. The time, azimuth, and elevation values of each radial are written onto disks for later hand editing via a CRT display. Attempts to automate the editing process were unsuccessful. No algorithm could be developed to handle all the errors every time. Hand editing consists of checking the flagged data against a paper printout of all time, azimuth, and elevation data that are produced by the COMBINE program. Errors are usually obvious and correction of data from one

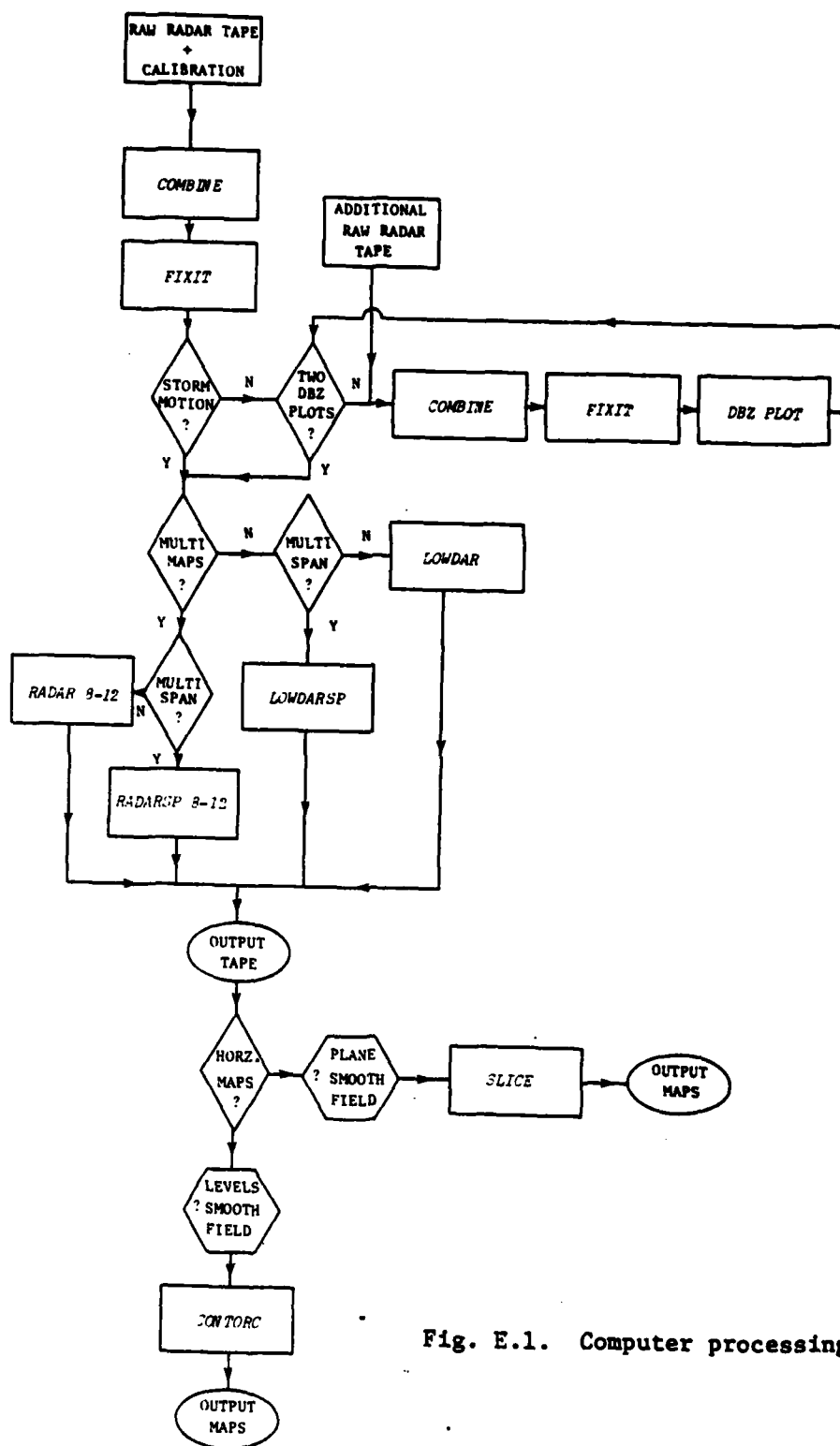


Fig. E.1. Computer processing flow.

raw tape takes about 2 hr.

The next step in the process is to grid the data. As Fig. E.1 shows, information on mean storm motion by layer is required. This motion is calculated by tracking the centroids of high reflectivity cells over a specified time interval. Reflectivity maps from two time intervals for each 1-km height are required. The DBZPLOT program produces these maps. It also provides an additional check for data that were not edited correctly. The DBZ:LOT program grids the data in the same manner as the RADAR 8 (12) (see section on Grid and analyses programs) program but only reflectivity data are gridded. The smoothing and objective contour portions are designed for quick execution.

The details of the RADAR 8 gridding programs are discussed in the next section. The basic idea is to generate a zone of influence for each data point along the radial. Grid points that fall within the zone are weighted by a function of their distance from the actual data sample. After many tests, a spherical zone of influence was selected with a 1-km radius and an exponential weighing function. Ellipsoid influence zones and other weighing functions (r^n and Cressman) all produced similar results.

As Fig. E.1 shows, several versions of the grid program are available, each for specific purposes. If multiple vertical levels are desired, the RADAR 8 (12) programs are used. Concatenating data sets over various tilt sequences that may span two "raw" data tapes requires an "SP" version of the program. If a quick look at one specific level is needed, the LOWDAR series is used.

The objective analysis and contouring are done in a separate

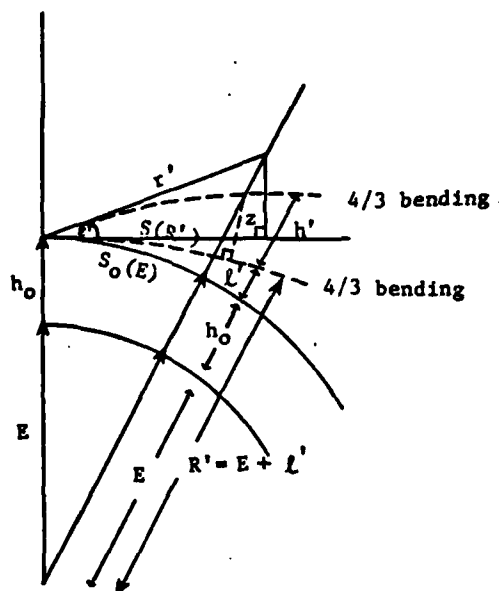
series of programs. The CONREC package interfacing with a VERSATEC plotter was used by the CONTOR and SLICE programs. Maps of the three observed fields of reflectivity, radial velocity, and spectrum width are available in horizontal (or CONTOR programs) or vertical (SLICE programs) cross sections. Computed fields of radial stretching and cross-beam shear are also produced by subroutines in the CONTOR and SLICE programs. Liquid water content can be objectively analyzed and contoured with SLICE subroutines, and vertically integrated liquid water (over varying vertical depths) is an option in the CONTOR programs. Rainfall rates, from Z/R relations, can be easily inserted for the liquid water computations.

The modular nature of program selection highlighted in Fig. E.1 is also reflected within each of the individual programs. For example, in the RADAR 8 program, changes in the zone of influence, the weighing function, or data collection mode are accommodated by changing one card. In addition, the programs are designed to allow for easy adaptation if data from two or more Doppler radars are desired.

Grid and analysis programs. The RADAR 8 and its companion RADAR 12 (for 12 vertical levels) are designed to grid the three Doppler moments of reflectivity, radial velocity, and spectrum width in one step. Instead of presmoothing one moment at a time for all radials, all the data (for each moment) are gridded in one step. This results in better resolution, shorter turnaround times, and reduced cost.

The geometry of the RADAR 8 program is depicted in Figs. E.2a and E.2b. A point on a radial with elevation ϵ' and range r' will be located a distance h_E above the earth's surface where:

a



b

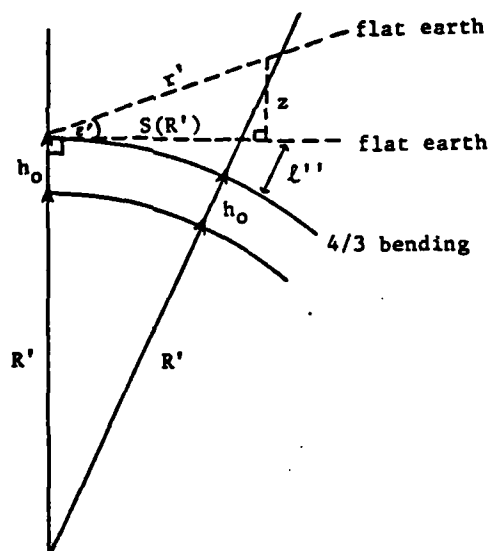


Fig. E.2. Computation geometry. (a) Geometry of ray propagation for the true earth. (b) Propagation over a fictitious earth with $R' = 4/3 E$.

$$h_E \equiv h_0 + \ell' + h' . \quad (E.1)$$

The height of the radar above the earth's surface is defined as h_0 . The height above the h_0 surface resulting from 4/3 beam bending is ℓ' and the height above the $h_0 + \ell'$ surface due to an elevation angle ϵ is h' . If one selects the grid base as that of a ray with elevation angle of 0° under normal atmospheric propagation (ray bending with a curvature of 4/3 the earth's radius), rays propagating with an elevation angle ϵ' will appear as straight lines. Figs. E.2a and E.3b illustrate this propagation over a fictitious earth with radius $R' = 4/3 E$, where E is the real earth radius 6371 km. If we bend the grid base from a 4/3 curvilinear one to one perpendicular to the earth at the radar, i.e., assume a flat earth, additional simplifications are possible. If $S(R')$ is small (100 km) in relation to the earth's fictitious circumference (about 0.2%), then $z \approx h''$ in Fig. E.3b and the height above the R' earth is

$$h_R = h_0 + \ell'' + z . \quad (E.2)$$

The value z can be solved by trigonometry. In a similar manner it can be shown that $S^2(R') = 2\ell''R'$, giving

$$h_R \approx h_0 + \frac{S^2(R')}{2R'} + S(R') \tan \epsilon , \quad (E.3)$$

or

$$h_R \approx h_0 + \frac{(r' \cos \epsilon)^2}{2R'} + r' \sin \epsilon . \quad (E.4)$$

A discussion of the errors involved in this equation, and simplified forms of it, appear in the next section. In general, these errors are minimal.

The radar grid used in this study is a 1 km x 1 km x 1 km grid that is 116 km (north and south), 97 km (east and west) and 8 km (in the vertical). The version with 12 vertical levels was not routinely run because relatively few tilt series had high-level data and only small variations were noted in the higher levels. In addition, considerable computer time was saved by reducing the storage allocation requirement. This significantly reduced the cost per run but more importantly it reduced the turnaround time.

Consideration was given to producing maps in polar projections. Polar maps retain the spatial detail of the data, and the cost is about the same as the rectangular projections. This approach was rejected because it would limit the scope of the software package. With data in rectangular form, modifications to accommodate a multiple Doppler gridding algorithm are straightforward. If data are preserved in cylindrical form, at least half of the data must be interpolated to a common reference coordinate system. In addition, finite difference computations of vorticity divergence and vertical velocity are faster in a rectangular grid because the computations require fewer calculations.

After defining the grid, the next step is placing the spherical Doppler data on the grid points. Considerable time was invested in investigating potential interpolating schemes. Exponential weighing (Barnes, 1973; Brandes, 1977), Cressman weighing (Brown, 1976), and

quadratic interpolation (Sieland, 1977) were compared. Objectively contoured maps showed very little difference between the interpolating schemes for reflectivity values greater than 20 dBZ. The maps presented in this study were gridded with an exponential weighting function with a 1-km spherical radius of influence. The weight value at the maximum radius of influence is 0.37. This weighing function closely approximates a Cressman function with a 2-km influence radius truncated after 1 km from the grid point. Data are interpolated to a common reference time, at 15-min intervals. This required a quasi steady-state assumption during the entire volume scan. Scans that required extrapolation in time of more than 8 min were not used. After all the data are read and weighed to grid points, the values of the three observed Doppler fields are divided by the sum of the weights at each grid point. The procedure is similar to that used with the two-dimensional rainfall data. The gridded fields are then written to tape by vertical levels.

Many investigators have tried to estimate two-dimensional kinematic motions from single-Doppler data (see Chapter I). The Velocity Azimuth Display (VAD) technique (Caton, 1963; Browning and Wexler, 1968) and more sophisticated techniques (Esterbrook, 1975; Waldteufel and Corbin, 1979) have been used with some success for stratiform type precipitation over a wide area. A study by Peace *et al.* (1969) suggested an approach for estimating motions within local storms by single-Doppler radar. As noted in Chapter I, the main hypothesis of this approach is to assume that the kinematic fields within the storm do not change as the storm moves across the radar field of view, so

that a simulated dual-Doppler field can be constructed by a time/space transform. Since one of the goals of this research was to study the change in surface precipitation as the single-Doppler field changes over short time intervals, the technique of Peace et al. was not used because it required a steady-state assumption for two complete scans. In this study two-dimensional kinematic motions are inferred by computing Cartesian fields of radial stretching and cross-beam shear, in the CONTOR and SLICE programs.

This approach does not allow the calculation of vertical motion but it does have some attractive features. It is easy and fast to compute. It does not require a storm motion connection if the finite difference distances are small. It identifies rotation zones in a reliable manner, and it may provide insight into areas of intrastorm convergence by the radial stretching field if the beam-flow configuration is favorable.

If one neglects the vertical contribution of the Doppler velocity by using low angles (see Donaldson, 1970), these calculations can be made on a horizontal plan after the radial velocity data are gridded. Consequently, radial stretching is a horizontal stretching in the radial direction from a vertical axis, not a shear along the ray path. Shear along the ray is often referred to as radial shear (see Donaldson et al., 1972). Cross-beam shear is also calculated on a horizontal plane. These calculations are very simple once the data are interpolated into cylindrical coordinates. Early experiments were conducted to test whether or not the value of these computed fields produced significant kinematic information in cylindrical form. The

success of these experiments convinced the author that, even with the many limitations involved, valuable information about storm kinematic flow could be inferred from the radial stretching and cross-beam shear fields.

Since the RADAR and LOWDAR programs store information in a Cartesian array, a transformation is required to directly compute the radial stretching and cross-beam shear in cylindrical form. Another approach is to define the radial velocity (a scalar number) as a vector with its direction defined in reference to the radar. This new vector is then resolved into components and the radial stretching is computed by calculating the dot product with the del operator, i.e., $R.S. \equiv \vec{\nabla} \cdot \vec{V}_r$. The actual computations are performed by central finite difference methods with one pass through a three-point smoothing function in both the x and y directions. Computations across the cloud boundary are filtered during the contouring. Cross-beam shear (CBS) is calculated with similar logic. The CBS is defined as $CBS \equiv \vec{\nabla} \times \vec{V}_r$. Errors in these calculations are discussed in Appendix F.

The CONTOR and SLICE programs contain options to correct the radial velocity and the fields computed from the values for the computation of storm motion necessary to produce true storm relative radial flow. This correction is crucial in dual-Doppler research. In single-Doppler research, the correction is largely a matter of preference. Correcting for storm motion shifts the origin from radar centered to cloud centered. The reflectivity field is not affected by this correction. The contoured fields of radial stretching and

cross-beam shear are only slightly affected because the trigonometric variation of storm motion across the small grid distances used in the calculation (2 km) is small. This variation is masked by the objective analysis routines. A comparison of maps of radial stretching and cross-beam shear produced with and without storm motion confirms these ideas.

A common practice is to correct all levels of a contoured field with one storm motion value based upon mid-level translation of the reflectivity centroids. Since the movement of the maximum reflectivity core may vary with height and all cells may not move with the maximum core, this correction may introduce additional error (this error is discussed in more detail in Appendix F). In addition, storm motion correction also increases the execution time of the grid program by 1 to 2 min. Consequently, to minimize error, the maps presented in this report do include storm motion.

Liquid water and partial vertically integrated liquid water (1-4 km and 5-8 km) are also computed in subroutines of the SLICE and CONTOR programs, respectively. The equation used is from Greene (1971) for 10-cm radars.

$$\text{Liquid Water} = 3.44 \times 10^{-3} Z^{4/7} \quad (\text{E.5})$$

(gm m⁻³)

where Z is reflectivity in mm⁶ m⁻³. The partial vertical sums are computed by integrating (E.5) over the appropriate intervals. This integration results in values of liquid water in kg m⁻³. The 4-km level was selected to estimate the liquid water content below and

above the melting level. Rawinsonde soundings were used to determine the height of the melting level.

The program description would be incomplete without a few descriptive words of the objective analysis programs. The SLICE program contains two basic options for east-west or north-south vertical cross sections. All fields or selected fields can be contoured from a RADAR 8 (12) output tape. The CONTOR program performs the horizontal analyses. All or part of the data can be analyzed for one or 12 levels. Both programs are modular in form; a typical setup required changing two or three data cards.

The objective analyses are performed by the CONREC subroutine. The actual objective analysis is accomplished by bilinearly interpolating between grid points throughout all or a portion of the grid domain. A variety of options is available for labeling contours, selecting thresholds, and spacing contours. Many tests were run to determine which options presented the significant data in the most understandable format.

Surface and Upper-Air Observations

The surface fields used in this study are derived from the NSSL mesometeorological (27 sites) data network. These data are used primarily to complement the radar and raingage fields. Objectively analyzed maps of streamflow, wind components, temperature, dew point, pressure, divergence, vorticity, mixing ratio, and isotachs were provided by Dr. Kenneth Johnson (NSSL). The map used is a Lambert conformal projection with standard parallels at 34°N and 37°N.

The lower left corner of the grid is 34.9632°N and 98.3950°W . The upper right corner is 35.5066°N and 97.3513°W . The grid increment is 5 km with 17 points in the x direction and 14 points in the y direction. Maps were available every 30 min with excellent data on 1 May (7 maps) and 20 May (11 maps). Data availability on 19 May reduced the number of maps to two at 1400 and 1430 CST.

No additional processing of the objectively analyzed maps was required. The techniques used in the analysis are discussed in Barnes (1973) and Barnes (1978a). A description of the NSSL upper-air network is given by Ray *et al.* (1977). The basic network consists of four stations (Clinton Sherman, Fort Sill, Elmore City and the KTVY Tower at Oklahoma City). These sites surround the study area. All stations were operational on 19 and 20 May. Soundings were taken approximately 90 min apart during the afternoon and evening hours. Equipment problems forced some sites to miss certain launch time, but 12 soundings were available for 19 May and 16 were processed on 20 May. These figures do not include the Oklahoma City synoptic sounding. On 1 May the Oklahoma City sounding provided the only upper-air data available. The 1 May data were acquired in reduced form from the U.S. Air Force Environmental Technical Application Center (USAFETAC). Additional synoptic soundings were analyzed on the days of interest from Longview, Texas, Stephenville, Texas, Little Rock, Arkansas, Monett, Missouri, Amarillo, Texas, and Dodge City, Kansas, to determine synoptic scale forcing of the severe storm environment. The reduction techniques for the NSSL data are described in Barnes *et al.*, 1971. The USAFETAC data were processed by algorithms developed by the

author and the USAFETAC staff.

Additional software was written to compute potential wet-bulb temperature (θ_w). The algorithm used was based on a polynomial approximation (Prosser and Foster, 1966) supplied by Stanley Barnes. A Fortran program was also developed to compute mesoscale divergence by the Bellamay method using the NSSL rawinsonde data as input.

APPENDIX F

ERROR ANALYSIS OF RADAR DATA

General

One basic problem in comparing radar with other meteorological data lies in the sampling process. Radar data are sampled nearly instantaneously by averaging pulses over a volume. Precipitation features smaller than approximately twice the signal averaging time are smoothed by radar averaging. Such precipitation streaks may very well appear over a raingage giving a high gage reading but a low reflectivity factor. This is part of the reason for the high variance in Z-R relations. Correlations between radar rainfall and surface rainfall decrease as the distance to the storm increases. Many microphysical and kinematic factors such as evaporation, advection, and vertical motion (see Wilson, 1976; Brandes and Sirmans, 1976) are significant. Quantifying the radar sampling error is extremely difficult. This error is normally assumed to be random, and assumptions of steady state are employed in comparing surface and radar data. Space-time data transforms usually require the same assumption, but it must always be employed with care.

Another potentially serious problem is side lobe effects. Under a normal scan, most of the returned power comes from the main lobe. In cases of 50 to 70 dBZ echoes, the returns from the side lobes may be significant (see Brown et al., 1980). As the main lobe moves off the echo, the side lobes will make the echo appear taller or wider

than it actually is. This is a problem if the signal-to-noise ratio is set too low. While several cells in this study are greater than 50 dBZ, there are no indications of poorly adjusted signal-to-noise ratios. Some editing procedures attempt to filter the side lobe effects by flagging dBZ values which have wide velocity spectrum widths. While side lobe effects do exhibit wide spectrum widths, Brown et al. (1980) have noted that meteorologically significant phenomena, such as turbulence, also have wide velocity spectrum widths. Since turbulence may be investigated in future studies, high velocity spectrum width data are not filtered out and it is assumed the signal-to-noise setting is high enough to minimize side lobe problems. It is usually assumed the data are free of systematic calibration errors. There is no reason to suspect serious calibration errors for the data used in this study. The Norman Doppler radar is routinely checked for calibration. The 1 May 1977 objectively analyzed Doppler fields were compared with objectively analyzed WSR-57 fields (see Beaver, 1980). While the sampling times were not identical, the maps showed excellent agreement at all levels. Direct comparison of data between the WSR-57 (or the Cimarron Doppler) and the Norman Doppler were not made on 20 May 1977. The 20 May data have been used extensively, and the NSSL staff are not aware of any calibration problems. While the 19 May data have not received as extensive study as the 20 May data, the calibrations for the two dates are similar. Nevertheless, a sensitivity study was made to evaluate the effect of potential calibration errors.

NSSL provided estimates of the true antenna position by daily

leveling checks and periodic sun scan calibrations. Eight measured elevation and nine azimuth checks were available for the 1977 data. These corrections ranged from -0.85° to -0.06° for the elevation and 0.05° to 0.38° for the azimuths. Estimated corrections, based on partial measurements, were slightly higher. Since these are post-analysis corrections, a sensitivity analysis was made to see how these corrections affected the objectively analyzed maps. The goal was to determine if significant map features were sensitive to antenna precision. Typical worst case corrections (0.84° in elevations and 0.38° in azimuth) were applied to reflectivity, radial velocity, radial stretching, and cross-beam shear maps, at 1, 3 and 5 km, for showery and intense rainfall in supercell storms. No significant differences were detected with the corrections. Threshold contours varied but the higher value contours and gradients were unchanged. The relative and absolute positions of the significant map features were also unchanged. This suggests that precise antenna positioning may not be crucial for the detection of many significant storm features with single-Doppler radar.

Other errors can result from ground clutter and radome attenuation. Considerable ground clutter was noted at the 0.1 and 0.2 degree elevation angles, especially close to the radar. These data are filtered during the gridding program and leave a data hole. The amount of missing data is very sensitive to elevation angle. Data sensed at elevation angles above 0.50 are generally free of significant ground clutter. Ground clutter is not a serious problem in this study because the storms are outside the ground clutter pattern.

Radome attenuation consists of two basic parts. The first is the attenuation due to the radome structure (about 2 dB for the Norman Doppler) and the second is due to attenuation by rain on the radome. Wilson (1978) has reported a two-way attenuation of 1 dB for C band (5-cm) radars for rainfall rates greater than 40 mm hr^{-1} . These results are similar to those of Cohen and Smolski (1966), who reported a 2 to 3 dB loss at rates of 40 mm hr^{-1} . Other investigators such as Hudlow et al. (1976) have estimated rainfall attenuation of 5 dB for 50 mm hr^{-1} rainfall rates. In any event, the rainfall attenuation of S band (10-cm) radars will be significantly less and radome rainfall attenuation is not considered to be a serious error.

It is usual to assume no significant losses due to scattering or absorption between the radar and target. Hitschfeld et al. (1954) have shown this is not a significant problem for 10-cm radars such as the Norman Doppler. In any event, a two-way attenuation loss due to atmospheric effects is computed from empirical relations suggested by Blake (1970). The error in this correction is less than 0.2 dB

A potentially serious problem results from the implicit assumption that the beam is filled with precipitation-size scatterers. This problem increases as the sampling range increases. These errors tend to mask fine-scale details. This phenomenon may explain some of the vertical inconsistency in the radial velocity maps in the vicinity of mesocyclones.

Thunderstorm ducting of the radar beam is another potential problem. This is caused by the spread of relatively cool air from the base of the storm and the consequent effects on low elevation scans.

These pools of cool air can affect beam propagation even after the source has moved a considerable distance. Wilk and Kessler (1970) have reported a decrease in intensity of 6 dB of echoes which move across anomalous propagation areas. These cool air zones are eventually dissipated by turbulent eddies. A scan of the NSSL upper-air data suggested several potential soundings that may have significant anomalous propagation in the lower layers. Detailed calculations of the refractive modulus gradients (Battan, 1973) revealed only minor superrefractive conditions. While large storms may have considerable effects on the environment many kilometers from the storm, it is difficult to extrapolate the effects of anomalous propagation at a sounding site a large distance from the storm to the near-storm area. In this study, no scheme was used to objectively filter anomalous propagation affects.

Effective Reflectivity Factor (dBZ)

As in most radar studies, it is assumed that the power returned comes from a filled volume of Rayleigh scatterers. This assumption breaks down when the scatterers are not spherical liquid-water drops and the drop diameters exceed 0.07 times the radar wavelength. Battan (1973) notes that when this assumption is valid, errors of 1.5 dB can be expected. Severe storms will contain large water drops and hail, both of which invalidate the Rayleight assumption. The fact that hail, in various forms, has a different complex refractive index than water complicates the resolution process. These factors pose problems when attempting to correlate high rainfall rates with radar

reflectivity. No attempt was made to filter ice, hail, or large drop data from the data base. The radar constant was not adjusted to compensate for ice in the upper levels.

Another important consideration, especially in objective analysis schemes, is the reflectivity resolution. The Norman Doppler can resolve reflectivity to within 1.3 dB. This resolution problem alone implies a significant variability in radar-derived rainfall rate.

Vertically Integrated Liquid Water (VIL)

In this study, VIL is integrated from 1 km to 4 km, inclusive, and then from 5 km to 8 km. Rawinsonde soundings showed the melting level to be between 4 and 5 km. The lower level VIL probably contains mostly liquid water while the upper level VIL is likely contaminated by ice and, on occasion, hail.

The VIL maps are computed from the reflectivity factor by integrating (F.5). The reflectivity factor resolution (1.3 dB) can be used to estimate the sensitivity of the VIL calculations. For a reflectivity factor of 40 dBZ in the lower level, VIL will be approximately $2.66 \pm 0.46 \text{ kg m}^{-2}$. This implies an error of $\pm 18\%$ due solely to the radar resolution. The error is only slightly sensitive to changes in the measured reflectivity.

Several vertical averaging schemes were investigated for the liquid water computation. The approach selected implies that the level values at each 1 km are average values of liquid water 0.5 km above and below the standard km levels.

As mentioned above, hail contamination is always a problem in

such measurements. Showalter (1969) has suggested a method for estimating liquid precipitation rate as a function of the draft speed, the terminal velocity of the drops, and the liquid water content. In strong downdrafts, the drops probably travel close to the median terminal velocity. Gunn and Kinser (1949) have shown this to be 6-8 m s^{-1} . Wilson and Fujita (1979) have measured net fall speeds with a vertically pointing Doppler and found maximum values of -35 m s^{-1} in intense sections of downdrafts with -20 m s^{-1} observed routinely. Using the maximum surface rainfall rate observed in this study (175 mm hr^{-1}) and the maximum terminal and draft velocities provides a crude estimate of the highest liquid water content that one might expect in the absence of hail. Such calculations show that as the net downdraft velocity decreases, the amount of liquid water required for a certain rainfall rate increases. If one assumes a net draft speed of -35 m s^{-1} , only 5.5 kg m^{-2} are required, while over 9.6 kg m^{-2} are needed if the -20 m s^{-1} speed is encountered. This assumes a rainfall rate of 175 mm hr^{-1} through 4 km, which is probably unlikely. However, decreasing the rainfall rate also decreases the amount of liquid water required to produce it. For these reasons, the author believes that integrated liquid water values above 12 to 15 kg m^{-2} are unreliable in the sense that hail is contaminating the measurement. Since the complex index of refraction for hail in the radar equation is roughly one-fifth that of water, the peak liquid water values do not represent the total hail content, and they should be scaled down considerably to reflect real conditions. It is difficult to estimate how much hail there is in a particular cloud during a particular time. This implies

that reflectivity values greater than 55 dBZ are probably hail contaminated and liquid water estimates derived from them are unreliable. Using changes in the size of a lower integrated liquid water area (5 or 10 kg m⁻²) will give a better reflection of changes in the liquid water loading.

Radial Velocity

Many of the problems inherent in sampling reflectivity produce similar errors in the radial velocity measurements. The mean radial velocity for each gate (600 m or 150 m in length) is composed of 56 samples. The mean values are computed by a Pulse Pair Processor, operating with a signal-to-noise ratio of at least 10 dB. The standard deviations of the means sampled in this manner are between 0.5 and 1 m s⁻¹. In 1977 the Norman Doppler was configured for maximum unambiguous velocity measurements of ± 34.24 m s⁻¹ (specified by a 1300 Hz PRF). This implies a maximum unambiguous range of 115 km.

Some of the radial velocity data available for this study were available with 150-m range increments (normal mode). To save cost, every fourth point was selected for gridding. This procedure simulated an expanded mode (600 m) sampling. Processing normal mode data as expanded mode gives better resolution than true expanded mode data because the antenna revolution is reduced. This increases the number of radials sampled per sector. Every azimuth is used in the gridding regardless of the sampling mode. Processing all normal mode data significantly increases the run time for the gridding programs.

Sample griddings showed that processing every fourth range gate and every azimuth nearly doubled the run time over similar data recording in the expanded mode. No significant differences were noted in objectively analyzed maps that used all the normal mode data when compared with those that simulated expanded mode calculations. In this study, the errors introduced by filtering the normal mode data are not significant.

Much of the radial velocity had to be unfolded, especially in regions of intense rotation. The unfolding process used in this study (Beaver, 1980) compares the mean radial velocities at successive gates. If the difference is greater than $\pm 34 \text{ m s}^{-1}$ the data are unfolded by adding the value for gate "n" to -68 or +68. The sign of the doubled unambiguous velocity is determined by the sign of the "n - 1" gate. This process is shown in Fig. F.1. No check is made for double folding, which implies that true radial speeds $> 68 \text{ m s}^{-1}$ do not exist in the data. This is a potential source of error. While double folding is rare, one radial in the 1708-1713 20 May scan appears to contain some double folded data. These data are located near the center of an intense mesocyclone, with a reported tornado.

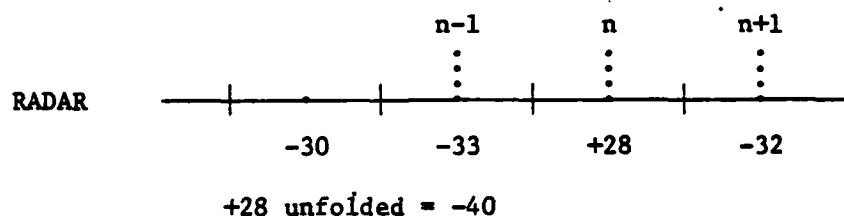


Fig. F.1. Typical unfolding.

While 70 m s^{-1} velocities are possible with tornadic rotations, it is doubtful if such intense rotations would maintain sufficient precipitation scatterers in the volume to routinely detect double folding when it occurred. However, this is a potential error source. Since this problem would be encountered only in extreme conditions it was decided that it would not be cost effective to check every data bin (or even every folded data bin) for this type of error. In addition, the gridding procedures were not designed to resolve tornadic circulations.

Additional comments should be made concerning the assumption that the radial plane velocity is composed of only horizontal motion. While it is common practice in Doppler research to assume that vertical drafts do not contribute to the horizontal motion if the elevation angles are small, this assumption may not be valid. If we encounter a downdraft of -35 m s^{-1} with a 10° elevation angle, about -6 m s^{-1} will be projected onto radial direction due solely to downdraft. If the elevation angle doubles, the downdraft radial component also doubles. In this study we are generally concerned with heights to 8 km beyond an 8-km range from the radar. This implies a worst case angle of 45° . Significant vertical draft contamination of the horizontal field could occur in this situation. In general, elevation angles were below 10° , the significant storms were well beyond the 8-km range, and the draft speeds were probably less than 35 m s^{-1} . Nonetheless, this effect may play an important role in certain situations. It is assumed that any draft influence will be spread over several grid points in a nearly uniform fashion thereby making the radial stretching and cross-beam

shear fields reasonably unbiased. In some instances, however, this effect will confound interpretation by superpositioning a vertical projection onto the horizontal flow. It must be kept in mind.

Spectral Width

These data measure the variance about the mean radial velocity value for each gate. The Norman Doppler Pulse Pair Processor estimate of spectral width is biased for weak signals and for extremely narrow or wide spectra. The worst bias reduces the accuracy by 2 to 3 m s^{-1} . Spectral width resolution is 0.5 m s^{-1} .

A serious problem with the spectral width data lies in interpreting the scale it represents. Several investigations, such as Kraus (1973) and Zrnic and Doviak (1975), demonstrated the use of spectral width as a turbulence indicator in the vicinity of tornadoes. In less intense phenomena, such as weak downdraft outflow, it is questionable whether or not spectral width data reflect the turbulence due to the downdraft or smaller-scale eddies not resolvable by the gridding. The objective analysis and plotting schemes used in this study should filter most small-scale eddies. Problems will still arise when the variance is composed of contributions from several length scales. This study did not attempt to resolve these contributions. After many tests, it was decided to abandon spectrum width data as a tracer for changes in kinematic flow.

Radial Stretching and Cross-Beam Shear

The principal error in these fields resides in error of the

radial velocity measurement. These fields are computed by taking the two-dimensional dot product of the del operator and the radial velocity for the radial stretching and the two-dimensional cross product of the del operator and the radial velocity for the cross-beam shear, i.e.,

$$RS \equiv \vec{\nabla}_2 \cdot \vec{V}_r$$

$$\vec{CBS} \equiv \vec{\nabla}_2 \times \vec{V}_r$$

If one assumes that the total variance of radial stretching (or cross-beam shear) is composed of two equal parts in the x and y directions ($\sigma_{RSx}^2 = \sigma_{RSy}^2$), and the components of the variance are uncorrelated, the total variance, neglecting smaller terms, can be written as

$$\sigma_{RS}^2 = 4 \left(\frac{\sigma_u}{\Delta x} \right)^2$$

and the percent error is simply

$$\% \text{ error} = \frac{\sigma_{RS}}{RS} \times 100$$

If $\sigma_u = \sigma_v = 0.75 \text{ m s}^{-1}$ and $\Delta x = 2000 \text{ m}$ yields a standard deviation in the radial stretching of about $7.5 \times 10^{-4} \text{ s}^{-1}$. Selecting a minimum control level of $2 \times 10^{-3} \text{ s}^{-1}$ results in a percentage error on the order of 38%. Since the standard deviation of the Doppler velocity is not constant in ranging from 0.5 to 1 m s^{-1} , the standard deviation of the radial stretching will vary from $5 \times 10^{-4} \text{ s}^{-1}$ to $1 \times 10^{-3} \text{ s}^{-1}$.

With the same minimum control level, the percentage error in the radial stretching varies from 25% to 50%. This analysis shows that resolution of radial stretching (and cross-beam shear) is possible from single-Doppler data if the computations are performed over an appropriate scale and the contouring is done with care. If the other parameters are constant, selecting a minimum contour level smaller than $2 \times 10^{-3} \text{ s}^{-1}$ will certainly add detail to the analysis. However, this detail will often be due to noise, and statistical confidence in the results will be low. In this study conclusions are based only upon contour patterns of at least $2 \times 10^{-3} \text{ s}^{-1}$. Such a threshold value is compatible with those found by Strauch and Merrin (1976), Donaldson et al. (1972), and K. W. Johnson et al. (1980).

These values may appear large to readers familiar with synoptic-scale divergence and vorticity. While radial stretching and cross-beam shear are not divergence and vorticity, the values of storm-scale divergence and vorticity are comparable to results found in this study (see Brandes, 1979 K. W. Johnson et al., 1980).

An additional point that must always be kept in mind is the importance of the beam-flow angle. If, for example, flow is non-uniform but is perpendicular to beam, a weak stretching zone may result when in fact strong divergence exists. Worse still, a zone may fall below the threshold value when one actually exists. Since we are attempting to sense strong areas of radial stretching and cross-beam shear that extend over several kilometers, this problem may not be as serious as it first appears. Nonetheless, estimates of the spatial yields will be biased on the low side under unfavorable beam-flow

alignments; knowing the beam-flow angle allows some subjective compensation of this effect.

Grid Errors

Since a new gridding program was developed for this study, considerable effort was expended in quantifying the errors introduced by the necessary assumptions. This was especially true in estimating errors in the beam geometry calculations.

Inherent gridding errors are introduced by transforming the radar data from spherical to rectangular coordinates. A common procedure is to define the grid base as coincident with a ray of elevation 0° . This convention was used in this study. Since the ray path curves, a grid base defined in this manner will not be orthogonal in all three dimensions. Deforming this grid into a completely orthogonal one does not introduce serious errors. Brown et al (1980) have shown an error of 0.3% for columns 30 km apart at a height of 20 km.

If the range of interest is relatively close to the radar, height calculations can be made by simple trigonometry with curvature neglected. Errors introduced by beam bending increase slowly with increasing range. At 10 km, the difference in heights calculated with and without bending is only 0.002 km. This difference increases to 0.15 km at 50 km, 0.40 km at 80 km, and 0.58 km at 100 km. All these errors are well within the position uncertainty due to beam spreading. Tests of objectively analyzed maps produced with heights computed by the two methods showed no significant differences within 100 km of the radar.

Heights computed by (F.4) are subject to errors in range (r') and the accuracy of the elevation angle measurements. At 100 km with a symmetric beam width of 0.8° , the uncertainty in the position measurement is ± 1.4 km. At this range the effect of errors in the elevation angle (accurate to about ± 0.05) are smaller. The range measurements along the beam are a function of recording mode. Normal-mode data can refine a location to 150 m, and expanded mode data are averaged over 600-m bins.

Another source of error results from the objective analysis schemes. Early in the planning of this study, a hypothesis was formulated that contoured maps of reflectivity produced by exponential weighting of the data would be different from those produced by linear-quadratic interpolation (Greene, 1971). Since both techniques use the same contouring package (adaptation of NCAR CONREC), the objective gridding routines would account for the differences. When identical data were processed, the resulting maps were nearly identical at all levels. A comparison of radial velocity maps showed the same results. Since the difference hypothesis was rejected, plans to compute root-mean-square errors by grid point for comparison with Greene's algorithm were abandoned. Errors introduced by gridding are similar to those computed by Greene (1971).

This result is not surprising. Brown (1980) noted that all interpolation schemes used in Doppler analysis produce many similar results. Heymsfield (1978) has also shown that even sophisticated statistical interpolation schemes do not significantly improve the accuracy in handling dual-Doppler data, and they often significantly

increase the run time.

A final gridding error is introduced by the hardware used in producing the computer plots. The variability in the Versatec plotter paper feed produces maps with an east-west resolution of ± 0.75 km on a 100-km scale. No north-south variation was noted.

Spatial Density Function Analysis

When data are gridded, some information is lost. In this investigation a 1-km Cartesian grid spacing was selected. If the bulk of the data information were resident in wavelengths less than 1 km, subsequent analysis would be meaningless. Since many investigators (Brandes, 1977; Heymsfield, 1978) grid radar data in a fashion similar to the techniques developed in this experiment, a hypothesis was formulated that most of the data information would be resident at wavelengths considerably longer than twice the grid distance.

To test this idea a spatial density spectrum algorithm was derived. This algorithm is analogous to the temporal density spectrum commonly called "power spectrum." In power spectrum analysis, an implicit assumption is that one samples data at a point over time. The resulting spectrum is a function of frequency. In a spatial density spectrum, one assumes all data are sampled at the same instant. Radar data comprise neither a pure time spectrum nor a pure spatial spectrum. The pulses, which are recorded at one point, represent data from points along the radar beam. Over a small time interval, e.g., the time to record 2046 sample gates, one can assume the data are sampled instantaneously. This suggests that a spatial density

spectrum would give a good representation of the wavelength information. In addition, a spatial spectrum is a function of wavelength (or wavenumber), which is directly comparable to grid distance. Details of the algorithm are described in Appendix H.

The results of three typical spatial density plots for reflectivity, radial velocity, and spectrum width information are shown in Fig. F.2a, b, and c. The data used in these plots were selected at random, with 2046 expanded mode samples for each field. The data had been interpolated onto a polar coordinate grid by an exponential weighting function. A fast Fourier transform (FFT) method was used to compute the spectra. Applying a hanning smoother ten times reduces the amplitude of the $10 \Delta x$ wave by 63%. After 100 applications, the $10 \Delta x$ waves vanish into the noise level. A more direct approach to producing smooth spectra is to use auto correlation techniques (Blackman and Tukey, 1958). In this study, the main concern is to determine if gridding the data maintains significant wavelength information beyond that resolvable by the grid.

All the spectra analyzed showed patterns similar to those in Figs. F.2a, b, and c. There is significant information beyond $2 \Delta x$ for the reflectivity and radial velocity. The spectra of the spectrum width data routinely contained a considerable number of zero values at the longer wavelengths. This suggests that the spectrum width fields typically contain information that is difficult to distinguish from the noise level. Most of the work with spectrum width data has concentrated on areas with mesocyclones. Spectra in these areas may differ from the random samples examined in this study. Data recorded

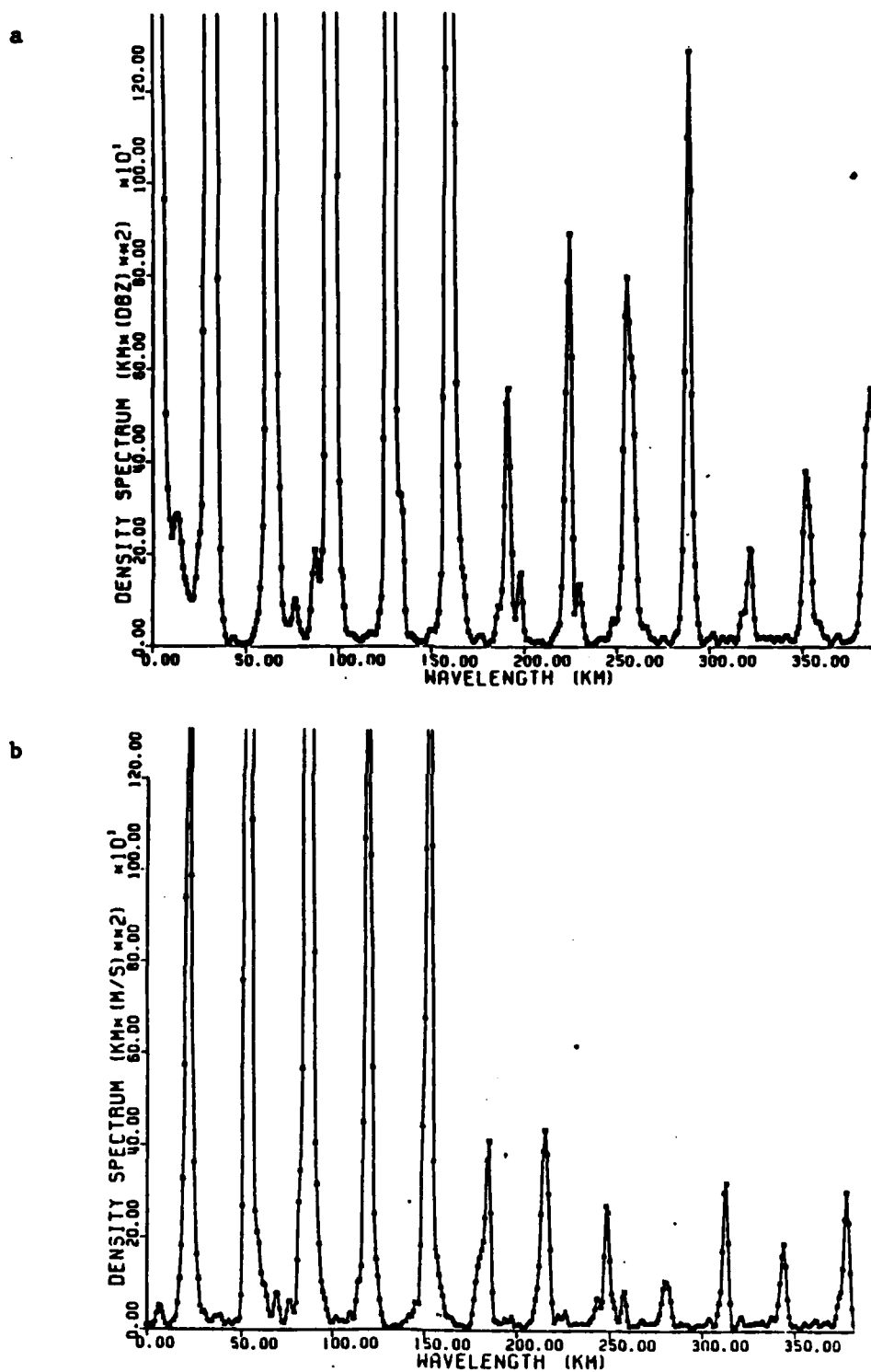


Fig. F.2. Spatial density spectrum. (a) Reflectivity. (b) radial velocity.

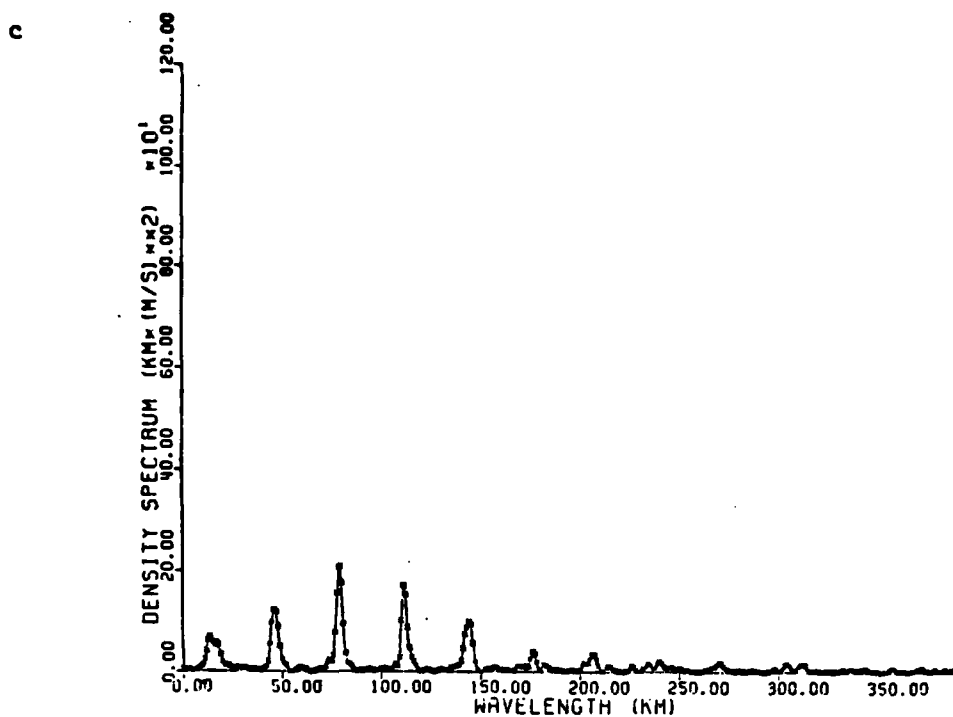


Fig. F.2. (Continued) (c) Spectrum width.

in a high PRF mode should also improve the detection problems encountered with the spectrum width data.

Interestingly, these ideas tend to confirm those of Battan and Theiss (1971), who found 94% of spectrum width data consisted of values of 4 m s^{-1} or less. This makes a definitive interpretation of the cause of the variance a risky venture under typical sampling conditions.

Surface and Upper-Air Data

Minimal error analyses were made of the surface and upper-air data in comparison to the other data sets. These data sets are used exclusively to estimate approximate environmental conditions. A sensitive study showed that the mesonet data contained an average of one site per 15 km, with portions of the network containing considerably better data resolution. A storm midway between stations would have to influence (or be influenced by) a site 8 km away. For the type of intense convection under study in this investigation, this station spacing seems adequate. Nonetheless, errors introduced by assuming spatial continuity probably impact more upon the conclusions than other error sources such as instrument errors. This error could be reduced by analyzing the data more often and using a time-space transform (Fujita, 1963). This approach was considered but it would require extensive software development to handle the raw mesonet data. Since the impact of slightly imprecise surface data on the anticipated conclusion of this study is very small, this step was not taken. It should be emphasized that the author has no information to indicate

that the surface data are inaccurate or that the gridding and objective analyses schemes used introduce significant error. Experience in gridding and objectively analyzing the rainfall and Doppler data by procedures similar to the ones used at NSSL to process the mesonet data suggests that the errors are smoothed by the processing.

The upper-air data were taken with standard National Weather Service rawinsondes and then interpolated to levels 150 m apart with additional significant level information. The errors in the wind speed and direction are a function of elevation angle, altitude, and the balloon tracking system. Fuelberg (1974) has shown typical RMS speed errors are about $3\text{--}5\text{ m s}^{-1}$, while the RMS direction errors are about $5^{\circ}\text{--}10^{\circ}$ below 500 mb. Temperature errors are less than 1°C (RMSE), relative humidity has a RMSE of 10% and RMS height errors are less than 20 GPM below 5 km.

A check of the propagation of temperature and relative humidity errors on the θ_w calculations showed that their impact was small. Typical height errors, which increase with altitude, contributed less than 1% to the total θ_w error. Temperature errors of 1°C resulted in a 2% error of θ_w for arbitrary low, mid- and high-altitude calculations. The most significant error source is that involving the relative humidity. A 10% error in the relative humidity resulted in a 6% θ_w error at the surface. Similar humidity errors at higher altitudes had less effect on θ_w , and dropped to 4% at 3 km and 3% at 5 km. The combined effect of typical rawinsonde errors on θ_w are summarized in Table G.1.

This appendix has attempted to address some of the more important

TABLE F.1. Errors in potential wet-bulb temperature with altitude.

Height (GPM)	θ_w Error (%)
550	6%
3000	4%
5000	2%

Based upon typical soundings with sensor errors of 1°C for temperature, an RH error of 10%, and a height error of 10 GPM at 3000 m and 20 GPM at 5000 m (from Fuelberg, 1974).

sources of error in this investigation. Many of these errors are difficult to quantify. Some may be significant. The cumulative effect of the different errors also is difficult to estimate. It is hoped that they are randomized throughout the time and space scales of this study. Some of the unusual flow patterns discussed in the next appendix may be due to anomalous flow, but they also may be due to a sporadic accumulation of significant errors. While it may be expedient to assume that the errors are randomly distributed, it is never prudent to ignore their effect.

APPENDIX G

Spatial Density Spectra

This derivation follows that presented in Bendat and Piersol (1971) for temporal data.

Given a record of spatial data with a total length of 24 km and discrete data every 1 km, one can define a Nyguent wavelength (λ_{\min}) below which only noise exists. If the sampling distance decreases, one can sense shorter wavelengths of real data. Conversely, if the sampling distance increases, the cutoff wavelength for real information also increases.

If Δx is 1 km,

$$\lambda_{\min} = 2 \text{ km.}$$

The number of points in the sample is simply the total distance (L) divided by Δx , and it is defined as N. We can define our data as an infinite Fourier transform of a real (or complex) record, $X(\ell)$, where $\ell = 2\pi/\lambda$, the wave number. Therefore

$$X(\ell) = \int_{-\infty}^{\infty} x(x) e^{-i\ell x} dx \quad (G.1)$$

If we restrict the limit to a finite interval (0, L), we have a finite Fourier transform

$$X(\ell, L) = \int_0^L x(x) e^{-i\ell x} dx \quad (G.2)$$

If the data are sampled at N equally spaced intervals x apart, then

$$x_n = x(n\Delta x), \quad n = 0, 1, 2 \dots N-1, \text{ or}$$

$$x_n = \Delta x \chi_n.$$

We can write equation (G.2) in discrete for M

$$X(\ell, L) = \Delta x \sum_{n=0}^{N-1} \chi_n \exp^{-i\ell n \Delta x}. \quad (G.3)$$

The raw density spectrum can then be defined by

$$\tilde{G}_x(\ell) = \frac{2}{L} [X(\ell, L)]^2. \quad (G.4)$$

If one defines a fundamental wave number, (ℓ_k) , as

$$\ell_k = k\ell = \frac{2\pi k}{L} = \frac{2\pi k}{N\Delta x}, \quad k = 0, 1, 2 \dots N-1,$$

the Fourier components of ℓ_k are given by

$$X_k = X(\ell_k, L) = \Delta x \sum_{n=0}^{N-1} \chi_n \exp \frac{-ikn2\pi}{N}, \quad (G.5)$$

where $k = 0, 1, 2, \dots, N-1$.

Then the spatial density spectrum becomes

$$\tilde{G}_k = \tilde{G}_x(\ell_k) = \frac{2}{N\Delta x} |X(\ell_k, L)|^2 = \frac{2\Delta x}{N} |X_k|^2, \quad (G.6)$$

where $|X_k|^2 = (RX_k)^2 + (IX_k)^2$.

APPENDIX H

PRECIPITATION CLIMATOLOGY

In an effort to determine if the rainfall rates on the three days of interest were unusual, climatological estimates of the 1-min point rates were calculated. The method used is described by Davis and McMorrow (1976). Briefly, one compiles clock-hourly precipitation amounts over an extended period, e.g., 10 hr, conditional on precipitation occurring at a particular location. These data are then stratified by precipitation rate categories, by month, as illustrated in Table H.1. An annual distribution of the number of clock hours for each precipitation rate category or a distribution of the mean number of hours of precipitation by month is easily tabulated by summing the appropriate rows or columns of the table. A scan of Table H.1 shows that for Oklahoma City, May is the month with the highest mean number of hours of precipitation and also the month of the highest rainfall rates.

One must realize that clock-hourly data by their very definition (precipitation recorded from on the hour to 59 min, 59 sec after the hour) act as a smoother of the actual precipitation distribution. A high rainfall rate that spans two clock-hourly increments will be smoothed into two moderate rainfall intensities. Consequently clock-hourly data tend to underestimate high rainfall rates associated with thunderstorms. The best way to minimize this problem is to start recording when precipitation begins and stop when it ends. If automatic digitization is used, sampling over small time steps and then

integrating will produce more realistic precipitation distributions. Both of these options require sophisticated sampling procedures which are seldom available for a dense raingage network. The next best solution is to minimize the sample time for a clock-hour time summation. While a clock 15-min time sample was used in this study, this relatively large sample interval is far from optimum for convective storms. Several investigators (see Jones and Sims, 1978) have published records of clock 1-min intensity distributions for a variety of locations. From these data one can estimate the 1-min distributions for other locations with a few assumptions.

If one assumes that the 1-min and clock-hour rainfall rate distributions for spring thunderstorms in rural central Illinois (Urbana) are similar to the rainfall rate distributions for spring thunderstorms in central Oklahoma (Oklahoma City), one can estimate the 1-min distribution for Oklahoma if the central Illinois distribution is known. This assumption allows for differences in total rainfall at two locations due to more storms or other variations (see Table I.2 and Table H.3). The procedure involves simply scaling the Oklahoma clock-hourly data by the Illinois clock 1-min percentage by the clock-hourly rate category. The result is an estimate of the clock 1-min precipitation distribution for a point in Oklahoma. In this study we desire a close similarity of the higher end of the precipitation distributions for the two sites. Aberrations in the similarity at low rates will not affect the conclusions. The similarity comparison can be made with monthly, seasonal, or annual data under suitable assumptions. A comparison made with annual distributions usually does not

TABLE H.1. Precipitation data for Oklahoma City, Oklahoma, 1968-1977.

mm hr ⁻¹	CLOCK-HOUR DATA (HOURS)												
	JAN	FEB	MAR	APR	MAY	JUN	JUL	AUG	SEP	OCT	NOV	DEC	ANNUAL
< 0.5	9.0	11.0	10.1	7.6	6.8	3.9	3.7	3.9	9.4	7.6	8.0	9.5	90.5
0.5 - 2.4	10.9	14.0	20.2	12.4	11.7	11.1	8.8	8.8	15.0	18.8	17.1	11.9	160.6
2.5 - 6.2	2.0	1.9	6.2	6.2	10.1	3.8	3.4	3.4	7.8	7.2	3.5	2.1	57.6
6.3 - 12.6	0.5	0.8	0.9	1.6	3.4	2.7	2.3	1.7	2.2	1.6	0.6	0.2	18.5
12.7 - 25.3			0.6	1.1	1.3	1.3	1.1	1.1	1.3	0.8	0.4	0.1	9.1
25.4 - 50.7				0.2	1.0	0.3	0.3		0.6	0.1			2.5
> 50.7													
MEAN PRECIP (mm)	24.1	31.0	63.8	72.4	140.0	85.3	72.4	55.4	112.0	78.0	41.6	26.4	802.0
MEAN # DAYS > .25 mm	5.2	5.6	7.3	7.4	9.9	7.6	6.0	5.7	7.8	7.1	5.8	5.2	80.6

TABLE H.2. Clock hour precipitation rate distributions (number of hours).

	Oklahoma City, OK (1968-1977)			Urbana, IL (1965-1974)		Wet Season Model (per mo.) ¹	ANN
	MAY	JUN	ANN	MAY	JUN		
mm hr^{-1} < 0.5	6.8	3.9	90.5	7.4	6.1	2.7	132.3
0.5-2.4	11.7	11.1	160.6	24.7	12.3	16.2	299.7
2.5-6.2	10.1	3.8	57.6	8.4	7.0	5.8	78.2
6.3-12.6	3.4	2.7	18.5	1.9	3.2	2.5	22.3
12.7-25.3	1.3	1.3	9.1	0.6	0.9	1.2	7.9
25.4-50.7	1.0	0.3	2.5	0.2	0.2	0.2	1.2
> 50.7							0.1

¹Compiled from 1 min data (from Davis and McMorrow, 1976).

TABLE H.3. Clock hour precipitation rate distributions - annual (number of hours).

	Urbana, IL ¹	Pleiku, Vietnam ²	Bet Dagan, Israel ²
mm hr^{-1} < 0.5	38.1	45.4	33.8
0.5-2.4	199.2	224.3	185.5
2.5-6.2	61.4	75.1	73.1
6.3-12.6	20.9	26.1	22.9
12.7-25.3	9.0	13.6	1.1
25.4-50.7	1.0	6.3	0
> 50.7	0	1.0	0

¹Compiled from 1 min data.

²Compiled from 4 min data.
(from Davis and McMorrow, 1976)

introduce significant bias because the very high rainfall rates are due primarily to spring thunderstorm rainfalls in the wetter months. It should also be noted that while Oklahoma City clock-hour data do underestimate the high rates, the same is true for the Urbana, Illinois, data. The normalization process accounts for this variance since the conversion multipliers are ratios of the two clock-hour distributions for each rate category. If it is assumed that both locations underestimate the high clock-hour rates by a similar amount, the estimate of the 1-min rate distribution for Oklahoma City based on that measured at Urbana may be reasonably good. The results of this analysis appear in Table H.4.

Since the variance in rainfall rates increases as the sampling interval decreases, the climatological clock 1-min rate distribution should have more hours of high-intensity rates than the climatological clock 15-min rate distribution. If a sampled clock 15-min rate distribution, selected at random, contains more time of higher rates, after normalization, than the 1-min distribution, then that sample is experiencing extremely high rates. Table H.5 illustrates these ideas for the three periods in 1977 examined in this study and compares them to the climatologically expected values. The table contains the three maximum grid-point rainfall rate values for 15-min periods. One minute rates will be considerably higher.

These data suggest that moderate to high rainfall rates occurred on 1 May 1977, while 19 and 20 May experiences excessively high rates beyond climatologically expected values. An extreme value analysis could be conducted to estimate the return period of such rare-event

TABLE H.4. Estimated 1-min rainfall distribution (in hours) for Oklahoma City, Ok (May).

CHR*/1 MR*	< 0.1	1.0	2.5	6.3	12.7	25.4	50.8	127	> 254	TOTAL
		2.4	6.2	12.6	25.3	50.7	126	253		
< 0.5	5.85	0.76	0.17	0.008	0.006	-	-	-	-	6.8
0.5-2.4	7.10	3.16	1.22	0.17	0.039	0.014	0.001	-	-	11.7
2.5-6.2	3.05	1.95	3.47	1.20	0.290	0.013	0.017	-	-	10.10
6.3-12.6	0.854	0.376	0.757	0.747	0.412	0.196	0.005	-	-	3.4
12.7-25.3	0.272	0.117	0.199	0.191	0.212	0.181	0.116	0.112	-	1.3
25.4-50.7	0.067	0.056	0.089	0.133	0.194	0.200	0.256	0.006	-	1.0
> 50.7	-	-	-	-	-	-	-	-	-	-
	17.20	6.42	5.90	2.45	1.15	0.72	0.45	0.02**		34.30

*Units are mm hr⁻¹

**Model estimates about 1 min of rainfall 127 mm/hr.

TABLE H.5. Maximum grid point 15-min rainfall rates (mm hr^{-1}) and ending times of occurrence (CST).

1 May 77	19 May 77	20 May 77
104 (1800)	201 (1530)	176 (1700)
95 (1745)	158 (1545)	175 (1715)
73 (1845)	148 (1445)	165 (1715)

Estimated time of maximum 1 min rate for:

Oklahoma City, OK > 127 mm hr^{-1} for May 1 min.

Urbana, IL > 127 mm hr^{-1} for one wet season month 0.7 min.

Estimated time of maximum 4 min rate for:

Pleiku, Vietnam > 127 mm hr^{-1} for one wet season month 8.4 min.

Bet Dagan, Israel > 127 mm hr^{-1} for one wet season month 0 min.

statistics, but that would only reinforce the point that it rained heavily on 19 and 20 May 1977.

High rainfall rates in themselves do not constitute a serious problem, but if they persist for an extended period (several hours), serious flooding will develop if the ground conditions warrant. On 19 and 20 May 1977, serious flash flooding was observed throughout the Washita watershed.

APPENDIX I

SYNOPSIS OF SURFACE RAINFALL FOR THE DEL CITY-HAILSTORM MERGING

Light rainfall rates were observed (peak 18 mm hr^{-1}) prior to 1630. During the 1615-1630 period, the Hailstorm had entered the raingage network. Between 1630 and 1645 the Hailstorm showed a peak rainfall intensity of 131 mm hr^{-1} (see Table I.1). This was located on the left front flank of the storm and not associated with the peak reflectivity. The rainfall axis was nearly aligned with the storm motion track. On the next map, the left front cell intensity weakened to a rate of 71 mm hr^{-1} , while a new core was observed on the left rear of the Hailstorm between the reflectivity core and the suspected updraft. Intensity of the new core was 131 mm hr^{-1} . This might lead to a conclusion that the "new core" was really the old core from the previous map with the 71 mm hr^{-1} rate simply new development. Such an explanation would require the 131 mm hr^{-1} core to move at 5 m s^{-1} while the storm at 1 km is moving at 14 m s^{-1} . The Del City storm also entered the raingage network during the 1645-1700 period with a maximum rate of 176 mm hr^{-1} . The rainfall axis shifted to a northeast-southwest alignment with individual cells still aligned in a more east-west manner. The 1700-1715 period showed little change in the Hailstorm rainfall intensity or area. The two-cell configurations translated to the northeast at about 12 m s^{-1} . The Del City storm rainfall followed the lower edge on the network and moved east at 20 m s^{-1} while maintaining an extremely high rate in the core (165 mm hr^{-1}). The Del City storm was now east of Hailstorm. The

TABLE I.1. Summary of peak rainfall rates and areas of Del City-Hailstorm complex.

20 May 1977	Cell Location (Distance from NSSL of maximum rate)	Maximum Grid Point Rates (mm hr ⁻¹)	Area of $\frac{25 \text{ mm hr}^{-1}}{55 \text{ mm hr}^{-1}}$ Rates (km ²)	
Time (CST)				
1615-1630	<u>C1</u> 56W 58W	18	0 — 0	
1630-1645	<u>C1</u> <u>C2</u> 56W 56W 58S 43S	37 131	36 109 — 0 33	
1645-1700	<u>C2</u> <u>C3</u> <u>C4</u> 52W 52W 64W 26S 38S 54S	71 131 176	49 ← 267 → — 5 190	
1700-1715	<u>C2</u> <u>C3</u> <u>C4</u> 44W 48W 50W 14S 30S 52S	63 129 165	← 468 → — 5 38 113	
1715-1730	<u>C5</u> <u>C2</u> <u>C4</u> 37W 44W 34W 46S 10S 28S	68 62 104	← 575 → — 12 3 135	
1730-1745	<u>C5</u> <u>C2</u> <u>C4</u> 32W 39W 25W 30S 10S 18S	81 65 129	← 616 → — 15 8 139	
1745-1800	<u>C2</u> <u>C4</u> 26W 24W 4N 10N	33 146	36 241 — 0 134	
1800-1815	Storms beyond network			

precipitation pattern was aligned in a broad north-south configuration.

The next time frame, 1715-1730, showed a severely weakened Hailstorm with only the original left front flank cell remaining at about 65 mm hr^{-1} . The Hailstorm's southern core had been absorbed by the Del City storm. A small new development was occurring due south of the major core. Intensities weakened as the storm shifted its track and reorganized its internal structure. A bow-shaped precipitation pattern developed, with the vortex of the bow showing the direction of storm motion. The bow pattern was also evident for the 1730-1745 period but its dimensions were more compact. Peak storm rainfall intensity was now increasing while translation speed of the precipitation remained at 12 m s^{-1} to the northeast. The storm complex remained over the network for one additional 15-min period with little change in its configuration and small changes in rainfall intensities.

APPENDIX J

SYNOPSIS OF SURFACE RAINFALL FOR THE FT. COBB STORM

The first reliable rainfall map was valid for the 1645-1700 period (see Table J.1). During this time, a strong mesocyclone was observed east-southeast of the peak precipitation. Very high rainfall rates over a relatively large area were observed downshear on the left storm flank. After the tornado dissipated, the mesocyclone maintained its circulation and the rainfall rate increased. The rainfall core moved into a more northeast-southwest alignment with the highest rates still on the left flank. Rainfall on the right flank was relatively light and none was observed upwind of the storm motion direction. At 1715 another mesocyclone and tornado appeared northeast of the old one. The tornado appeared on the boundary of the suspected updraft zone and the 45-dBZ isopleth near the hook pattern. Rainfall rates decreased in intensity and areal coverage. The rainfall intensity map for 1730-1745 contains only the remnants of the storm that were quickly moving beyond the raingage network, so it is difficult to verify an additional increase in precipitation.

A comparison was also made of the rainfall pattern from the 1 May storms. Two mesocyclonic patterns were observed in the 5-km radial stretching map. One associated with the splitting storms was a partial pattern, while the other associated with the companion cell to the northwest was more symmetric. The companion cell pattern occurred during the time period of the most intense and largest areal coverage of the precipitation. The splitting storm precipitation maximum

TABLE J.1. Summary of peak rainfall rates and areas for the Ft. Cobb storm.

20 May 1977	Cell Location		Maximum Grid Point Rates		Area of	
Time (CST)	(Distance from NSSL of maximum rate)		(mm hr ⁻¹)		25 mm hr ⁻¹ 55 mm hr ⁻¹	Rates
					(km ²)	
1615-1630	D1 84W	D2 89W	15	58	0	86
	25N	14N			0	0
1630-1645	D1 78W	D2 91W	38	49	←199→	
	18N	00			0	
1645-1700	D2 90W	D3 84W	103	88	←497→	
	6N	25N			170	92
1700-1715	D2 88W	D3 80W	175	127	←530→	
	14N	25N			←294→	
1715-1730	D2 84W	D3 76W	116	83	←312→	
	18N	26N			←153→	
1730-1745	D2 87W	D5 87W	29	19	45	
	18N	8S			0	0
1745-1800	D2 82W	D5 88W	26	33	1	54
	20N	4S			0	0
1800-1815	D2 93W	D5 86W	29	41	22	294
	25N	6N			0	0
1815-1830	D6 87W	D5 72W	43	61	49	260
	8S	6N			0	19
1830-1845	D6 91W	D5 67W	76	113	←520→	
	2S	20N			57	77

TABLE J.1. (Continued).

20 May 1977	Cell Location	Maximum Grid Point Rates	Area of		Rates	
Time (CST)	(Distance from NSSL of maximum rate)	(mm hr ⁻¹)	$\frac{25 \text{ mm hr}^{-1}}{55 \text{ mm hr}^{-1}}$	(km ²)		
1845-1900	D6	D5	76	94	408	133
	84W	67W	76	94	—	—
	3N	19N			130	95
1900-2100	New growth over western portions of network covering a considerable area with peak rates over 100 mm hr ⁻¹ until 2000					

(intensity and coverage) occurred just after the mesocyclone period. In both storms the precipitation cores were located east of the maximum rotational zones on the left storm flank. In addition, the mid-level mesocyclone patterns were observed on the same updraft-downdraft boundaries. Precipitation intensities increased during and after the mesocyclone patterns appeared. The area upwind of the mesocyclone patterns was devoid of precipitation. No tornadoes were observed with these storms, and the mesocyclone patterns were confined to the mid levels (higher than 3 km). These results lend support to the vortex valve theory (Lemon *et al.*, 1975), which implies an decrease in rainfall with the development of a strong rotation due to the conservation of energy. The location of the increased precipitation close to the updraft zone is consistent with the idea of increased liquid water loading.

APPENDIX K

SYNOPSIS OF SURFACE RAINFALL FOR THE SQUALL LINE (19 MAY 1977)

Table K.1 summarizes the squall-line precipitation patterns. The squall line entered the raingage network between 1330 and 1345. The low rainfall rates recorded at this time were due to cell-gage alignment and were not attributed to weak convection. The next rainfall period saw rates of 120 mm hr^{-1} . The 55-mm hr^{-1} area amounted to 103 km^2 . These rates were associated with the right-front flank of the Ft. Cobb storm. (The other supercell storms produced the highest rates along the left flank.) Inflow into the squall-line supercell was along the left flank. In each case, heavy rain fell under the location of the mid-level portion of the updraft. The 1400-1415 period saw a general increase in rainfall rates. The total 55-mm hr^{-1} area had grown to 263 km^2 with most of the increase resulting from the principal Ft. Cobb echo. The highest rates continued to fall on the right-front flank of the supercell. The satellite cell produced rates above 65 mm hr^{-1} during this period. The radial velocity maps showed an increase in the moisture jet into the northern side of the storm at 1400. This pattern was very similar to the one noted in the later Gracemont storm, which also produced high rainfall rates. Peak rates decreased between 1415-1430. The area of the 55-mm hr^{-1} isopleth also dropped 210 km^2 . This decrease in size was due to a shrinking of both the Ft. Cobb parent cell and its satellite. The 1430-1445 period showed the rainfall rates and areas increasing due to the development of the Gracemont echo south of the radar scan.

TABLE K.1. Summary of squall-line precipitation.

	Cell Location			Maximum Grid Point Rates				Area of			
	(Distance from NSSL of maximum rate			(mm hr ⁻¹)				25 mm hr ⁻¹ Rates			
	(km)							55 mm hr ⁻¹ Rates			
								(km ²)			
1345	<u>E1</u> 82W 26S	<u>E</u> 91W 00	<u>E3</u> 91W 16N	15	15	15					
1345-1400	<u>E1</u> 83W 27S	<u>E2</u> 80W 14S	<u>E4</u> 87W 9S	<u>E5</u> 97W 26N	39	120	75	72	52 — 0	←207→ — ←103→	Open
1400-1415	<u>E1</u> 84W 28S	<u>E2</u> 76W 6S	<u>E6</u> 56W 2S	<u>E7</u> 68W 25S	67	128	90	67	←768 339	36→ 223	9 28
1415-1430	<u>E2</u> 67W 2N	<u>E7</u> 68W 11S	<u>E8</u> 60W 43S	<u>E9</u> 76W 46S	136	77	55	66	←864 141	→ 26	1 43
1430-1445	<u>E2</u> 60W 10N	<u>E10</u> 51W 8N	<u>E8</u> 60W 36S	<u>E9</u> 72W 38S	148	102	121	120	←498 ←175	←767→ ←363→	
1445-1500	<u>E2</u> 45W 1S		<u>E8</u> 56W 30S	<u>E11</u> 63 14	68		152	95	←1086 24	→ ←289→	
1500-1515	<u>E2</u> 43W 1N		<u>E8</u> 52W 27S	<u>E12</u> 72W 46S	71		145	53	←1052 23	→ 276	117 0
1515-1530	<u>E2</u> 32W 2N	<u>E13</u> 56W 51S	<u>E8</u> 44W 22S	<u>E14</u> 60W 2S	68	91	201	54	246 58	←945→ 69	276 0
1530-1545	<u>E2</u> 31W 5N	<u>E15</u> 52W 48S	<u>E8</u> 32W 14S	<u>E13</u> 64W 54S	53	64	158	89	←878 22	→ 225	366 35

TABLE K.1. (Continued).

	Cell Location			Maximum Grid			Area of		
	(Distance from NSSL of maximum rate (km)			Point Rates (mm hr ⁻¹)			$\frac{25 \text{ mm hr}^{-1}}{55 \text{ mm hr}^{-1}}$ Rates (km ²)		
1545-1600	<u>E2</u>	<u>E8</u>	<u>E12</u>	94	126	41	← 1002 →		45
	32W 6N	32W 10S	56W 57S				← 481 →		0
1600-1615	<u>E2</u>	<u>E8</u>	<u>E16</u>	60	84	59	← 446 →		55
	27W 2S	23W 10S	38W 48S				18	110	1
1615-1630	<u>E2</u>	<u>E8</u>	<u>E16</u>	27	44	33	20	34	30
	24W 3N	23W 12S	25W 40S				0	0	0
1630-1645			<u>E16</u>						62
			20W 35S			35			0

The Ft. Cobb storm still was producing the highest peak rates (148 mm hr⁻¹), but its 55-mm hr⁻¹ isopleth area had decreased to 175 km². By comparison, the Gracemont 55-mm hr⁻¹ area was 363 km² with two cores of rates of 120 mm hr⁻¹. The radar maps at 1445 contained the only good look at the Gracemont storm. A weak jet intrusion north of the storm was evident, thus suggesting higher rainfall rates in the 1445-1500 period. The peak rates in the storm increased about 30 mm hr⁻¹ to 152 mm hr⁻¹ while the size of the 55-mm hr⁻¹ contour area decreased. The 1500-1515 period showed little change in the rainfall pattern. The 1515-1530 rainfall contained a peak rate of 201 mm hr⁻¹ with the 55-mm hr⁻¹ area remaining constant. Radar coverage of the echo was unavailable, but the 1515 map suggested a break in the echo line south of the 270° radial. The high rates of the Gracemont storm continued through the next period (1530-1545), while the Ft. Cobb satellite cell showed signs of a revitalization.

For the 1545-1600 period, the Gracemont cell began to weaken. Its peak rate dropped to 126 mm hr⁻¹. The Ft. Cobb satellite cell increased its peak rate to 94 mm hr⁻¹; however, it proved to be a short-lived increase. Table K.1 summarizes the demise of the squall line precipitation.

APPENDIX L

SYNOPSIS OF SURFACE RAINFALL FOR THE SPLITTING STORM (1 MAY 1977)

Light rainfall was observed over the raingage network prior to 1730. During the 1730-1745 period the peak rainfall rate increased to 62 mm hr^{-1} , however it was confined to a relatively small area. A strong increase in rainfall intensity (to 104 mm hr^{-1}) and area was noted in the next 15-min period (see Table M.1). The rainfall orientation was now ellipse-shaped with the major axis roughly perpendicular to storm motion.

The period 1800-1815 witnessed little change in the rainfall rates. The 55-mm hr^{-1} isopleth area, however, was nearly cut in half as the right flank updraft dominated the rainfall. The surface rainfall was located to just northeast of the 1-km reflectivity core at 1815. The first rainfall from the northwest companion cell was observed during this period. The peak rate of 48 mm hr^{-1} encompassed a 25-mm hr^{-1} isopleth of 17 km^2 . In the 1815-1830 period, the peak rates dropped in the parent storm as did the rainfall areas. This was reflected in a more vertical tilt of the updrafts. Little change in the peak rates was observed in the companion cell, while the 25-mm hr^{-1} area nearly doubled. By 1830 the core splitting had been completed and the environmental wind began to play a dominant role in enhancing the right-moving echo of the parent storm. Its rainfall rate increased to 73 mm hr^{-1} with a doubling of the 25-mm hr^{-1} isopleth area. The left moving cell actually decreased its peak rate and rainfall size. No change was evident in the companion cell. For the 1845-1900 period

TABLE L.1. Summary of peak rainfall rates and areas of splitting storm (Cell A) and companion storm (Cell B).

Time (CST)	CELL A				CELL B			
	(Distances from NSSL-km)		Maximum Grid Point Rate (mm hr ⁻¹)	Area of 25 mm hr ⁻¹ 55 mm hr ⁻¹ Rates (km ²)	(Distances from NSSL-km)		Maximum Grid Point Rate (mm hr ⁻¹)	Area of 25 mm hr ⁻¹ 55 mm hr ⁻¹ Rates (km ²)
	Max Cores or				Max Cores or			
	15 mm hr ⁻¹	15 mm hr ⁻¹			15 mm hr ⁻¹	15 mm hr ⁻¹		
1715-1730	A1 64W 14S		24	0 — 0				
1730-1745	A1 64W 14S		62	23 — 30				
1745-1800	A1 61W 15S		104	91 — 36				
1800-1815	A1 60W 18S		95	83 — 4	B1 80W 14N	48	17 — 8	
1815-1830	A1 59W 18S	A2 54W 5S	52 36	29 — 0	B1 78W 16N	49	47 — 0	
1830-1845	A1 60W 20S	A2 54W 5S	73 26	68 — 18	B1 79W 14N	45	49 — 0	

TABLE L.1. (Continued).

Time (CST)	CELL A				CELL B			
	(Distances from NSSL-km)		Maximum Grid Point Rate		(Distances from NSSL-km)		Maximum Grid Point Rate	
	Max Cores or		Area of		Max Cores or		Area of	
	15 mm hr ⁻¹	25 mm hr ⁻¹	55 mm hr ⁻¹	Rates (km ²)	15 mm hr ⁻¹	25 mm hr ⁻¹	Rates (km ²)	
1845-1900	A1 60W 20S	A2 55W 9S	A3 45W 5S	72 29 31 — 17 0	70 —	7 3 —	32 —	14 0
1900-1915	A1 59W 22S	A2 55W 10S	A3 44W 5S	28 52 42 — 0 0	2 0	72 0	42 0	
1915-1930	A2 52W 10S	A3 32W 2S		63 55 — 1	28 1	32 1		
1930-1945	A3 32W 2S			71 —		41 —		
1945-2000	No rainfall							

the right-moving cell remained strong while the rainfall from the left-moving cell revealed fragmented dual cores, both with weak intensity. After 1900, the right-moving cell quickly dissipated while the right portion of the left-moving storm intensified. Dissipation of the left-moving cell began after 1915, and by 1945 the complex had nearly vanished from the raingage network.

VITA

Daniel J. McMorrow was born in New York City, New York on 9 Dec 1947, to Patrick J. and Mary A. McMorrow. He was raised in College Point, New York where he attended parochial school and later graduated from Holy Cross High School in nearby Bayside.

In 1965 he entered New York University's School of Engineering from which he graduated with a Bachelor of Science Degree in Oceanography and Meteorology in 1969. In 1970 he received a Master of Science degree in Air Pollution Meteorology from New York University, as a USDPH fellow. In 1971 he entered the United States Air Force and served in a variety of operational and applied research positions with the Air Weather Service. He received a Master of Arts degree in Business Management from Webster College in 1977.

The author entered Texas A&M University in August, 1978 to pursue the degree of Doctor of Philosophy under the auspices of AFIT. His permanent mailing address is 1022 117th Street, College Point, New York 11356.

